Studies of acoustic scattering using a parametric array

Beckett, Carolyn

Award date:
1992

Awarding institution:
University of Bath

STUDIES OF ACOUSTIC SCATTERING USING A PARAMETRIC ARRAY

submitted by Carolyn Beckett
for the degree of PhD
of the University of Bath.

1992

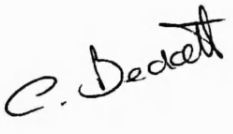

ProQuest LLC
789 East Eisenhower Parkway
P.O. Box 1346
Ann Arbor, MI 48106-1346

Abstract

The development of an experimental system and measurement technique to measure the scattering from discrete objects immersed in a fluid is described. A parametric array is used to provide a broad - band transient pulse. This enables the scattering response to be determined over a wide range of frequencies, typically 10 - 200kHz, and allows individual scattering returns to be identified.

Experimental measurements of the scattered field from spheres, cylinders and cylindrical shells have been obtained at arbitrary observation points, including the backscatter direction, and assuming a normally incident wavefield. Comparison of the results for cylinders with the 'form function' predictions revealed significant differences. A theoretical modification is presented to account for the plane wave spectrum of the parametric array and excellent agreement is obtained between the modified form function and the experimental data. It is also shown that, to a first approximation, the amplitude variations caused by the non-planar nature of the wavefield can be accounted for by a geometrical spreading factor.

For an obliquely incident wavefield the modified theoretical prediction of the form function is acceptable only at small angles of incidence. Experimental data and theoretical predictions are presented and the probable causes of the discrepancies discussed.

Complementary to the main body of this work, theoretical predictions are presented of the pressure distribution in the inner fluid of a cylindrical shell. This is of particular interest under resonance conditions when standing wave patterns are formed. A Schlieren system has been used to identify the resonances of a submerged, water filled brass shell. Resonances of the shell, the fluid column and Stoneley wave resonances were observed. Comparison of theoretical and observed images demonstrated excellent agreement, as did a comparison of the predicted and measured frequencies, which agreed to within 0.3% for the fluid column resonances.

Acknowledgements

There are many people I have to thank for their help and encouragement during the course of this work. Particular thanks must go to Victor Humphrey and Prof Berktay for their invaluable advice and guidance; Sharon Knapp who developed the Schlieren system and obtained the photographs shown here; Brian Gay for his advice and help with the fittings for the tank and for teaching me to play skittles and all those who, over coffee, knowingly or unknowingly, gave advice or help.

I am also grateful to The Procurement Executive of the Ministry of Defence for their financial support whilst at the University, and the support of Ray Bartlett and my colleagues at YARD / BAeSEMA during the writing up phase of this work.

Most of all I have to thank Andrew, for his love, humour and support.

Table of Contents

Abstract i
Acknowledgements ii
Table of Contents iii

1 Introduction 1

2 Experimental Facility 5
2.1 Background 5
2.2 Parametric Array 7
2.3 Equipment and Operation 8
2.4 Experimental Technique 9
2.5 Characteristics of the Experimental System 11
2.5.1 Acoustic Filter 11
2.5.2 Axial Field 11
2.5.3 Beam Characteristics 12
2.5.4 Hydrophone Shadowing 12
2.5.5 Pulse Shapes and Windowing 14
2.6 Potential Limitation of the System 15
Figures 17
19

3 A Theoretical Approach to Scattering 40
3.1 Normal Mode Series 40
3.2 Resonance Scattering Theory 41
3.3 Sommerfeld - Watson Transformation 42
3.4 T - Matrix 42
3.5 Other Techniques 43

4 Spheres 45
4.1 Literature Survey 45
4.2 Theory 48
4.3 Theoretical Predictions and Discussion 50
4.4 Experimental Results and Discussion 52
4.5 Summary 53
Figures 54

5 Solid Cylinders 60
5.1 Literature Survey 60
5.2 Theory 63
5.3 Computational Results and Discussion 68
5.4 Experimental Results : Normal Incidence 71
5.4.1 Plane Wave Spectrum 73
5.4.1.1 Theory 73
5.4.1.2 Results and Discussion 76
5.5 Experimental Results : Oblique Incidence 77
5.6 Summary 80
Figures 81

6 Circular Cylindrical Shells 105
6.1 Literature Survey 105
6.2 Theory 107
6.3 Computational Results and Discussion 109
6.4 Experimental Results and Discussion 112
6.5 Summary 114
Figures 115

7 Resonances in the fluid column of a cylindrical shell 129
7.1 Introduction 129
7.2 Theory 130
7.3 Results and Discussion 132
7.4 Summary 137
Figures 138

8 Conclusions and Recommendations 145

References 148

Appendix 1 Nomenclature 157
Appendix 2 Two models of a Parametric Array 161
Appendix 3 Material Properties 165
Appendix 4 Scattering Coefficient B_n for a solid elastic cylinder 166
Appendix 5 Implementation Notes 168
Appendix 6 Scattering Coefficient B_n for a circular cylindrical shell 170

Appendix 7 Scattering Coefficient A_n for scattering within a cylindrical shell ... 173

Appendix 8 Theoretical expression for the optical image of an acoustic field in a Schlieren system 175

1 Introduction

The detection and identification of submerged objects is of prime concern to both military and commercial organisations, including the fishing and oil industries. Several techniques are currently available which could be used to establish the characteristics of a submerged target. However these are often severely restricted by the hostile operating conditions and environment to be found in open waters. Optical methods, for example, are limited in range due to the high attenuation at these wavelengths, whilst electromagnetic techniques are only applicable for a small selection of materials. One potential method, which has few serious limitations on either range or object material is to insonify the target with an acoustic field. It should then be possible to establish the characteristics of, and ultimately identify, the object by examining the scattered field.

Clearly, in establishing the characteristics of an object from its scattered acoustic field one has to understand the factors that contribute to the scattered field. The shape and amplitude of an acoustic signal returned from a target will depend on a large number of variables. In the majority of published work, and certainly in the investigation that follows, a discrete target in a homogeneous fluid is considered, and so multiple scattering effects due to the close proximity of other targets (or the medium) are ignored as are the effects of a solid medium in contact with the object (for example, an object lying on the sea bed). Also neglected are any effects due to variations in the fluid medium - a pertinent factor when dealing with long range scattering in an ocean environment. With these restrictions the scattered signal will, for example, depend upon the shape, size, composition and material characteristics of the target, the frequency content and the nature of the incident wavefield, and the distance and direction of the receiver from the target. In order to limit the number of parameters to be assessed and hence reduce the problem there are several simplifications one can make. One could consider, for example, simple geometric objects such as spheres or cylinders; the target to be rigid (so there is no penetration of sound into the object); the incident wavefield to be a monochromatic plane wave; or the source and receiver to be coincident (monostatic).

In early theoretical work many, or indeed all, of the above approximations were made. Rayleigh (1878) was one of the first to theoretically model the acoustic scattering from a rigid sphere assuming a monochromatic plane wave in the limiting case where the scatterer is small compared to the wavelength. The solution for scattering by rigid spheres and cylinders was given by Morse (1948). Subsequent studies have examined a variety of targets of differing compositions and configurations and have employed analytical techniques involving both approximate and exact theories. Faran (1951) and Hickling (1962) first proposed exact solutions to the problem of monochromatic plane wave scattering from elastic spheres and cylinders using a technique known as the Normal Mode Series Solution. This approach has a limited range of applicability, being confined to objects of separable geometry

and, due to computational problems, to low *ka* (wavenumber * radius) values (typically 0 - 20). Consequently, in more recent studies, the Normal Mode Series has been abandoned in favour of integral transform techniques, such as the Sommerfeld - Watson Transform (Doolittle, Überall & Ugincuis, 1968; Überall & Huang, 1976) which extends the calculation range, or matrix methods of evaluation (Waterman, 1969, 1976) which allow more complicated structures to be modelled (Varadan & Varadan, 1979). These theoretical techniques have permitted the study of spheres (Gaunaurd & Überall, 1983), circular cylinders, cylindrical shells (Flax & Neubauer, 1977), elliptical cylinders and shells (Pillai, Varadan & Varadan, 1982; Simon & Radlinski, 1982) and of finite length objects, particularly cylinders (Überall, Stoyanov et al., 1987).

In recent work the prime concern has been an understanding of the physical processes behind the scattering phenomenon. Although there are many analytical and numerical techniques to provide a prediction of the acoustic scattering, few do anything to enhance our understanding of the physical processes involved. The Sommerfeld - Watson Transform aids our understanding somewhat as the Normal Mode Series is recast into three separate series (Dickey, Nixon & D'Archangelo, 1983) each of which represents a different type of wave travelling in or around the object. Possibly more informative is the Resonance Scattering Theory (Flax, Dragonette & Überall, 1978) which explains the scattering phenomenon in terms of individual resonance modes of an object. By decomposing the total Normal Mode Solution into two components, a background contribution and a resonance contribution it is possible to identify the type and order of each resonance.

As our understanding of the scattering phenomenon is enhanced, and as computational hardware and software improves, it becomes feasible to develop theoretical models for more complex structures hitherto ignored. In developing such models it is essential that existing models as well as new ones are validated by careful experimental work if we are to have any faith in the theoretical predictions.

Compared to the amount of theoretical work published, experimental measurements to validate scattering models are relatively scarce. Much of the early experimental work was performed in lakes using low frequency tone bursts (50 - 150kHz) and objects 1/4" to 7" in diameter to achieve a *ka* range of approximately 4 - 60 (Barnard & McKinney, 1961; Hampton & McKinney, 1961). These measurements demonstrated that submerged spheres and cylinders could not be treated as rigid objects but that their elastic nature had to be accounted for. However the long tone bursts used made interpretation of the results more difficult than, say, a pulse of 2 or 3 cycles would have. More recent experimental measurements, whilst being conducted in smaller laboratory facilities using different frequencies and sized objects, have been obtained using both long tone bursts and short or transient pulses. Nevertheless measurements have largely concentrated on simple geometrical objects such as spheres and cylinders. Neubauer, Vogt & Dragonette (1974)

investigated metal spheres using long tone bursts to approximate steady state conditions. They used a single transducer and varied the size of the sphere from 0.25 to 2.5" in order to cover a *ka* range 0 - 20. Determination of the scattering characteristics using the above technique has the serious limitation that many transducers (frequencies) and / or many different sized objects are required to cover a significant *ka* range. Dragonette, Vogt, Flax & Neubauer (1974) successfully demonstrated the use of transient pulses to obtain the form function, a measure of the scattering, over a broad range of *ka* values with a single experiment. They measured the form function for both spheres and spheroids in air, where the form function closely approximates that for a rigid object. They used a pulse centred on 26kHz and a sphere 0.75" in diameter to cover a *ka* range 0 - 10. Dardy, Bucaro, Scheutz & Dragonette (1977) used a transient pulse based on 1MHz to determine the form function for 'effectively' infinite cylinders over a *ka* range 4 - 21. De Billy's (1986) experiments measured the form function of cylinders this time using cylindrical wires up to 0.7mm in diameter to cover a *ka* range up to 20.

The recent laboratory work, due to the *ka* range of interest, has involved small objects and high frequency pulses. This combination will almost certainly lead to difficulties when fabricating more complex structures. Ideally one would use lower frequencies so that larger objects could be used.

An alternative acoustic source that is able to produce a low frequency, short, broad - band pulse is a parametric array. This type of source uses the non-linear interaction of high frequency waves through an acoustic medium (water) to produce a low frequency pulse. The length and the shape (and hence frequency content) of the pulse can be controlled by modifying the envelope of the tone-burst transmitted (Berktay 1965). In addition it has a distinct advantage over a conventional source, in that a far greater frequency range can be covered with one transducer. In the following study a parametric array has been used to generate pulses centred between 20 and 100kHz. This means that to examine the *ka* region 0 - 20 say, one is able to use objects several inches in diameter. This permits more complicated objects to be fabricated with relative ease.

This thesis describes the development of an experimental system and measurement technique using the parametric array. The aim is to investigate the acoustic scattering from submerged objects so as to obtain a better understanding of the scattering phenomenon. A tungsten carbide sphere has been used as a target to assess the performance of the experimental system and to validate the technique. The choice of this target as a reference or standard was based on several criteria:- Firstly, the sphere has been used by many investigators in recent years and there is well documented theoretical and experimental data on its acoustic performance. Secondly, the very high density of tungsten carbide leads to quasi rigid behaviour at low *ka* values so that the scattered field is more readily analysed.

It is also worth noting that precision tungsten carbide spheres are relatively easy to obtain and are regularly used as calibration targets.

Subsequent measurements have examined the scattering from solid cylinders and cylindrical shells when insonified at both normal and oblique incidence. Also of interest are the differences between air filled and water filled shells. Due to the nature of this study individual chapters concentrate on different scatterers rather than a more conventional 'method - results - discussion' layout. Hence Chapter 2 describes the experimental system, its performance and some potential limitations. Chapter 3 briefly reviews several of the many theoretical techniques available that are mentioned or used in subsequent Chapters. The use of the experimental system to investigate the acoustic scattering from a tungsten carbide sphere, solid cylinders and cylindrical shells is described in Chapters 4, 5 and 6 respectively. Chapter 7 presents the findings of a study of the acoustic field within a submerged water filled cylindrical shell. The acoustic field was of special interest under resonance conditions and the theoretical predictions were compared to Schlieren images of the field. This investigation is complementary to the main body of this work, and was carried out in collaboration with Sharon Knapp who developed the Schlieren system and obtained the Schlieren images presented here. Chapter 8 draws together the conclusions reached during the course of this investigation and discusses the potential avenues for further work. These have arisen in two ways, firstly to clarify some of the questions raised by this investigation, and secondly as logical extensions to the work contained within this document.

2 Experimental Facility

2.1 Background

One common measure of the scattered signal from a target is called the 'Target Strength'. For the case of a monochromatic plane wave, of pressure p_i incident on a discrete target, the Target Strength TS is defined by,

$$TS = 20\log\frac{p_{sc}(r=1)}{p_i}$$

where p_{sc} is the scattered pressure extrapolated from the far field to 1m ($r = 1$) from the acoustic centre of the target, it being assumed that the observation point (r) is in the far field of the target. The Target Strength, as defined, will in general be a function of frequency and describes how strongly the target backscatters acoustic energy. For targets of the same shape and material, the Target Strength at a particular frequency will depend on the physical size of the target. For a rigid (i.e. impenetrable) sphere for example, where the radius is large compared to the wavelength, the scattered pressure at a distance r from the sphere is related to the incident pressure by

$$p_{sc} = p_i\frac{a}{2r} \quad ,$$

where a is the radius of the sphere (Kinsler, Frey, Coppens, Sanders, 1982). Thus at a reference distance of 1m the Target strength becomes

$$TS = 20\log\frac{a}{2} \quad .$$

In the Target Strength example given above, the composition of the sphere was neglected as a rigid sphere was considered. In order to emphasise the variations in scattering due to material properties alone, it is possible to define a 'form function' that is independent of the size of the target. For a sphere, the far field form function (f_∞) is defined by (Hickling, 1962; Neubauer, Vogt, Dragonette, 1974)

$$|f_\infty(ka)| = \frac{2r}{a}\left|\frac{p_{sc}}{p_i}\right| \quad ,$$

where k is the acoustic wavenumber. With this definition the form function is the same for all spheres of the same material and is only a function of the normalised wavenumber,

$ka = 2\pi a/\lambda$. This expression assumes monochromatic plane wave incidence of a steady state signal and that the reflection measurements are made at a far field point, usually greater than ten sphere diameters from the target.

Experimentally, a short duration, broad-band pulse has several advantages over a continuous wave or long tone burst when one wishes to perform controlled experiments in the confined area of a laboratory tank at relatively low frequencies. The broad frequency spectrum makes it possible for the form function to be determined over a wide frequency range from a simple set of experimental data using Fourier techniques. In addition, the ease with which the reflected signal can be isolated from the transmitted signal and from unwanted multiples, make short pulses particularly useful.

For a non sinusoidal signal, such as a transient, the form function can be obtained by Fourier analysis using a modified expression (Dragonette, Vogt, Flax, Neubauer, 1974)

$$|f_\infty(ka)| = \frac{2r}{a} \left| \frac{g_{sc}(ka)}{g_i(ka)} \right| ,$$

where $g_{sc}(ka)$ is the frequency spectrum of the backscattered signal, and $g_i(ka)$ is the frequency spectrum of the incident signal.

Over recent years experimental measurements of the form function have been made using mono-frequency tone bursts (Neubauer et al., 1974), short pulses of two or three cycles (Dragonette et al., 1974; Dardy, Bucaro, Schuetz, Dragonette, 1977; Dragonette, Numrich, Frank, 1981) or transient techniques (Dragonette, Vogt, Flax & Neubauer, 1974; de Billy, 1986). From the discussion earlier (Chapter 1) it will be observed that in general measurements have used high frequency pulses (typically 0.5MHz or 1MHz) and small objects. This may lead to problems when more complicated structures are required as fabricating objects on such a small scale will be difficult.

The need for a low - frequency acoustic source was outlined in Chapter 1 and this work uses the parametric array. The versatility of a parametric array as a laboratory source for making detailed and accurate acoustic measurements over a wide frequency range has been demonstrated by measurements of the acoustic properties of submerged panels (Humphrey, 1981, 1985; Humphrey & Berktay, 1985). In this work, performed at the University of Bath, a parametric array was used as the acoustic source to measure the reflection loss and insertion loss of limited size panels in a laboratory tank (1.8m x 1.2m x 1.2m). As a result of the expertise and knowledge gained in the above work it seemed feasible that the facility could be used to make measurements of backscattering from small objects. Initial backscattered form function results for tungsten carbide and stainless steel spheres were certainly encouraging and agreed reasonably well with theoretical curves

(Humphrey, Murphy & Moustafa, 1987). Improvements have been made to the experimental system since the initial results were taken, and the modified system and its operation are described in the following sections.

2.2 Parametric Array

The use of non-linear propagation of high frequency waves in an acoustic medium to generate a useful low frequency wave was first proposed by Westervelt (1957, 1963). Since then the properties of parametric sources have been the subject of considerable experimental and theoretical work (Berktay, 1965; Bjørnø, 1975).

In the simplest mode of operation, often known as the 'spot frequency mode', two frequencies, close to the resonant frequency of the transducer, are transmitted simultaneously. Non-linear interaction of these two 'primary' frequency waves generates various secondary frequencies (the interaction frequencies and harmonics). These additional frequencies can be considered to come from 'pseudo - sources' distributed throughout the interaction region of the primary waves. By adopting a quasi - linear analytical approach only the sum and difference frequencies need be considered, and the relatively small contributions due to the interaction of the secondaries with each other and with the primaries can be ignored.

The sum frequency is rarely of practical interest as it is attenuated very quickly. However the difference frequency term is of considerable use since it can easily be controlled by the choice of the two primary frequencies. Small changes in the primary frequencies permit generation of a difference frequency covering the complete bandwidth of the transducer. Whereas to cover this range (typically 2 - 100kHz) with a conventional source would require several transducers.

A second mode of operation is used when a transient pulse is required. A carrier frequency, close to the resonant frequency of the transducer is modulated by a lower frequency envelope and the resultant pulse is applied to the transducer. Non-linear propagation causes self - demodulation of the pulse in the water (Berktay, 1965), to produce a low frequency pulse whose shape and duration is controlled by the shape of the envelope. The shape of the pulse, on-axis, has been shown to be equal to the second derivative of the square of the modulating envelope. Variation of the length of the envelope, in this application a raised cosine bell, allows the centre frequency and the bandwidth of the pulse to be altered to enable measurements to be made over several frequency bands.

In the confined environment of a laboratory tank, a second advantage of the parametric source is the characteristic narrow beam of the lower frequency wave, devoid of any sidelobes.

The main disadvantage of using a parametric array is that the conversion of energy from the primary frequencies is quite inefficient, being a second order process. However,

in this application we are not limited by the magnitude of the pressure generated at the difference frequency and experimental measurements have shown there to be enough signal for our purposes.

2.3 Equipment and Operation

The experimental arrangement used in these investigations is illustrated in Figure 2.1, and is similar to that used by Humphrey (1985). The transmitting equipment used to generate the transient pulse is shown in Figure 2.2, whilst the receiving electronics is shown in Figure 2.3.

A raised cosine bell, see Figure 2.4a, is used to modulate the carrier frequency, in this case 920kHz. The raised cosine is produced from a single cycle of a sine wave, which has been phase shifted and had a d.c. offset added. A raised cosine bell of length 50μs, for example is based on a single cycle of a sine wave at 20kHz. The modulated carrier (Figure 2.4b) is then amplified and transmitted from a transducer, 0.05m in diameter, placed at one end of a 1.8m tank (Figure 2.1). The input to the amplifier is restricted to 1V p/p by the use of a diode limiter (Figure 2.2), while a low pass filter with a cut-off at 1.5MHz prevents the possibility of feedback sending the system into oscillation. The resultant theoretical low frequency self demodulated pulse, generated on-axis is shown in Figure 2.4c.

The frequency content of the output signal can be varied by changing the length of the envelope. Figure 2.5 shows the spectra of three typical pulses used to cover the frequency range 10 - 150kHz and the respective regions that they cover. The differing shapes of the spectra are due to limitations in the transmitting system, the presence of the low pass acoustic filter, and the response of the hydrophone and low pass filters used on reception. The spectrum of the lowest frequency pulse, 25kHz, is the most 'ideal' and falls off to a first minimum at approximately three times the base frequency, i.e. 75kHz as expected. The distortion seen in the 60kHz and 100kHz pulses is primarily due to the hydrophone response, and the preceding low pass filter which protects the hydrophone and removes any remaining high frequency carrier. (The majority of the carrier signal will have been removed by the acoustic filter.) A less significant cause of distortion is due to the fact that the function generator is unable to produce a perfect raised cosine bell (Figure 2.4a). As the resultant low frequency demodulated pulse is given by the second derivative of the cosine bell squared, the subsequent spectra will obviously be affected.

Due to the restricted dimensions of the experimental tank (1.8m x 1.2m x 1.2m), an acoustic 'low pass' filter is used to truncate the parametric array approximately 0.53m beyond the transducer (Figure 2.1). This filter attenuates the primary frequencies, whilst allowing the demodulated pulse to pass without significant loss and permits the measurements to be made in a region free of primary frequencies and secondary sources. This simplifies the measurement technique and prevents errors due to non-linearity in the hydrophone response

(Humphrey & Hsu, 1980; Moffet & Henriquez, 1982). The polyeurethene filter, which is 0.01m thick, has been made as large as is practicable (1.1m x 0.9m) in order to reduce diffraction effects from the edges. The characteristics of the acoustic filter are described in section 2.5.1.

The experimental signal is measured with a commercially available cylindrical hydrophone, a Brüel and Kjær 8103. It has a quoted sensitivity of about -211dB re 1V/μPa, to within 2dB, from 0 to 125kHz, whilst above 125kHz there are pronounced resonances. The flat response of the hydrophone over the frequency range of interest and the relatively small size, make it very suitable for this application.

The acoustic filter and the hydrophone are attached to mountings on an optical bench over the tank. This allows convenient measurement of the distances between components in the tank and facilitates movement of the filter, hydrophone and target object.

The hydrophone output is passed through a passive low pass filter (Figure 2.3) to further attenuate any high frequency primary signal still present and protect the hydrophone. Two filters are used depending on the frequency range required, one has a 3dB cut-off point at 125kHz, while the other has a 3dB cut-off point at 250kHz. The filters are 5 - pole Butterworth filters based on a design given by Geffe (1963), and attenuate any remaining carrier frequency (920kHz) by approximately 30dB. The filtered signal is then amplified by approximately 70dB before recording and processing within an ANALOGIC DATA 6000E. An IEEE-488 interface to a micro-computer allows data to be transferred for storage or plotting.

2.4 Experimental Technique

The measurement technique uses the stability of the acoustic output to enable any coherent background signal in the tank to be subtracted leaving only the scattered signal due to the object. To enhance this technique the signal to noise ratio was improved by averaging each signal over a number of pulses prior to further processing or analysis. The number of pulses averaged varies with the object, but during the course of this work varied from 256 for spheres to 64 for the solid cylinder measurements.

For a normally incident wavefield the test object was placed on the acoustic axis of the transducer (Figure 2.6a) and the averaged scattered signal recorded with the hydrophone at a known range r and observation angle ϕ. The object was positioned on the acoustic axis of the transducer with the use of fishing line. In the case of a sphere this took the form of a net, whilst for cylindrical objects lines tied to either end were sufficient. The fishing line overcame the problems of suspending the objects as it was undesirable to mark them or make permanent attachments, as the use of supports for example would interfere significantly with the scattered field. Prior to immersion the object was carefully wetted to ensure that air bubbles etc. were not trapped on the surface. The object was then removed and the

coherent reverberation in the tank recorded. This included surface and side wall reflections which may not be able to be time resolved from the scattered signal. The coherent reverberation could then be subtracted from the scattered signal to leave only the signal due to the test object. The hydrophone was then moved to the position of the centre of the object and the incident signal recorded. In doing so, the hydrophone was rotated by 180° in order to avoid any effects due to its directionality. For the case where the scattered signal was observed at an angle ϕ other than 180° (backscatter), a rotation table and an arm were added to the experimental facility. This arrangement allowed the hydrophone to be positioned at distances between 0.06m and 0.40m from the object, which was aligned with the rotation axis, and allowed angular measurements to be obtained at angles from 0° to 360°. Unfortunately there were two 'blind spots' due to the position of the optical bench, but as most measurements were made from 0° to 180° due to the symmetry involved, these blind spots did not seriously affect our measuring capabilities.

Figure 2.7 shows the scattered signal, coherent reverberation and the incident signal for a 100kHz pulse incident on a 0.0381m diameter aluminium cylinder at an observation range of 0.30m and an observation angle of 180°. Figure 2.8 shows an additional set of signals for the same cylinder but this time at an observation angle of 90°. In this example the first pulse in the scattered signal time window is the outgoing signal. This appears unlike the on-axis signal due to the fact that the pulse is observed off-axis. A similar set of signals are shown in Figure 2.9 for a 0.0254m diameter tungsten carbide sphere insonified by a pulse based on 25kHz. In this case the scattered signal is of a much lower amplitude and so the subtraction of the coherent background has a more noticeable effect.

The experimental configuration used when insonifying cylinders at oblique incidence is illustrated in Figure 2.6b. The hydrophone was placed in the specular direction to record the scattered signal as it was felt this would give the most acceptable comparison with the theory considering the finite nature of the beam.

For all the signals recorded on the DATA 6000E, the input amplitude range was optimised so that digitisation errors were minimised. In addition the length of the buffer and the sampling period were adjusted, to provide an acceptable resolution in the frequency domain whilst keeping the averaging time to a realistic figure. Typically 512μs of signal was recorded at a sampling period of 1μs. This gave a frequency resolution of 1.95kHz and a maximum frequency of 500kHz, although not all of this information was significant.

From section 2.1 it can be seen that the form function is essentially obtained by dividing the spectrum of the scattered pulse by that of the incident pulse. When taking the Fourier Transform of the scattered signal the background signal was removed, but it was also necessary to zero portions of the signal as the subtraction of the background occasionally left artificial spikes in the trace. A window was therefore applied which was unity over the central 8/10th of its length and had a cosine taper at either end. The signals were always

positioned so that they lay in the central flat portion of the window. The incident signal had the d.c. level removed before a similar window was applied and the Fourier Transform taken. The ratio of the two spectra was then multiplied by a normalising factor which depended on the geometry of the object (see sections 4.2 and 5.2). In the case of the cylinder this factor is $\sqrt{2r/a}$, whilst for a sphere the factor becomes $2r/a$.

2.5 Characteristics of the Experimental System

The previous section discusses the experimental technique and describes how the experimental results can be expressed in terms of the form function. The following measurements were used to characterise the experimental system so that we were in a better position to identify and explain any differences that arose between the experimental results and the theoretical predictions. The experimental form function results are relative measurements in that they have been normalised with respect to the incident signal, and for this reason the results presented below have also been normalised appropriately.

2.5.1 Acoustic Filter

The attenuation of the acoustic filter used to truncate the parametric array has been measured over the frequency range 10kHz to 1MHz and is shown in Figure 2.10. The high frequency response (i.e. > 100kHz) was obtained by using a short tone burst to measure the field on-axis first without, then with the filter present. At lower frequencies (i.e. 10 - 100kHz) the attenuation was measured using the short parametric pulse illustrated in Figure 2.4. In this case it was necessary to use an additional piece of the filter material to truncate the parametric array. Again the attenuation can be calculated from measurements both with and without a second piece of filter in place. Figure 2.10 shows that over most of the frequency range of interest (10 - 150kHz) the attenuation of the filter increases smoothly with frequency and is less than 4 or 5dB, while the carrier frequency, at 920kHz, is attenuated by more than 30dB.

2.5.2 Axial Field

Experimental measurements of the acoustic field on-axis beyond the filter are shown in Figure 2.11. Tone bursts of 20kHz, 50kHz and 100kHz have been used and the measurements have been normalised to the measured 'far field' value, taken in this instance to be the value at a range of 0.64m beyond the filter. In the region of interest, approximately 0.30 - 0.60m beyond the filter (equivalent to $\ln(r/(r-l_T))$ of approximately 2.7 - 1.9, where l_T is the distance from the transducer to the truncating filter), the results at all frequencies show a $\ln(r/(r-l_T))$ fall off consistent with the predictions of Berktay & Shooter (1973). Closer to the filter (the end of the array) the results show a deviation from this, the deviation

increasing with increasing frequency. This is because at high frequencies the primary beam cross section is not small compared to the difference frequency and the simple line array model (Appendix 2) breaks down.

2.5.3 Beam Characteristics

As this work deals with finite sized objects, it is of interest to examine the beamwidth across the truncated array in relation to the size of the objects under consideration. The parametric source beamwidth across the acoustic axis has been measured at three distances and for three frequencies at each distance. The first position was 0.025m behind the filter (Figure 2.12), the second 0.323m beyond the filter, in a position typical of the hydrophone position, (Figure 2.13) and the third 0.621m beyond the filter, typically where the object would be placed (Figure 2.14). In each case the beam profiles were recorded using 20kHz, 50kHz and 100kHz difference frequency tone bursts, and these are shown in parts a), b) and c) of each diagram respectively. Also shown in each figure are theoretical predictions of the beam width given by two different theoretical models of the parametric source. The first model (Berktay & Shooter, 1973) assumes the parametric array to consist of a line of pseudo sources, while the second (Humphrey, private communication; Humphrey & Beckett, 1990) considers the pseudo sources to form a column the diameter of the transducer element and of a length equivalent to the truncation length l_T. The theory for each of these models is described briefly in Appendix 2.

It is easily observed that as the frequency is increased for a given axial distance the beam profile gets narrower. Also, as one increases the axial distance for a given frequency the beam width generally increases. For objects a few centimetres in diameter, located between 0.30m and 0.60m beyond the filter the beamwidth at these frequencies appears to be broad enough to ensure fairly uniform insonification over the whole of the object.

From the comparisons of the experimental data with the theoretical predictions shown in Figures 2.12 - 2.14, it can be seen that the line array model tends to over-estimate the beamwidth of the field. It also predicts significant side lobes which are not seen in practice. The column model is a significant improvement providing a much closer estimate of the beam width and less significant side lobes. However it does not provide an accurate prediction of the features observed in all situations. It should be noticed that for both theoretical predictions the fit to the data becomes increasingly worse with distance off-axis.

2.5.4 Hydrophone Shadowing

A great deal of the work that follows is recorded in the backscatter direction. In this configuration the hydrophone will be located between the transducer and the object, and may well interfere with the wavefield, adversely affecting the results. It should be remembered that the shadowing effects measured here using a second hydrophone will only

provide an estimate of what one might expect to see when measuring the scattered field from a sphere or cylinder. This is because the objects are, in general, much larger than the hydrophone and thus will be insonified by a greater region of the incident field than the hydrophone.

The following procedure was used to obtain an estimate of the effect due to a hydrophone present between the source and the object. One hydrophone was positioned in the tank on the acoustic axis of the transducer and a signal recorded - the reference signal. A second hydrophone was then placed a known distance in front of the first hydrophone, that is between the transducer and the hydrophone, and a second signal recorded. Both signals were Fourier Transformed and the ratio of the shadowed signal's spectrum to that of the reference signal was obtained. Figures 2.15 and 2.16 illustrate the effect on the amplitude and phase when inserting the hydrophone 0.323m beyond the filter, a typical measuring position, whilst measuring the beam profile at a typical object location, 0.621m beyond the filter, for two difference frequency tone bursts.

The effects of the hydrophone on the amplitude of the beam profile are shown in Figure 2.15 for both the 50kHz and 100kHz measurement. The figure clearly shows that for the 50kHz tone burst the variations oscillate about 0dB having a maximum deviation of approximately ± 0.5dB at an off-axis distance of 0.30m. Within 0.10m of the axial position however the deviations are slowly varying and are of the order of 0.2 - 0.4dB. The 100kHz measurements vary more rapidly and have a greater magnitude variation, showing deviations of up to ± 0.7dB within 0.10m of the acoustic axis and up to ± 2dB at 0.30m. The phase variations, shown in Figure 2.16 are quite smooth up to 0.10m off-axis, but beyond this there are rapid variations, again more so in the 100kHz measurement.

The loss in the shadowed signal on-axis for both the 50kHz and 100kHz measurements shown in Figure 2.15 is approximately 0.2dB, for this case where the two hydrophones were 0.30m apart. This amount is slightly less than that shown in Figure 2.17a which shows the loss in the shadowed signal on-axis as a function of frequency for a distance of 0.20m between the two hydrophones. Figure 2.17a illustrates that in general there is an increase in the shadowing effect with frequency, and in the frequency range of interest, 10 - 100kHz, this is less than 0.3dB. There is however, one anomaly visible in Figure 2.17a between 40 and 60kHz. Investigation of the processing technique and of any possible sources of signals in the tank showed that the anomaly was due to a signal caused by the resonance of the tube supporting the hydrophone.

Decreasing the range of the shadowing hydrophone from 0.20m to 0.05m gave the result shown in Figure 2.17b. Reducing the measuring distance has increased the general level of the shadowing and has introduced a ripple which is not observed in Figure 2.17a. The ripple on a smooth background implies that we are receiving a delayed signal which is virtually a replica of the initial signal but at a lower amplitude. The period of this ripple is

about 15kHz, and corresponds to a time delay of the delayed signal of approximately 67μs. This represents a distance of about 0.10m in water, and indicates that for short ranges the multiple reflection between the hydrophone and the object can be significant. It should be noted that 0.05m is much closer than we would normally work for measurements with spheres. However for evacuated or air filled objects where the returned signal is greater this effect may become noticeable at even greater ranges.

It can be observed from Figures 2.15 and 2.17 that the effect of the shadowing hydrophone is related to the separation between the two hydrophones. Figure 2.18 illustrates the location of the two hydrophones with respect to the transducer and the truncating filter. The filter is placed a distance l_T from the transducer, and the shadowing hydrophone and the reference hydrophone at locations A and B respectively. On-axis, and in the far field of the array the parametric array can be approximated by a spherical source located mid-way between the transducer and the filter. Thus, P_1, the incident pressure at A is given by

$$P_1 = \frac{P_0}{l_T/2 + R_1},$$

and P_2, the pressure at B, in the absence of the shadowing hydrophone at A,

$$P_2 = \frac{P_0}{l_T/2 + R_1 + R_2}.$$

The hydrophones used in this study are mounted in cylindrical aluminium tubes which can be easily attached to optical benches over the tank. From the shape of the tube one might expect that any scattering from the tube would be cylindrical in form. Thus when measuring the field at B, with a hydrophone present at A, the measured signal will consist of two components, P_2 and a component scattered from the shadowing hydrophone. This scattered pressure we shall denote by P_s and is given by

$$P_s = \alpha \frac{P_1}{\sqrt{R_2}},$$

where α indicates a scattering coefficient.

Ignoring the phase relationships, the maximum relative error in a measurement at B due to introducing a hydrophone at A is

$$\frac{P_s + P_2}{P_2},$$

which can be written

$$1 + \frac{P_s}{P_2} = 1 + F.$$

The fractional difference F is given by

$$F = \frac{P_s}{P_2} = \alpha \frac{(l_T/2 + R_1 + R_2)}{(l_T/2 + R_1)\sqrt{R_2}}.$$

For the data presented in Figure 2.17, l_T = 0.53m, $R_1 \approx$ 0.32m and $R_2 \approx$ 0.20m. Hence the fractional difference with a separation of 0.20m, F_{20}, is

$$F_{20} = \alpha \frac{(0.265 + 0.32 + 0.20)}{(0.265 + 0.32)\sqrt{0.20}} = 0.30\alpha.$$

If the separation is reduced to 0.05m then

$$F_5 = \alpha \frac{(0.265 + 0.32 + 0.05)}{(0.265 + 0.32)\sqrt{0.05}} = 0.49\alpha,$$

and the ratio of the two values is approximately 1.6.

If cylindrical spreading is the main cause of the shadowing effects observed in the results presented in Figure 2.17, then using the 0.20m results we should be able to predict the level of shadowing in the 0.05m case. For example, for a separation of 0.20m and a frequency of 80kHz the shadowing is approximately 0.15dB. Therefore the ratio of the shadowed signal to the reference signal is

$$10^{0.15/20} = 1.0174 = 1 + F_{20}.$$

The error at a distance of 0.05m can be estimated from

$$\begin{aligned} error &= 1.0 + F_5 \\ &= 1.0 + 1.6 * F_{20} \\ &= 1.0 + 1.6 * 0.0174, \end{aligned}$$

giving a shadowing effect of 0.24dB, which is comparable to the value seen in Figure 2.17b at 80kHz.

Thus it would appear that we can explain the shadowing effect in terms of cylindrical spreading from the hydrophone and its support tube, and the resonance effect observed from the support tube.

2.5.5 Pulse Shapes and Windowing

One difficulty in processing any experimental signal is to decide whether or not to apply a windowing function, and if so, of what length and shape. The effects of windowing can be quite significant. If one uses a Hanning window for example when Fourier Transforming, shortening the window can result in the spectrum being 'smoothed' with a subsequent loss of detail. This type of effect could become important when measuring the scattered signal from elastic objects such as spheres as too much smoothing could mask out the narrow resonance features due to the elastic properties of the object. One also has to decide where to place the end of the window so that the window is long enough to include all of the necessary signal but not too long so that too much noise is included. Experimentally

this is a difficult decision to make and all too often one has to rely on the intuitive 'feel' of the experimentor for where the window should be placed.

In order to understand what may happen to the resultant form function when the signals are windowed a computer program was written to theoretically evaluate the effect. The program calculates the shape of the backscattered pulse (Figure 2.19a) from a tungsten carbide sphere assuming an incident pulse (Figure 2.4c), based on 40kHz, to be ideal. The backscattered pulse is then windowed and a modified form function calculated. Figures 2.19b, c and d illustrate the resultant form function when the backscattered signal is windowed with a window of 350μs, 450μs, and 550μs duration respectively. The form function due to this signal in the absence of any window is illustrated by the solid line in Figure 4.2. The window is set to unity for most of its duration but has a cosine taper over about 10% of the points at either end. As the signal due to the elastic resonances of the sphere is being truncated one would expect any differences visible in the form function to be in the region of the resonance features. Examination of Figures 2.19b-2.19d shows that windowing the signal has introduced a ripple of different periods and amplitudes in each case.

This can perhaps be best explained by considering the case of a sinusoidal signal modified by an exponential envelope (Figure 2.20a). This can be considered to approximate to the tail of the backscattered signal $g(t)$, when a resonance is excited (see Figure 2.19a), and which is Fourier Transformed to give a spectrum $G(\omega)$, where

$$g(t) \leftrightarrow G(\omega) \cdot$$

Now consider this pulse reduced in amplitude by a factor β and time delayed by τ, as in Figure 2.20b. Then

$$\beta g(t-\tau) \leftrightarrow \beta G(\omega) e^{-i\omega\tau} \cdot$$

When windowed, the signal shown in Figure 2.20a is truncated after a time τ, to produce the signal shown in Figure 2.20c, which can be represented as the difference of the two signals shown in Figures 2.20a and 2.20b, and is given by,

$$g(t) - \beta g(t-\tau) \leftrightarrow G(\omega)(1-\beta e^{-i\omega\tau}) \cdot$$

Examination of the above equation shows that in truncating a signal one introduces a ripple onto the spectrum $G(\omega)$ with an amplitude β and a period $1/\tau$. Hence as τ is increased, the period of the ripple gets smaller (Figure 2.19d), but the ripple amplitude is reduced as β is proportional to an attenuation factor which goes as $e^{-\alpha\tau}$. Conversely as the window length decreases the magnitude of the ripple increases (Figure 2.19b) but is of a longer period and is much more noticeable. Although this explanation has been made for a sinusoidal signal modified by an exponential, one can clearly see using Figure 2.19 that this is applicable to the pulses we are dealing with.

2.6 Potential Limitations of the System

The previous sections have outlined the performance of the system and by their very nature have made us aware of many of the potential problems and limitations inherent in the experimental system and the measuring technique.

As we have seen, one of the major difficulties in measuring any of the signals is going to be due to the location of the hydrophone and any 'shadowing' effects that may be observed. The shadowing introduced by the hydrophone has been discussed in section 2.5.4 and has two distinct components. Firstly the amplitude reduction seen to vary with frequency and observation range and secondly a resonance of the hydrophone support tube at 40 - 60kHz and multiples thereof. It may be possible to reduce these effects by the careful choice of a new support tube for the hydrophone which is better matched to water. Also significant will be the random errors associated with the location and orientation of both the hydrophone and the scattering object.

The hydrophone shadowing and the random positional uncertainties are, at first glance, the two major factors limiting the accuracy of the system. However, there are other factors which, though less significant at present, may ultimately limit the accuracy and performance of the experimental system and measurement technique.

When positioning the hydrophone one assumes, for practical purposes, the receiving point to be at the centre of the hydrophone. Due to the finite size of the hydrophone and its construction this will not be exact and some uncertainty will be introduced in the location. Unfortunately reducing these errors by increasing the range between the object and the position of the hydrophone when measuring the reflected signal is at the expense of signal level, which will introduce its own difficulties. In addition the frequency response of the hydrophone and its directivity pattern may have to be taken into account. However, the effect of these two factors has been minimised as the experimental results are computed from the ratio of two spectra and the hydrophone is rotated during the measurement sequence to ensure the signal is received by the same part of the hydrophone.

The great advantage of this experimental system over more conventional systems is the ease with which a large frequency range (e.g. 10 - 120kHz) can be covered using only two or three pulses. Figure 2.5 demonstrated the use of three pulses to cover the frequency range of interest and showed how decreasing the envelope length by using a cosine bell based on a higher frequency, increases the bandwidth and hence broadens the *ka* range over which reliable measurements can be obtained. However, it is difficult to extend the frequency range upwards indefinitely due to the frequency response of the recording system, which is largely determined by the response of the hydrophone, which has pronounced resonances above 125kHz. In order to obtain values for the form function at higher *ka* values, the alternative to replacing the hydrophone and filter is to increase the size of the target. At present, values of the form function can be ascertained up to *ka* values of about 15 using

objects 0.0381m in diameter.

Where the upper frequency limit of the system is controlled by the hydrophone, the lower end is determined by the transmitting system. Small imperfections in the function generator can cause it to produce a signal that deviates slightly from a perfect raised cosine bell. This deviation is scarcely discernible to the eye but due to the relationship between the shape of the envelope and the demodulated pulse (Berktay, 1965), slight deviations in the shape of the envelope can become pronounced in the resultant pulse and their subsequent spectra (e.g. Figure 2.5). The effect is especially noticeable at lower frequencies (less than 15kHz), however, this should have no effect on the final form function which is determined from the ratio of the scattered to the incident spectra. At present the form function can be determined down to *ka* values just below one. It may be possible, by improving the generating system, to extend this range, although ultimately we will be limited by the size of the tank and the diminishing signal level as the base frequency of the modulating envelope is reduced. Also to be considered will be amplitude and frequency instabilities in the generating system and the random noise inherent in any experimental system.

It is expected that the *ka* range over which measurements can be made will not be a restriction in this application as we are specifically interested in a low *ka* range (less than 20). However the shadowing effects of the hydrophone, as discussed above, may well limit the accuracy of the results when comparisons are made with theoretical predictions.

Figure 2.1 Positioning of equipment within the tank.

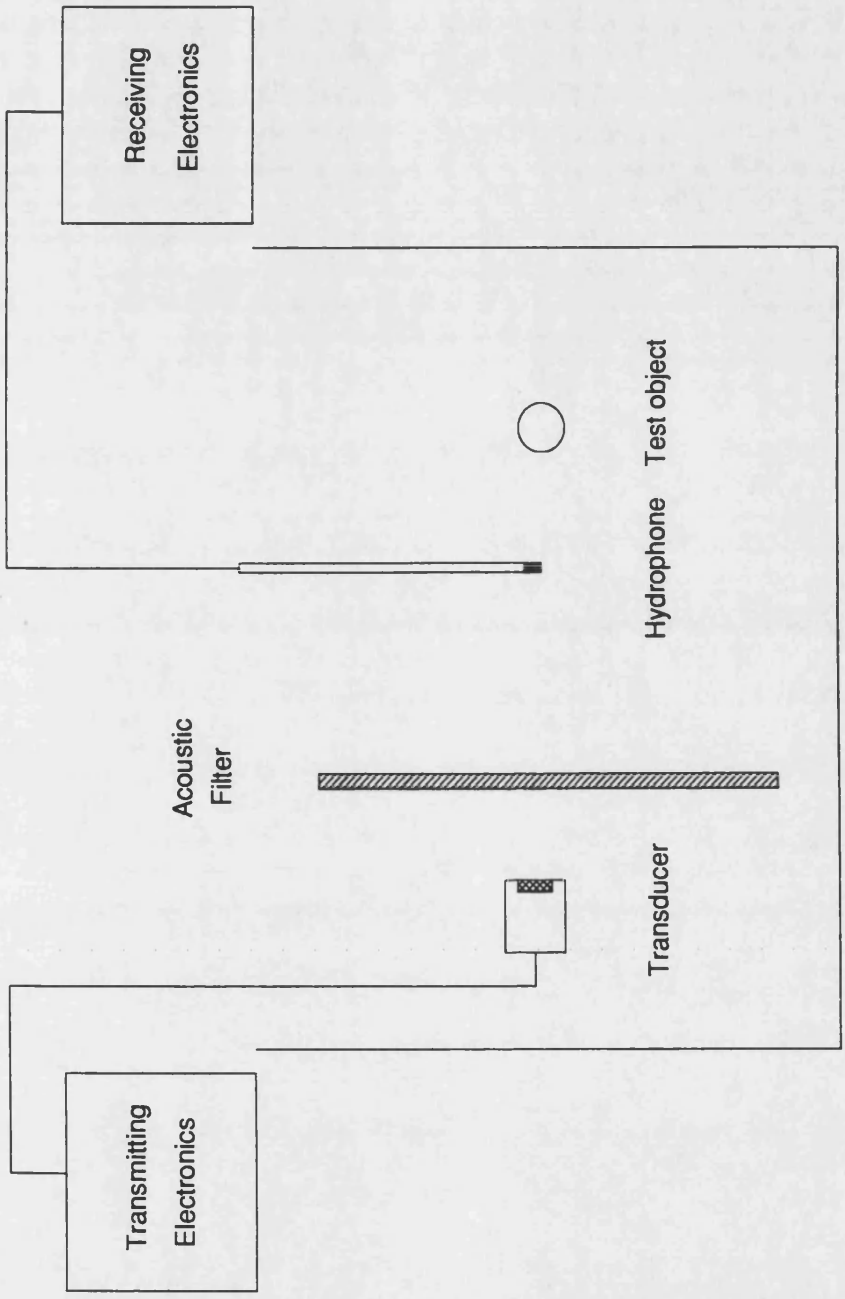

Figure 2.2 Block diagram of transmitting equipment.

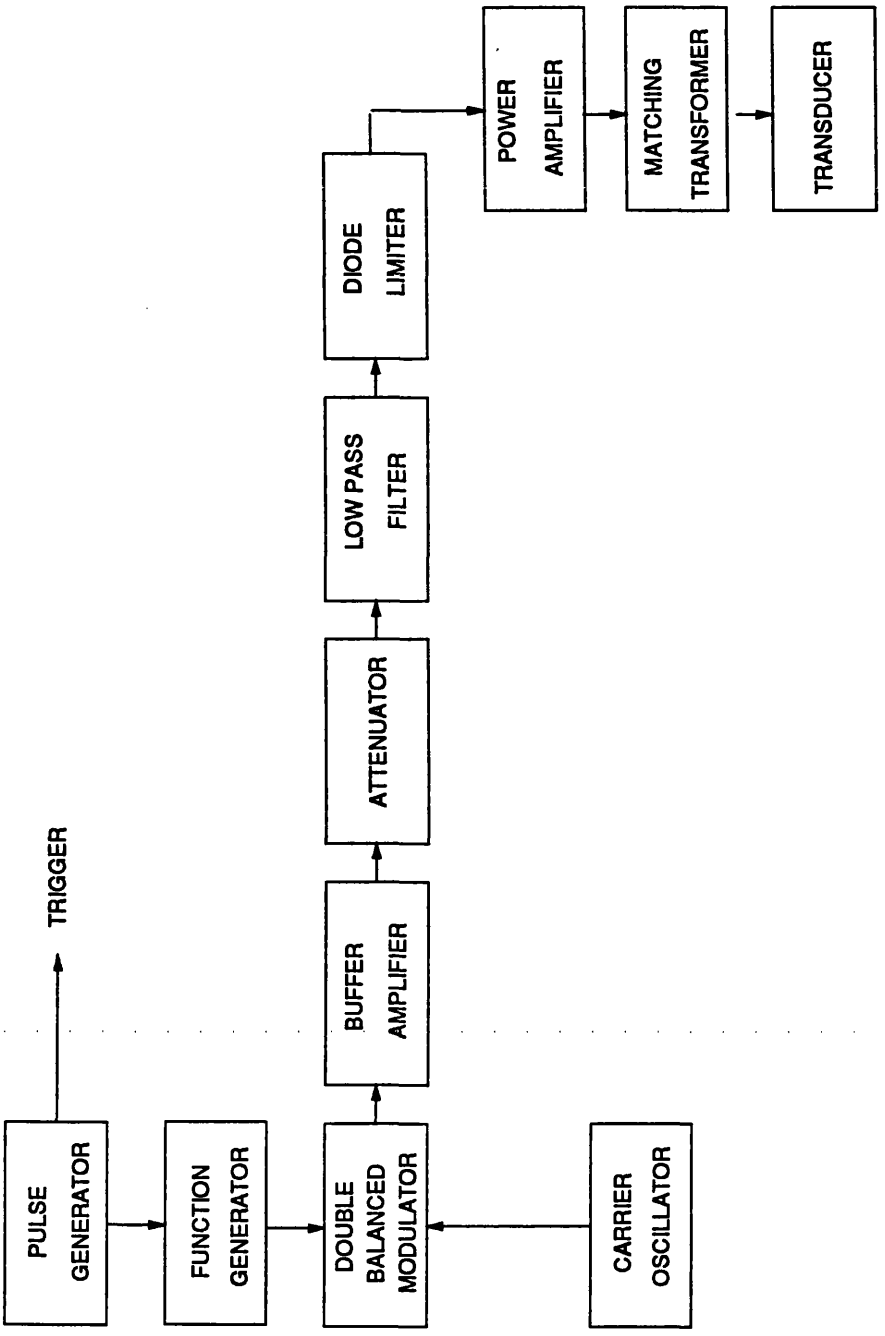

Figure 2.3 Block diagram of receiving equipment.

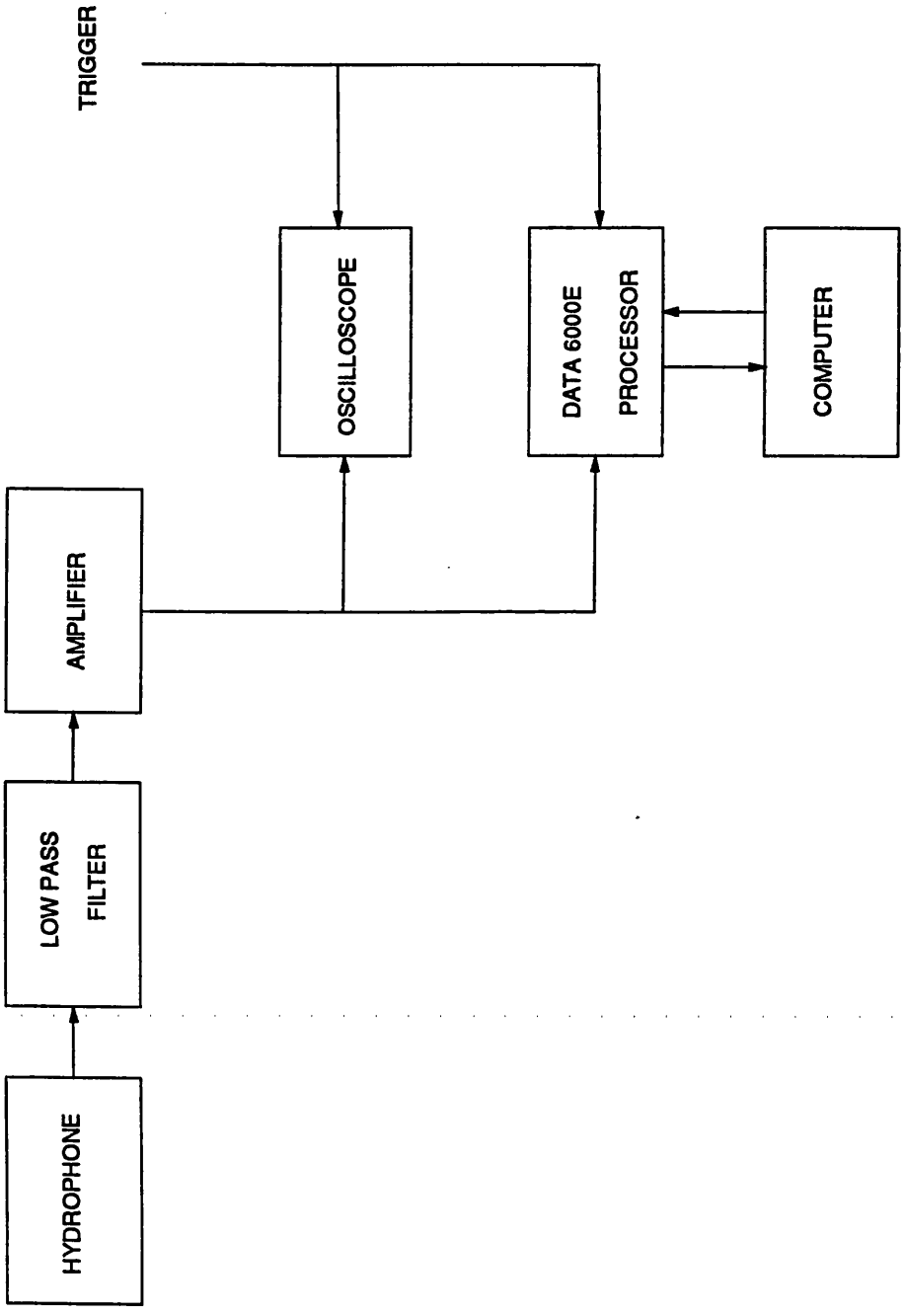

Figure 2.4 Theoretical signal waveforms.

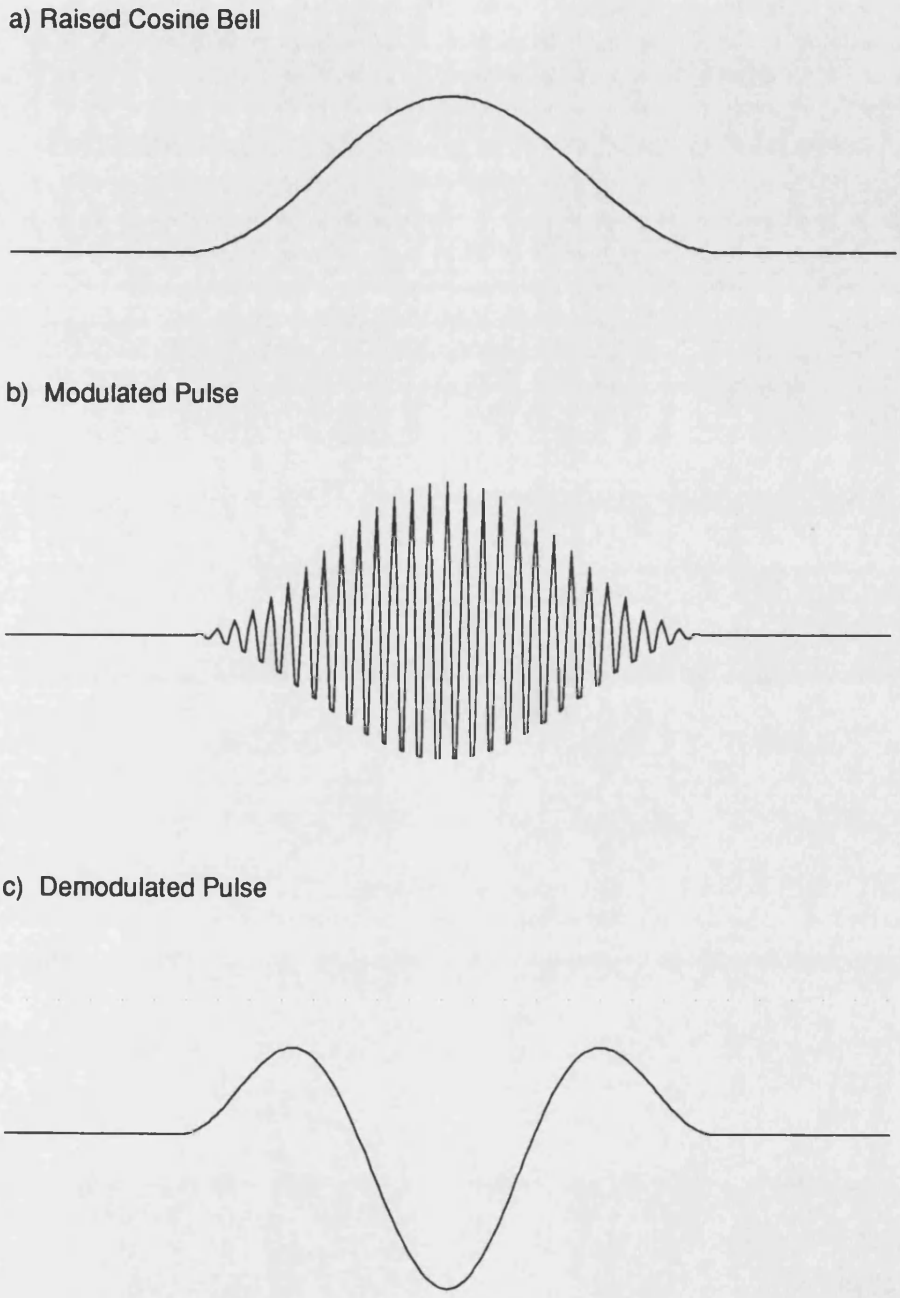

Figure 2.5 Spectra of three typical pulses, based on cosine bells of 100kHz, 50kHz, and 25kHz.

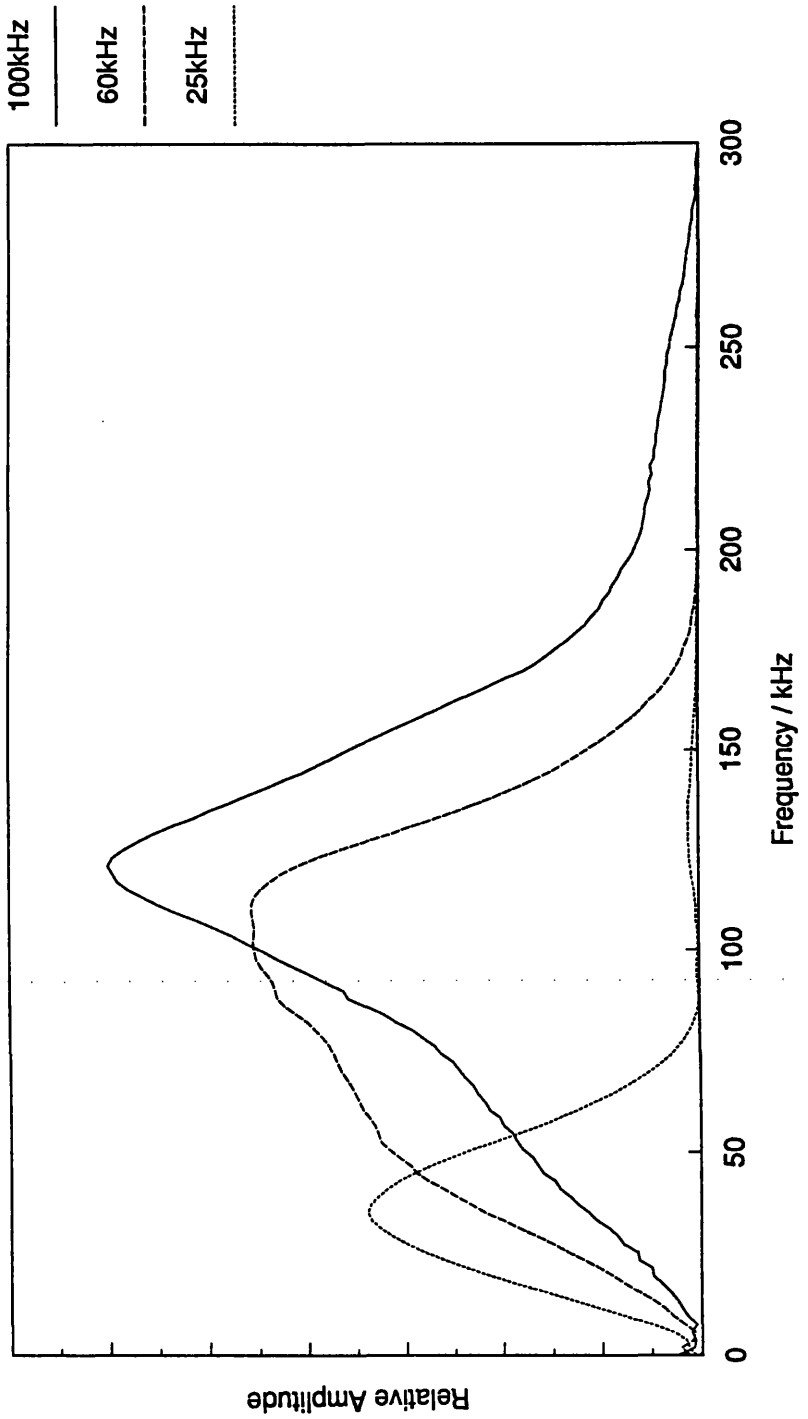

Figure 2.6 Scattering geometry and location of objects for normally and obliquely incident wavefields.

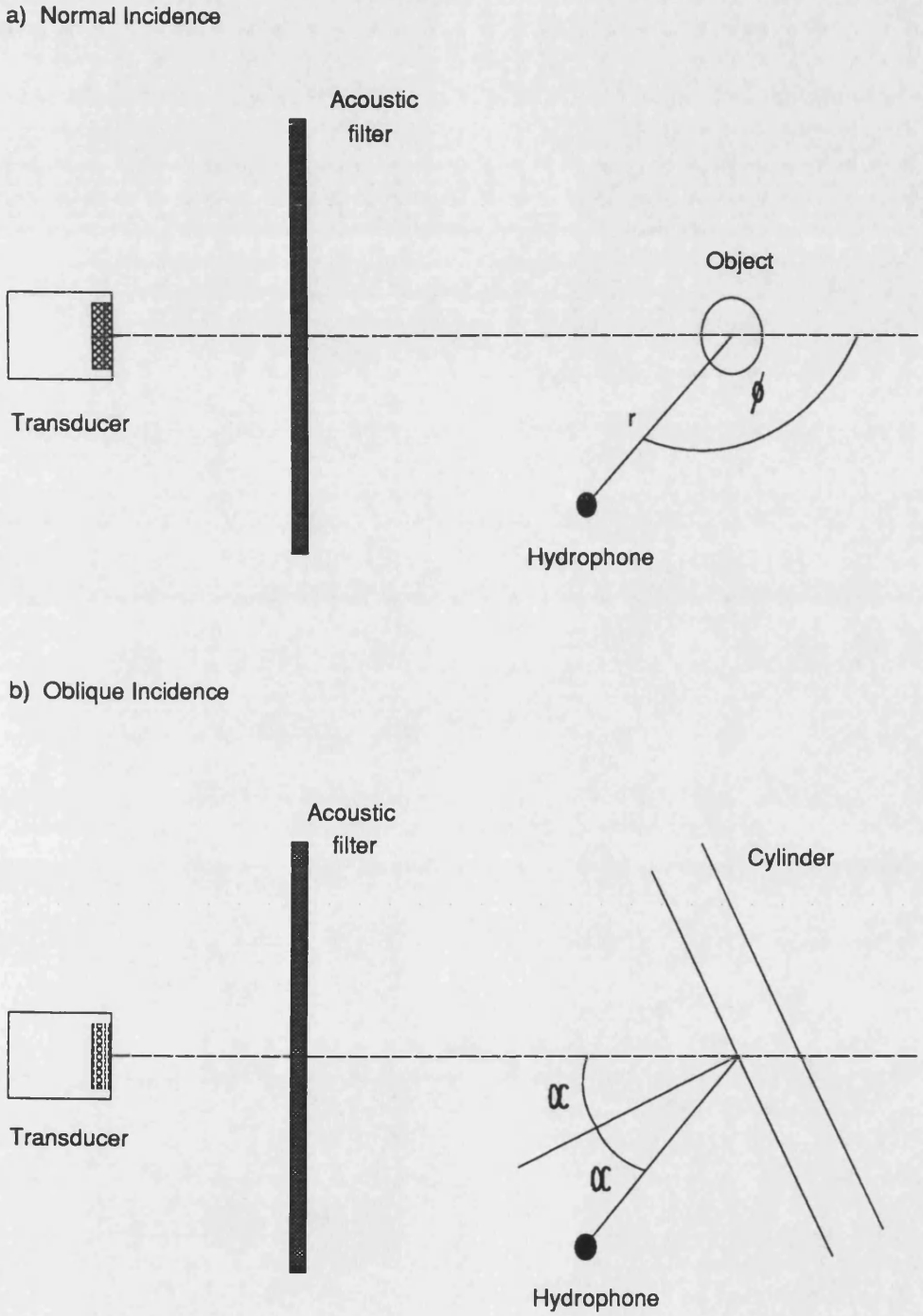

Figure 2.7 Scattered signals from a solid aluminium cylinder, observed at 180 °, for an incident pulse based on 100kHz.

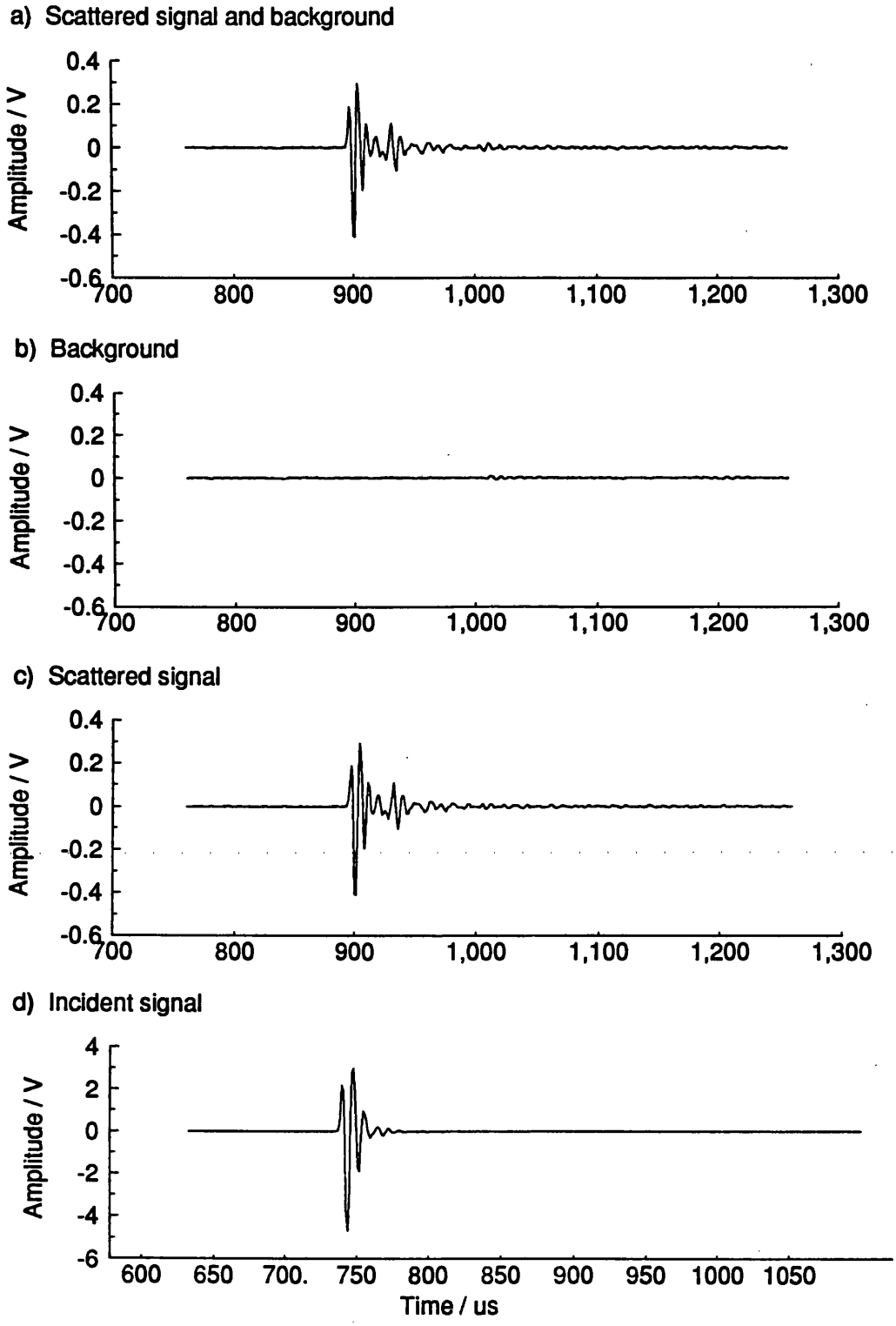

Figure 2.8 Scattered signals from a solid aluminium cylinder, observed at 90 °, for an incident pulse based on 100kHz.

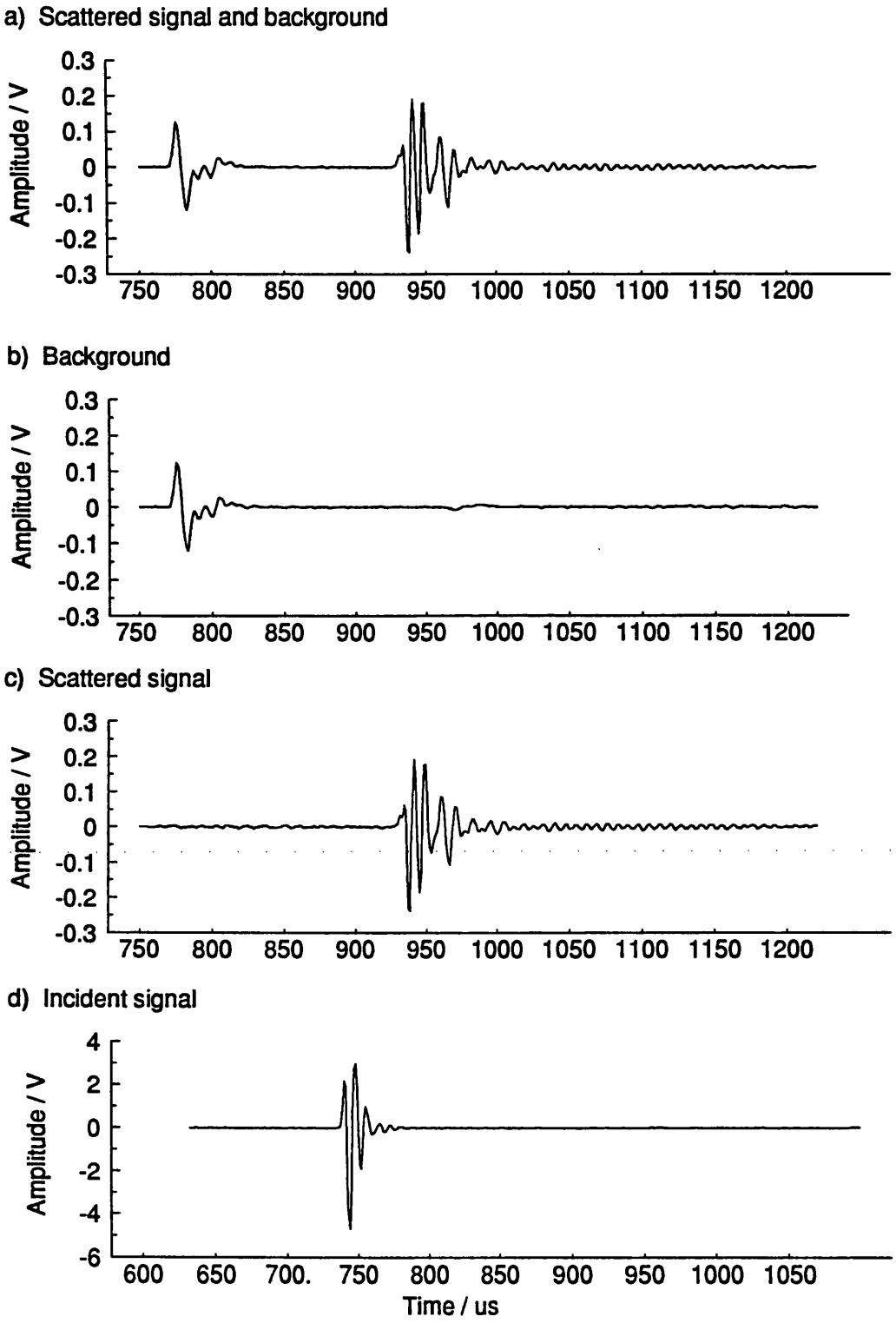

Figure 2.9 Backscattered signals from a 0.0254m tungsten carbide sphere, for an incident pulse based on 25kHz.

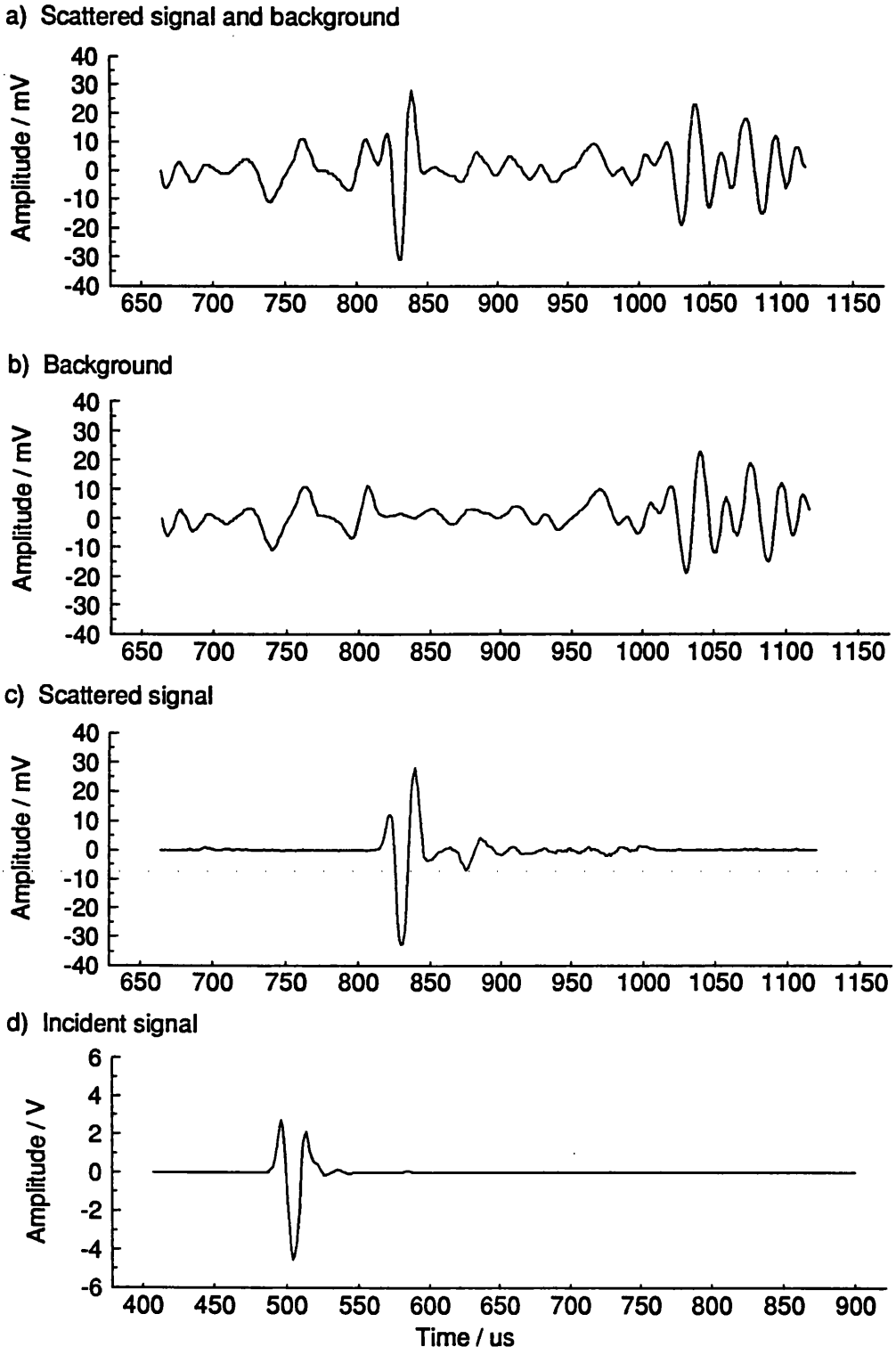

Figure 2.10 Transmission Loss for the acoustic filter.

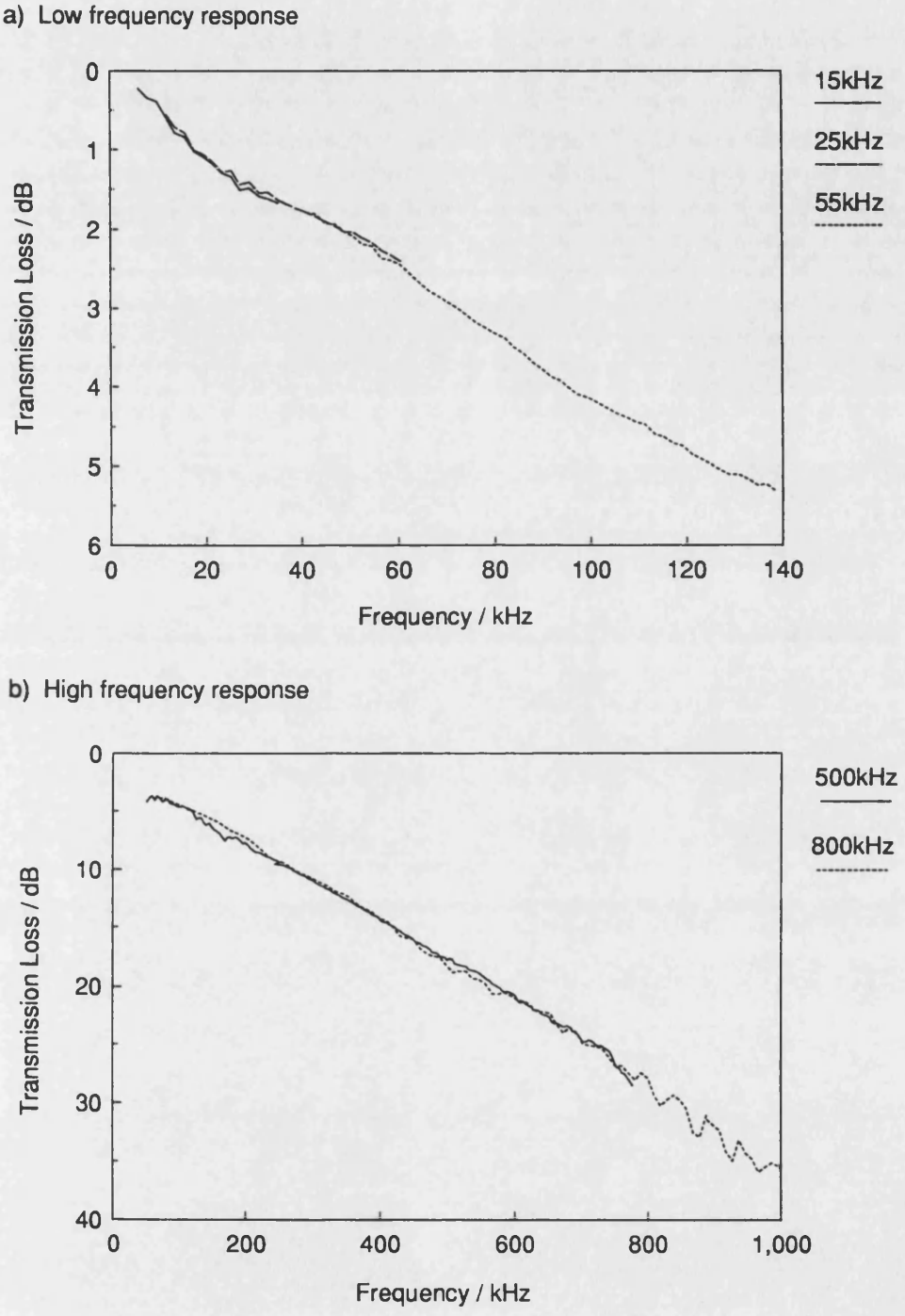

Figure 2.11 Fall off of truncated parametric array output beyond acoustic filter.

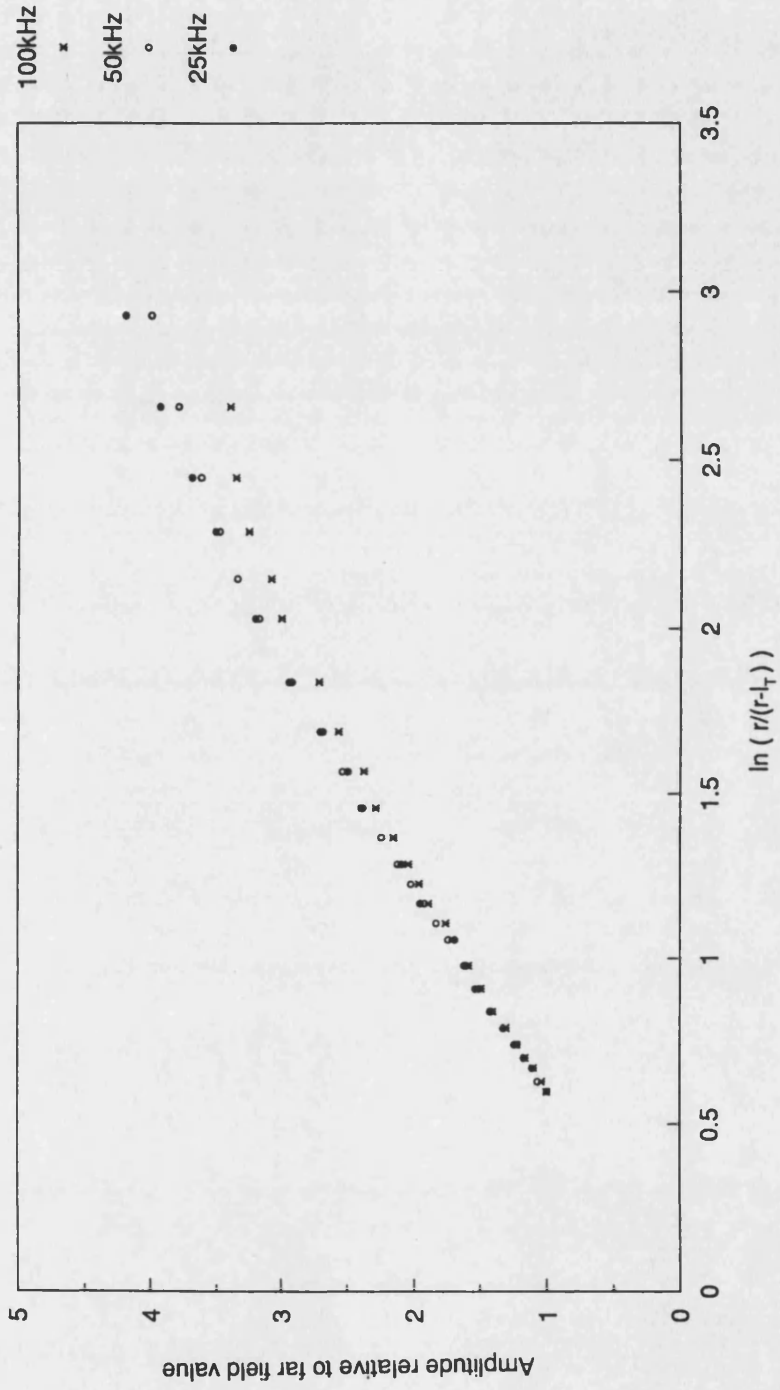

Figure 2.12 Beam profile 0.025m beyond the truncation point for difference frequency tone bursts of 20kHz, 50kHz and 100kHz.

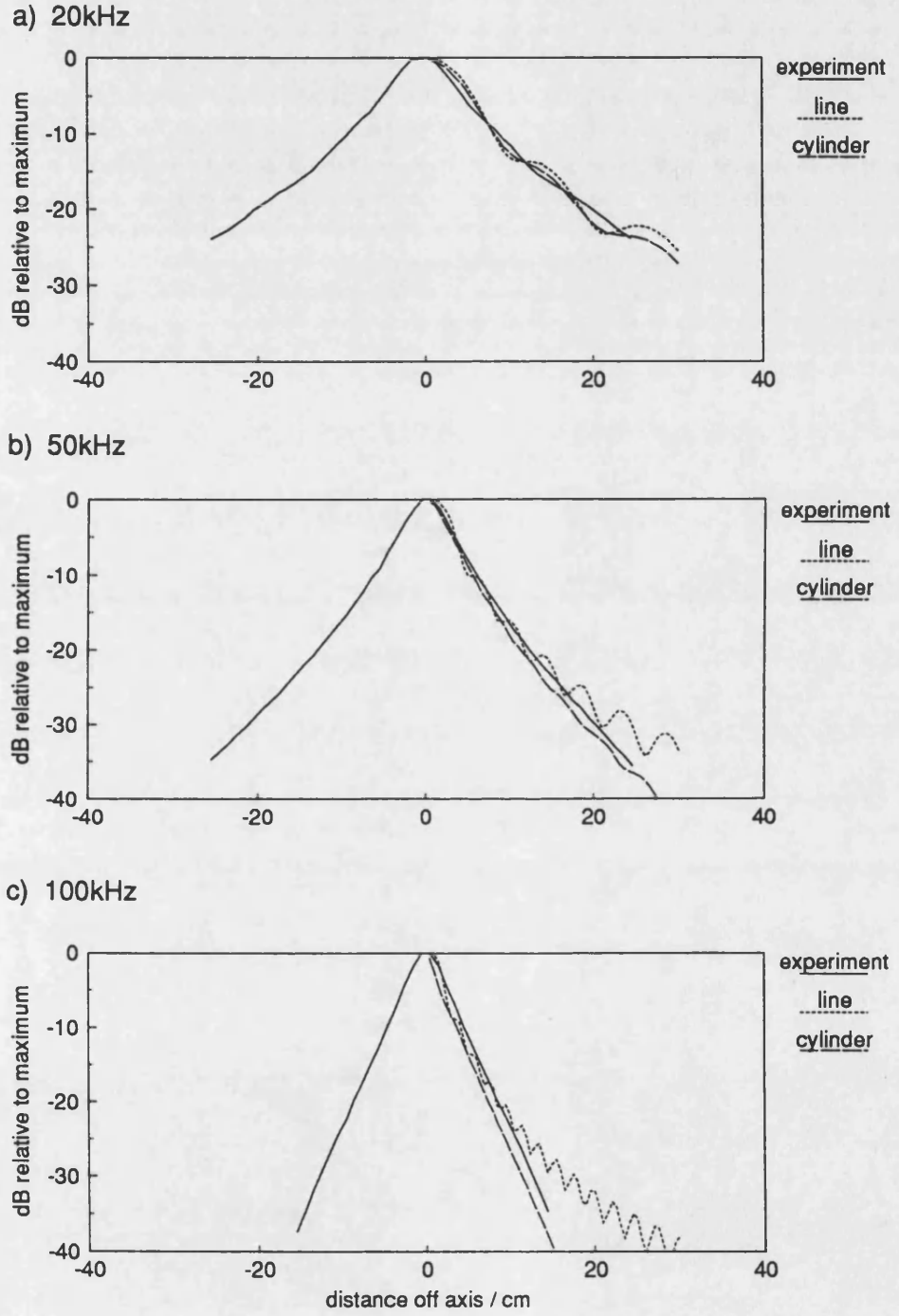

Figure 2.13 Beam profile 0.323m beyond the truncation point for difference frequency tone bursts of 20kHz, 50kHz and 100kHz.

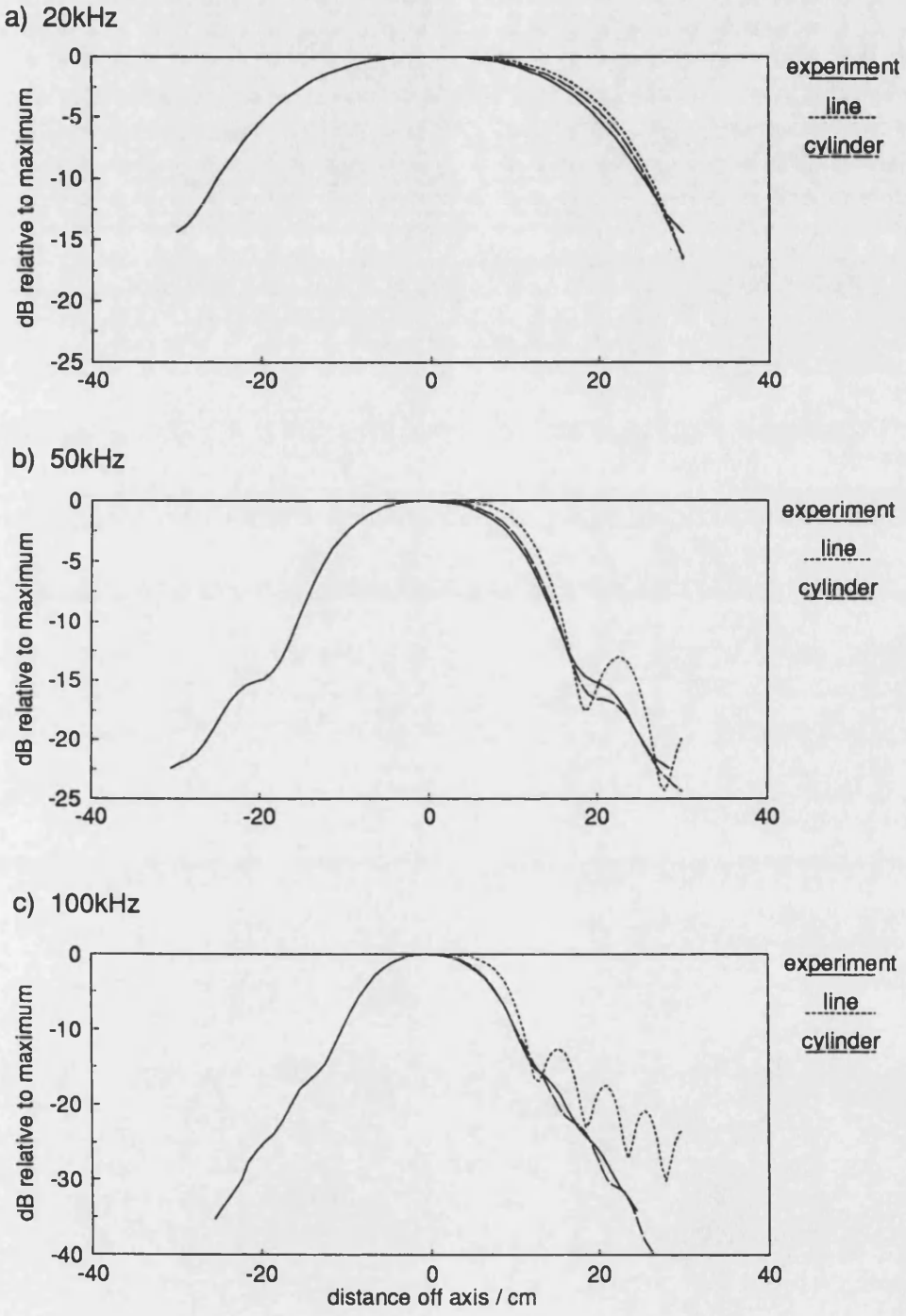

Figure 2.14 Beam profile 0.621m beyond the truncation point for difference frequency tone bursts of 20kHz, 50kHz and 100kHz.

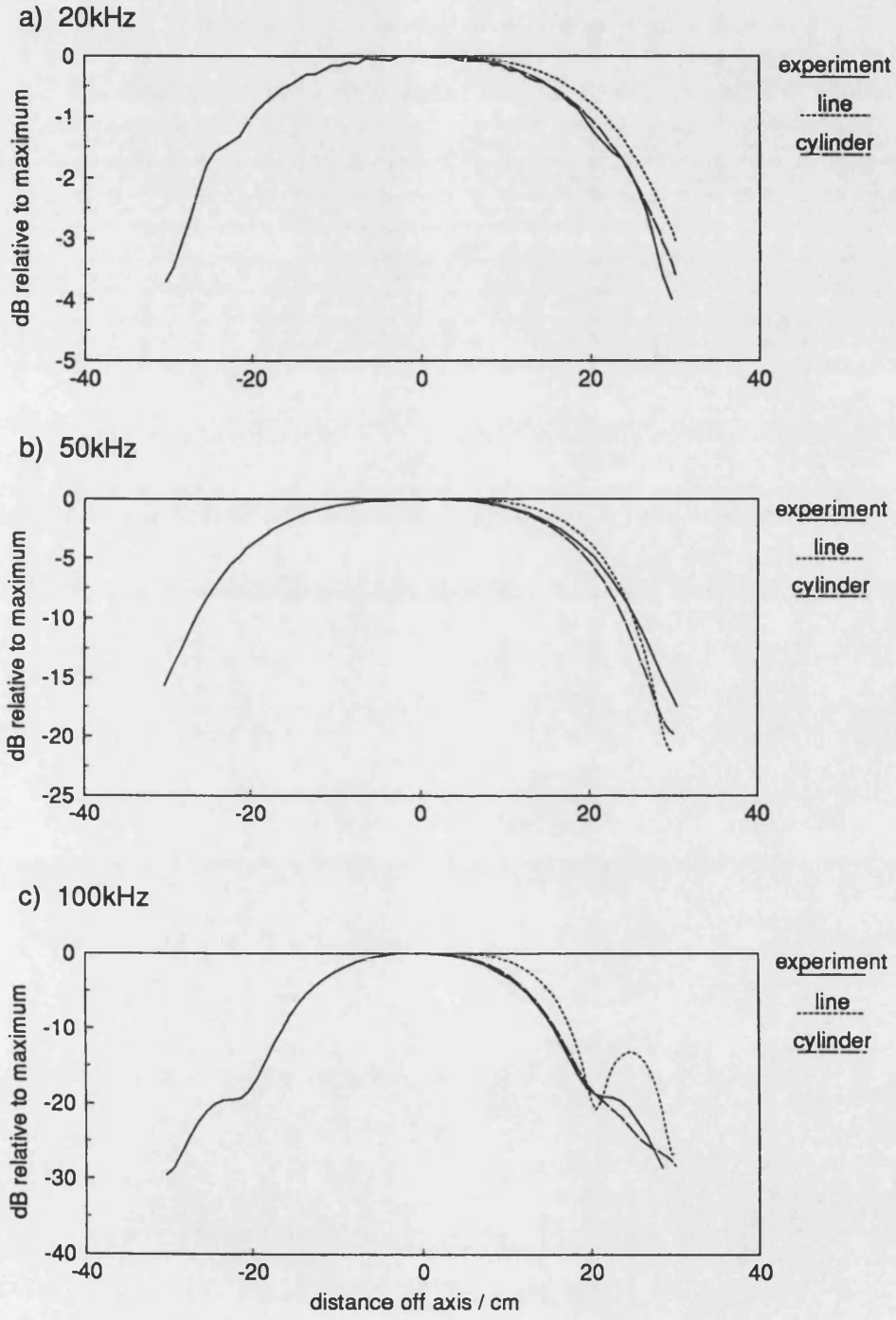

Figure 2.15 Effect of hydrophone shadowing on the amplitude of the beam profile.

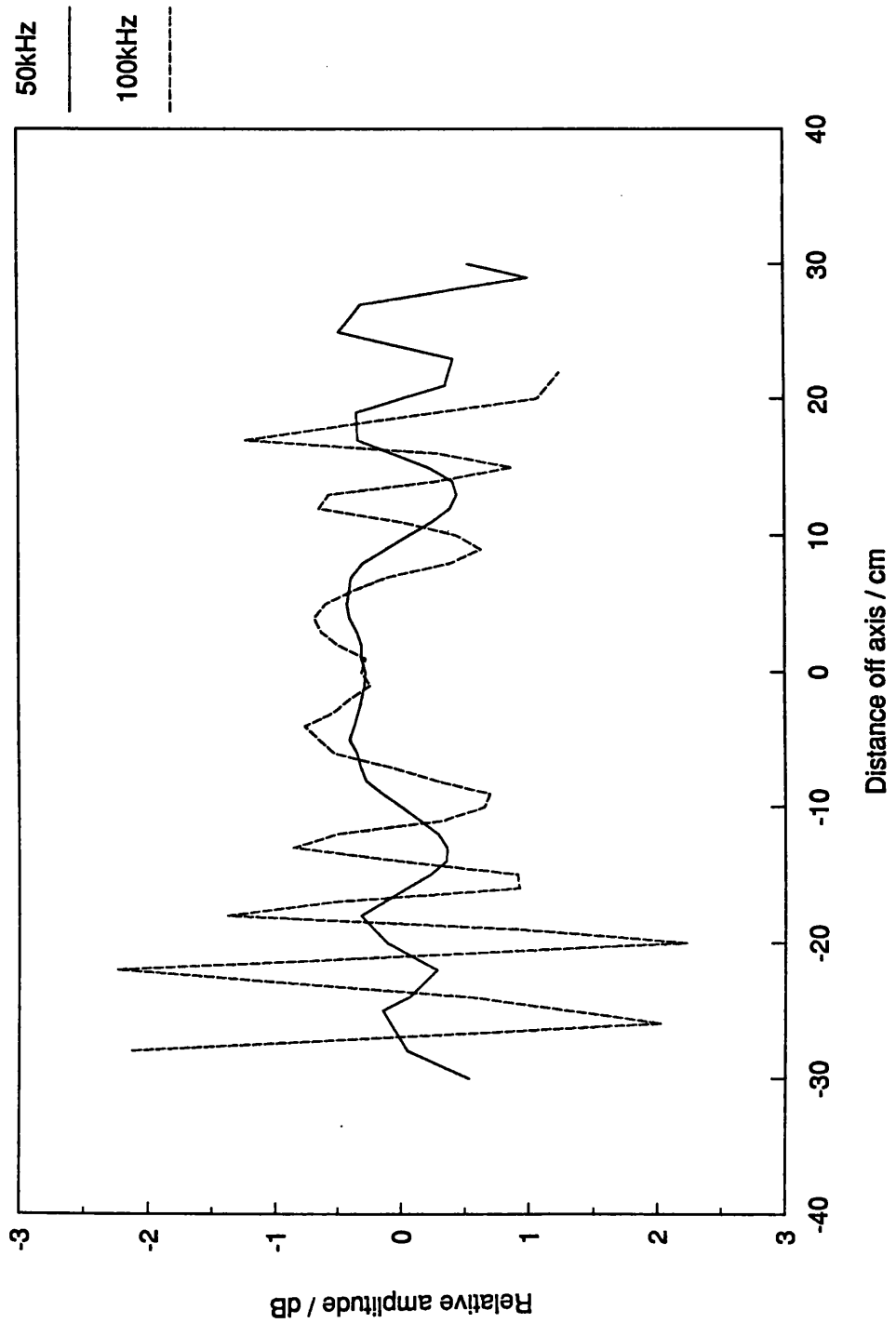

Figure 2.16 Effect of hydrophone shadowing on the phase of the beam profile.

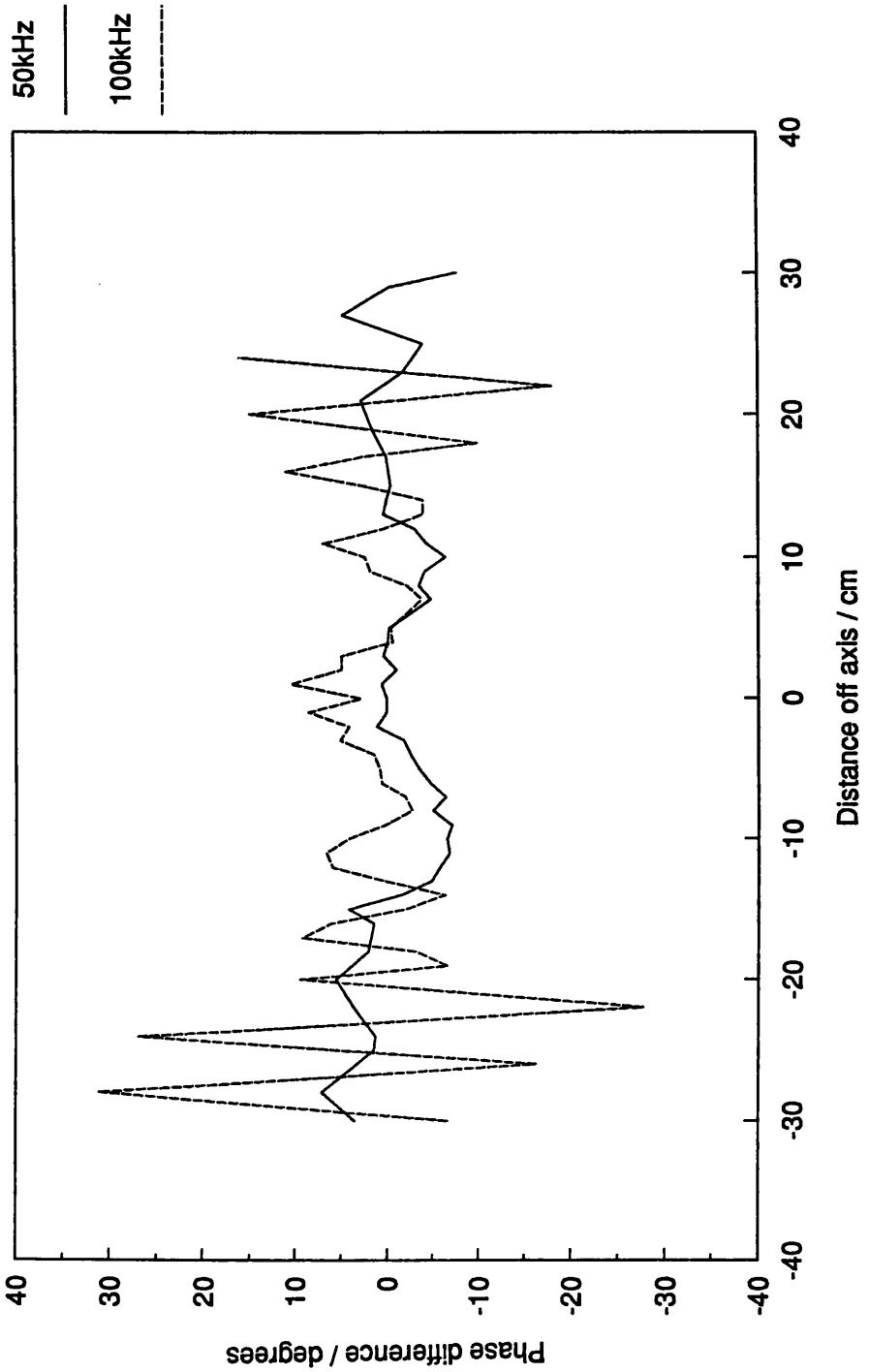

Figure 2.17 Effects of hydrophone shadowing with frequency.

a) 20cm between hydrophones

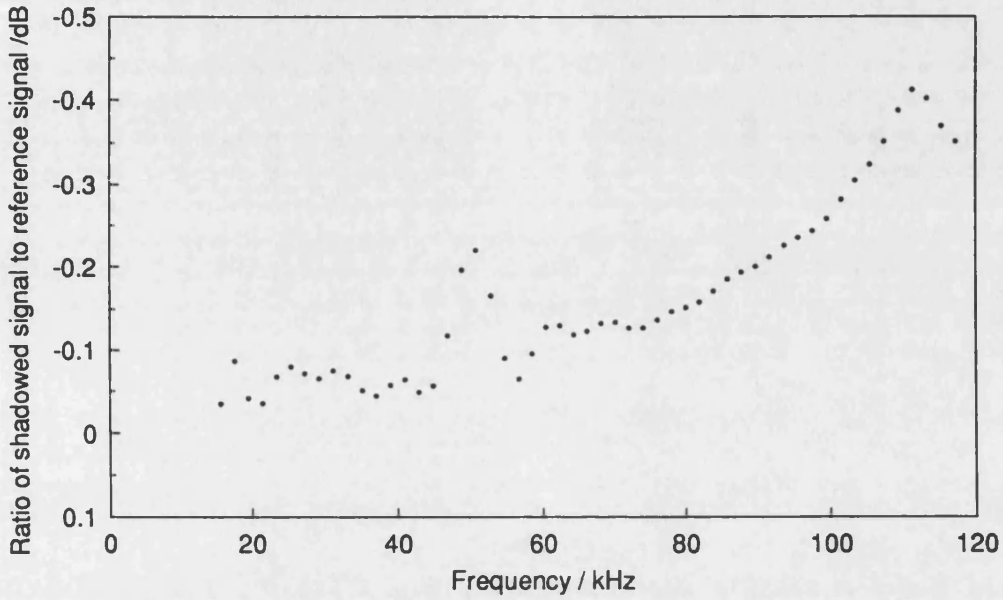

b) 5cm between hydrophones

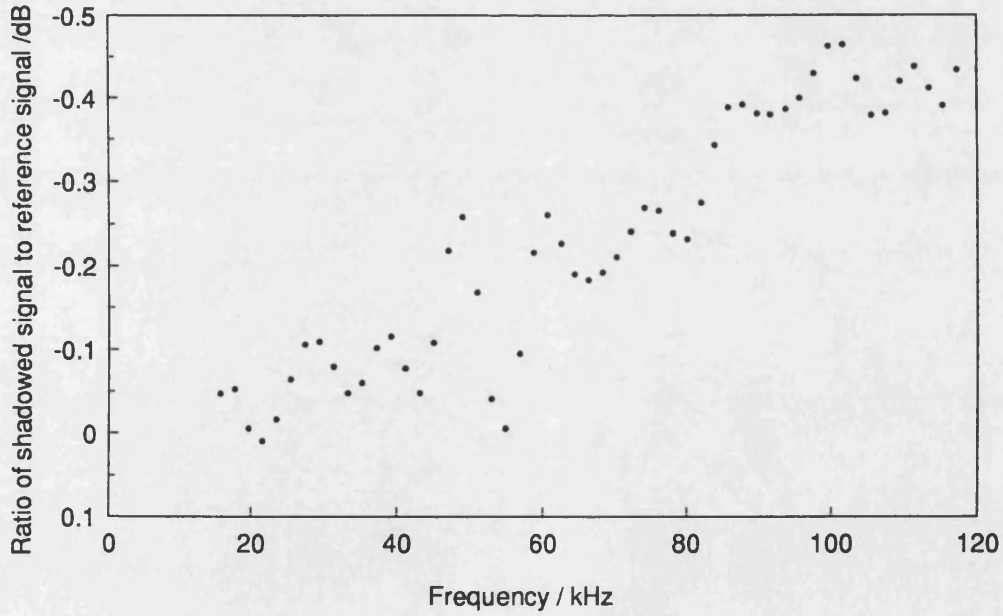

Figure 2.18 Location of hydrophones for 'shadowing' measurements.

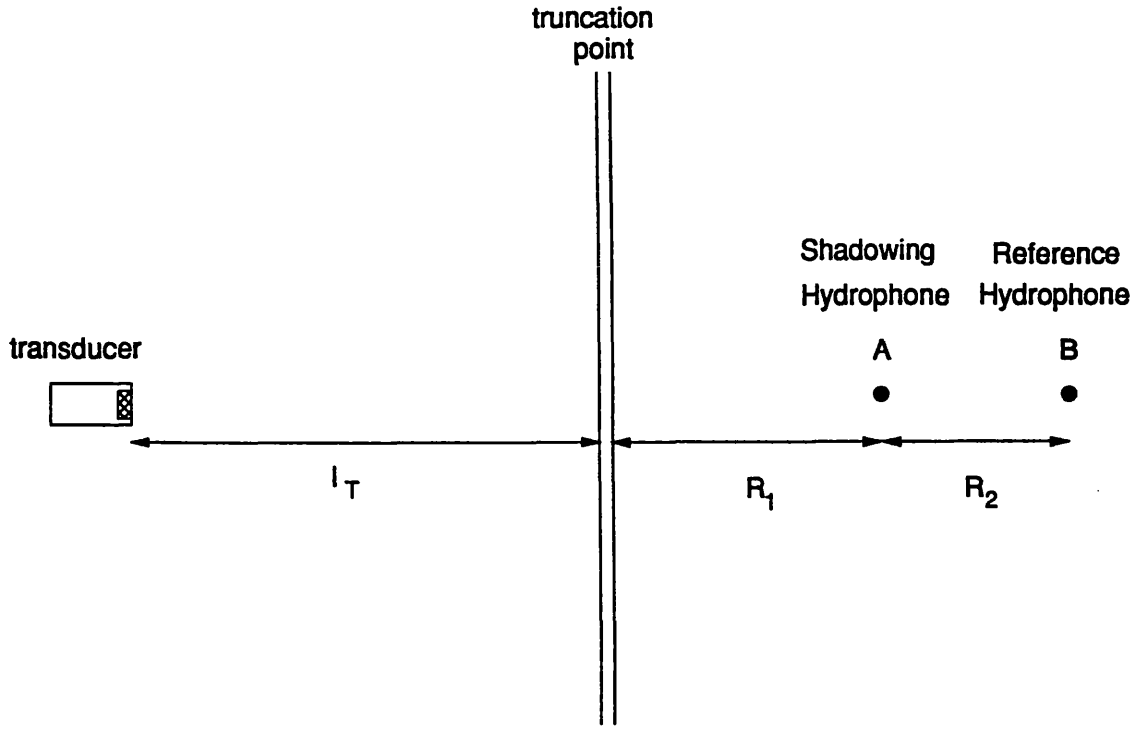

Figure 2.19 Windowing the scattered signal, and the effects on the form function.

a) Theoretical scattered signal based on a 40kHz incident pulse.

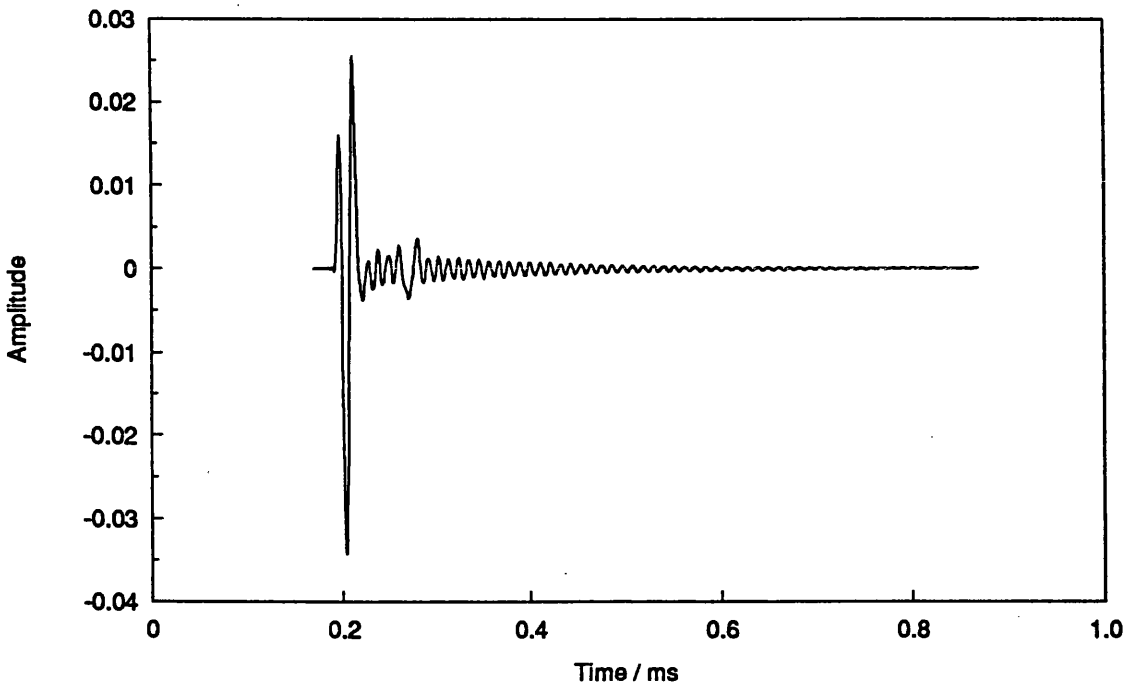

b) Resultant form function for a signal windowed with a 350 μs window.

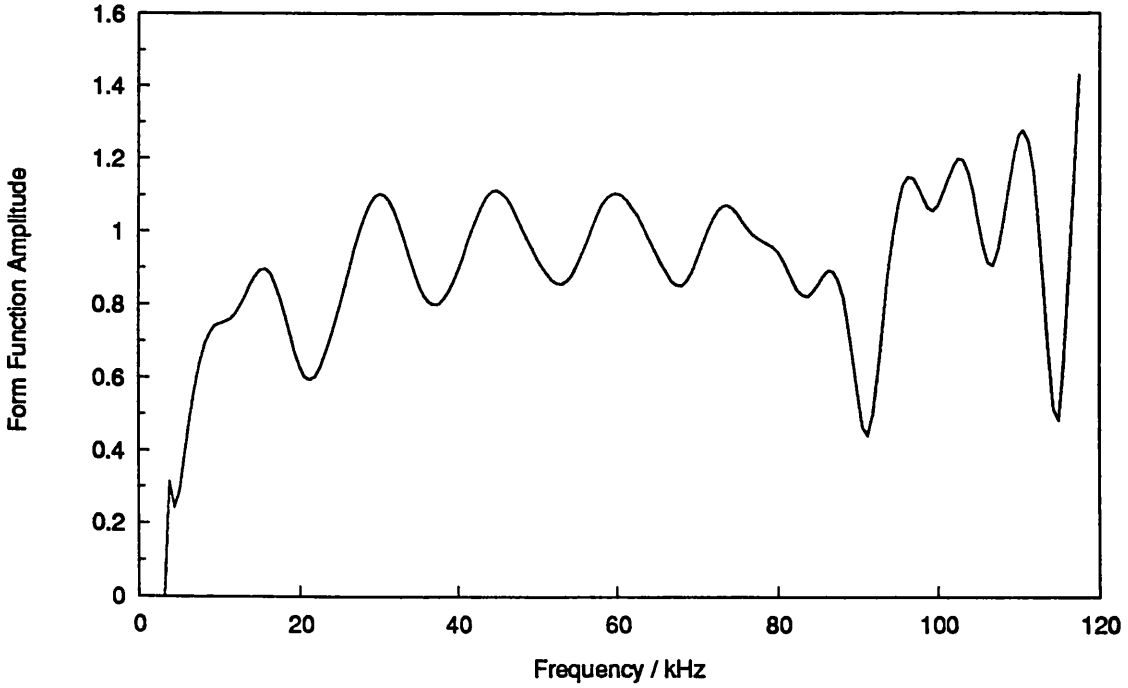

c) Resultant form function for a signal windowed with a 450 μs window.

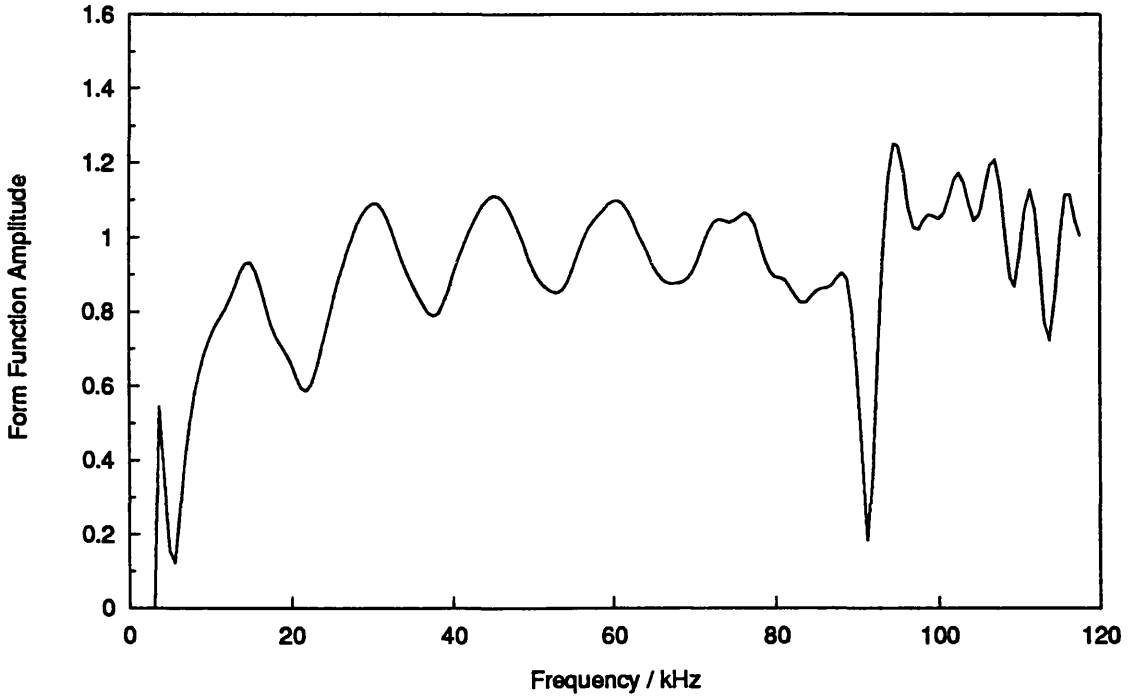

d) Resultant form function for a signal windowed with a 550 μs window.

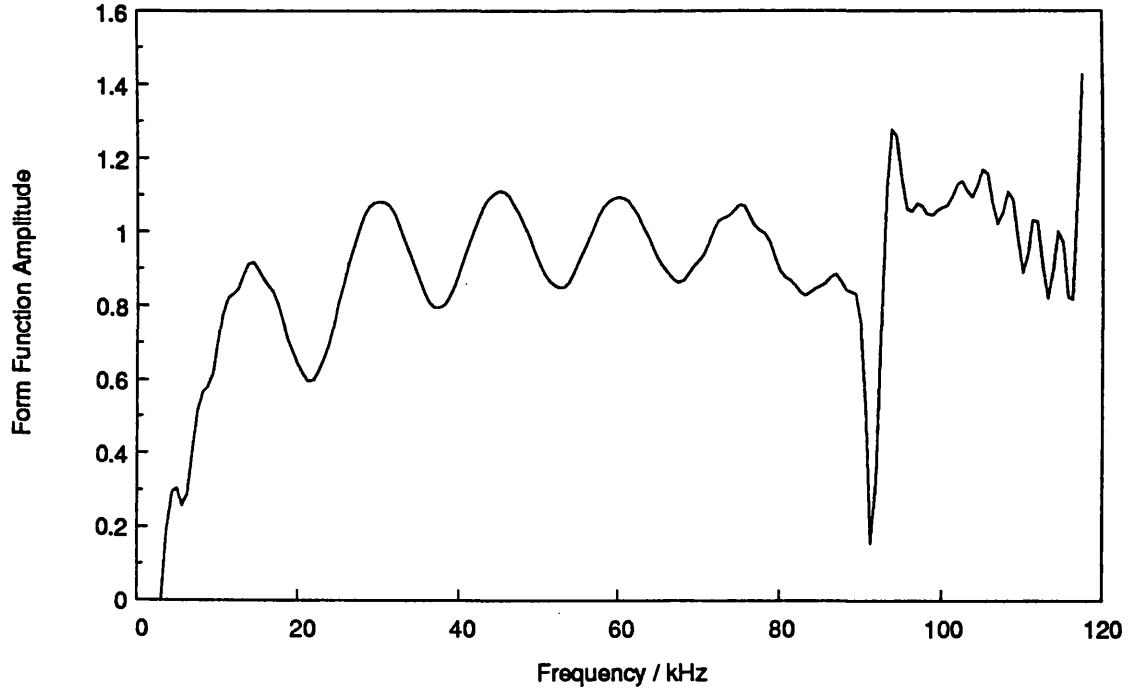

Figure 2.20 Windowing a resonant signal and the implications for the spectrum.

a) Approximation to resonant pulse $g(t) \leftrightarrow G(\omega)$.

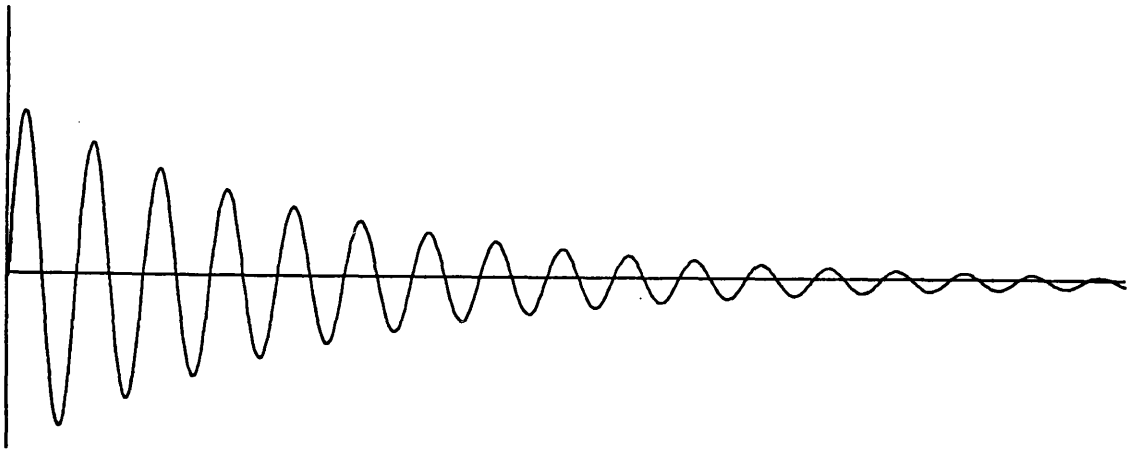

b) Time delayed pulse $\beta g(t-\tau) \leftrightarrow \beta G(\omega)e^{-i\omega\tau}$.

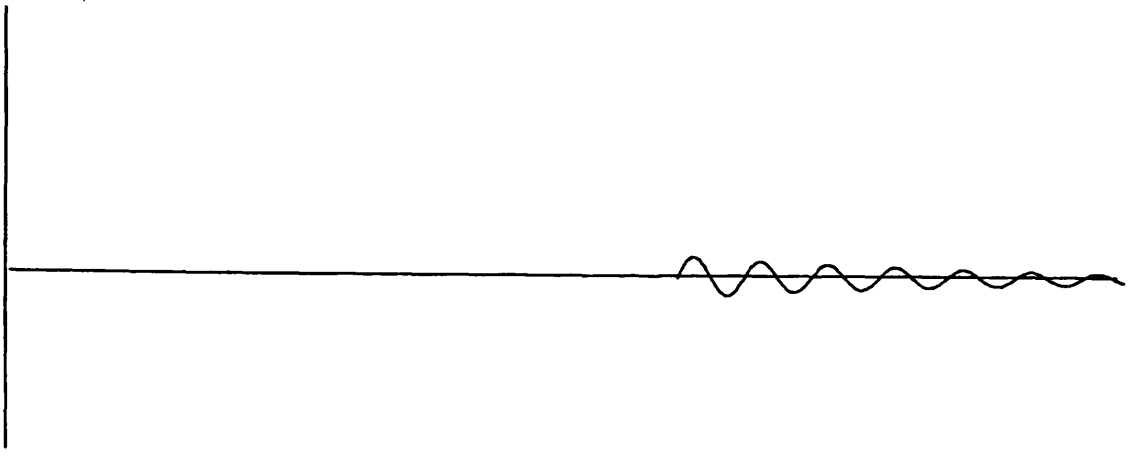

c) Truncated pulse $g(t)-\beta g(t-\tau) \leftrightarrow G(\omega)(1-\beta e^{-i\omega\tau})$.

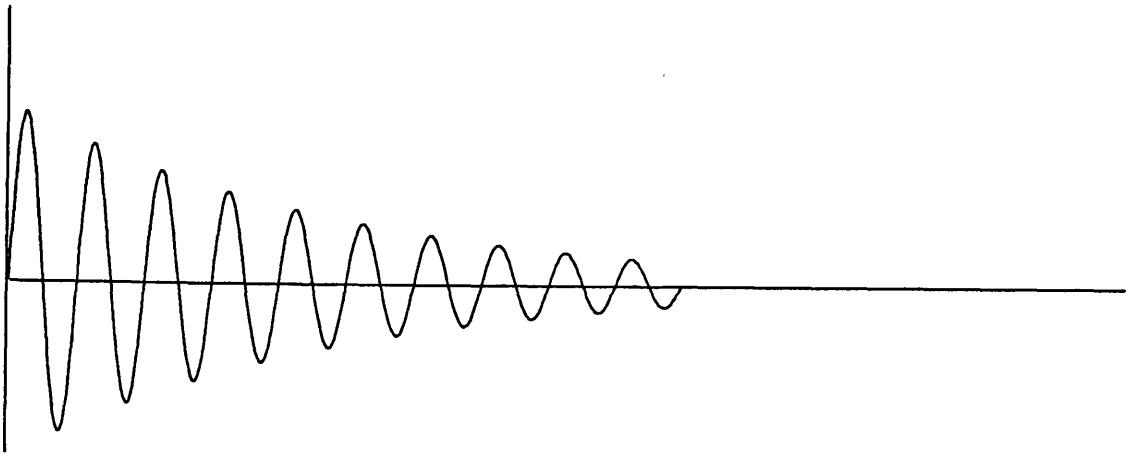

3 A Theoretical Approach to Scattering

In the study of acoustic scattering from discrete objects immersed in a fluid there are several commonly used theoretical techniques to model the scattering phenomenon, each of which has its own advantages, disadvantages and ranges of applicability. The complexity and composition of the target, the frequency range of interest and the required accuracy of the result often determine the type of theoretical approach. The aim of the following Chapter is to outline some of the theoretical techniques available and to identify their particular advantages and areas of use.

3.1 Normal Mode Series

The Normal Mode Series approach to scattering was successfully used by Faran (1951) and Hickling (1962) to calculate the exact solution for the scattering of a monochromatic plane wave from an elastic sphere. Since then the technique has been used to further study the scattering from spheres (Gaunaurd and Überall, 1983), cylinders and cylindrical shells (Doolittle & Überall, 1966; Flax & Neubauer, 1977). Due to the way the Normal Mode Series is formulated the technique is restricted to objects of separable geometry, for example spheres or cylinders, preventing its use once one progresses from 'simple shapes' to more complex realistic objects.

The Normal Mode Series expresses the incident (p_i) and scattered (p_{sc}) plane wave pressures as harmonic series. For example, for spherical geometry,

$$p_i = p_0 e^{-i\omega t} \sum_{n=0}^{\infty} (2n+1)(i)^n j_n(k_1 r) P_n(\cos\theta)$$

and

$$p_{sc}(r,\theta) = p_0 e^{-i\omega t} \sum_{n=0}^{\infty} (2n+1) i^n b_n h_n^1(k_1 r) P_n(\cos\theta)$$

where $j_n(k_1 r)$ is the Spherical Bessel Function, $h_n^1(k_1 r)$ is a Hankel function of the first kind, $P_n(\cos\theta)$ is the Legendre Function, and b_n is the scattering coefficient. The displacements within the elastic object can be expressed in terms of scalar and vector potentials in a similar form. The solution of the wave equations using the boundary conditions at the surface of the sphere gives an expression for b_n which then allows the scattered pressure to be evaluated.

Hickling (1962) presented his results in terms of the form function, f_r. This dimensionless quantity is obtained by normalising the scattered pressure with respect to the incident pressure, the radius of the target (a) and the range (r) of the observation point from the centre of the target in the following way (Neubauer et al., 1974),

$$p_{sc} = p_0 \frac{a}{2r} e^{ikr} f_r(\theta)$$

where the form function can be expressed as the sum over n partial modes $f_n(\theta)$,

$$f_r(\theta) = \sum_{n=0}^{\infty} f_n(\theta) \quad .$$

The Normal Mode Series solution for scattering from an object is ideal for 'simple' objects of separable geometry at relatively low *ka* values. However for higher frequencies the Normal Mode Series takes many terms of the series to converge and computational rounding errors can become very significant. In this case other approaches or approximations such as the Sommerfeld - Watson Transform may need to be considered. However over the relatively small *ka* range considered in the following work (typically $ka = 0 - 20$), theoretical predictions using the Normal Mode Series are relatively straightforward to calculate and computational difficulties such as those described above can be avoided.

One other disadvantage of the Normal Mode Series technique is that whilst one obtains a solution, the technique does little to explain the different contributions to the scattered field. However in recent years a technique used in nuclear physics known as the Resonant Scattering Theory has been introduced in order to explain the contributions to the scattered field in terms of resonances of the object under investigation.

3.2 Resonance Scattering Theory

The formalism of the classical resonance theory of nuclear reactions (Breit & Wigner, 1936; Feshbach, Peaslee & Weiskopf, 1947) was first applied to the problems seen in acoustic scattering by Flax, Dragonette & Überall (1978). The scattering problem is formulated in a similar way to the Normal Mode Series solution, but the form function is then decomposed into two further components, a background component and a resonance contribution, which enables the response of the target to the incident field to be understood and explained more easily.

The background component is the response of the target due solely to its shape, and is usually the response of a 'rigid' or 'soft' target, depending on which the object most closely resembles. For those targets that do not approximate rigid or soft behaviour one can also consider an intermediate background (Murphy, Breitenbach & Überall, 1978; Murphy, George & Überall, 1979). For the metallic objects investigated within the course of this work, the background can be considered to be that of a rigid sphere or cylinder as appropriate. The background term is then subtracted from the form function, partial mode by partial mode, to leave a term that is known as the resonance contribution. The resonance contributions are due exclusively to the elasticity or penetrability of the target, and permit each individual resonance to be isolated. The resonances are revealed as both sharp narrow features and broader peaks in the resonance contribution. It is possible to attribute each of the resonant peaks to a particular type and mode of resonance (e.g. Rayleigh Wave resonances or Whispering Gallery Waves), thus enhancing our physical understanding of the features seen in the scattered field and hence the form function.

3.3 Sommerfeld - Watson Transformation

For higher values of *ka* (often considered to be greater than 30) the Normal Mode Series is no longer appropriate as computational rounding errors and the speed of convergence of the solution make calculations difficult. However, it is possible to recast the Normal Mode Series using the Sommerfeld - Watson Transformation or Watson - Sommerfeld Transformation (Sommerfeld, 1949; Überall, Doolittle & McNicholas, 1966). This improves the convergence of the solution and also provides physical insight into the scattering process.

By recasting the sum of the partial modes as an integral, the Sommerfeld - Watson Transformation converts the Normal Mode Series into three separate series (Dickey, Nixon & D'Archangelo, 1983) each of which is finite or converges quite rapidly and offers no computational difficulties. One of the series represents the through-waves which are refracted into the target and re-radiate to an outside observer as they 'bounce around' inside (Brill & Überall, 1971), another series represents the diffracted Franz or creeping waves (including the Stoneley wave) and the third series represents a finite number of whispering gallery or surface waves (including the Rayleigh wave).

The technique is generally appropriate in the *ka* range 30 to infinitely large, and has been used to study the scattering from spheres (Williams & Marston, 1985), cylinders (Ugincuis & Überall, 1968; Neubauer, 1969) and cylindrical shells (Gaunaurd, 1977; Dickey, Nixon & D'Archangelo, 1983).

As the Sommerfeld - Watson Transform is based on the Normal Mode Series it too is restricted to objects of separable geometry. In order to calculate the scattered field for more complex structures several techniques such as the T-Matrix approach have been developed and these are discussed below.

3.4 T-Matrix

The T-Matrix approach to scattering, first proposed by Waterman (1969), concerns those objects of nonseparable geometry, where the scattering phenomenon is more difficult to model. The general theory of scattering of acoustic waves is contained in the theory of Huygen's Principle, which states that the scattered field is created by point sources induced on the surface of the scatterer. The scattered waves outside a body of arbitrary shape are represented by the Helmholtz integral formula over the surface of the body, which contains a distribution of secondary sources. A general procedure to determine these unknown surface sources is to let the receiver point approach the surface source point. The integral equation is then reduced to an integral equation for the unknown surface sources. When the scatterer is enclosed by a confocal quadratic surface, the integral equations can be solved in terms of wave functions special for the quadratic surface. The most commonly known are the cylindrical wave functions for circular cylinders and spherical wave functions for spheres.

Otherwise they are solved by numerical methods or other special techniques.

Waterman (1969) proposed a new formalism which starts directly with the Helmholtz integral formula and uses only cylindrical or spherical wave functions for bodies of arbitrary shape. Both incident and scattered waves are expanded in series of the common wave functions known as the basis functions. From the integral formula and the orthogonal properties of these basic functions, Waterman (1969) showed that the unknown coefficients of the scattered wave series are related to the coefficients of the incident wave by the transition matrix (T-Matrix). The elements of the infinite T-Matrix are integrals of the basis functions over the bounding surface of the scatterer, which can be evaluated numerically even for bodies of complex geometry.

Much of the relevant background prior to 1980 is collected together in one volume (Varadan & Varadan, 1979). In subsequent investigations the T-Matrix technique has been used to study elliptical cylinders (Pillai, Varadan & Varadan, 1982), and shells (Simon & Radlinski, 1982), cylindrical shells of non-circular cross section (Pillai, Varadan, Varadan & Radlinski, 1983), and finite length objects with end caps (Su, Varadan, Varadan & Flax, 1980; Überall, Stoyanov et al., 1987). Cylindrical objects with hard corners (Varadan, Varadan, Tsao & Neubauer, 1982) and a cylinder with periodically varying cross section (Lundqvist, 1986) are just two of the rigid objects to be considered using this method. The T-Matrix has been extended to prolate spheroidal co-ordinates (Hackman, 1984; Hackman & Todoroff, 1985) to account for high aspect ratio solids where the more usual equations generated by the T-Matrix become ill conditioned and the number of terms required increases dramatically.

3.5 Other techniques

The techniques described above to theoretically predict the scattering from discrete objects are the principle ones encountered during the course of this study. Of these, only the Normal Mode Series and the Resonance Scattering Theory have been used to predict and examine the scattered field for the investigations that follow. However, in addition to these four, there are many other techniques available depending upon the particular application of interest.

Many theoretical approaches concern themselves with special or limiting cases. For example, for thin circular cylinders there are many approximate theories to predict the scattered field. These have been reviewed by Greenspon (1960) and compared to an exact theory. He found that as long as the shell did not become too thick the approximate theories accurately predicted the frequencies and displacements. Baskar, Varadan & Varadan (1984) developed a thin shell theory in terms of the T-Matrix formalism. Comparison with other thin shell theories showed good agreement again as long as the shell remained thin (inner to outer radius ratio > 0.8).

For rigid bodies it is possible to use the Physical Optics or Kirchhoff approximation. This assumes that the acoustic pressure at any point exterior to a body is the sum of the incident wave at that point, and of the reflected wave as if the latter were reflected by an infinite plane tangential to the surface element in question. A further assumption is that the scattered wave contains no contribution from the geometrical shadow.

Where the scattering problem is more complex exact analytical solutions are often difficult to formulate. For a body of complex shape it is often possible to express the problem in such a way that numerical techniques can be used to obtain a theoretical prediction. Probably the most powerful of these is the finite element method. Using this approach the body of interest is divided into many small plates or facets. The resultant scattered field at a point can be calculated by summing the contributions from each facet. The technique is not restricted to rigid bodies however but can be used to model elastic bodies and those with interior structure. With the developments in computational hardware and software over recent decades it is becoming feasible to investigate scattering problems which were hitherto regarded as being too complicated to solve analytically in closed form and were therefore largely ignored.

If the incident field departs from an infinite plane wave then the scattering problem may need to be treated differently. Gaunaurd and Überall (Überall & Gaunaurd, 1981; Gaunaurd & Überall, 1985) used the Singularity Expansion Method (SEM) of Baum (1976) in their study of transient fields incident on a sphere. They were able to demonstrate how, for impenetrable spheres, the poles in the complex frequency plane represented the creeping waves that propagate around the sphere. A similar investigation for a circular cylinder has been undertaken by Heyman & Felsen (1986).

The above discussion mentions only a few of the theoretical techniques that are available for use in the problems of acoustic scattering. However, the purpose of this Chapter was primarily to review the principle techniques that are used in this area of acoustic scattering and to identify their ranges of applicability, and any associated problems or advantages. The precise approach chosen to deal with a particular problem will all too often depend on the objects, frequency range and scenario of interest.

4 Spheres

The development of any new experimental facility or measurement technique requires it to be calibrated against known standards so that one is aware of any significant deviations in the results due solely to errors or artifacts in the system or technique. In order to assess the performance of the system and measurement technique described in Chapter 2, a tungsten carbide sphere has been used as a calibration target. This Chapter primarily discusses the performance of the experimental system and the measurement technique, little attention is paid to an analysis of the features found in the scattered field except where the results obtained here differ from those expected or reported elsewhere in the literature. The choice of target was based on several criteria. Firstly, the sphere has been used by many investigators in recent years and there is well documented theoretical and experimental data on its acoustic performance. Secondly, the very high density of tungsten carbide leads to quasi - rigid behaviour at low *ka* values so that the scattered field is more readily analysed. It is also worth noting that precision tungsten carbide spheres are readily available and are often used as calibration targets (MacLennan, 1981).

4.1 Literature Survey

Rayleigh's pioneering work on scattering (1878) included an investigation of the effects of a fluid sphere in a sound field when the sphere was small compared to a wavelength. Rayleigh and later other workers theoretically evaluated the scattering phenomenon from both fluid (Anderson, 1950) and rigid spheres (e.g. Morse, 1948). The exact solution for a solid elastic sphere in a fluid, neglecting absorption in the sphere, was put forward by Faran (1951) and Hickling (1962) using a Normal Mode Series approach. In presenting their results they defined a form function which was independent of the incident wavefield and the size of the sphere. The form function is a measure of the scattering characteristics of a target with normalised frequency (*ka*), and will be the same for targets of the same shape and material.

For metallic spheres it is often appropriate to neglect absorption, however for other materials this is clearly not the case. Vogt, Flax, Dragonette & Neubauer (1975) modified the existing theory (by the standard technique of introducing complex wavenumbers) to account for absorption and demonstrated good agreement between the modified theory and their experimental data for a lucite (perspex) sphere. In a later theoretical paper Davies Dragonette & Flax (1978) considered the scattering from silicone rubber spheres and cylinders. Due to the extremely low shear velocity they found it possible to neglect shear in their calculations and computed the form function for an identically shaped liquid cylinder with the same density and longitudinal velocity.

The Normal Mode Series approach used by Faran (1951) and Hickling (1962) is limited to objects of separable geometry, and experiences computational difficulties for

higher *ka* values (>20). Thus, in recent theoretical work the Normal Mode Series approach has been abandoned in favour of either Integral Transform techniques (e.g. Überall & Huang, 1976) or matrix methods of evaluation (Waterman, 1969, 1976) that are able to cope with a wider range of objects and, by overcoming the computational difficulties, a wider frequency range.

Williams & Marston (1985) applied the Sommerfeld - Watson Transformation (SWT) to the problem of backscattering from a fluid loaded elastic sphere. Their analysis concentrated on the specular reflection and the Rayleigh wave contribution to the scattering at small backscattering angles. Experimental measurements of the first and second Rayleigh wave contributions from tungsten carbide spheres over a *ka* range 24 - 80 appeared to confirm the SWT predictions, although there were several discrepancies attributed to either theoretical approximations / assumptions or experimental difficulties, such as the method by which the sphere was supported.

One of the most recent theoretical techniques to be applied to the problem of acoustic scattering is the Resonance Scattering Theory (Flax, Gaunaurd & Überall, 1981) the principles of which have been outlined in Chapter 3. An analysis of the backscattered echoes from an elastic sphere using the Resonance Scattering Theory (RST) has been presented by Gaunaurd & Überall (1983). The RST has recently been extended by Ayres & Gaunaurd (1987a) to look at the more complex problem of scattering from visco-elastic spheres. In a subsequent paper (Ayres & Gaunaurd, 1987b) they look at the inverse problem, that is, to try to determine the material properties of elastic spheres from the information contained within the form function. A review outlining much of the RST work on spheres has been presented by Brill & Gaunaurd (1987).

The first of many experimental observations were made by Hampton & McKinney (1961). They used a steady state pulse incident on brass and aluminium spheres from which they found that a considerable amount of energy penetrated the sphere and resulted in a very complicated echo structure in the backscattered signal. Similar investigations on solid cylinders (Barnard & McKinney, 1961; Neubauer, Ugincuis & Überall, 1969) showed that it was possible to identify a direct reflection and a wave which apparently 'crept' around the sphere, which was linked to the 'creeping wave' ideas of Franz (1954). The creeping wave is highly attenuated and slower than the speed of the wave in the surrounding fluid. It depends mainly on the geometry of the scatterer, unlike the Rayleigh type wave which is slightly attenuated with a speed greater than that in the fluid and owes its existence solely to the scatterer's elastic properties.

In 1974 Neubauer et al. presented two papers concerned with measuring the far field form function of spheres in the backscatter direction. In the first paper Neubauer, Vogt, Dragonette (1974) demonstrated excellent agreement between experimental results and the

theoretical predictions for aluminium and tungsten carbide spheres under steady state conditions. A single transducer was used and the sizes of the spheres varied from 0.25 to 2.5" to cover a *ka* range 0 - 20. The second paper (Dragonette, Vogt, Flax & Neubauer, 1974) describes how a transient pulse may be used to experimentally determine the monostatic form function for tungsten carbide, aluminium and brass spheres in air, where, for metallic spheres, the form function closely resembles that of a rigid sphere. A *ka* range of 0 - 10 was covered using a transient pulse centred on 26kHz and a sphere 0.75" in diameter. Again excellent agreement was found between theory and experiment and it was noted that the position of the minima in the form function were very sensitive to the shear wave velocity and insensitive to the compressional wave velocity. This sensitivity of the form function to the shear wave velocity proved useful to MacLennan & Dunn (1984) who used the experimentally measured form function to determine the shear velocity of their samples of tungsten carbide.

Amongst the more recent experimental work Dragonette, Numrich & Frank (1981) used the tungsten carbide sphere as a calibration target for use in laboratory scattering measurements. The short pulses of two or three cycles centred on 0.5MHz or 1MHz enabled the form function to be calculated over the *ka* range 14 - 70. Their results were later used by Gaunaurd & Überall (1983) who compared them to the theoretical RST results discussed in that paper.

The common use of spheres as calibration targets has led to a body of work considering the properties of various materials for this purpose. As an aid to calibration and ultrasonic beam assessment, Chivers & Anson (1982) presented theoretical results for the form function of over forty different materials. Often the spheres are of tungsten carbide or copper and Foote & MacLennan (1984) carried out a detailed comparison of the properties of these two materials.

The review presented above has been confined to works that consider or directly relate to the computation or experimental determination of the form function of an elastic sphere, and, whilst not comprehensive, does serve to illustrate the attention the sphere has received. Hence a great deal of work pertinent to other aspects of the scattering phenomenon from spheres, spherical shells and spheroids has been omitted.

4.2 Theory

Consider a sphere centred at the origin of a spherical co-ordinate system (Figure 4.1). The sphere consists of an isotropic material with compressional and shear wave velocities given by c_l and c_t respectively and a density ρ_s, surrounded by a fluid, infinite in extent, of density ρ_1 and velocity c_1. Let a steady state plane wave travelling in the direction of the positive z-axis be incident on the sphere which is of radius a. The incident plane wave is given by,

$$p_i = p_0 e^{i(\underline{k}\cdot\underline{r}-\omega t)}$$

$$= p_0 e^{-i\omega t} e^{ik_1 r\cos\theta} \quad .$$

Here ω and k are the angular frequency and the wavenumber respectively and the expression can be assumed independent of ϕ. The above can be rewritten

$$p_i = p_0 e^{-i\omega t} \sum_{n=0}^{\infty} (2n+1)(i)^n j_n(k_1 r) P_n(\cos\theta) \quad , \tag{4.1}$$

where $j_n(k_1 r)$ is the Spherical Bessel Function and $P_n(\cos\theta)$ is the Legendre Function.

The acoustic field incident on the sphere results in a scattered wave in the fluid (p_{sc}), which at an observation point (r,θ) can be expressed as

$$p_{sc}(r,\theta) = p_0 e^{-i\omega t} \sum_{n=0}^{\infty} (2n+1) i^n b_n h_n^1(k_1 r) P_n(\cos\theta) \tag{4.2}$$

where $h_n^1(k_1 r)$ is a Hankel function of the first kind. The coefficient b_n is the scattering coefficient and is to be determined from the solution of the wave equations using the boundary conditions at the surface of the sphere.

The incident wave results in a displacement in the sphere which can be expressed in terms of a scalar and a vector potential. A separable variables technique can be used to solve the appropriate wave equations to give expressions for the potentials.

In order to obtain the scattering coefficient b_n it is necessary to apply the boundary conditions at the surface of the sphere $r = a$. At the surface the displacement and normal stresses are continuous and the tangential stresses must be zero. Substitution of the expressions for the potentials in the sphere and the pressures in the fluid into the boundary conditions result in a system of simultaneous equations which can be solved for b_n. This scattering coefficient, neglecting absorption, is given by

$$b_n = \frac{\begin{bmatrix} \beta_1 & \alpha_{12} & \alpha_{13} \\ \beta_2 & \alpha_{22} & \alpha_{23} \\ 0 & \alpha_{32} & \alpha_{33} \end{bmatrix}}{\begin{bmatrix} \alpha_{11} & \alpha_{12} & \alpha_{13} \\ \alpha_{21} & \alpha_{22} & \alpha_{23} \\ 0 & \alpha_{32} & \alpha_{33} \end{bmatrix}}$$

where, (Gaunaurd & Überall, 1983)

$$\beta_1 = -x_l^2 \frac{\rho_1}{\rho_s} j_n(x_1)$$

$$\beta_2 = x_1 j_n'(x_1)$$

$$\alpha_{11} = x_t^2 \frac{\rho_1}{\rho_s} h_n^1(x_1)$$

$$\alpha_{21} = -x_1 h_n^{1\prime}(x_1)$$

$$\alpha_{12} = (2n(n+1) - x_t^2) j_n(x_l) - 4x_l j_n'(x_l)$$

$$\alpha_{22} = x_l j_n'(x_l)$$

$$\alpha_{32} = 2(j_n(x_l) - x_l j_n'(x_l))$$

$$\alpha_{13} = 2n(n+1)(x_t j_n'(x_t) - j_n(x_t))$$

$$\alpha_{23} = n(n+1) j_n(x_t)$$

$$\alpha_{33} = 2x_t j_n'(x_t) + (x_t^2 - 2n(n+1) + 2) j_n(x_t)$$

with

$$x_1 = k_1 a, \qquad x_t = k_1 a \frac{c}{c_t}, \qquad x_l = k_1 a \frac{c}{c_l}$$

and the primes imply differentiation with respect to the argument.

The form function $f_r(\theta)$ at a position (r, θ) can be defined (Neubauer et al., 1974) such that,

$$p_{sc} = p_0 \frac{a}{2r} e^{ikr} f_r(\theta) \cdot$$

Substitution of p_{sc}/p_0 from equation 4.2 results in the following expression for $f_r(\theta)$

$$f_r(\theta) = \frac{2r}{a} e^{-ikr} \sum_{n=0}^{\infty} (2n+1) i^n b_n h_n(k_1 r) P_n(\cos\theta) \qquad (4.3)$$

where the time dependence has been suppressed. For certain geometries and/or ranges it is possible to simplify equation 4.3. In this application the far field backscattered field is of interest. For backscatter $\theta = \pi$ and the Legendre Function reduces to $(-1)^n$. In the far field, usually considered to be at a distance greater than ten sphere diameters, the Hankel function can be replaced by its asymptotic form

$$h_n^1(kr) \underset{r\to\infty}{\sim} (i)^{-n-1} \frac{e^{ikr}}{kr} \quad .$$

Thus equation (4.3) reduces to

$$f_\infty(\pi) = \frac{2}{ika} \sum_{n=0}^{\infty} (2n+1)(-1)^n b_n \quad . \qquad (4.4)$$

The expressions for the finite range and the far field form function were implemented in FORTRAN 77 (Humphrey - private communication). In both cases only the backscatter direction was considered.

4.3 Theoretical Predictions and Discussion

In order to assess the performance of the system experimental measurements were made at two distinct ranges. The first at a finite range (equation 4.3) and the second at a distance large enough to make the far field approximations (equation 4.4). The theoretical predictions for a finite range of 0.15m and the far field form functions for a tungsten carbide sphere, over a *ka* range 0.5 - 12, are shown together for comparison in Figure 4.2. Both curves exhibit an oscillatory background, most noticeable in the *ka* range 0.5 - 7, but present throughout. Superimposed on this are several sharp 'resonance' features most clearly visible at *ka* values of 7.3, 9.2 and 10.8. The Resonance Scattering Theory (Flax, Gaunaurd & Überall, 1981; Gaunaurd & Überall, 1983) has shown how the form function can be decomposed into a background component and a resonance contribution, which depends solely on the elastic properties of the scatterer. For metallic spheres the background approximates that of a rigid sphere, shown in Figure 4.3.

Comparison of the finite range and far field calculations presented in Figure 4.2 reveals several significant differences. The finite range calculation, computed for a range of 0.15m and a 0.0381m diameter tungsten carbide sphere, is greater than the far field calculation for all *ka* values in the range 0 - 12. It is also noticeable that the peak to peak amplitude variation for the oscillatory part of the form function (*ka* = 0-7) is less in the finite range case. These extrema are also shifted to slightly lower *ka* values, and for this example typically the shift is of the order 0.1 *ka*.

These differences can be explained in the following way. The oscillatory part of the

form function is produced by the interaction of the creeping wave and the specular reflection from the front of the sphere. If one considers Figure 4.4, the upper diagram illustrates the far field case whilst the lower diagram illustrates the finite range case. In the far field example the incident plane wave causes a creeping wave which traverses exactly half of the sphere's circumference, and is returned to the observation point in a direction parallel to the incident wave. The observation point will see two signals scattered from the sphere, the specular reflection and the creeping wave identical in shape but smaller than the specular reflection and delayed by a time τ. This has been noticed experimentally in Figure 2.9c, where the creeping wave can be seen approximately $50\mu s$ behind the specular reflection. Fourier Transforming the returned sequence of specular reflection and creeping wave will introduce a 'ripple' on to the spectrum of the first signal. This ripple has a period given by $1/\tau$ and a magnitude proportional to the magnitude of the delayed signal. In the near field example (Figure 4.4b), the creeping wave traverses more than half of the circumference of the sphere. The speed of the creeping wave is less than that of the speed of the wave in water, resulting in a greater time difference between the front face reflection and the creeping wave, and hence a shorter period to the ripple in the frequency domain (Figure 4.2). In addition the creeping wave will undergo a greater attenuation in traversing a greater portion of the sphere and thus the amplitude of the ripple on the form function will be reduced.

Also of note in Figure 4.2 are the sharp resonance features seen at *ka* values of about 7.3, 9.2 and 10.8. It can be seen that the position of these features does not change between the two plots. This is because these resonance features are caused by the elastic properties of the sphere which have not changed.

In order to predict the form function as accurately as possible it is necessary to know the elastic properties (ρ,c_l and c_t) of the sphere. It is also desirable to know how sensitive the form function is to changes in these parameters. A theoretical study was made of the variation in the position of two of the minima, at *ka* values of 7.3 and 10.8, with variation in the density and wave velocities. These parameters were varied either side of nominal values given by Kaye & Laby (1986) and found in the literature. Changes in the location of the resonance minima due to variation of the density or compressional wave velocity were found to be negligible and subsequent calculations use the nominal values provided by Kaye & Laby (1986) and listed for reference in Appendix 3. However variation of the shear wave velocity significantly altered the position of the minima, an increase in c_t moving the minima to higher *ka* values. From the comparison of the experimental data with the form function calculated for various values of the shear wave velocity it was possible to ascertain that the shear velocity for the tungsten carbide spheres used in this work was in the region of $4160ms^{-1}$. This agrees well with published values, a few of which are shown in Table 4.1. This technique to determine the shear wave velocity of metal spheres has been used previously by MacLennan & Dunn (1984).

Table 4.1 Published values of the shear wave velocity of tungsten carbide.

Shear wave velocity/ms^{-1}	Source
4160	Kaye & Laby (1986)
4171	MacLennan & Dunn (1984) - experimental
4185	Vogt & Neubauer (1976) - experimental
3984	Chivers & Anson (1982)

4.4 Experimental Results and Discussion

Experimental measurements were recorded at two ranges using the procedure described in Chapter 2. The first at a finite range, in this case at r =0.15m, and the second in the far field. In this instance a range of 0.25m proved adequate although as a 'rule of thumb' ten object diameters is the usual distance. Scattering measurements were made using a 0.0381m diameter tungsten carbide sphere which was positioned on the acoustic axis of the transducer with the use of a net constructed from fishing line. A net overcomes the problem of suspending the spheres as it is undesirable to mark them or make permanent attachments.

The comparison of the theoretical far field form function and the experimental data is illustrated in Figure 4.5. Measurements were taken using two pulses, one based on 30kHz and a shorter one based on 60kHz. The results agree well with the theory for *ka* values less than 7 with the exception of a small region between *ka* values of 4 and 5. For *ka* values greater than 7 the experimentally determined values are lower than the theoretical prediction although they do follow the same trend.

Figure 4.6 illustrates the finite range results for the same sphere compared to the appropriate theoretical prediction. Measurements were made at a distance 0.15m from the centre of the sphere using three pulses based on 30kHz, 50kHz, and 65kHz. The overlap between these three sets of results is good and again the agreement between experiment and theory is acceptable except for a region between *ka* values of 4 and 5. Above a *ka* value of approximately 7 the experimental values are significantly lower than the theoretical prediction.

The discrepancies visible in Figures 4.5 and 4.6 are largely attributable to the effects of the hydrophone being located between the source and the object. From Figure 2.17a one can identify an anomaly between 50 and 60kHz which has been attributed to the hydrophone tube resonance. For a 0.0381m diameter sphere this anomaly would correspond to *ka* values

between 4.0 and 4.8. This feature can be seen in both Figure 4.5 and Figure 4.6. The general lowering of experimental values is attributed to the hydrophone shadowing effects. This is clearly visible at higher ka values ($ka > 7$) and is greater in the finite range case. One would not expect to see identical results for the hydrophone shadowing here as when measured with a hydrophone due to the area of the sphere being much greater and effectively 'integrating' over a finite portion of the beam.

In addition to a comparison of the frequency domain results in terms of the form function it is also possible to predict and hence compare the signals in the time domain. If the ideal theoretical pulse produced on-axis is given by the second derivative of the square of the pulse envelope (Berktay, 1965) then for a pulse envelope given by $(\cos \omega t - 1)/2$, the shape of the transmitted pulse is given by $(\cos \omega t - \cos 2\omega t)/2$. From our knowledge of the form function for a sphere, and Fourier analysis, it is possible to predict the scattered pulse from the relationship

$$|f_\infty(ka)| = \frac{2r}{a} \left| \frac{g_{sc}(ka)}{g_i(ka)} \right| ,$$

where $g_{sc}(ka)$ is the frequency spectrum of the backscattered signal, and $g_i(ka)$ is the frequency spectrum of the incident signal (Dragonette, Vogt, Flax, Neubauer, 1974).

A theoretical pulse based on 50kHz incident on a tungsten carbide sphere produces the backscattered pulse shown in Figure 4.7a. An experimental measurement of a similar pulse scattered from a tungsten carbide sphere 0.0381m in diameter is shown in Figure 4.7b for comparison. The two signals have not been overlaid as the experimental incident pulse is not as symmetrical as the theoretical pulse and so there are difficulties in directly comparing the two signals. However it is possible to compare the period of the ringing in the pulse which agrees well, and to identify the creeping wave, which is shown by an absence of ringing, at a time of approximately 140μs in both the theoretical and experimental pulses.

4.5 Summary

Measurements of the form function for a tungsten carbide sphere have been obtained for both far field and finite range conditions. The short pulse generated by the parametric array has allowed experimental data to be obtained over the frequency range 10 - 100kHz ($ka = 0.5$ - 12) using just two or three different pulse lengths. Comparison of experimental data with the theoretical predictions demonstrates good agreement for both the far field and a finite range case, the most significant discrepancy due to the 'shadowing' effect of the hydrophone. With this knowledge of the behaviour of the experimental system it will now be possible to progress to cylindrical objects and eventually more complex shapes, taking due care in any backscattering configurations.

Figure 4.1 Spherical Geometry.

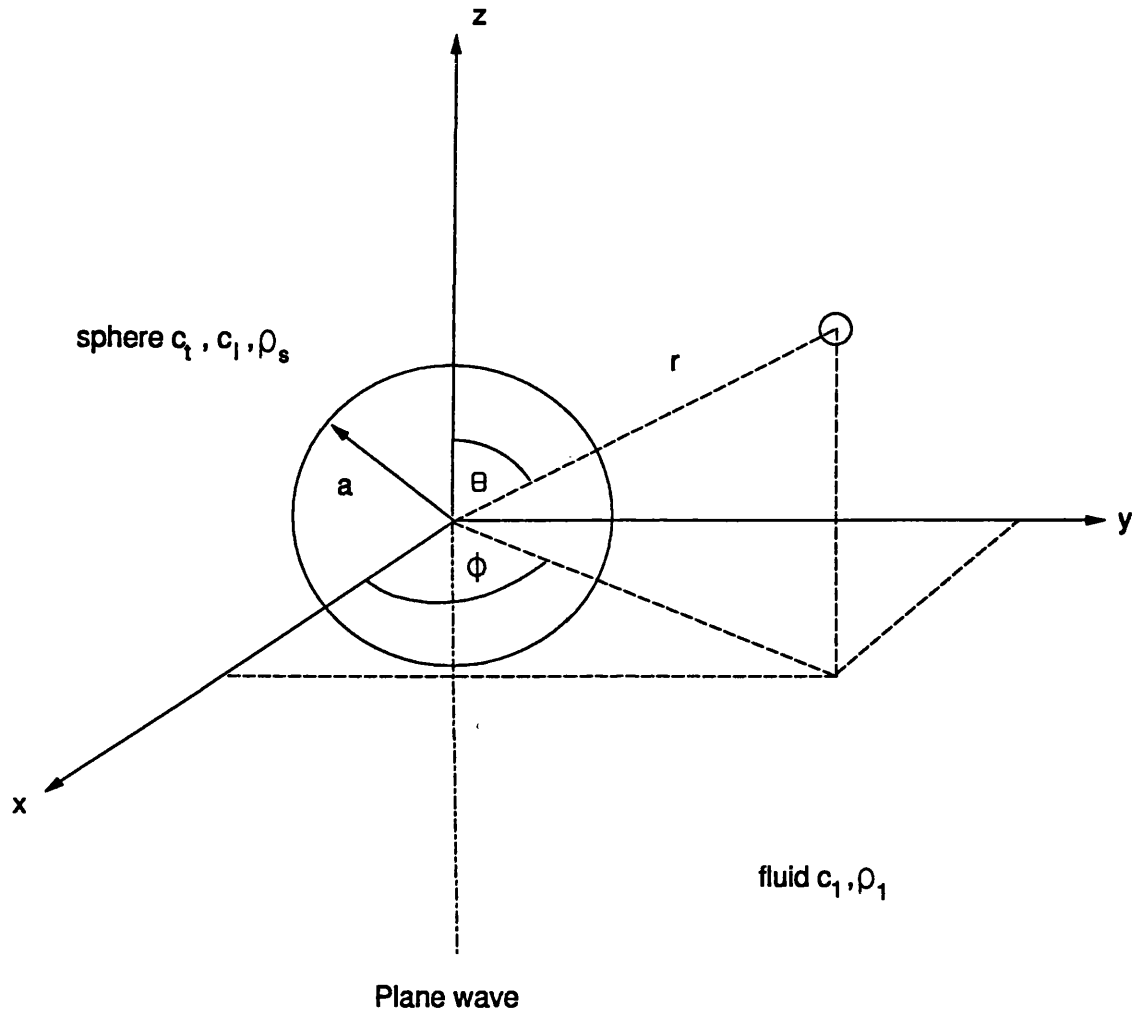

Figure 4.2 Comparison of near field and far field form function for a tungsten carbide sphere.

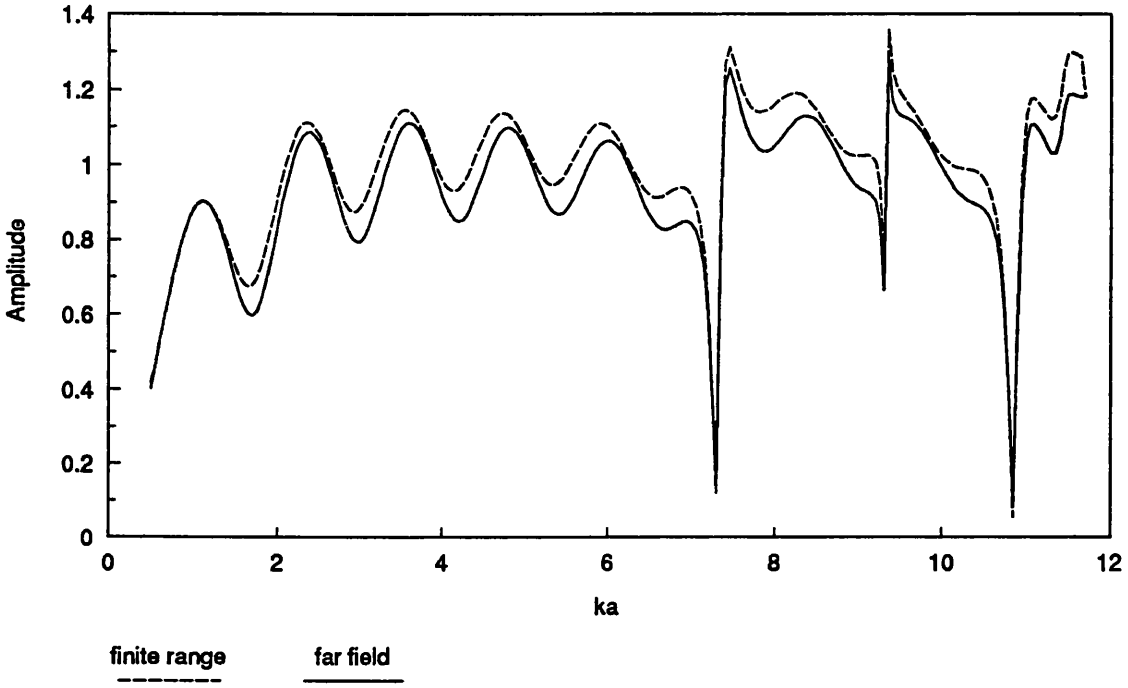

Figure 4.3 Form function for a rigid sphere.

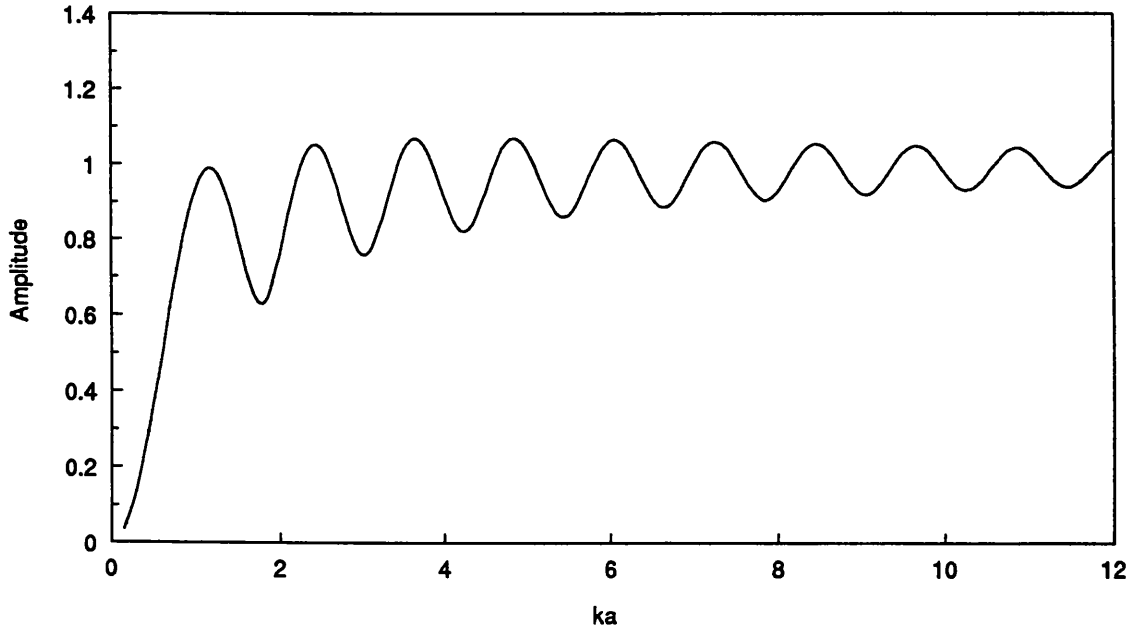

Figure 4.4 Effect of the observation point on the path of the creeping wave.

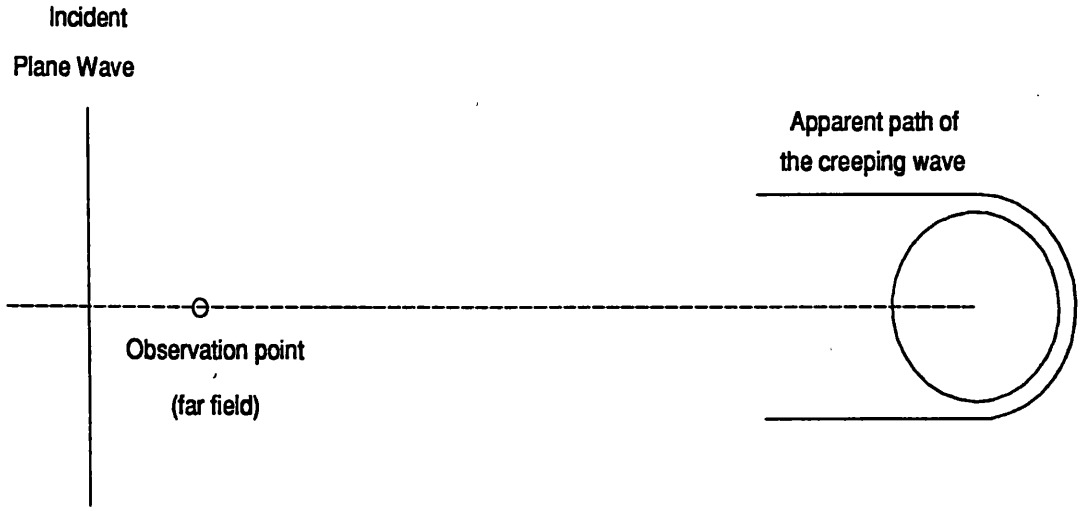

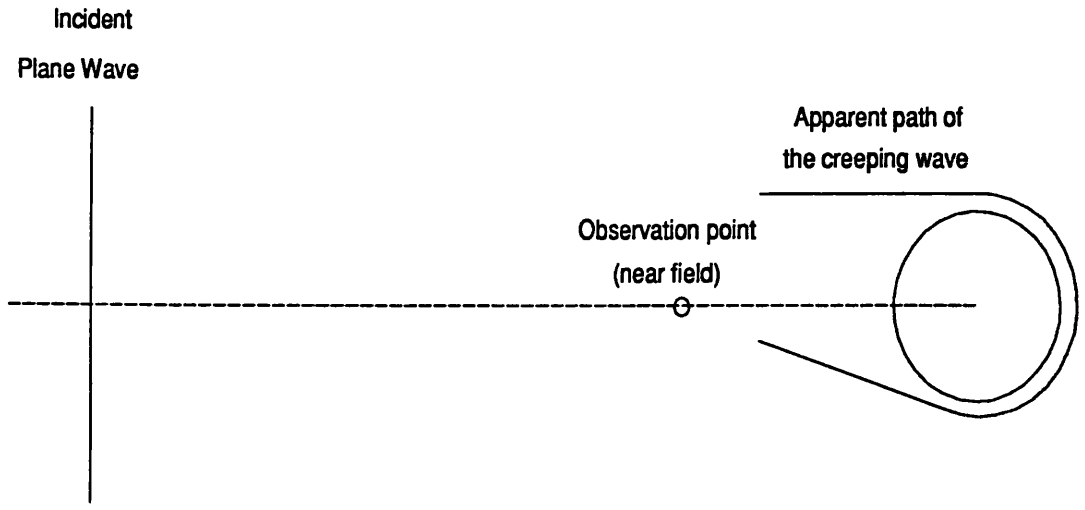

Figure 4.5 Far field form function for a tungsten carbide sphere.

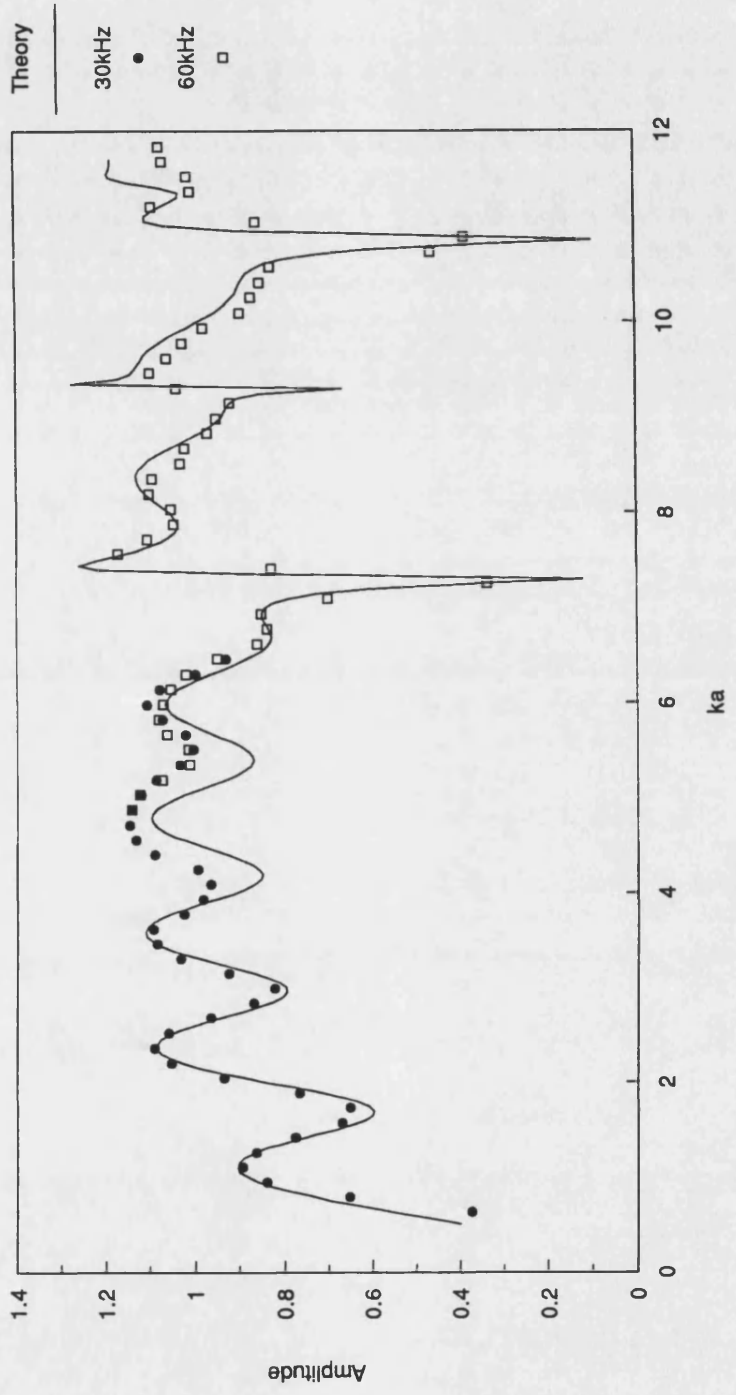

Figure 4.6 Near field form function for a tungsten carbide sphere.

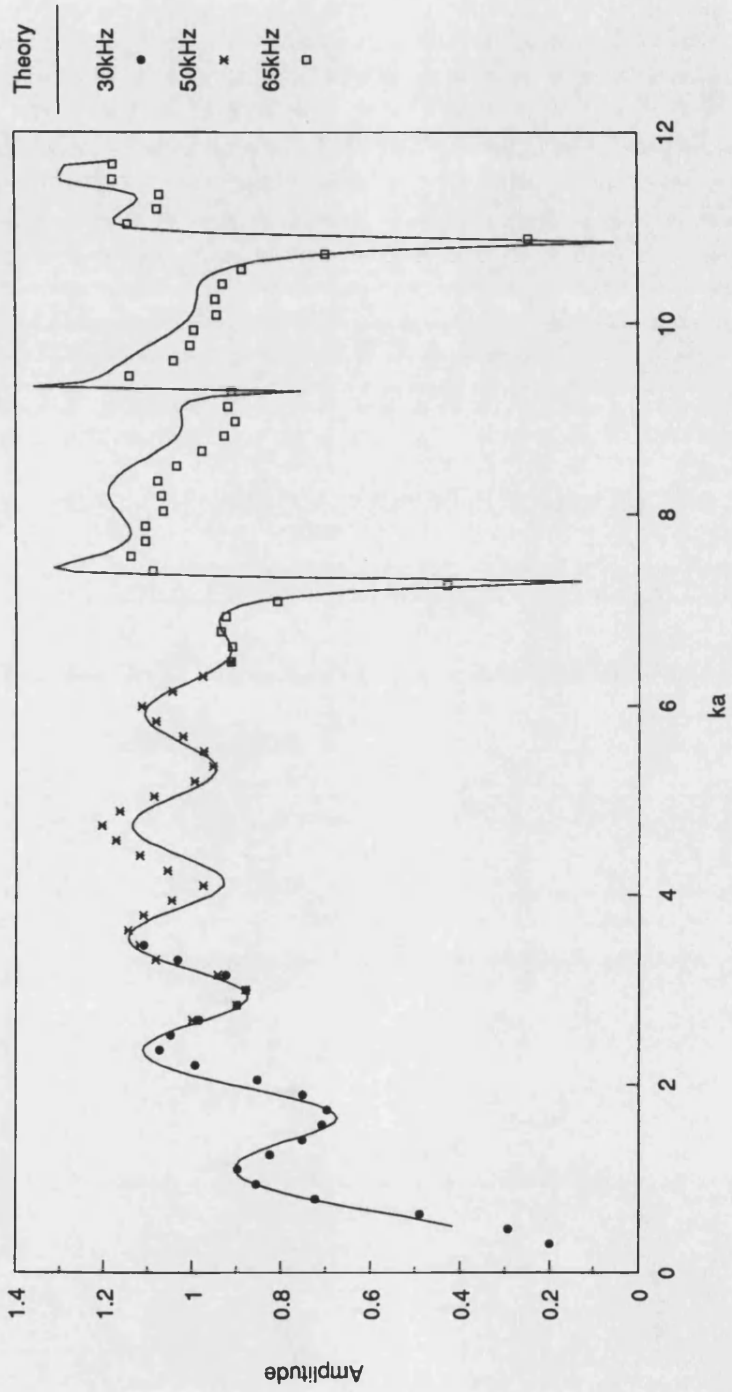

Figure 4.7 Comparison of theoretical and experimental signals scattered from a tungsten carbide sphere, with an incident pulse based on 50kHz.

a) Theoretical signal

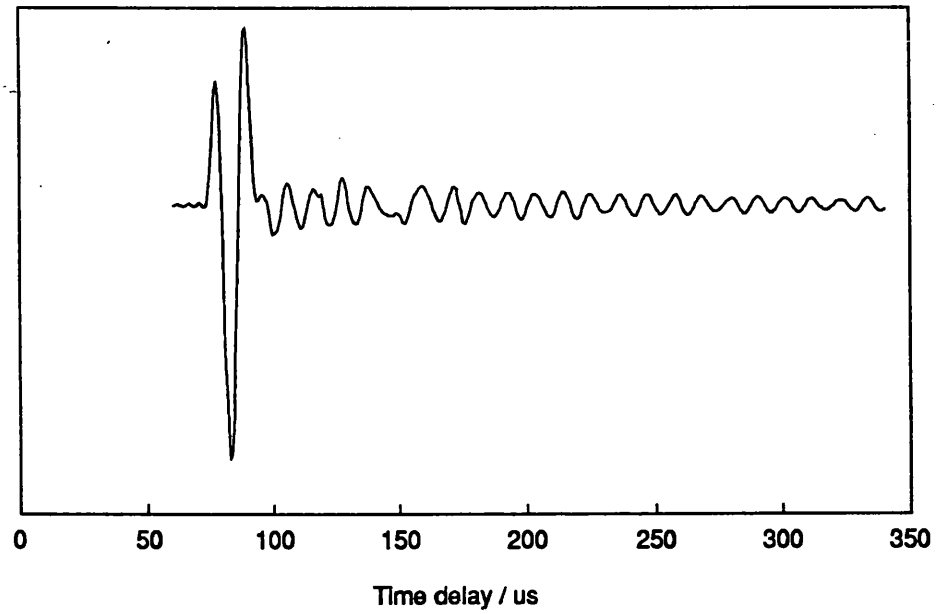

b) Experimental signal

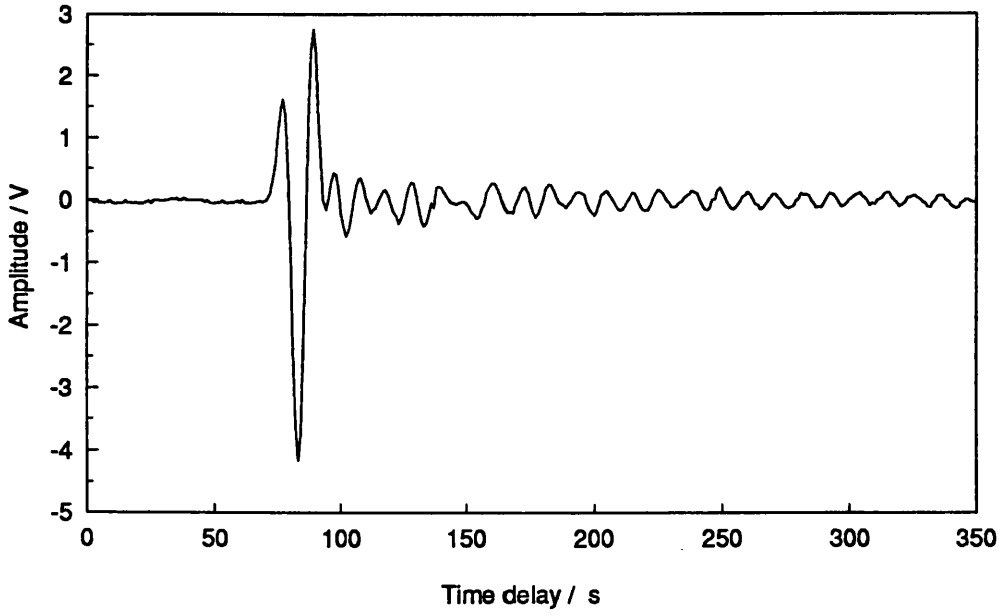

5 Solid Cylinder

5.1 Literature Survey

The scattering of sound by an infinite solid elastic cylinder immersed in a fluid was investigated by Faran (1951). He presented a theoretical development using the Normal Mode Series, and experimental results for angular scattering from metal cylinders (steel, brass, copper and aluminium) which showed excellent agreement with the theory. The cylinders were typically 0.1" in diameter and measurements were made at 1MHz.

Experimental investigations that followed considered scattering from solid cylinders (Barnard & McKinney, 1961) and cylindrical shells (Hampton & McKinney, 1961; Horton, King & Dierks, 1962; Dierks, Goldsberry & Horton, 1963). During this period, investigations into the two objects were related, in that a finding in one field fuelled a new avenue of study in the other. Barnard & McKinney (1961) presented experimental results for scattering from both finite length solid cylinders and air filled shells. The scattered signals they observed had a periodic structure which could be explained as the observation of a circumferential creeping wave.

The observation of a creeping wave led to a considerable amount of theoretical work on their existence (Überall, Doolittle & McNicholas, 1966) and properties, such as velocity and attenuation (Grace & Goodman, 1966).

In addition to the Franz - type creeping wave, which has most of its energy in the fluid and is due to the geometry of the object, there are also other surface waves that can propagate due to the body's elastic nature, namely Rayleigh waves and Whispering Gallery waves. The problem of the circumferential waves attracted much interest with Doolittle, McNicholas, Überall & Ugincuis (1967) presenting theoretical developments for Franz, Stoneley and Rayleigh type waves, while Goodman, Bunney & Marshall (1967) confirmed the theoretical predictions, and isolated an elastic Rayleigh - type wave

Doolittle, Überall & Ugincuis (1968), extended their early work by using the Sommerfeld - Watson Transformation on the Normal Mode Series to identify the poles in the complex frequency plane due to the creeping waves and the elastic Rayleigh and Stoneley waves. In addition they present a useful review of the early work on creeping waves which were first observed with radio waves around the earth.

Neubauer (1969) used Schlieren images to isolate the creeping wave, and two elastic circumferential waves, one of which he identified as the Rayleigh wave. In a memorial paper dedicated to Arnold Sommerfeld, Neubauer et al. (1969) explain the theory of creeping waves and present experimental results for the differential scattering cross section (the square of the modulus of the form function) over a *ka* range 5 - 25 for an aluminium cylinder. They also demonstrated the existence of the surface waves using a Schlieren system.

In a series of papers Frisk and co-workers (Frisk, Dickey & Überall, 1975; Frisk & Überall, 1976; Dickey, Frisk & Überall, 1976) considered the surface wave modes on elastic

cylinders. They theoretically investigate the Rayleigh and Whispering Gallery modes, which have velocities close to the bulk wave speeds in the solid, and Franz and Stoneley modes, which have velocities close to the wave speed in the fluid. Numerical results are presented for the zeros of the various waves and their phase velocities, dispersion and attenuation.

Until this point, most theoretical investigations of the scattering phenomenon had used the Normal Mode Series approach, or used the Sommerfeld - Watson Transform in order to identify the poles of the various wave modes in the complex frequency plane. However, in 1978 Flax, Dragonette & Überall presented their definitive work on the Resonance Scattering Theory (RST). Subsequent studies have either considered the physical meaning of the scattering from the solid cylinder in terms of the RST for example (Brill & Gaunaurd, 1983), or have extended the scattering problem. More complicated problems have included the study of finite cylinders (for example Su, Varadan & Varadan, 1980; Muzychenko & Rybak, 1986, 1988) and the investigation of obliquely incident wavefields, which are discussed in more detail below.

Early experimental investigations, such as those used by Barnard & McKinney (1961) had used a short single frequency tone burst. Dardy, Bucaro, Schuetz & Dragonette (1977) presented a technique which used a broad - band pulse to measure the form function for an aluminium cylinder immersed in water. They were able to cover a *ka* range from 4 to 21 using a 1MHz pulse of three cycles and three samples 0.381cm, 0.699cm and 1.27cm in diameter and demonstrated agreement with the far field form function to within 10%. Dragonette (1979) used a short pulse to experimentally identify a leaky Rayleigh wave on the solid cylinder which had been predicted by Überall, Doolittle & McNicholas (1966). Only two Rayleigh wave traverses of the cylinder were visible due to the high attenuation. However, the phase shift (180°) and the group velocity ($c_g/c = 1.9$) were in close agreement with predicted values. High frequency experimental results ($ka \approx 240$) were obtained by Welton, de Billy, Hayman & Quentin (1980) from solid brass, aluminium and lucite (perspex) cylinders. They confirmed the theoretical predictions of Brill & Überall (1971) who proposed that in the high frequency limit the internally reflected waves would obey the laws of geometrical optics, and were able to derive expressions for the arrival times and amplitudes of the reflected and transmitted waves.

The resonances of the cylinder, caused by surface waves and internal reflections, set up standing wave patterns on and in the cylinder. Flax, Raju, George & Überall (1980) looked at resonating fields within elastic cylinders, using optic-elastic birefringance to visualise the field inside glass cylinders embedded in water. They were able to interpret the resonances in terms of surface waves.

The first paper containing an experiment based on the Resonance Scattering Theory appeared in 1981 (Maze, Taconet & Ripoche, 1981). An experimental system and technique was developed to isolate and identify the resonances of an elastic object. The technique has

been called the "Resonance Isolation and Identification Method" (RIIM) or the "Méthode d'isolement et d'identification des résonances", (MIIR) (Maze, Taconet & Ripoche, 1981; Maze & Ripoche, 1983a,b). By insonifying the target with a long tone burst, Maze et al. were able to identify three regions of the scattered signal, an initial transient vibration, a permanent vibration during which the amplitude of the signal can be considered constant, and a second transient vibration after the end of the forced vibration. It is possible to make two measurements from this signal, the first during the steady state region, to obtain the 'backscattered signal spectrum', and the second during the second transient vibration, which corresponds to the free vibration of the cylinder, to obtain a 'resonance spectrum'. Much of the work carried out by the French acousticians has been brought together in one volume by Gespa (1987). In a more recent work Maze & Ripoche (1983b) made additional photographic observations of the scattering by using a Schlieren visualisation technique. Brill & Gaunaurd (1983) studied the experimental work of Maze et al. (1981) in the light of the RST and interpreted the results. They also explain why some of the predicted resonances were not visible, and how the Schlieren photographs of Maze & Ripoche (1983b) verified the RST predictions for the cylinder.

Tsui, Reid & Gaunaurd (1986) and Gaunaurd & Tsui (1988) present an experimental technique to confirm RST when applied to solid elastic cylinders immersed in water. The technique is similar to the MIIR technique used by Maze et al. (1981, 1985). However, Gaunaurd et al. use the results to obtain several variables, such as the 'skewness' and amplitude of the resonances and the area under each resonance, which do not appear to have been considered by Maze et al..

As described above, the Normal Mode Series solution and latterly the Resonance Scattering Theory, have been used to investigate scattering from a solid cylinder. In these and many other papers, the incident plane wave was considered to be at normal incidence to the cylinder axis. This generates modes of vibration within the cylinder which are related to circumferential waves. However, a plane wave incident at an angle to the cylinder axis should excite modes of vibration having both axial and circumferential dependence, giving rise to helically propagating waves and making the scattering problem more complicated.

The case of an obliquely incident wave on a solid cylinder was first considered by White (1958). He theoretically investigated the case of a plane compressional or shear wave obliquely incident on an elastic cylinder embedded in a different elastic solid at a given frequency. Although White used the Normal Mode Series solution, he presented his results as an angular scattering at a given frequency, rather than the frequency dependent results often seen today. In a later work Flax, Varadan & Varadan (1980) treated the case of an obliquely incident plane compressional wave on an elastic solid cylinder immersed in a fluid. They presented their computational results in terms of the frequency dependent form

function. Although they were able to explain the effects of interference between the specular reflection and a geometric or Franz type circumferential wave taking a helical path, there were several features in the form function which they were unable to explain.

To further the understanding of the processes involved, Nagl, Überall, Delsanto, Alemar & Rosario (1983) undertook a theoretical study of the refraction effects in the generation of surface helical waves on a cylinder. They found that the phase matching of the helical waves as they repeatedly propagate around the cylinder give rise to resonances. Mathematically the resonances manifest themselves in the form of 'poles' of the scattering amplitude situated at the complex eigenfrequencies. Überall and co-workers (1985) studied the eigenfrequencies and the associated eigenvibrations for obliquely insonified cylinders and the resulting helical waves. They also were able to numerically obtain phase and group velocities and the absorption coefficients of the surface waves.

Some of the first experimental results came from Maze, Izbicki & Ripoche (1984, 1985) using the experimental MIIR technique. They found that the directivity pattern of the transducer was causing the incident beam to diverge, so that even at so called normal incidence the cylinder is in fact being insonified obliquely. Consequently shear waves can be generated which can lead to guided waves in the cylinder with a direction of propagation parallel to the axis of the cylinder. These lead to extra resonances being observed which are not predicted by the Resonance Scattering Theory for normal incidence. Maze et al. (1985) extended the theory to account for oblique incidence. However they only considered the propagation of the wave within the cylinder, i.e. the free vibration of the cylinder, and based their work on that of Meeker & Meitzler (1964) and Zemanek (1972).

In a later work Izbicki, Maze & Ripoche (1987) studied the effects of a cylinder of finite length when looking at the guided waves and surface helical waves. Molinero and de Billy (1988) experimentally confirm that in the case of an obliquely incident plane wave, leaky guided waves propagate in elastic cylinders. They also experimentally determined the phase velocity dispersion curves for both longitudinal and flexural modes of propagation within the cylinder, by measuring how the resonance frequencies change with angle of incidence.

5.2 Theory

The scattering of an infinite plane acoustic wave obliquely incident on an infinite solid cylinder, neglecting absorption, is investigated by considering the solution to the wave equation and the associated boundary conditions. The incident and scattered waves in the fluid can be represented essentially as a summation series of Bessel functions, the expression for the scattered wave containing a scattering coefficient B_n which needs to be evaluated. The propagation in the cylinder can be described in terms of vector and scalar potentials. These are used, along with the expressions for the waves in the fluid, to satisfy the boundary

conditions at the surface of the cylinder. Solution of the subsequent set of simultaneous equations result in an expression for the scattering coefficient B_n which is used to calculate the form function (Flax, Varadan & Varadan 1980).

Figure 5.1 illustrates the geometry of the problem. The cylinder lies with its axis co-incident with the z-axis of a cylindrical co-ordinate system (r, ϕ ,z). The incident plane wave is assumed to lie in the xz plane without any loss of generality due to the symmetry involved.

The incident plane wave propagation vector k_1 makes an angle α with the x-axis. The solid cylinder has material properties given by a density ρ_c , compressional wave velocity c_l and shear wave velocity c_t , while the surrounding fluid has a density and wave velocity ρ_1 and c_1 respectively.

In the fluid the incident wave is given by;

$$p_i = p_0 e^{i(\underline{k}_1 \cdot \underline{r} - \omega \cdot t)}$$

$$= p_0 e^{-i\omega t} e^{ik_1(r\cos\alpha\cos\phi + z\sin\alpha)}$$

$$= p_0 e^{-i\omega t} e^{ik_1 z\sin\alpha} \sum_{n=0}^{\infty} \varepsilon_n i^n J_n(k_1 r\cos\alpha)\cos n\phi \quad . \tag{5.1}$$

Similarly the scattered wave can be written as

$$p_{sc} = p_0 e^{-i\omega t} e^{ik_1 z\sin\alpha} \sum_{n=0}^{\infty} \varepsilon_n i^n B_n H_n^1(k_1 r\cos\alpha)\cos n\phi \tag{5.2}$$

where

B_n is the scattering coefficient to be determined from the boundary conditions,

$H_n^1(x)$ is the cylindrical Hankel function,

$J_n(x)$ is the cylindrical Bessel function,

and the Neumann factor $\varepsilon_n = 1$ for $n = 0$ and $\varepsilon_n = 2$ for $n > 0$.

Within the cylinder, the displacement vector $\underline{u}$ can be expressed in terms of a scalar potential ψ , and a vector potential $\underline{A}$, in the following form (Flax, Varadan & Varadan, 1980),

$$\underline{u} = -\nabla\psi + \nabla \wedge \underline{A} \tag{5.3}$$

The displacement equations of motion can be expressed in terms of ψ and $\underline{A}(A_r, A_\phi, A_z)$ as

$$u_r = -\frac{\partial\psi}{\partial r} + \frac{1}{r}\frac{\partial A_z}{\partial\phi} - \frac{\partial A_\phi}{\partial z} \tag{5.4}$$

$$u_\phi = -\frac{1}{r}\frac{\partial\psi}{\partial\phi} + \frac{\partial A_r}{\partial z} - \frac{\partial A_z}{\partial r} \tag{5.5}$$

$$u_z = -\frac{\partial \psi}{\partial z} + \frac{1}{r}\frac{\partial (A_\phi r)}{\partial r} - \frac{1}{r}\frac{\partial A_r}{\partial \phi} \quad . \tag{5.6}$$

These are satisfied if

$$\nabla^2 \psi = \frac{1}{c_t^2}\frac{\partial^2 \psi}{\partial t^2}$$

and (5.7)

$$\nabla^2 \underline{A} = \frac{1}{c_t^2}\frac{\partial^2 \underline{A}}{\partial t^2} \quad .$$

The condition $\nabla \cdot \underline{A} = 0$ is imposed in order to obtain a unique solution. Hence the three vector potential components satisfy,

$$\nabla^2 A_z = \frac{1}{c_t^2}\frac{\partial^2 A_z}{\partial t^2} \tag{5.8}$$

$$\nabla^2 A_\phi - \frac{A_\phi}{r^2} - \frac{2}{r^2}\frac{\partial A_r}{\partial \phi} = \frac{1}{c_t^2}\frac{\partial^2 A_\phi}{\partial t^2} \tag{5.9}$$

$$\nabla^2 A_r - \frac{A_r}{r^2} - \frac{2}{r^2}\frac{\partial A_\phi}{\partial \phi} = \frac{1}{c_t^2}\frac{\partial^2 A_r}{\partial t^2} \quad . \tag{5.10}$$

A separable variables technique is used to solve for A_z and ψ. A solution of a similar form is then assumed in order to solve the coupled equations for A_ϕ and A_r, giving;

$$\psi = e^{ihz} \sum_{n=0}^{\infty} C_n J_n(pr) \cos n\phi \tag{5.11}$$

$$A_z = e^{ihz} \sum_{n=0}^{\infty} E_n J_n(qr) \sin n\phi \tag{5.12}$$

$$A_r = e^{ihz} \sum_{n=0}^{\infty} K_n J_{n+1}(qr) \sin n\phi \tag{5.13}$$

$$A_\phi = -e^{ihz} \sum_{n=0}^{\infty} K_n J_{n+1}(qr) \cos n\phi \tag{5.14}$$

where

$$h = k_1 \sin\alpha$$

$$p^2 = k_t^2 - h^2$$

$$q^2 = k_t^2 - h^2 \quad ,$$

and the time dependence has been suppressed. The general solution of equations 5.7 - 5.10 include Bessel Functions of the second type $Y_n(x)$, however these are not retained as the

solution has to be finite at $r = 0$.

In order to evaluate the scattering coefficient B_n it is necessary to apply the boundary conditions at $r = a$, the radius of the cylinder. At the surface of the cylinder the displacements and normal stresses must be continuous and the tangential stresses must be zero. That is,

$$u_r = u_i + u_{sc}$$

$$\tau_{rr} = p_i + p_{sc}$$

$$\tau_{r\phi} = 0$$

$$\tau_{rz} = 0$$

where $u_{i,sc}$ is the displacement of the incident or scattered wave, and the stress relations are (Love, 1944; Achenbach, 1973)

$$\tau_{rr} = \lambda\Delta + 2\mu\frac{\partial u_r}{\partial r}$$

$$\tau_{r\phi} = \mu\left(\frac{1}{r}\left(\frac{\partial u_r}{\partial \phi} - u_\phi\right) + \frac{\partial u_\phi}{\partial r}\right)$$

$$\tau_{rz} = \mu\left(\frac{\partial u_r}{\partial z} + \frac{\partial u_z}{\partial r}\right)$$

where λ and μ are the Lame constants and the dilation Δ is defined as,

$$\Delta = \frac{\partial u_r}{\partial r} + \frac{1}{r}\left(\frac{\partial u_\phi}{\partial \phi} + u_r\right) + \frac{\partial u_z}{\partial z} \quad .$$

This results in a series of four linear simultaneous equations in B_n, C_n, E_n, K_n . The coefficient B_n can be determined using Cramer's rule and is of the form

$$B_n = -\frac{F_n J_n(x_1) - x_1 J_n'(x_1)}{F_n H_n^1(x_1) - x_1 H_n^{1\prime}(x_1)} \tag{5.15}$$

where

$$F_n = \frac{\rho_1}{\rho_c} x_t^2 \frac{Q_n}{R_n}$$

$$x_1 = k_1 a \cos\alpha$$

$$x_t = k_t a$$

and Q_n and R_n are three by three determinants, the elements of which are given in Appendix 4.

For the case of soft or rigid cylinders this expression for B_n simplifies considerably as one no longer has to account for the elastic nature of the material. For the case of a rigid cylinder, ideally as $\rho_c \to \infty$, but in practice where $\rho_c \gg \rho_1$, the scattering coefficient B_n reduces to

$$B_n^R = -\frac{J_n'(k_1 a)}{H_n^{1\prime}(k_1 a)}, \tag{5.16}$$

whilst for a soft cylinder i.e. where $\rho_c \to 0$, B_n reduces to

$$B_n^S = -\frac{J_n(k_1 a)}{H_n^1(k_1 a)} \quad . \tag{5.17}$$

The form function is defined to give a non-dimensional representation of the scattered pressure. In the most general case,

$$f_r(\phi) = \left(\frac{2r}{a}\right)^{1/2} e^{-ikr} \left| \frac{p_{sc}}{p_0} \right|$$

$$= \left(\frac{2r}{a}\right)^{1/2} e^{-ikr} \sum_{n=0}^{\infty} \varepsilon_n i^n B_n H_n^1(k_1 r \cos\alpha) \cos n\phi \quad . \tag{5.18}$$

It is possible to reduce this to the far field case by introducing the asymptotic form for $H_n^1(k_1 r \cos\alpha)$,

$$H_n^1(k_1 r \cos\alpha) \sim \left(\frac{2\pi}{k_1 r \cos\alpha}\right)^{1/2} e^{ik_1 r \cos\alpha} e^{-i\left(\frac{n\pi}{2}+\frac{\pi}{4}\right)} \quad .$$

Further simplification to the backscattered case involves replacing $\cos n\phi$ in equation 5.18 by $(-1)^n$. Hence equation 5.18 would reduce to,

$$f_\infty(\pi) = \left(\frac{2}{i\pi k_1 a \cos\alpha}\right)^{1/2} \sum_{n=0}^{\infty} \varepsilon_n (-1)^n B_n \tag{5.19}$$

The computer implementation of equations 5.18 and 5.19 is discussed briefly in Appendix 5.

5.3 Computational Results and Discussion

Figure 5.2 illustrates the form function as a function of *ka*, the normalised wavenumber, for a solid aluminium cylinder immersed in water. The incident angles are 0°, 10°, 20° and 30.3°, and the form function has been calculated at 0.05 intervals over a *ka* range of 0.5 - 15.0. The angles of incidence have been chosen to agree with those used by Flax, Varadan & Varadan (1980), 30.3° being the incident angle required for the generation of a Rayleigh wave on a flat aluminium plate. The material properties used are shown in Appendix 3.

The form function for $\alpha = 0°$ is shown in Figure 5.2a. The characteristic ripple on the form function, clearly observable for *ka* less than 5.5, is due to the interference of the specular reflection and a creeping wave which propagates around the cylinder (see Chapter 4). At higher *ka* values sharp features due to the elastic resonances of the cylinder are noticeable. In order to study the resonances of an object in greater detail, the Resonance Scattering Theory can be used to 'decompose' each partial mode (f_n) of the form function into a background term, in this case that due to a rigid cylinder, and a resonance contribution. In the far field backscattered case, when insonified at normal incidence, the resonance contributions are given by

$$r_r = f_\infty(\pi) - f_{rig}(\pi)$$

$$= \frac{2}{(\pi i ka)^{1/2}} \sum_{n=0}^{\infty} \varepsilon_n (-1)^n \left(B_n - \left(-\frac{J_n'(ka)}{H_n^{1'}(ka)} \right) \right)$$

where the nomenclature has been given in section 5.2 and is summarised in Appendix 1.

The first five partial modes and the resonance contributions for a solid aluminium cylinder are illustrated in Figures 5.3 and 5.4 respectively. Here *n* is the order of the partial mode within the Normal Mode Series. In addition, each resonance within a partial mode has been attributed a number '*l*' indicative of the order in which they appear. The positions of the resonances are found from the roots of $R_n = 0$ (for details of R_n see Appendix 4), and the number '*l*' is an indication of which resonance is associated with which of the many solutions of $R_n = 0$. These roots or eigenfrequencies are real for a free body ($\rho_1 \ll \rho_c$) but are complex for a loaded body (e.g. an aluminium cylinder in water). The complex eigenfrequencies of any scatterer locate the resonance poles in the complex frequency plane, and their real parts determine the resonance frequencies seen in the scattering amplitudes (Figure 5.3 and 5.4). The two indices are often bracketed and a resonance is known by its (n,l).

Überall, Dragonette & Flax (1977) proposed that resonances having the same eigenfrequency, *l*, belonged to 'families', and that these families could be identified with

an individual elastic circumferential wave. In terms of circumferential waves, the resonances occur at frequencies for which the circumference of the cylinder is an integer number (n) of circumferential wavelengths. Where n is related to the circumferential nodes, l describes the number of radial nodes. Each family of resonances can be characterised by their shapes, amplitudes and properties. Some of the resonances are noticeably broad (e.g. Figure 5.4, $l = 1$), while others are narrow (e.g. Figure 5.4, $l = 2$). The broad ones are usually associated with compressional modes and wave speeds, while the narrow ones are associated with shear modes and wave speeds. In addition the area under each resonance is proportional to the energy required to excite it, hence it is easier to excite a narrow resonance than a broader one of the same height (Tsui, Reid & Gaunaurd, 1986).

The $(n,1)$ family of resonances have been identified as the leaky Rayleigh circumferential wave (Dragonette, 1979; Überall, Dragonette & Flax, 1977) which becomes the Rayleigh surface wave in the limit as $ka \rightarrow \infty$ (Frisk & Überall, 1976). The Rayleigh Wave travels on the interface between the solid and the fluid with most of its energy in the solid. The Rayleigh Wave is termed 'leaky' as energy flows across the interface into the fluid, resulting in an attenuation in the direction of propagation.

Experimental observation of the Rayleigh Wave was reported by Dragonette (1979). The Rayleigh Wave was identified on an aluminium cylinder at ka values of 10.4 and 13.5, and the attenuation was such that only one or two transits of the wave were observed. The Rayleigh Wave was seen to be 180° out of phase with the specular reflection which was in agreement with observations of the Rayleigh wave on a flat plate (Neubauer, 1973).

For $l > 1$, the resonances are generated by the so-called Whispering Gallery waves, which are internally reflected around the inside of the cylinder, but stay close enough to the surface to be considered surface waves. There are two types of Whispering Gallery waves, a longitudinal and a transverse mode. The transverse modes are those which for high frequency or large cylinders tend towards the lateral wave that propagates with the bulk speed of transverse elastic waves. Similarly the longitudinal Whispering Gallery modes are those which tend to lateral waves propagating with the speed of longitudinal elastic waves (Dickey, Frisk & Überall, 1976). Brill & Überall (1971) presented diagrams for the behaviour of the Whispering Gallery waves at high ka and in fact labelled them according to the number of longitudinal and shear traverses made across the cylinder.

Although the (n,l) notation is still widely used (Gaunaurd & Tsui, 1988) it can be misleading when trying to associate a given l with a particular type of resonance as proposed by Überall, Dragonette & Flax (1977). In general, for low ka, it is possible to associate a particular l with a particular type of resonance. The exceptions are often to be found in the $n = 0$ term. For example in Figure 5.4 it would seem more appropriate to include the resonance marked $l = 1$ in the $n = 0$ partial mode as part of the series which continues with the $n = 1$, $l = 4$ resonance. Due to the different phase velocities ($c_p/c = ka/n$) of the

transverse and longitudinal Whispering Gallery waves it is also possible for the two different types of resonance to change order between two successive partial modes. Breitenbach, Überall & Yoo (1983) demonstrate that for higher frequencies it is not possible to associate a given l with a type of resonance. They illustrate the cross over of the longitudinal and transverse Whispering Gallery resonance families quite clearly with reference to a very thick cylindrical shell ($b/a = 0.1$) whose response closely resembles that of a solid cylinder. They considered the ka range 0 - 200 and the partial modes 0 - 80.

In addition to the resonances mentioned above there are two other circumferential waves. The Franz creeping waves are due solely to the geometry of the object and are the analogs of the Stoneley waves on the flat plate. The Stoneley wave of the flat plate is a pure surface wave, propagating parallel to the boundary without attenuation and with a speed less than that of the bulk wave in the fluid. For a cylinder however, the unique Stoneley wave of the plate is split into an infinite superposition of creeping wave modes ($l_s = 0, 1, 2...$), each mode being attenuated due to energy being radiated off tangentially at all points into the fluid. As the attenuation increases with l_s only the first few modes will be of practical importance. The waves are exponentially damped in both directions away from the interface with most of the energy residing in the liquid for $\rho_1/\rho_c \ll 1$.

For oblique incidence the surface waves no longer have a purely circumferential behaviour, the creeping wave for example, takes a helical path around the cylinder. It should be noticed that as the incident angle increases from 10° to 30° in Figure 5.2 the period of the ripple increases. This is due to the fact that the creeping wave velocity is dispersive and increases with both frequency and incident angle (Nagl et al., 1983). So although the path length around the cylinder increases, the increase in velocity means the time between the specular reflection and the creeping wave seen at an observation point decreases, hence giving rise to an increase in the period of the ripple on the form function.

As well as the 'Franz' type creeping wave, there is also a second type of surface wave, an internally propagating helical circumferential wave whose speed is close to c_l . The Franz type creeping waves are generated only at tangential incidence of the incoming wave, whereas the internal helical wave is created for both tangential and non-tangential incidence depending on the magnitude of the phase velocity relative to the speed of sound in the surrounding fluid (Nagl et al., 1983). If the phase velocity is greater than c_1 then internal surface waves are created for non-tangential incidence, however if the phase velocity is less than c_1 then internal helical waves can be generated only for tangential incidence. Nagl et al. (1983) also found that in the cases of generation at tangential incidence for both the Franz and the internal waves refraction effects are predicted and each of the waves (or modes) can be characterised by its own dispersion curve.

The sharp minima of Figure 5.2a, associated with elastic resonances are not as clearly

visible when the incoming wave is obliquely incident. This is because the symmetry necessary to create these circumferential resonances has been broken. However just as in the normal incidence case, there are two waves propagating, one 'clockwise' around the cylinder, the other 'anti-clockwise', only in this case they are helical rather than circumferential. The resonances still seen for higher *ka* in Figures 5.2b and 5.2c are caused by the phase matching of waves as they repeatedly propagate around the cylinder.

Molinero & de Billy (1988) and Maze et al. (1985) have found that for oblique incidence there exists a leaky guided wave which propagates in a direction parallel to the axis of the cylinder. This guided wave is thought to be the reason why the form function in Figure 5.2d is small for $ka > 8$ (Flax et al., 1980).

5.4 Experimental Results: Normal Incidence

Figures 5.5 - 5.10 illustrate the comparison of the experimentally measured form function with the theoretical predictions for a solid aluminium cylinder. The theoretical curves were computed from the plane wave theory described in section 5.2 and have been calculated at *ka* intervals of 0.05. The experimental results were obtained for an aluminium cylinder of radius 0.0135m, and length 1.18m, at an observation range of 0.30m, using two pulses based on raised cosine bell frequencies of 30kHz and 100kHz, normally incident and observed at intervals over the range $\phi = 180°$ (backscatter) to $\phi = 0°$ (forward scatter). Due to the sample length, the frequency resolution of the data is 1.95kHz.

The results have been presented at 30° intervals between 180° and 0°, with the exception of a measurement at 30°. In general the results were repeatable to within 3%, however for a small range of angles either side of 30° it was extremely difficult to obtain consistent results. This occurred most noticeably at a scattering angle of 30°, and had virtually disappeared 10° either side of this point. This effect was observed both sides of the acoustic axis, at different ranges, and with the cylinder located in different parts of the tank, ruling out the possibility that it was due to the arrival of an extra signal coincident with the scattered signal.

For most observation angles the scattered signal was very similar between subsequent sets of measurements, however at 30°, significant differences could be seen throughout the complete time waveform between subsequent readings. A long series of measurements revealed that this was not due to pulse instability, i.e. the outgoing pulse varying with time. Initially it was thought that perhaps the subtraction of the background signal was incomplete, leaving some extra signal that could not be time resolved from the scattered signal. In the preliminary stages of this investigation the outgoing signal was recorded, the cylinder immersed in the tank and all the scattered signals were then recorded. The cylinder was then removed and all the backgrounds recorded. This procedure could lead to errors in the positioning of the hydrophone and hence incomplete subtraction of the background from

the scattered signal. This would be especially important between 0° and 30° where the outgoing pulse could not be time resolved from the scattered pulse. However, this technique was changed so that the signal and background were recorded for one angle before going on to do the next. This ensured that the hydrophone was in exactly the same position, and eliminated the possibility of the differences in successive scattered signals being due to differences in the subtraction. Even with this alteration there were still significant differences between two consecutive measurements.

A theoretical investigation was carried out to see if the form function was particularly sensitive to observation angle ϕ, or incident angle α, around $\phi = 30°$. However it proved to be no more sensitive to angle than many other regions. At present it is not possible to explain why consistent results cannot be obtained around an observation angle of 30°. However, it would appear that the results are extremely sensitive to the positioning of the cylinder (on-axis rather than orientation or alignment), as many of the other possible causes, discussed above, have been ruled out.

The comparisons of the experimental data to the theoretical predictions illustrated in Figures 5.5 to 5.10 show significant differences both in the overall amplitudes and in the presence/absence of certain resonance type features. In the backscattered case (Figure 5.5) the shadowing effect of the hydrophone and its support becomes significant and this results in a lowering of the experimental values which becomes more pronounced at higher frequencies. This would also contribute to the differences seen between theory and experiment around a *ka* value of 3.5 where the 50 - 60kHz resonance of the hydrophone support tube is visible (see section 2.5 for more detail). However the 'shadowing effects' of the hydrophone are insufficient on their own to account for the discrepancy between theory and experiment and would have little effect on the results taken at observation angles other than backscatter.

All results in Figures 5.5 - 5.10, show a narrow resonance feature at a *ka* value of 8.1, which is not present in the theoretical predictions. The presence of this additional feature was confirmed using measurements from a second aluminium cylinder of radius 0.01905m. After ruling out possible processing artifacts, the observation of this feature at normal incidence was attributed to the fact that the incident wavefield is not a single plane wave but contains additional components that strike the cylinder at oblique incidence. This effect was not apparent in the measurements made on the sphere because the curvature of the sphere was far greater than the curvature of the wavefield and so the scattering process was dominated by the geometry of the sphere. However in the case of cylindrical objects, while this applies in one plane, it will not be true along the length of the cylinder where the curvature of the wavefield dominates over the curvature of the object. This means that the observed form function will include the response of the cylinder for a range of incident angles, not just normal incidence. It may be possible in this case to make an approximate correction to

account for the additional spreading term introduced by the curvature of the wavefield, however in more complex cases, for example where the wavefield is obliquely incident, this would not be adequate.

The presence of this resonance for small angles of oblique incidence is illustrated in Figures 5.11a and 5.11b which show the theoretical form function at observation angles (ϕ) of 180° and 90° respectively for two different angles of incidence, namely 0° (normal incidence) and 1°. The effect of this additional feature is most noticeable in the experimental results at 90° (Figure 5.8), whereas in the backscatter direction (Figure 5.5) only one or two data points are affected. The resonance feature observed experimentally at a *ka* value of approximately 8.1 corresponds to a frequency of 143kHz, which agrees well with the theoretically predicted value of 141kHz (Figure 5.11b), allowing for the uncertainty in the wave speeds in the cylinder.

There are other features visible in the theoretical plots (Figure 5.11) which are not seen experimentally. This is partially due to the frequency resolution of the experimental results not being adequate for such narrow band features, and in addition, the experimental measurements integrate the form function over a range of incident angles. A similar effect has been observed by Maze, Izbicki & Ripoche who found it necessary to account for the oblique components of the incident wavefield when using a short tone burst at normal incidence on a solid cylinder (Maze, Izbicki & Ripoche, 1985) and a cylindrical shell (Maze, Izbicki & Ripoche, 1986).

5.4.1 Plane Wave Spectrum

The discrepancies between experimental results and theoretical predictions described in the previous section were attributed to the fact that the experimental acoustic source, a parametric array, does not generate a single infinite plane wave, but is more realistically considered to generate a spatial spectrum of plane waves. In order to calculate the influence of a non-planar incident acoustic field on measurements of the form function one needs to consider the scattering of each component of the plane wave spectrum. The resultant form function can then be obtained by integrating over all plane wave components.

5.4.1.1 Theory

In this application we have chosen to represent the parametric source as a line array of sources. The line array model (Berktay & Shooter, 1973; Appendix 2) assumes that pseudo sources, each of strength Q_0 per unit length, are evenly distributed along a length 'l_T' of the x-axis (Figure 5.12). Each source will then have a phase *ks* determined by its

distance (s) from the transducer and will radiate spherically. At a point $\underline{R}$ (Figure 5.12) the field (ψ) is given by,

$$\psi = Q_0 \int_0^l e^{iks} \frac{e^{i\underline{k}\cdot\underline{r}}}{r} ds \tag{5.20}$$

which can be evaluated exactly at a point x_0 on the x-axis to give

$$\psi = Q_0 \ln\left(\frac{x_0}{x_0 - l_T}\right) e^{ikx_0}. \tag{5.21}$$

However we can express the spherical source in terms of a plane wave spectrum (Brekhovskikh, 1980) as,

$$\frac{e^{i\underline{k}\cdot\underline{r}}}{r} = \frac{i}{2\pi} \int_{-\infty}^{\infty}\int_{-\infty}^{\infty} e^{i\underline{k}\cdot\underline{r}} \frac{dk_y dk_z}{k_x}$$

and hence, using $\underline{r} = \underline{R} - \underline{s}$, equation (5.20) can be written as

$$\psi = Q_0 \frac{i}{2\pi} \int_{-\infty}^{\infty}\int_{-\infty}^{\infty}\int_0^{l_T} e^{iks} e^{-i\underline{k}\cdot\underline{s}} e^{i\underline{k}\cdot\underline{R}} ds \frac{dk_y dk_z}{k_x} .$$

As the source point $\underline{s}$ is on the x-axis $\underline{k}\cdot\underline{s} = k_x s$. We can also make the parabolic approximation and write,

$$k_x \approx k - \frac{k_y^2 + k_z^2}{2k} \quad \text{and} \quad \frac{1}{k_x} \approx \frac{1}{k}.$$

Hence substitution gives,

$$\psi = Q_0 \frac{i}{2\pi k} \int_{-\infty}^{\infty}\int_{-\infty}^{\infty}\int_0^{l_T} e^{i\left(k_y^2 + k_z^2\right)s/2k} e^{i\underline{k}\cdot\underline{R}} ds\, dk_y dk_z \tag{5.22}$$

For a point on the x-axis, $y = z = 0$ and so, at a reference point x_0,

$$\underline{k}\cdot\underline{R} = k_x x_0.$$

Thus the field at $R(x_0, 0, 0,)$ can be written

$$\psi = Q_0 \frac{i}{2\pi k} \int_{-\infty}^{\infty}\int_{-\infty}^{\infty}\int_0^{l_T} e^{i\left(k_y^2 + k_z^2\right)s/2k} e^{ik_x x_0} ds\, dk_y dk_z$$

i.e.

$$\psi = Q_0 \frac{i}{2\pi k} e^{ikx_0} \int_{-\infty}^{\infty}\int_{-\infty}^{\infty}\int_0^{l_T} e^{-i\left(k_y^2 + k_z^2\right)(x_0 - s)/2k} ds\, dk_y dk_z \quad . \tag{5.23}$$

Equation (5.23) is an expression for the incident field at the reference point x_0 where the cylinder will be inserted. In order to obtain the scattered field ψ_s, at an observation point (r',ϕ) in the xy plane (Figure 5.12), it is necessary to multiply each plane wave component by the appropriate scattering function and evaluate the integral over all plane wave components. Here the co-ordinates (r',ϕ) are measured relative to the centre of the cylinder, and the scattering function is related to the more usual form function (f) by

$$f(r',\phi,k_z,k_y)\left(\frac{a}{2r'}\right)^{1/2}e^{ikr'}$$

where f has been given explicitly earlier (Equation 5.18).

The principle contribution to the integral will come from the region where the exponential term in equation (5.23) is slowly varying, that is, from the region where k_z and k_y are small. For large k this will correspond to plane wave components making small angles to the x-axis. Observation of the predicted form function for small angles indicates that the variation with k_y is less rapid than that with k_z. As a first approximation it will, therefore, be assumed that the scattering function is independent of k_y and can be treated as a function of (r',ϕ,k_z). This enables the k_y integral to be evaluated analytically using

$$\int_{-\infty}^{\infty} e^{-ik_y^2(x_0-s)/2k}\,dk_y \;=\; \left(\frac{2\pi k}{x_0-s}\right)^{1/2}e^{i\pi/4}.$$

So the scattered field can be written

$$\psi_s = Q_0\frac{i}{(2\pi k)^{1/2}}\left(\frac{a}{2r'}\right)^{1/2}e^{ikx_0}e^{i\pi/4}e^{ikr'}\int_{-\infty}^{\infty}\int_{0}^{l_T} f(r',\phi,k_z)\frac{e^{-ik_z^2(x_0-s)/2k}}{(x_0-s)^{1/2}}\,ds\,dk_z.$$

The modified form function (f_{pws}) will be given by

$$f_{pws} = \frac{\psi_s}{\psi}\left(\frac{2r'}{a}\right)^{1/2}e^{-ikr'}$$

where ψ is given by equation (5.21). So,

$$f_{pws} = \frac{i}{(2\pi k)^{1/2}}\frac{1}{\ln(x_0/(x_0-l_T))}e^{i\pi/4}\int_{-\infty}^{\infty}\int_{0}^{l_T} f(r',\phi,k_z)\frac{e^{-ik_z^2(x_0-s)/2k}}{(x_0-s)^{1/2}}\,ds\,dk_z \qquad (5.24)$$

If k_z is written as $k\sin\alpha$, where α is the incident angle to the cylinder measured from the x-axis, equation (5.24) can be written

$$f_{pws} = \frac{i}{(2\pi k)^{1/2}} \frac{1}{\ln(x_0/(x_0 - l_T))} e^{i\pi/4} \int_{-\pi/2}^{\pi/2} \int_{0}^{l_T} f(r', \phi, \alpha) \cos\alpha \frac{e^{-ik^2 \sin^2\alpha(x_0 - s)/2k}}{(x_0 - s)^{1/2}} ds\, d\alpha. \qquad (5.25)$$

Equation (5.25) represents the real part of the α contour. Contributions from the imaginary part of the contour, which correspond to evanescent waves, can be neglected as $k(x_0 - l_T)$ is large. Equation (5.25) has been evaluated numerically using computational techniques. A change of variables permits the *ds* integral to be expressed as a Fresnel integral which can be calculated using Nag routines. Similarly the dk_z integral has been evaluated with the aid of an adaptive Nag integration routine.

5.4.1.2 Results and Discussion

Figures 5.13 - 5.16 illustrate experimental results and theoretical predictions for the form function for a solid aluminium cylinder, insonified by a normally incident wavefield. The experimental data were presented earlier in Figures 5.5, 5.8, 5.9 and 5.10. The theoretical predictions, calculated at the appropriate (r', ϕ), used the material parameters shown in Appendix 3. Two theoretical curves are shown; the solid line is the more usual form function (f), and the broken line represents the theory modified to allow for the plane wave spectrum of the source (f_{pws}).

For all the experimental results shown in Figures 5.13 - 5.16, the modified theory (f_{pws}) shows far better agreement with the data than the usual form function. It is important to note that the new theory not only predicts the amplitude levels, it also shows the sharp features seen in the experimental data, thought to be due to resonances generated by helical waves. At lower values of *ka* (i.e. less than 10) there is in general excellent agreement, to within 5%, between the data and the modified theory, and over much of this range the agreement is significantly better. The backscattered case (Figure 5.13) shows greater discrepancies due to the effects of the hydrophone and its support tube positioned between the source and the cylinder.

Above *ka* values of 10 there are greater deviations between the data and the modified theory. One possible cause of these differences is experimental error in the data. Although lower frequency pulses are very repeatable, the 100kHz data revealed differences of up to 3% between subsequent data sets. This cause however would only partially account for the differences seen between experimental data and theoretical predictions.

A second, and probably more significant, factor may be the validity of the assumptions in the theory at higher frequencies (*ka*). The line array model of the parametric source neglects the cross sectional area of the source distribution and makes the plane wave spectrum broader than it really is (see experimental beam profiles, Figures 2.12, 2.13 and 2.14). This is more significant at higher frequencies, and will have detrimental effects on the accuracy of the theoretical predictions. It could be overcome by using a more accurate representation

for the parametric array which accounts for the cross sectional area of the transducer (Appendix 2). However at low *ka* use of the line array model is clearly justified.

Earlier it was suggested that we could largely account for the effects of the non planar wavefield by correcting the data using a geometrical spreading factor introduced by the 'curvature' of the wavefield in the xz plane. In this example this cylindrical spreading factor is 1.18, that is $((x'+r')/x')^{1/2}$ where $x'=x_0-l_T/2$ i.e. the distance from the centre of the array to the cylinder. To see how well this geometrical factor would account for the differences between the plane wave theory and the modified theory, the ratio of the two theories has been plotted in Figure 5.17 for the observation angles shown in Figures 5.13 - 5.16. The mean value for all the plots in Figure 5.17 is 1.18, indicating that the major differences in amplitude between the modified theory (and hence the experimental data) and the form function prediction could be accounted for by a geometrical spreading factor. Hence to a first order approximation, the influence of the plane wave spectrum can be allowed for by multiplying the experimental data by the appropriate geometrical spreading factor. However, in all the cases shown in Figure 5.17 there are significant departures from the mean of 1.18, due to extra resonances and other phenomena introduced by components of the wavefield making oblique angles with the cylinder. Many of the 'sharp' features can be attributed to resonance behaviour generated by helically propagating waves. However there are other, more smoothly varying features (e.g. Fig 5.17b, $8 < ka < 12$), which are not so easily explained and which require further investigation.

5.5 Experimental Results: Oblique incidence

The experimental technique has also been used to measure the scattering from solid cylinders when insonified by an obliquely incident wavefield. Experimental results have been obtained for a solid aluminium cylinder, 0.0135m in diameter for a range of incident angles (α). The results for incident angles of 10°, 30° and 50° are shown in Figures 5.18, 5.19 and 5.20 respectively, the frequency on which the acoustic pulses are based are shown individually on each diagram.

The accuracy with which the cylinder can be located is of more consequence in the case of an obliquely incident wavefield. It is believed that the cylinder can be positioned to within 1° of the required angle. However Figures 5.11, which shows the form function for 0° and 1°, and 5.21, which illustrates the form function for 28°, 30° and 32°, indicate how significant this small difference could be. The effects of this have been seen in the deterioration of the repeatability of the results, which has gone from 3% in the normally incident case to approximately 10% when the cylinder is insonified obliquely.

The experimental results have been compared to the form function for a single plane wave and, as in the case of a normally incident wavefield, there are significant differences between the data and the theoretical predictions. The most significant cause of these

discrepancies is again thought to be due to the non planar nature of the wavefield. One should be able to account for this by integrating over all components of the plane wave spectrum in a similar way to the case of a wavefield normally incident on a solid cylinder (section 5.4.1.1).

The development of the expressions for the plane wave spectrum proceeds along similar lines to the case of a normally incident wavefield. The geometry of the situation is illustrated in Figure 5.22. Ideally one would re-work the expressions for the plane wave spectrum in terms of the cylinder coordinate system. However it was decided to simply weight the calculation of the form function by the nominal angle of incidence.

The resultant theoretical predictions of the form function modified by the plane wave spectrum are shown in Figures 5.23 and 5.24 for incident angles (α) of 10° and 30° respectively. The modified theoretical prediction for $\alpha = 10°$ (Figure 5.23) shows a better agreement with the experimental data than the single plane wave form function result. It appears to predict certain of the resonance features such as that seen at a *ka* value of approximately 6, and in general the overall amplitude of the prediction is much better. For $\alpha = 30°$ (Figure 5.24) the theoretical prediction due to the plane wave spectrum is significantly different to the single plane wave form function, but is no better a match to the experimental data. The comparison is even worse at 50° and is not shown here. It is appreciated that the error in the experimental measurements is more significant for oblique angles of incidence, however it is felt that the discrepancies between theory and experiment are too great to be explained by positional errors alone. There are several possible causes of the discrepancies observed between the experimental results and the theoretical predictions, all of which could be explored to further advantage.

There are several assumptions made during the development of the theoretical model for a normally incident wavefield which may not be valid for oblique incidence. Probably the most significant cause for concern is the assumption that the variation of the plane wave spectrum is negligible in one direction, thus reducing a 2 dimensional integral in k_x and k_y to a 1 dimensional integral in k_x. This assumption was clearly seen to be reasonable for a normally incident wavefield, and the results presented here (Figure 5.23) would indicate that the assumption is acceptable for small angles of incidence, but, in general, the assumption breaks down for oblique incidence. Evaluation of the two dimensional integral will be required to ascertain whether this is the principal cause of the deviation between the theoretical prediction and the experimental results. However evaluation of the full integral is not a trivial exercise.

Another probable cause of discrepancy between the theoretical prediction (f_{pws}) and the experimental results in Figures 5.23 and 5.24 is the range over which the α integral is evaluated (Equation 5.25). For normal incidence the integral is evaluated from $-\pi/2$ to $\pi/2$, however for oblique incidence we have chosen to weight the calculation of the form function

by the nominal angle of incidence. Hence the limits of evaluation for the integral should also be adjusted accordingly. For example, for a wavefield nominally incident at an angle γ the integration limits should run from $-(\pi/2-\gamma)$ to $(\pi/2-\gamma)$. However, initial results obtained using these limits did not look encouraging, containing a high frequency ripple on an otherwise promising background. It was felt that the components of the integral from $-(\pi/2-\gamma)$ to $-\pi/2$ were physically unrealistic in this situation. The results shown in Figures 5.23 and 5.24 were obtained with the limits $-\pi/2$ to $(\pi/2-\gamma)$.

A third possible cause of discrepancy at higher frequencies is the use of the line array to model the parametric array. For a normally incident wave discrepancies between experiment and theory, at *ka* values greater than about 10, were attributed to the breakdown of the line array model. There is no reason to suppose that this is not the case for an obliquely incident wavefield.

Finally, it cannot be ruled out that there are implementation errors in the code. However, running the code for normal incidence gave identical predictions to those seen in Figure 5.13, and the module which calculates the form function was used both in providing the plots in Figure 5.2 which agree well with those of Flax et al. (1980), and in the calculation of the modified form function for the normally incident wavefield.

In addition to possible causes of error in the theoretical prediction there are also experimental factors that need to be considered. It has already been mentioned that the results for an obliquely incident wavefield are only repeatable to within about 10%, clearly this will be significant. In addition, at higher incident angles (e.g. 50°) it is possible that the influence of the ends of the cylinder is being 'seen'. If this is the case, the way in which the cylinder is terminated will obviously have a significant effect on the way in which sound is reflected and diffracted from its ends.

All of the above possible causes of the discrepancies between the experimental results and the theoretical predictions require further investigation before any firm conclusions can be drawn as to the exact nature of the differences.

5.6 Summary

Experimental measurements of the field scattered from solid cylinders using a parametric array as an acoustic source have shown that the theoretical form function assuming a single plane wave needs to be modified to account for the plane wave spectrum of the parametric array. Comparison of this modified theory with experimental results for a normally incident wavefield shows excellent agreement for *ka* values less than 10. At higher frequencies there are some discrepancies as the line array model for the parametric array is not as good an approximation as at lower frequencies. It should be possible to improve this agreement by using a more accurate model for the parametric source. It has also been shown that the amplitude reduction, the major difference between the single plane wave theory and the modified theory, can be approximated by a geometrical spreading factor. However, this obviously does not take into account any additional resonances introduced by the obliquely incident components of the wavefield.

For an obliquely incident wave the modified theory appears to be reasonably accurate for small angles of incidence (say up to 10°) but breaks down thereafter. This is probably due to the inapplicability of approximations made during the development of the theoretical model, and further work is required to clarify this.

Figure 5.1 Scattering of an obliquely incident plane wave by a solid cylinder.

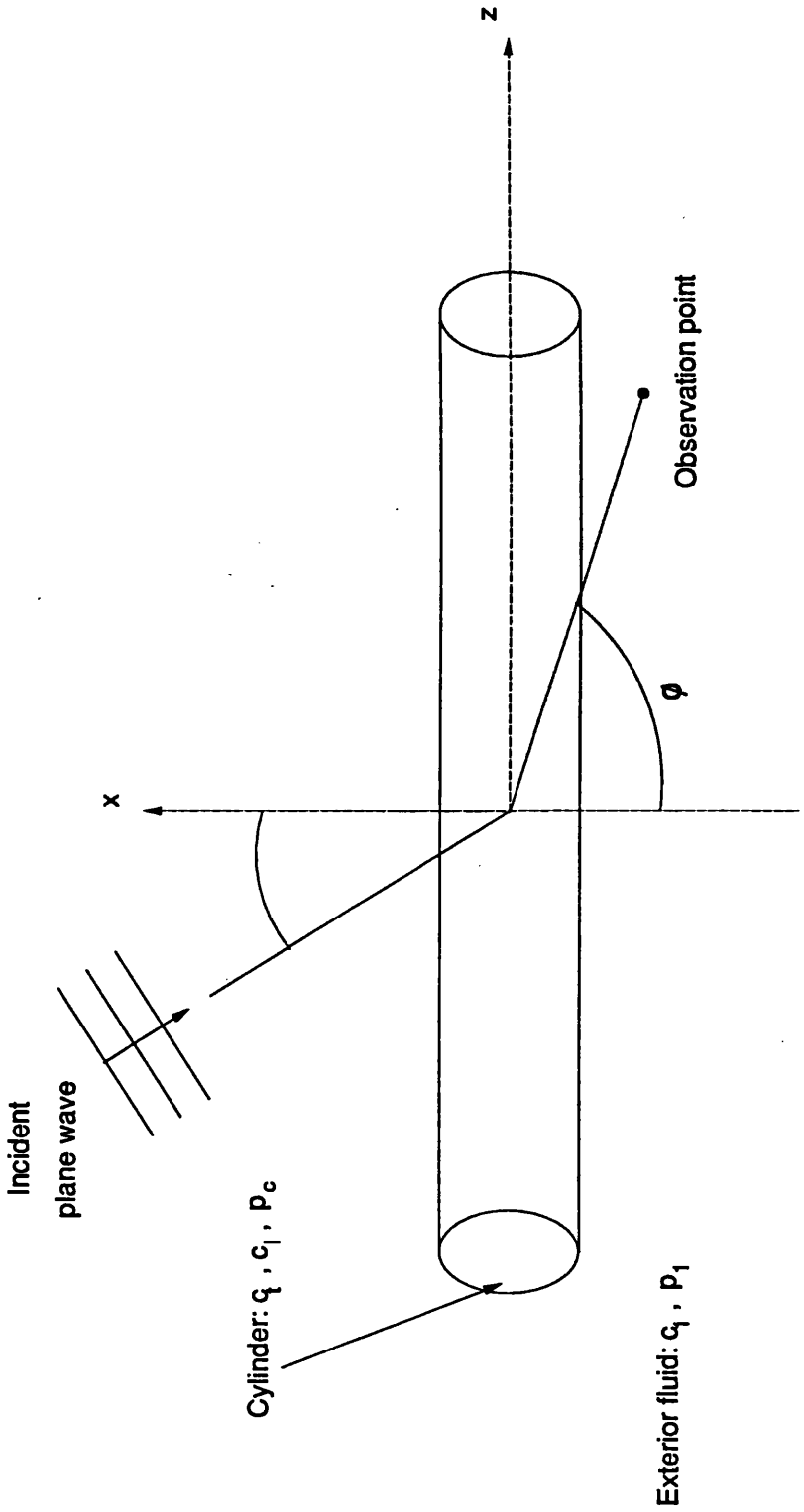

Figure 5.2 Form function for a solid aluminium cylinder for varying angles of incidence.

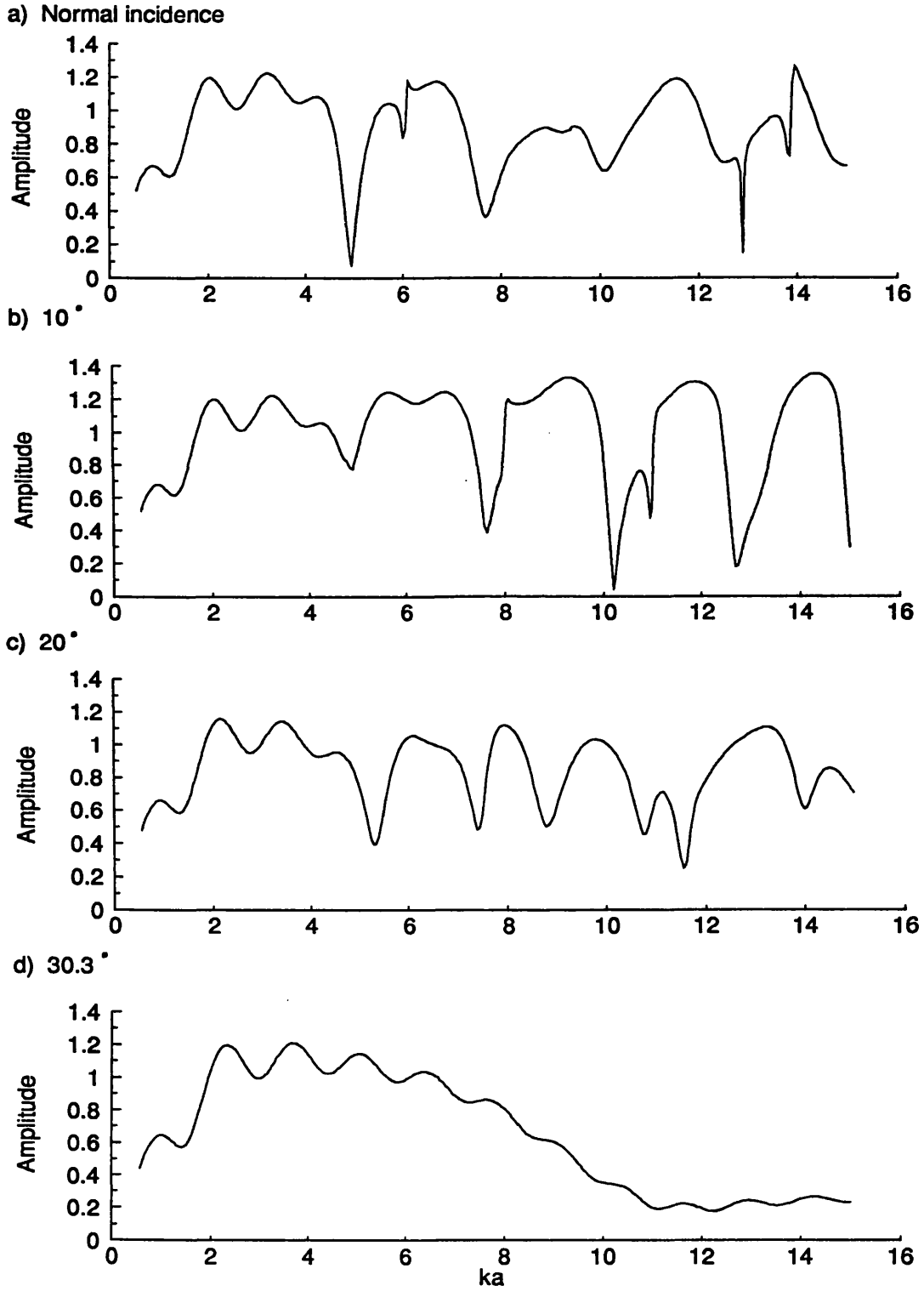

Figure 5.3 Partial modes for an aluminium cylinder.

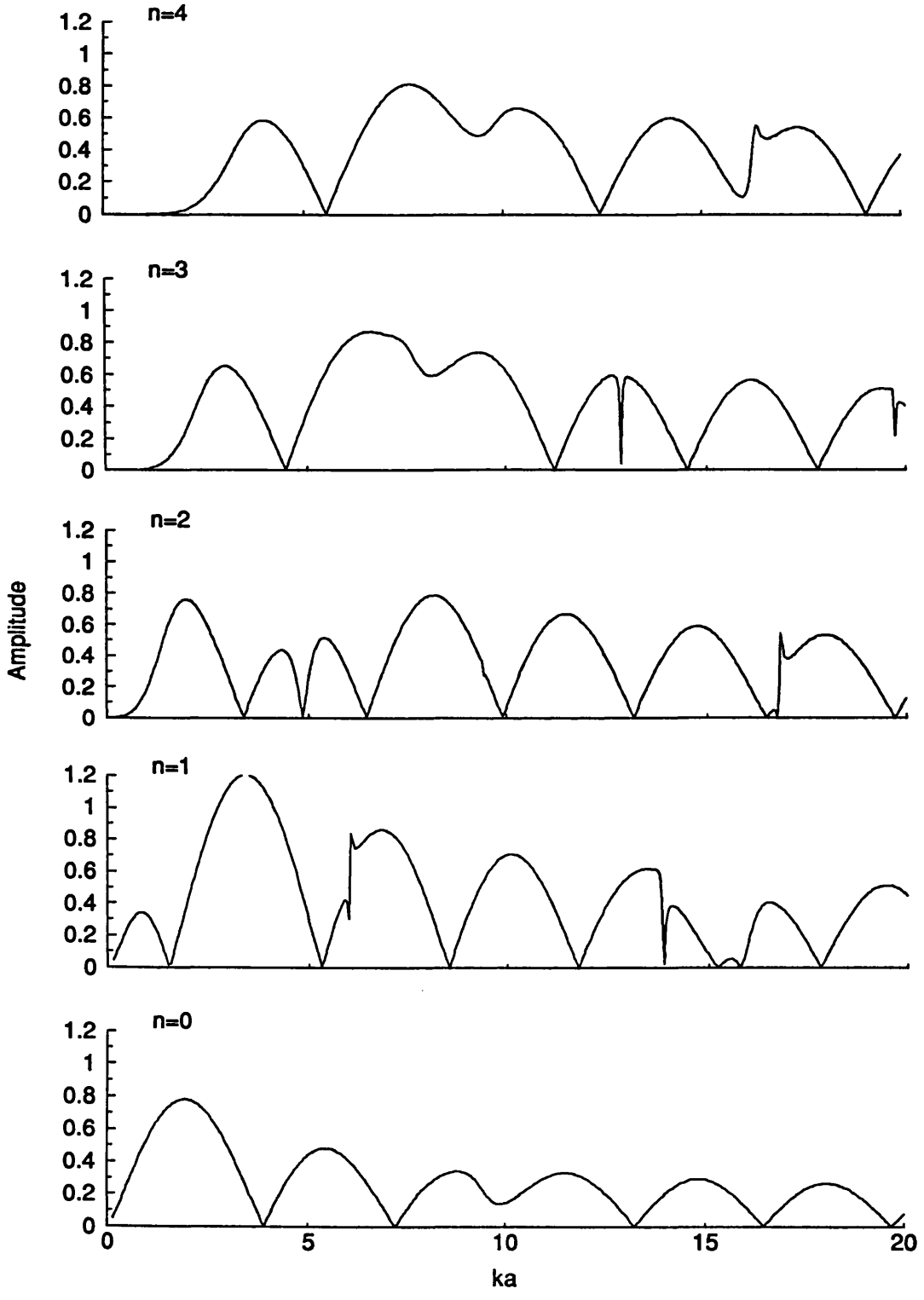

Figure 5.4 Resonance contributions for an aluminium cylinder.

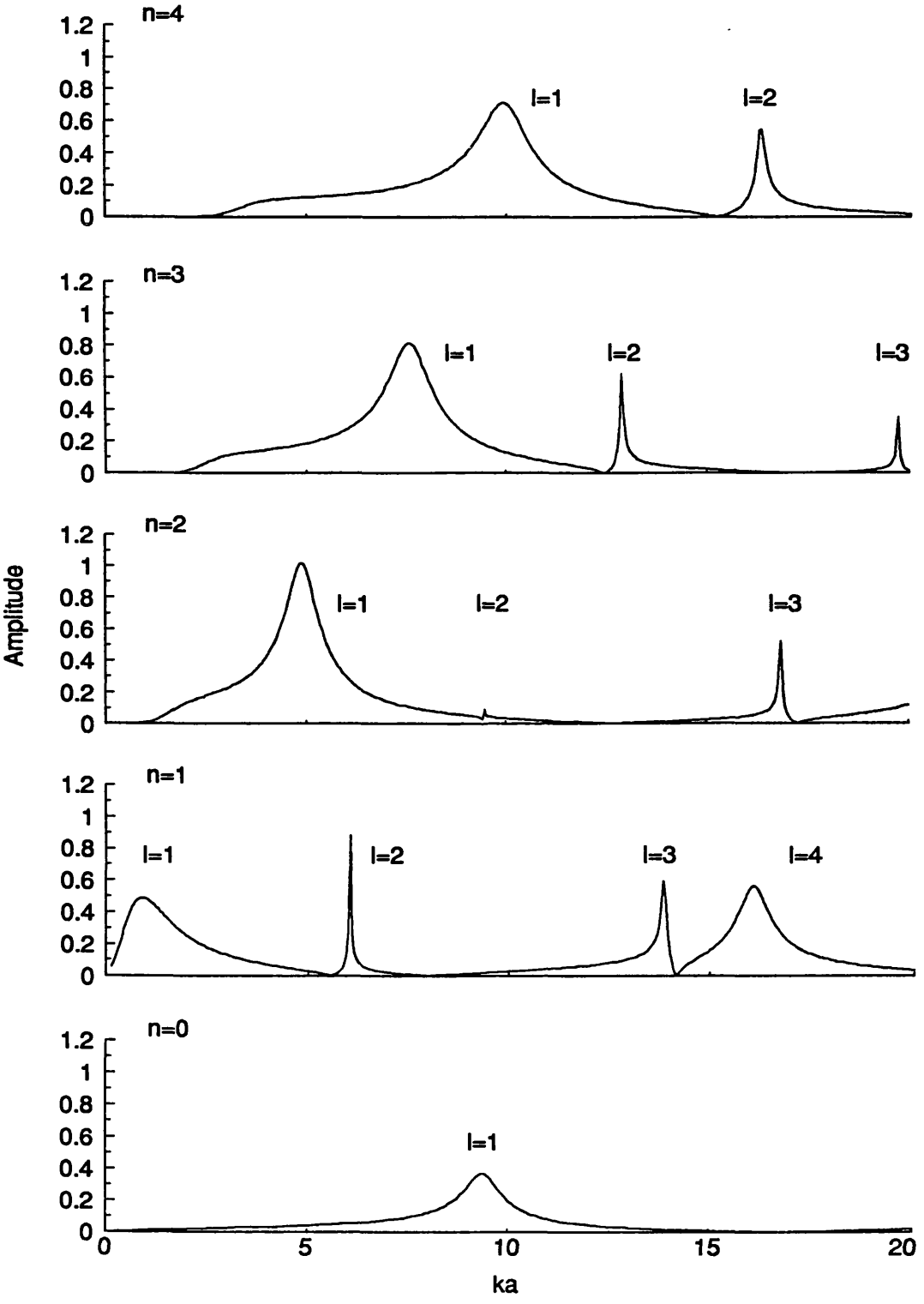

Figure 5.5 Form function for a solid aluminium cylinder, wavefield at normal incidence, observed at 180°.

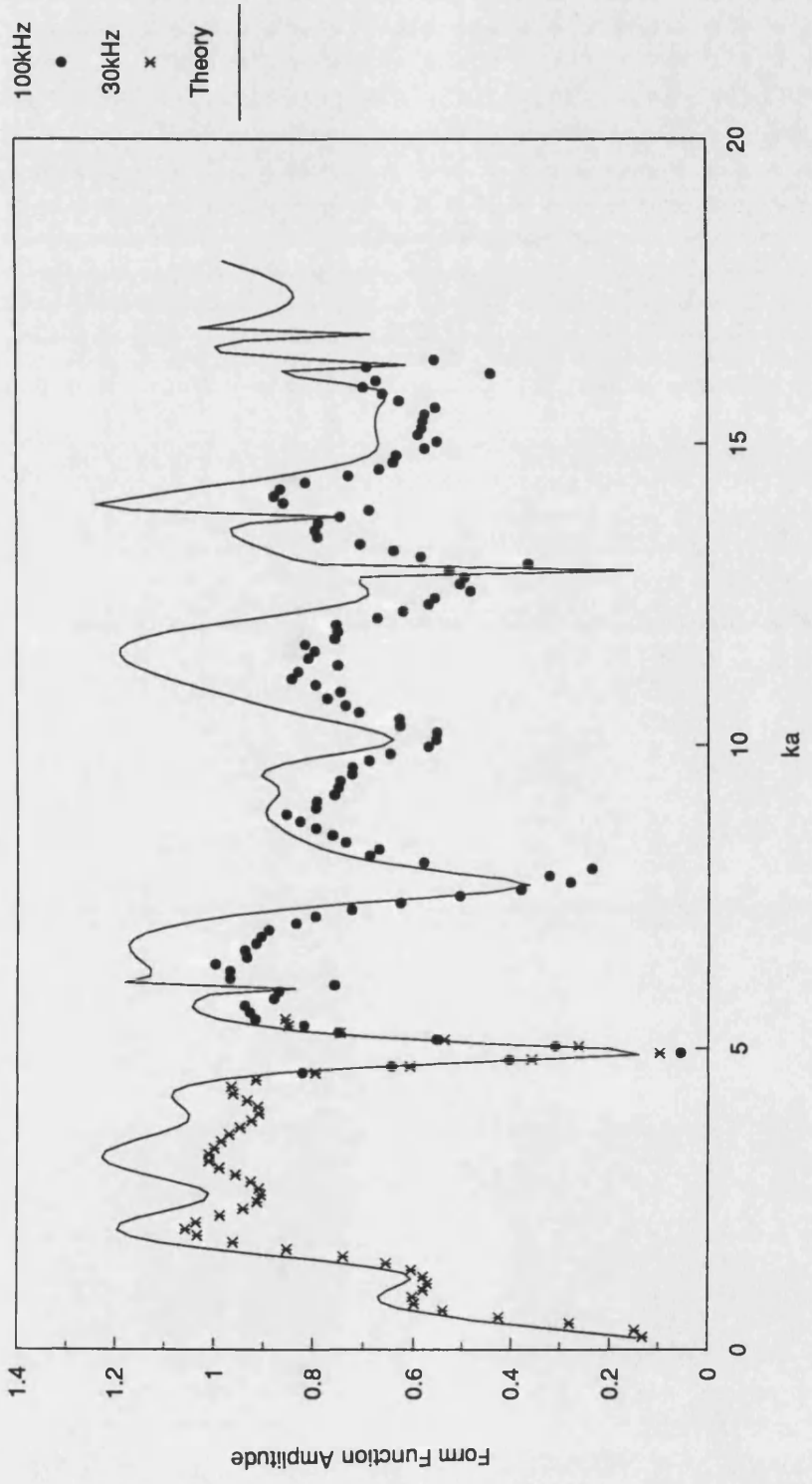

Figure 5.6 Form function for a solid aluminium cylinder, wavefield at normal incidence, observed at 150°.

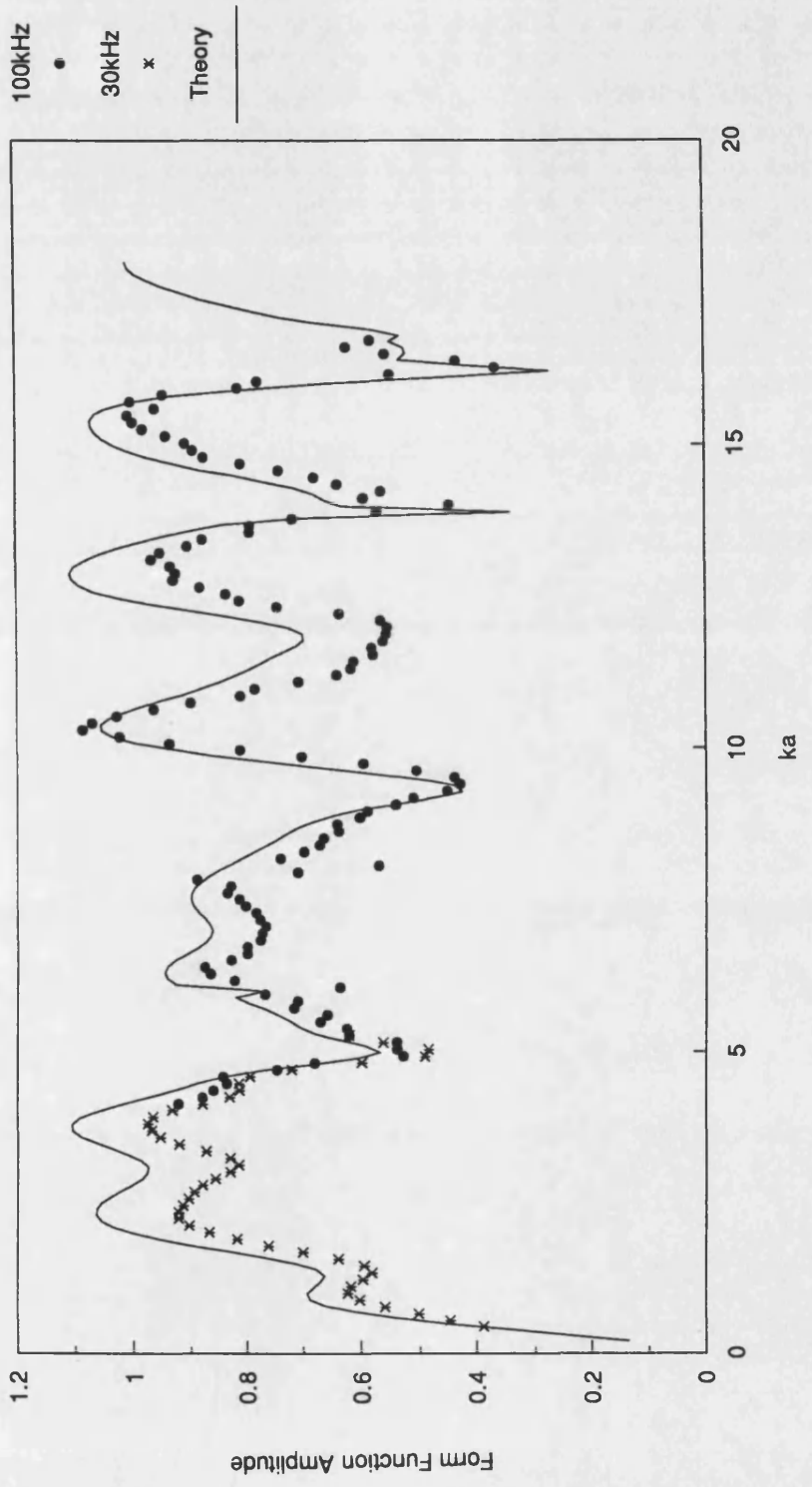

Figure 5.7 Form function for a solid aluminium cylinder, wavefield at normal incidence, observed at 120°.

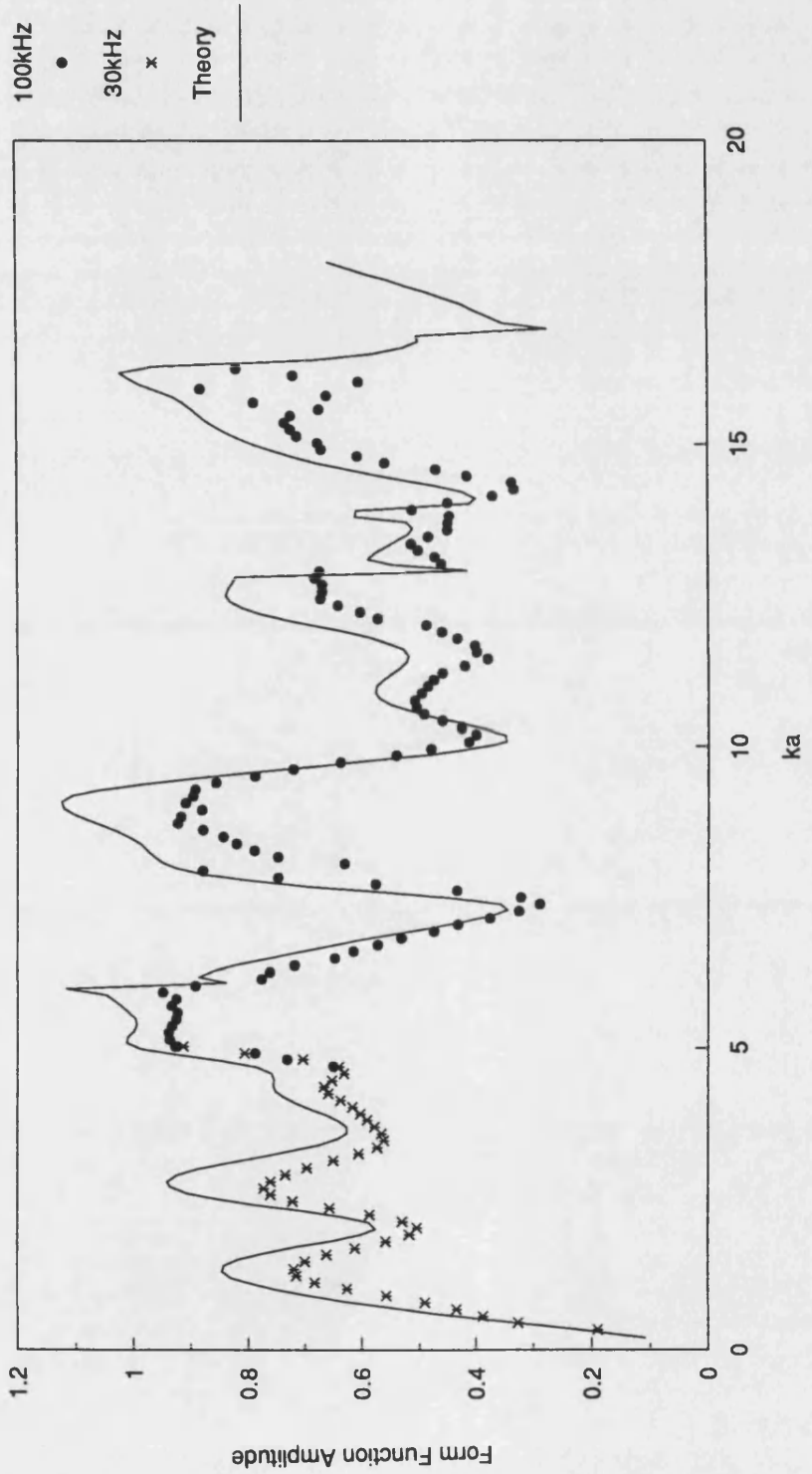

Figure 5.8 Form function for a solid aluminium cylinder, wavefield at normal incidence, observed at 90°.

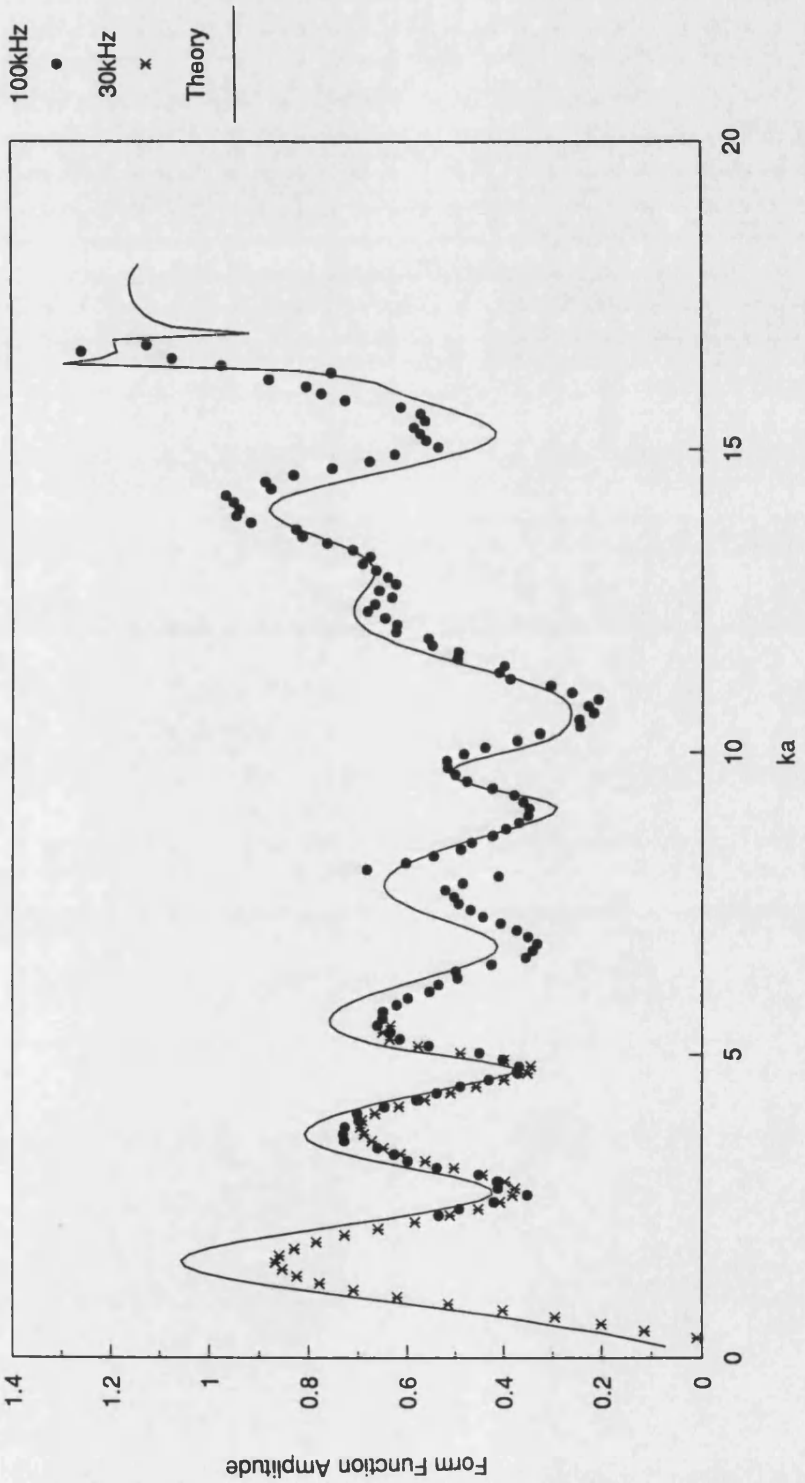

Figure 5.9 Form function for a solid aluminium cylinder, wavefield at normal incidence, observed at 60°.

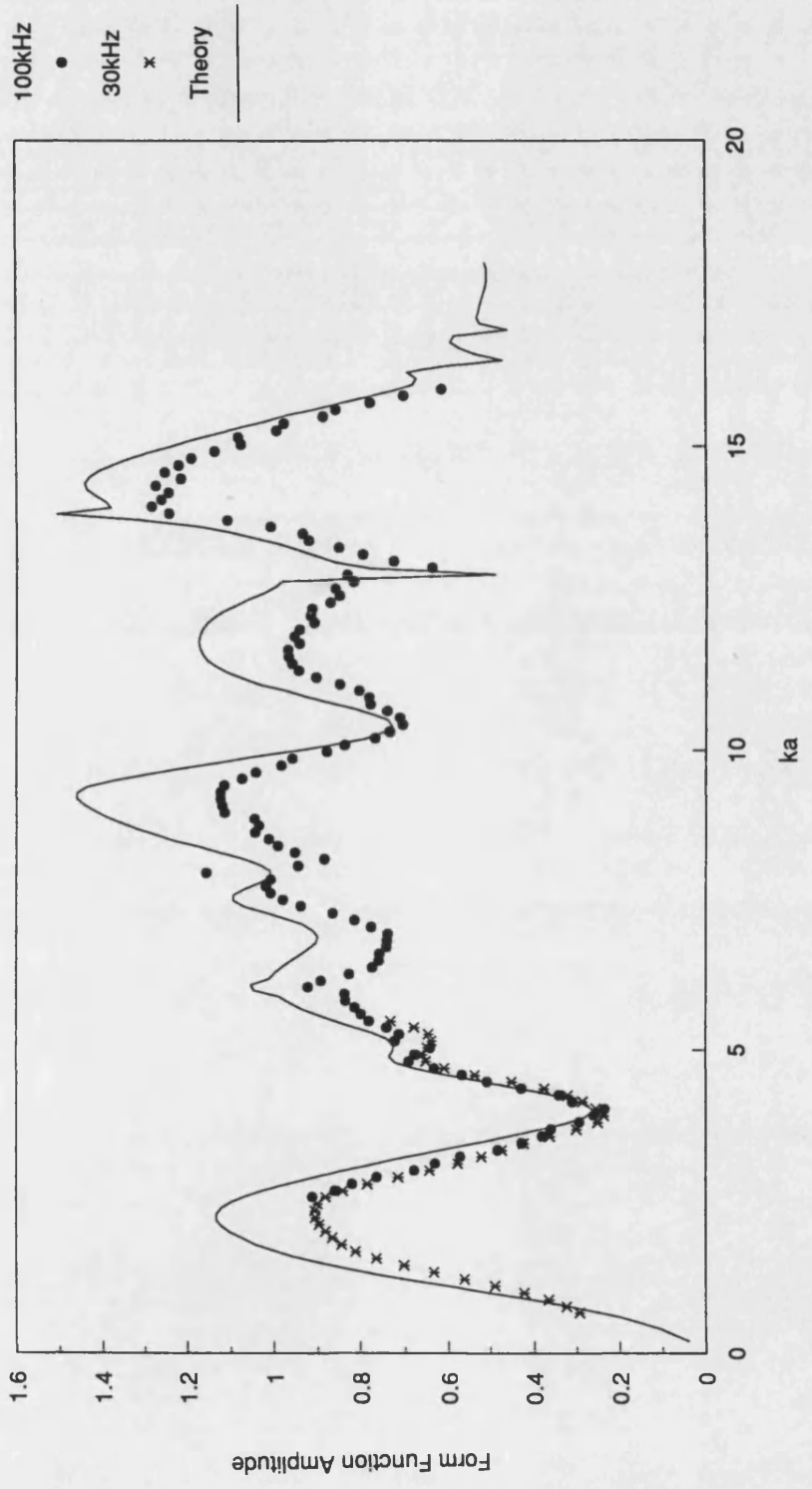

Figure 5.10 Form function for a solid aluminium cylinder, wavefield at normal incidence, observed at 0°.

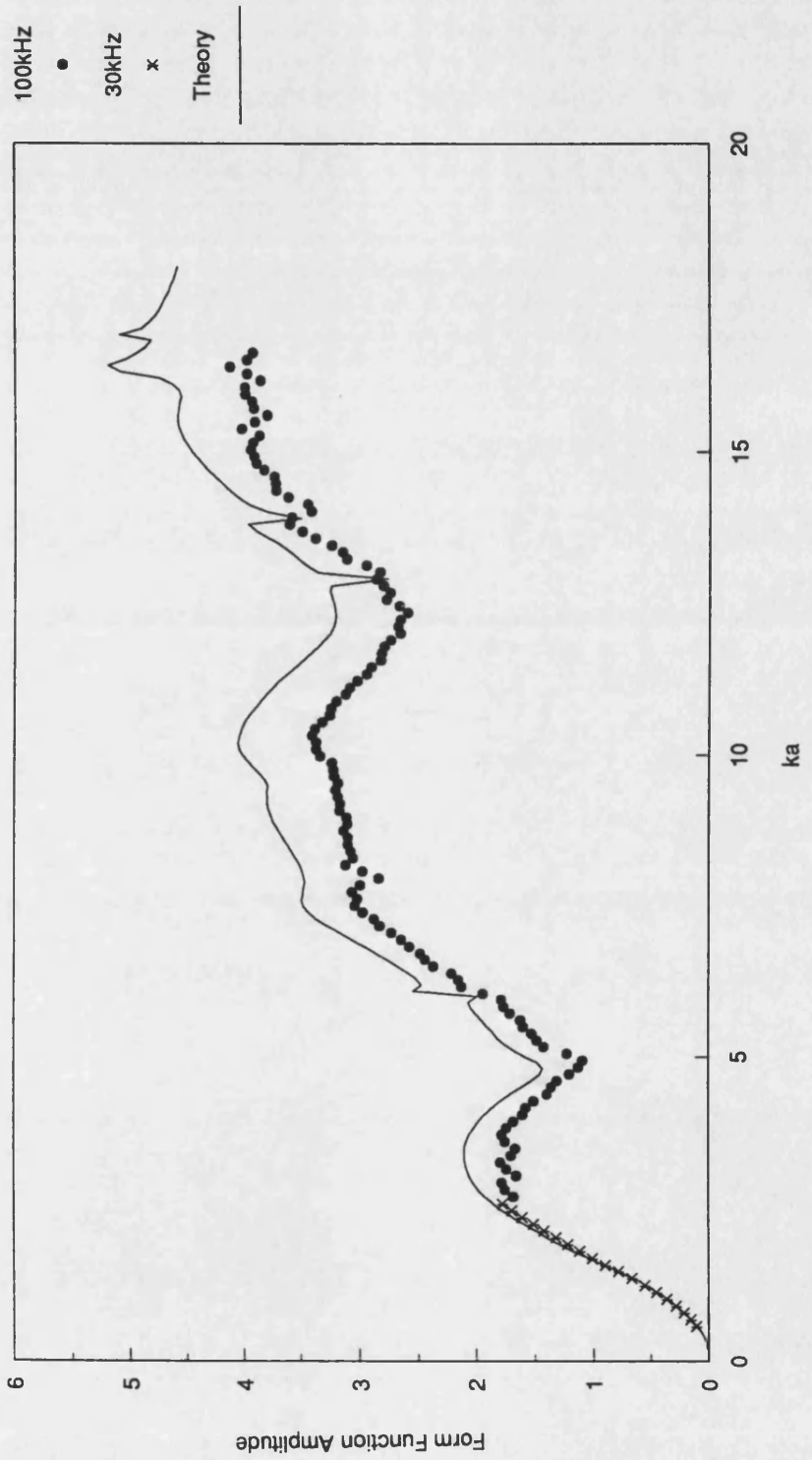

Figure 5.11 Form function for a solid aluminium cylinder at incident angles of 0° and 1° for two observation angles.

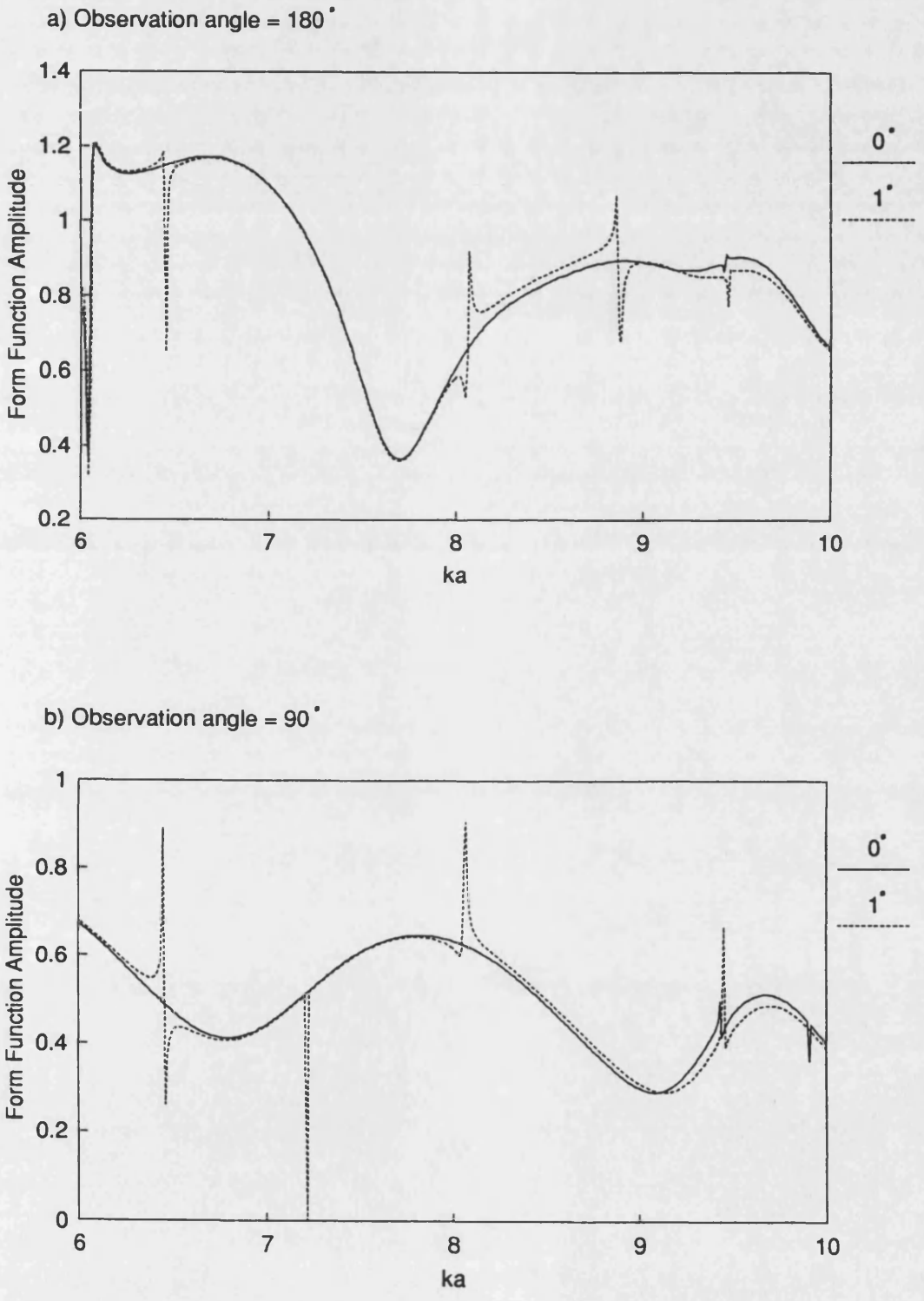

Figure 5.12 Geometry of the line array model for the plane wave spectrum at normal incidence.

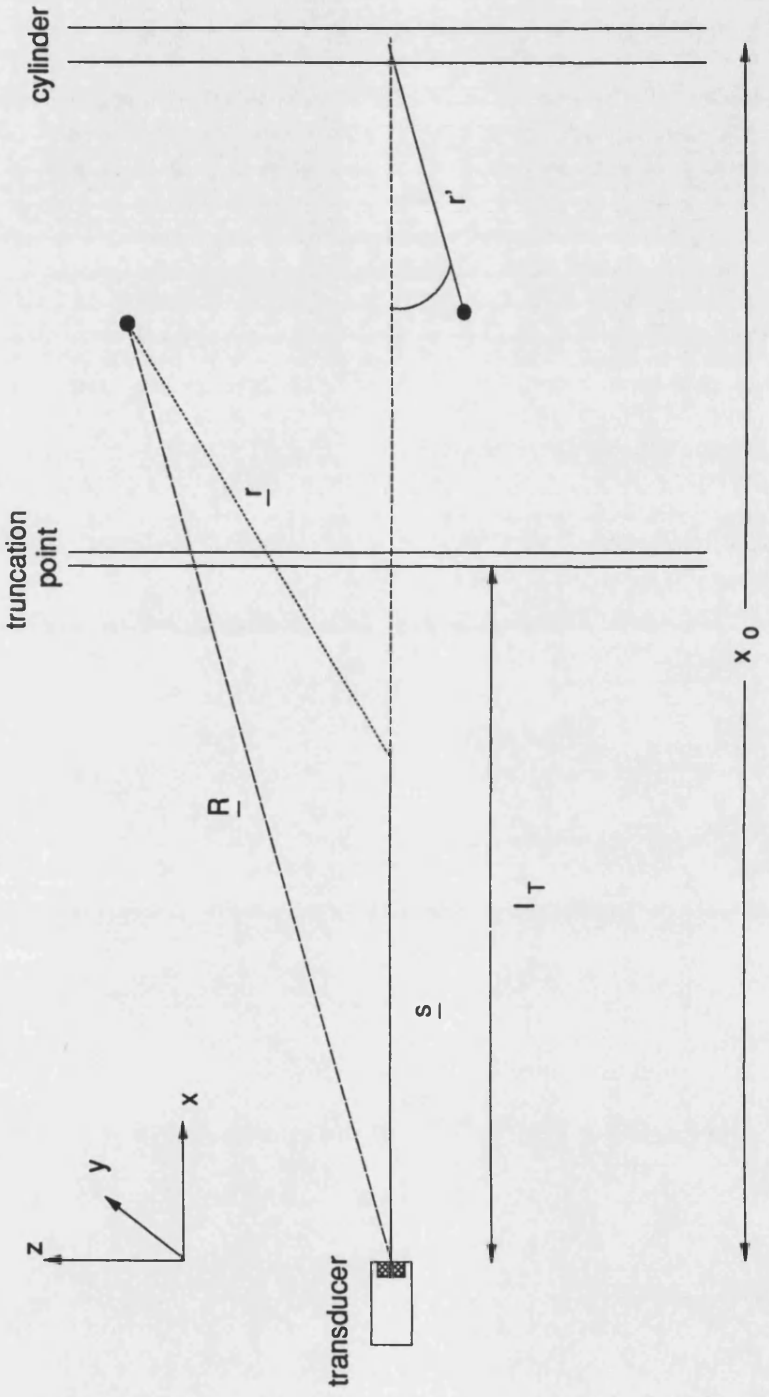

Figure 5.13 Form function for a solid aluminium cylinder, wavefield at normal incidence, observed at 180° showing the single plane wave form function and the modified form function.

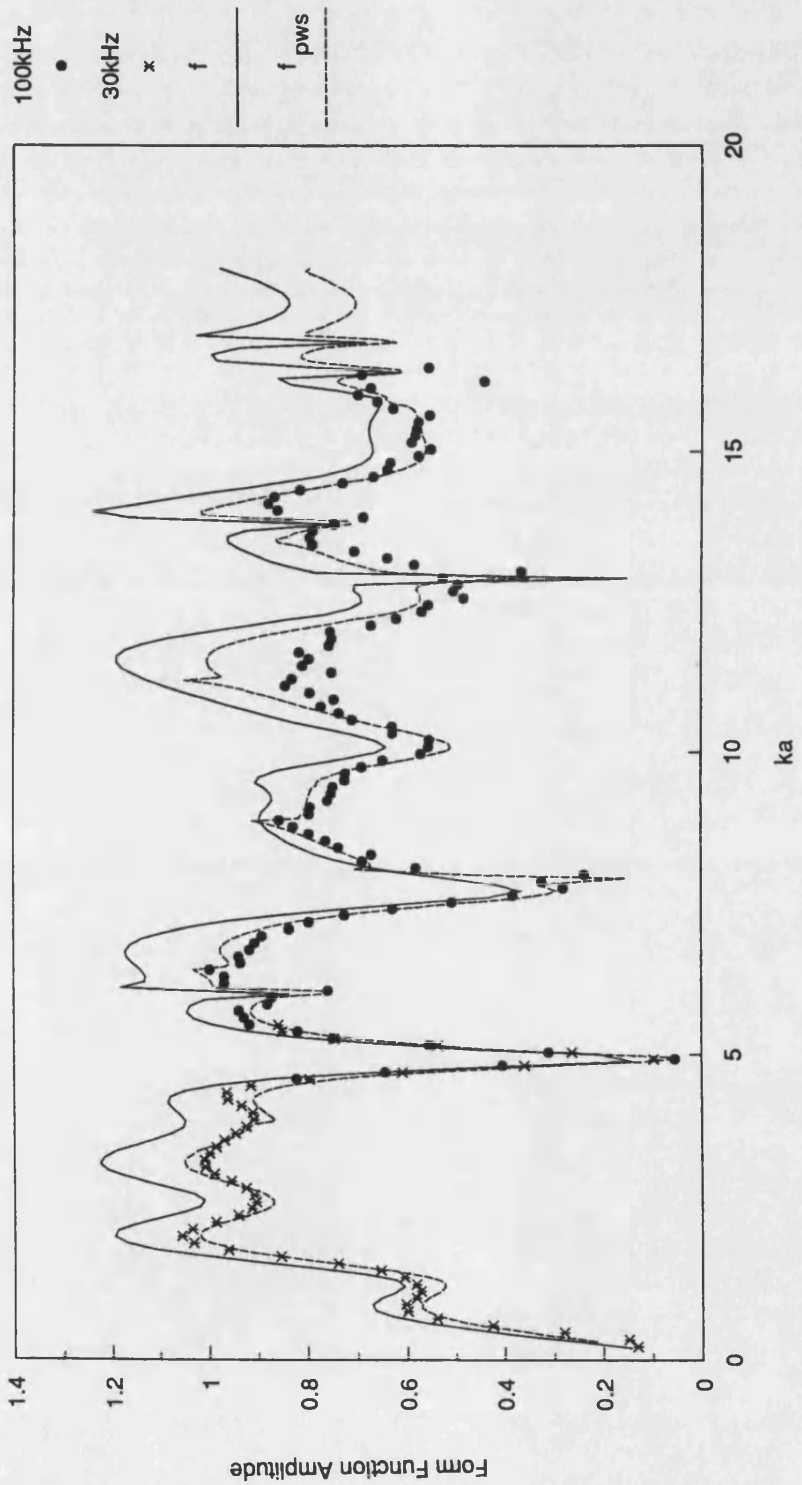

Figure 5.14 Form function for a solid aluminium cylinder, wavefield at normal incidence, observed at 90° showing the single plane wave form function and the modified form function.

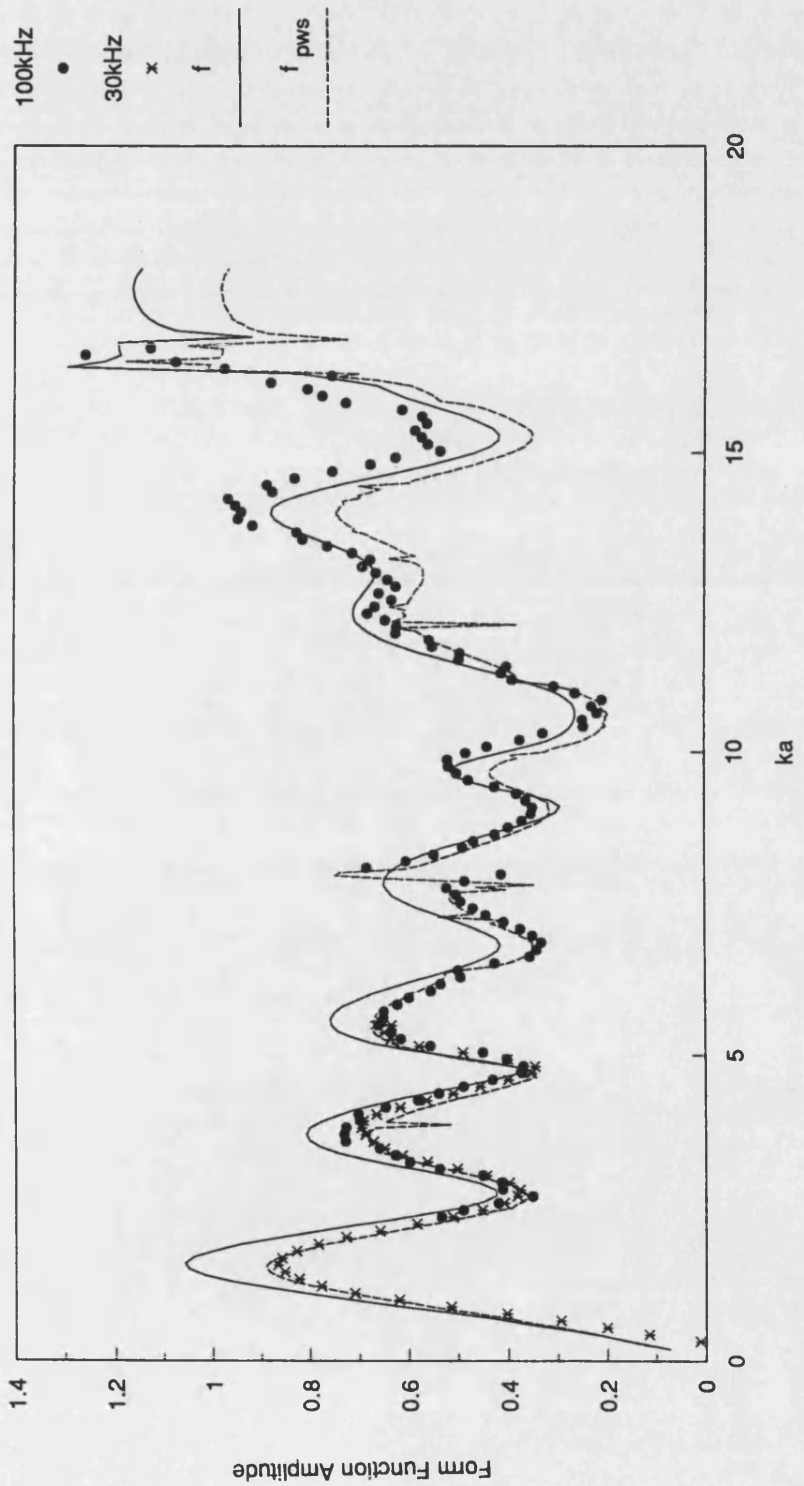

Figure 5.15 Form function for a solid aluminium cylinder, wavefield at normal incidence, observed at 60° showing the single plane wave form function and the modified form function.

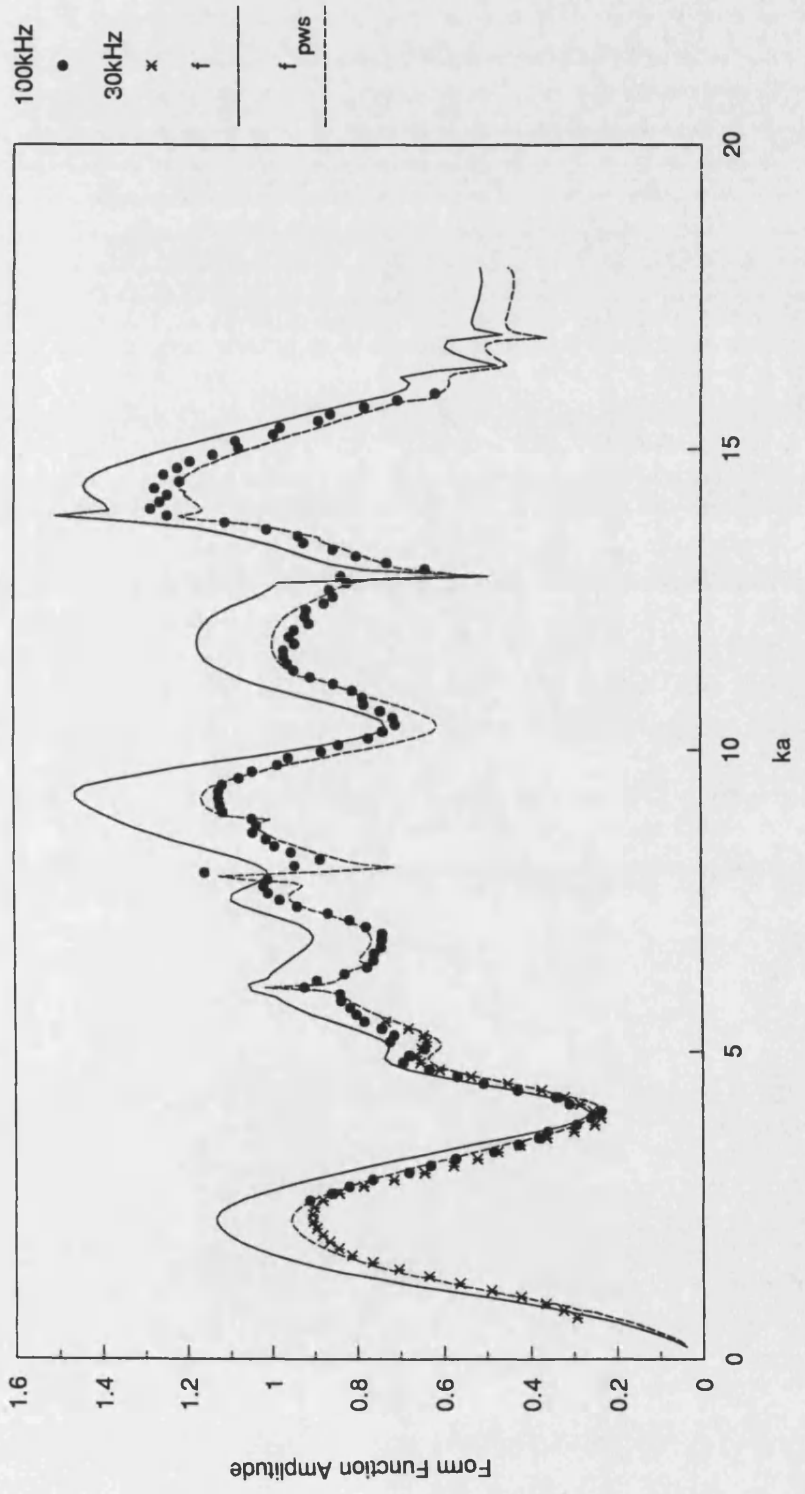

Figure 5.16 Form function for a solid aluminium cylinder, wavefield at normal incidence, observed at 0° showing the single plane wave form function and the modified form function.

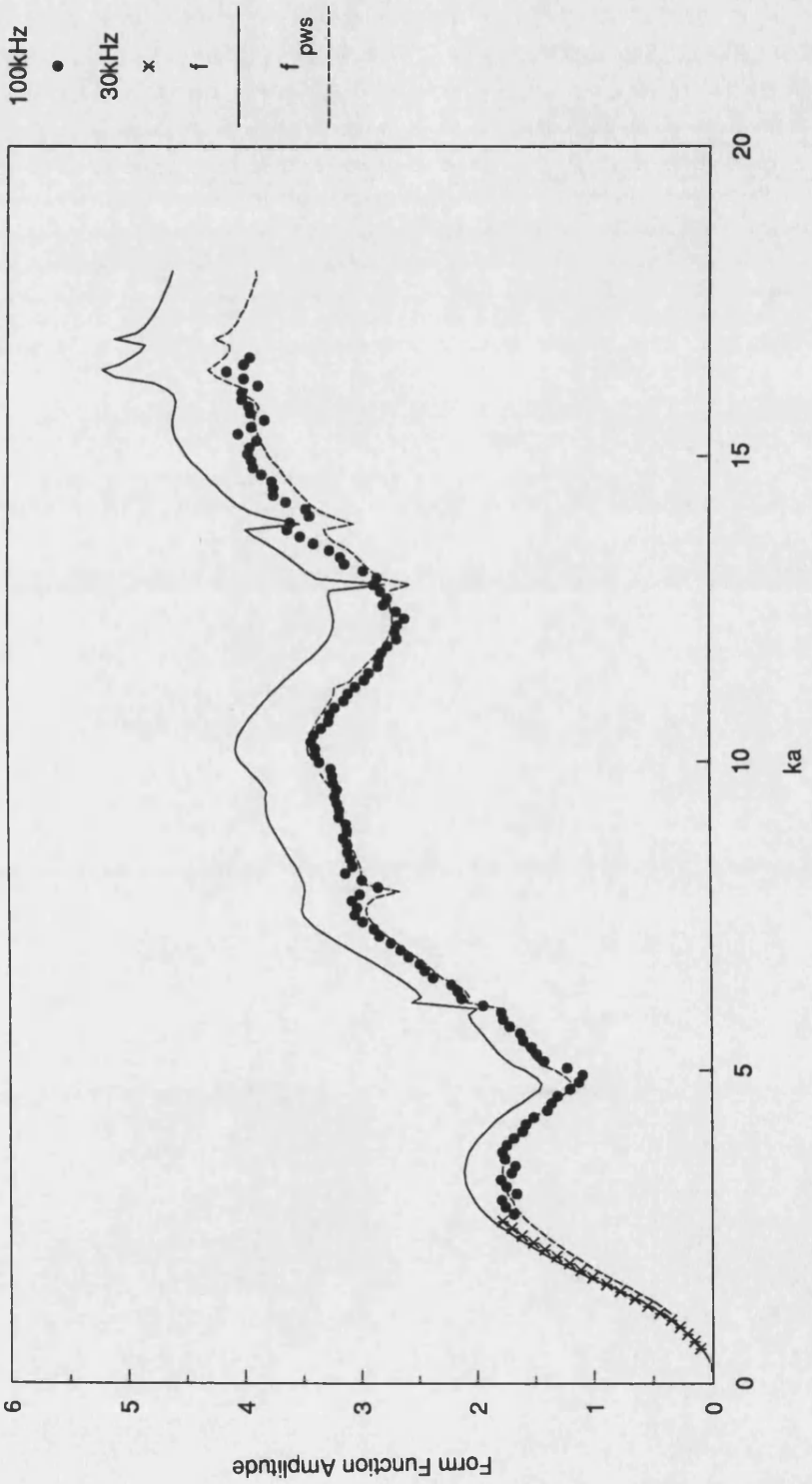

Figure 5.17 Ratio of the form function to the modified from function for varying angles of incidence.

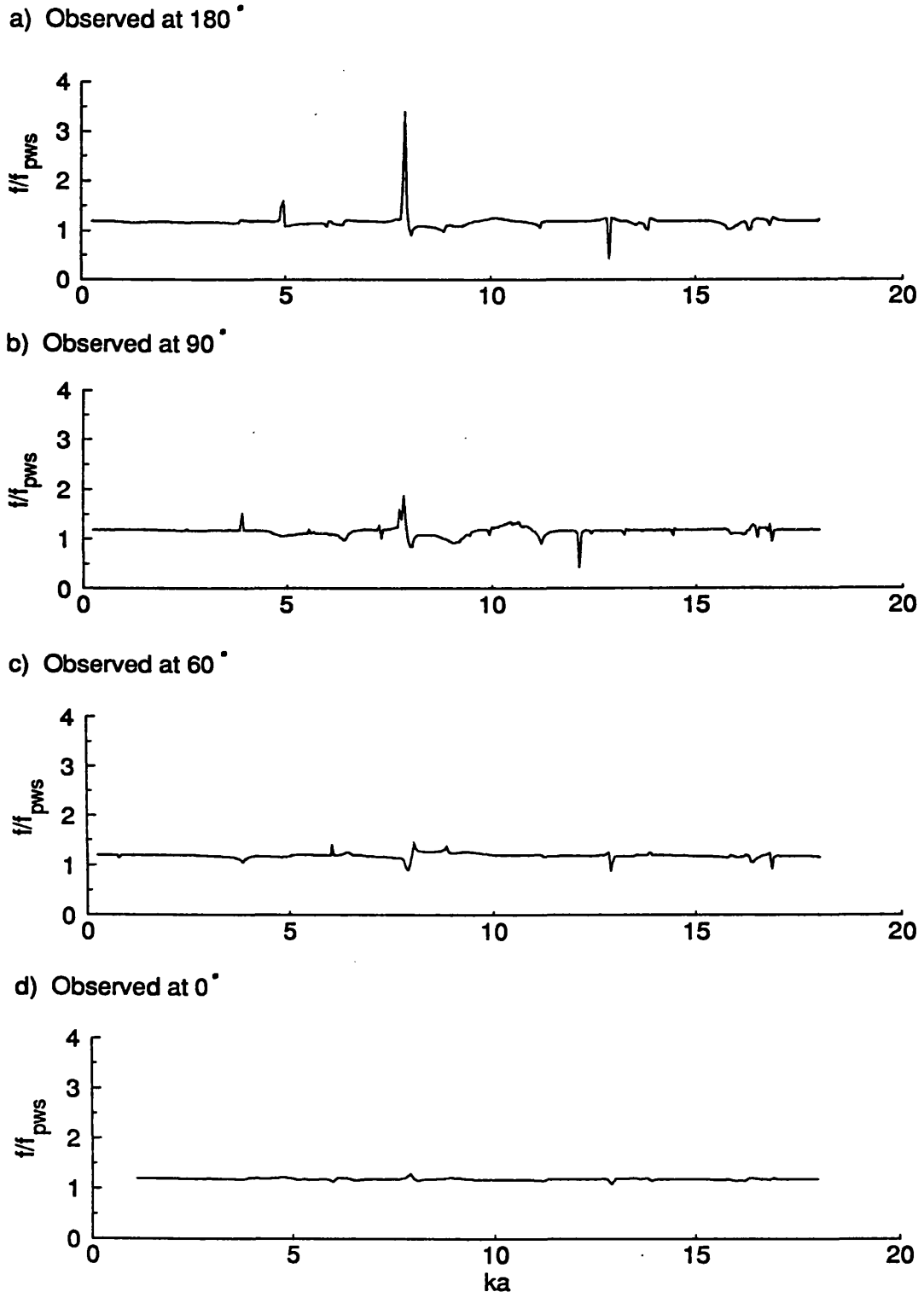

Figure 5.18 Form function determined for an obliquely incident wavefield at 10°.

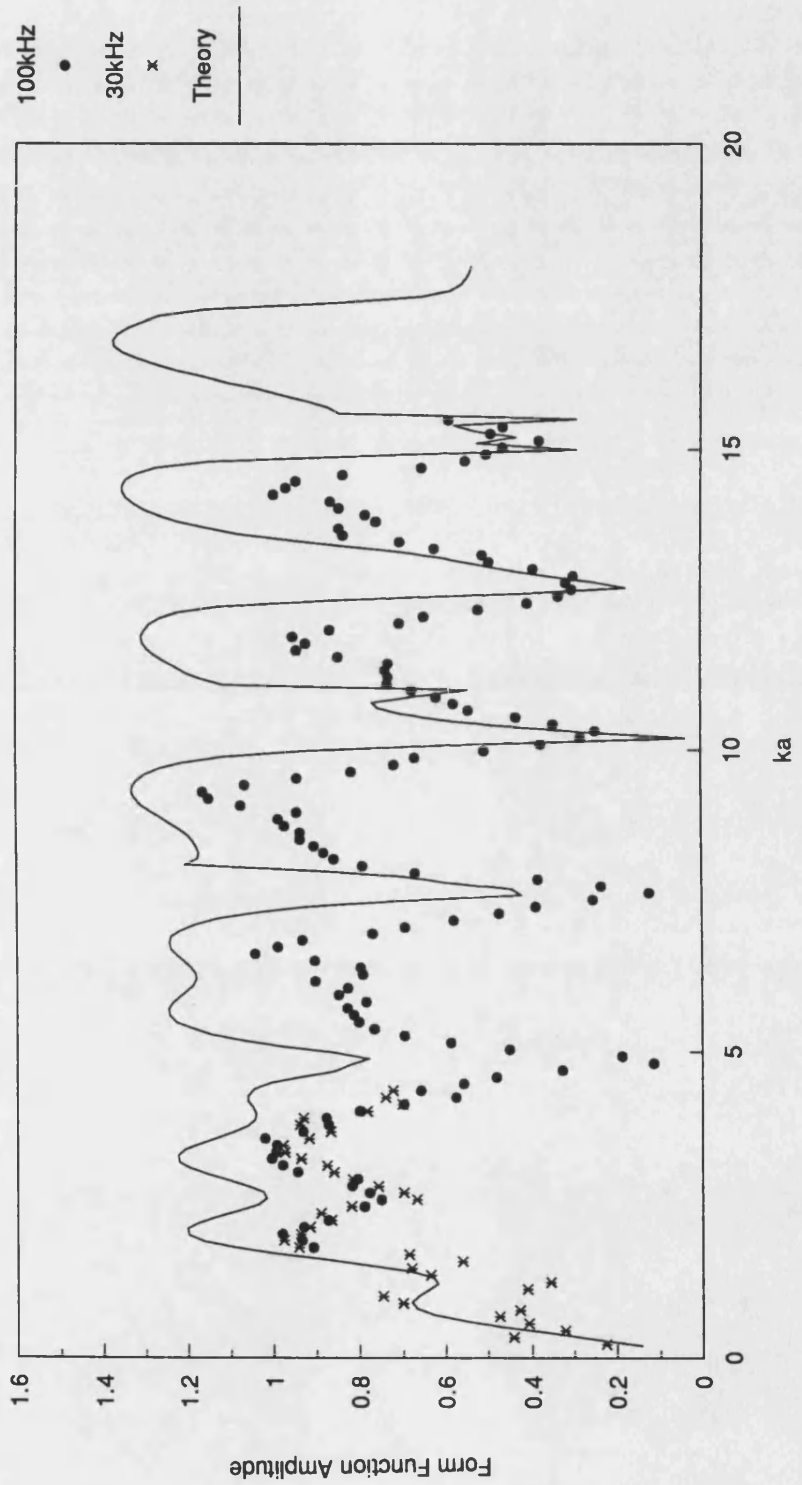

Figure 5.19 Form function determined for an obliquely incident wavefield at 30°.

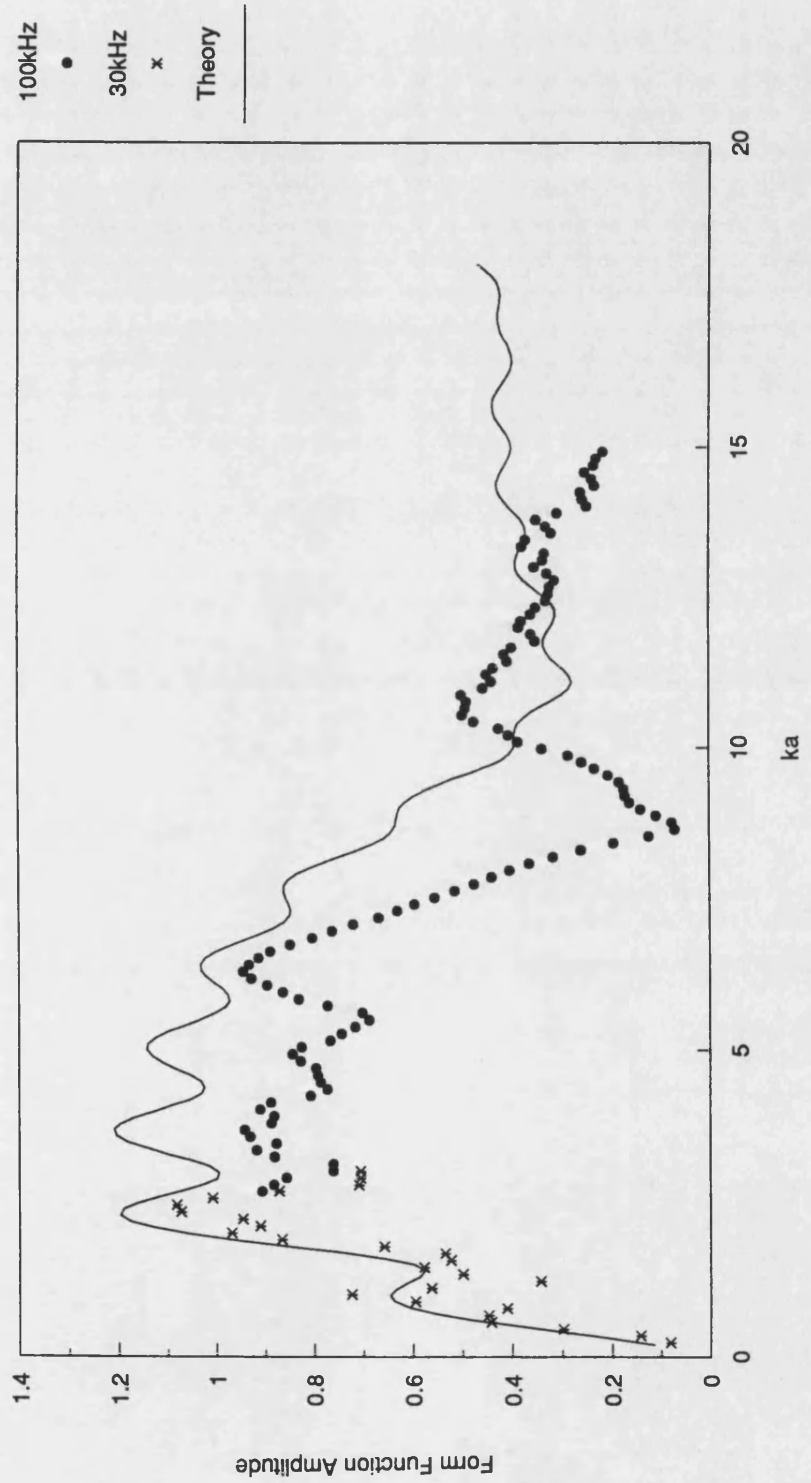

Figure 5.20 Form function determined for an obliquely incident wavefield at 50°.

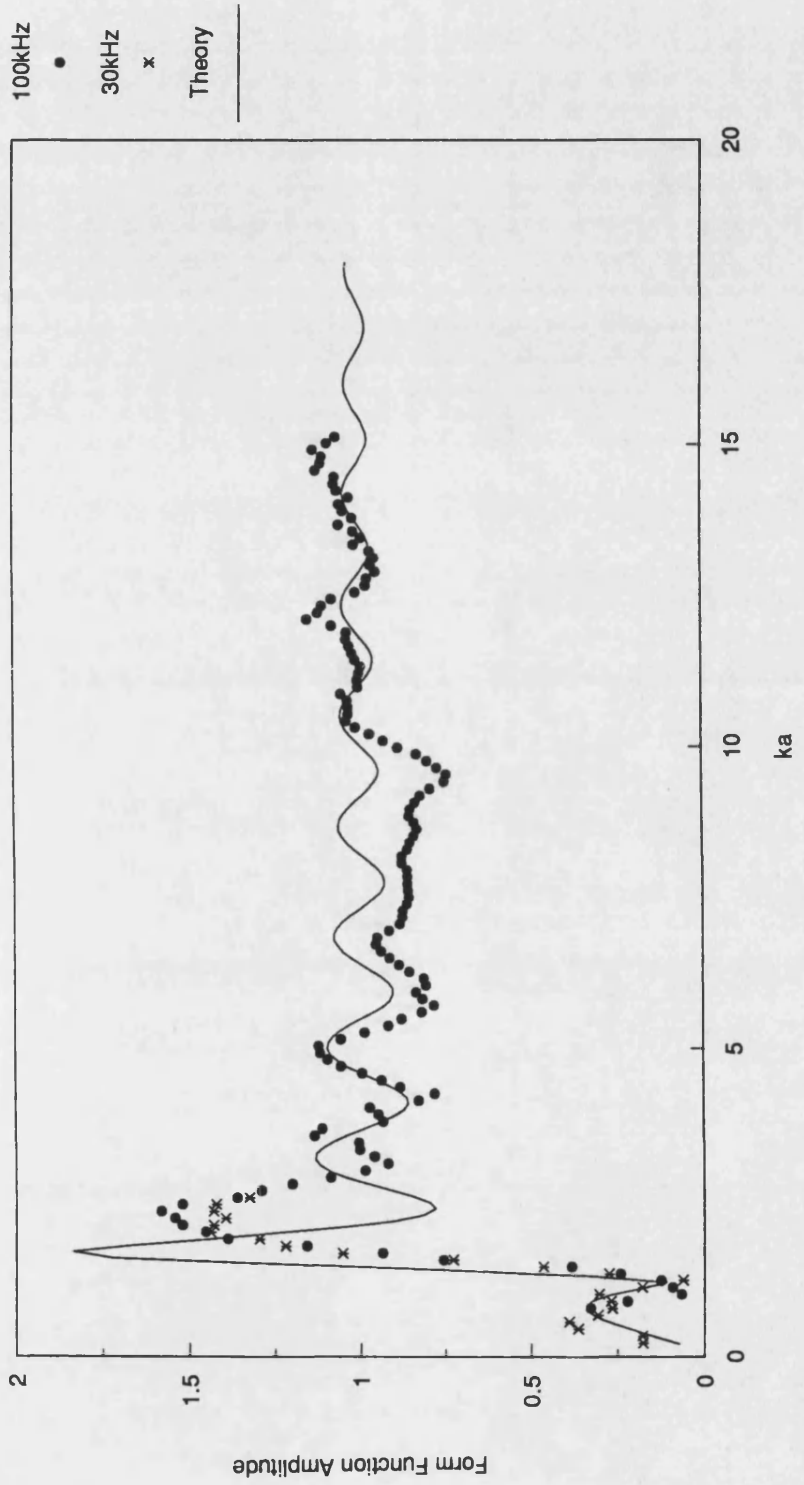

Figure 5.21 Variation in the form function with incident angle: 28°, 30° and 32°.

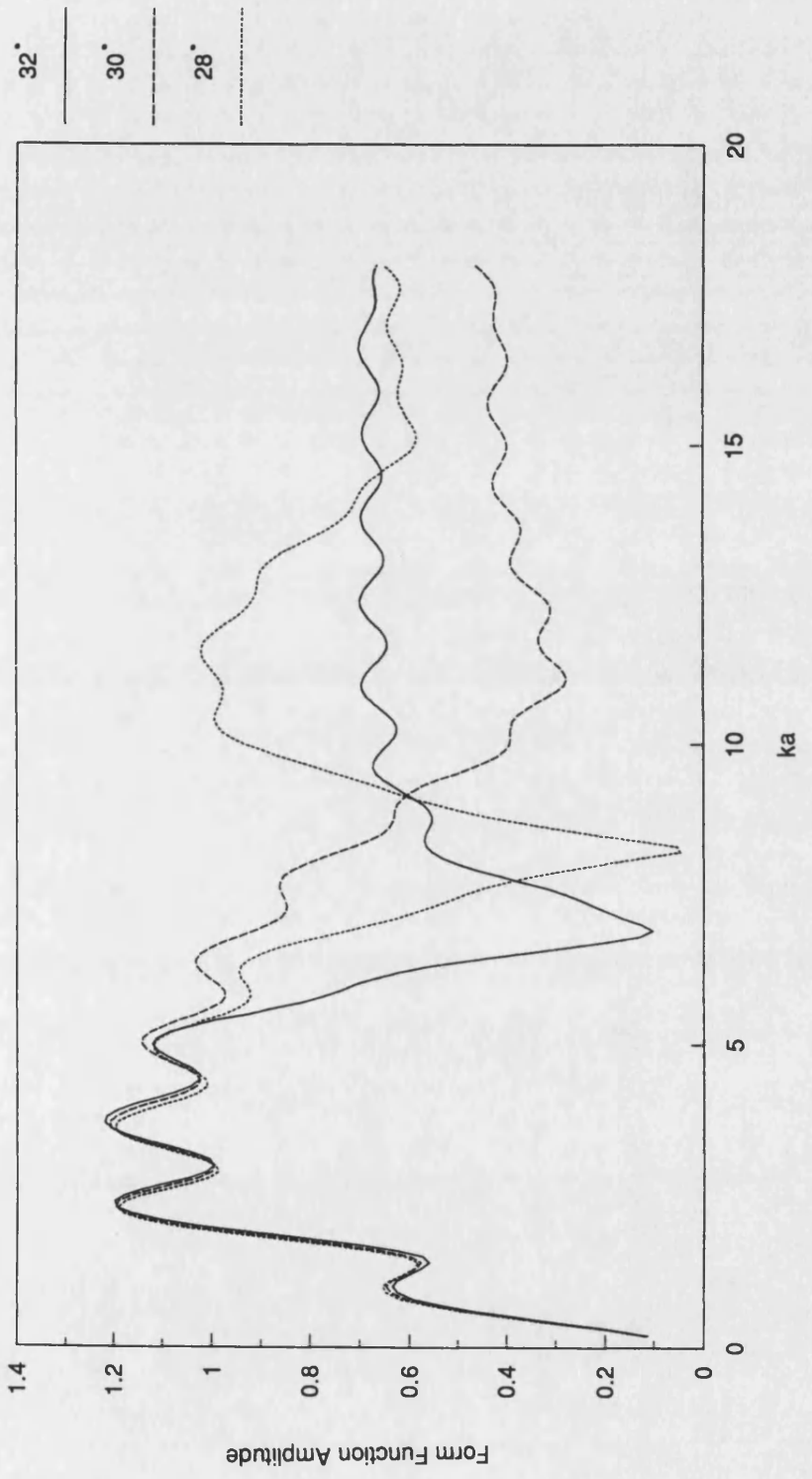

Figure 5.22 Geometry of the line array model for the plane wave spectrum at oblique incidence.

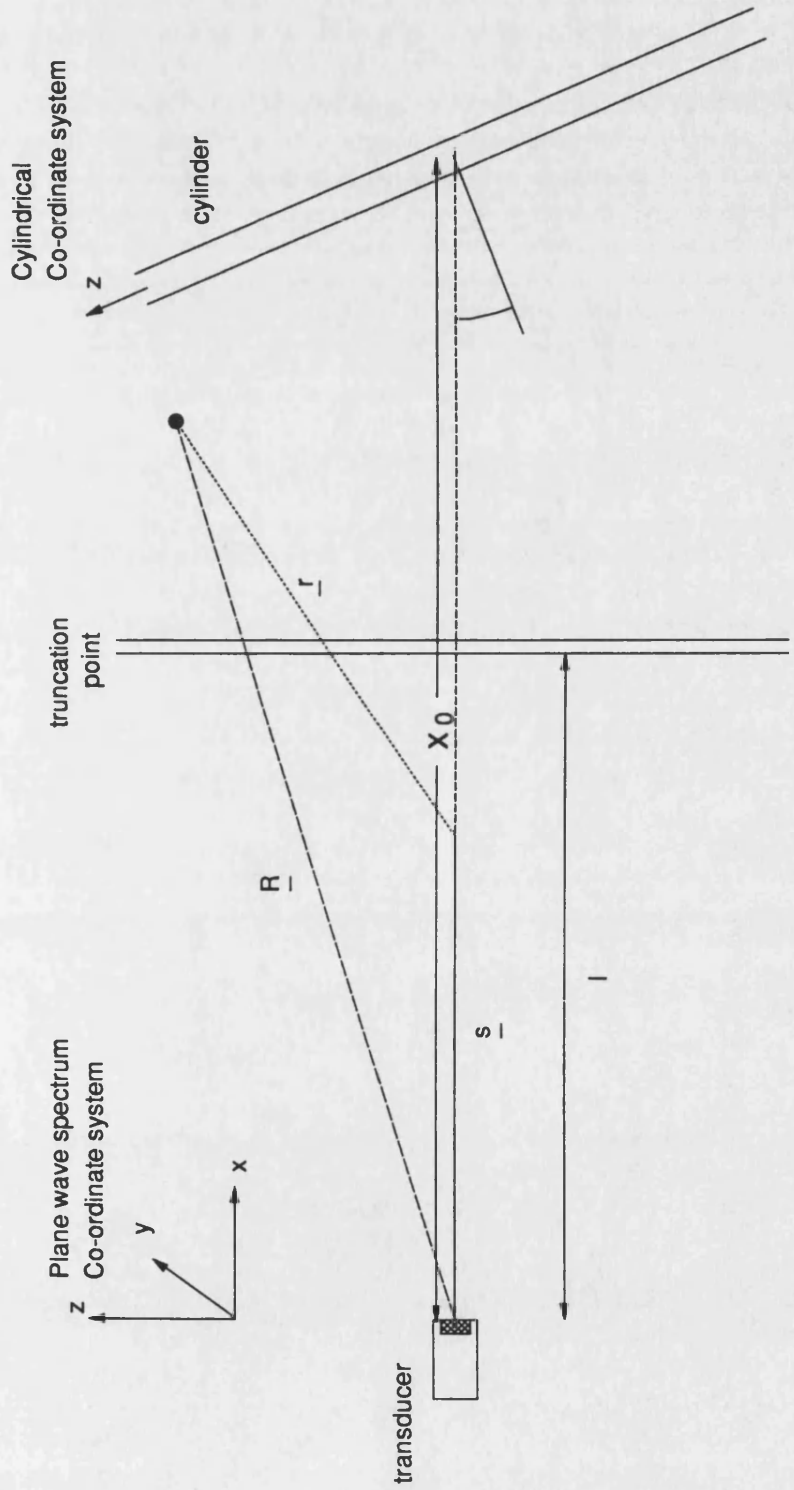

Figure 5.23 Results for an obliquely incident wave field at 10°, showing the usual form function and the modified form function.

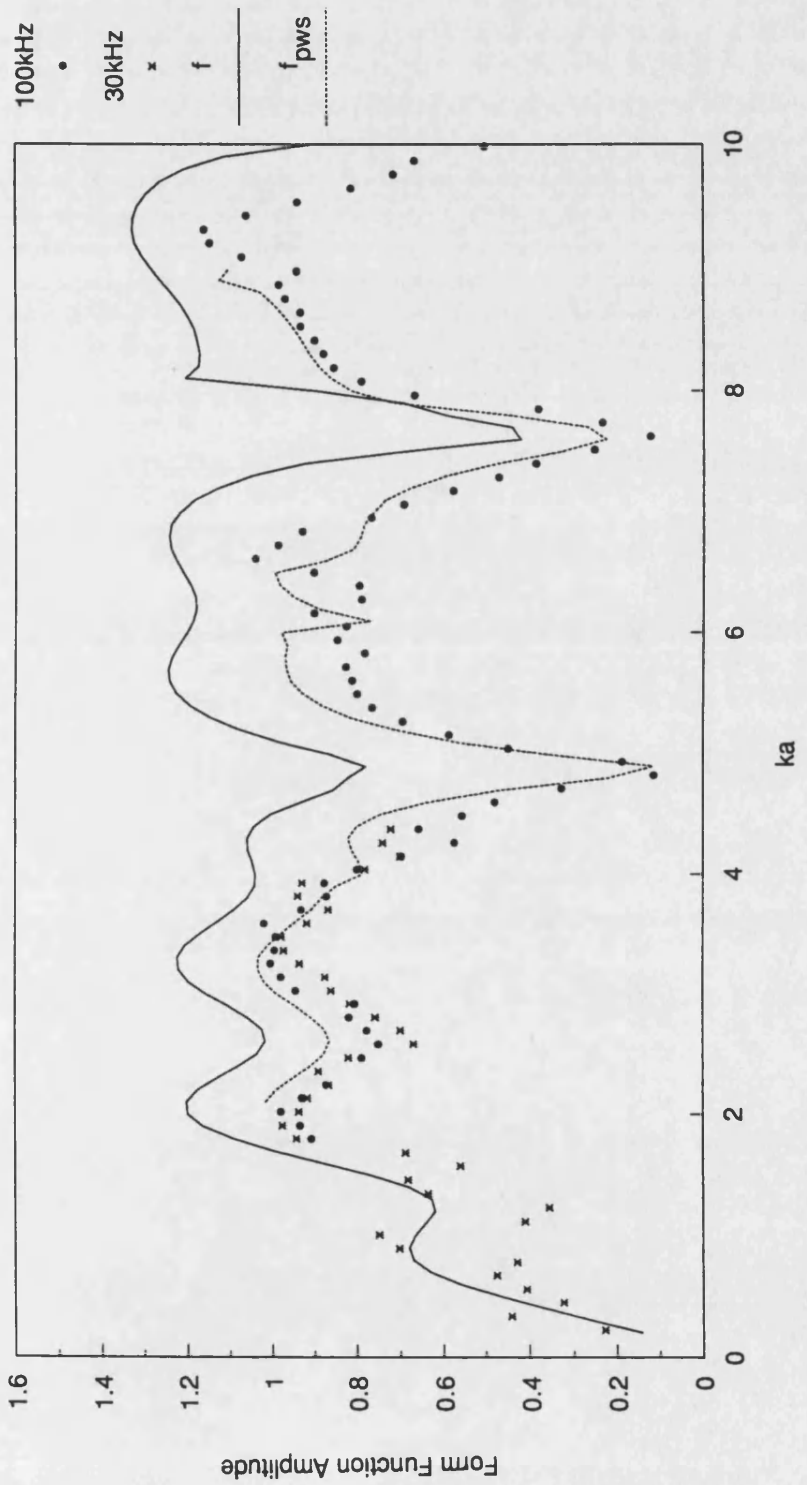

Figure 5.24 Results for an obliquely incident wave field at 30°, showing the usual form function and the modified form function.

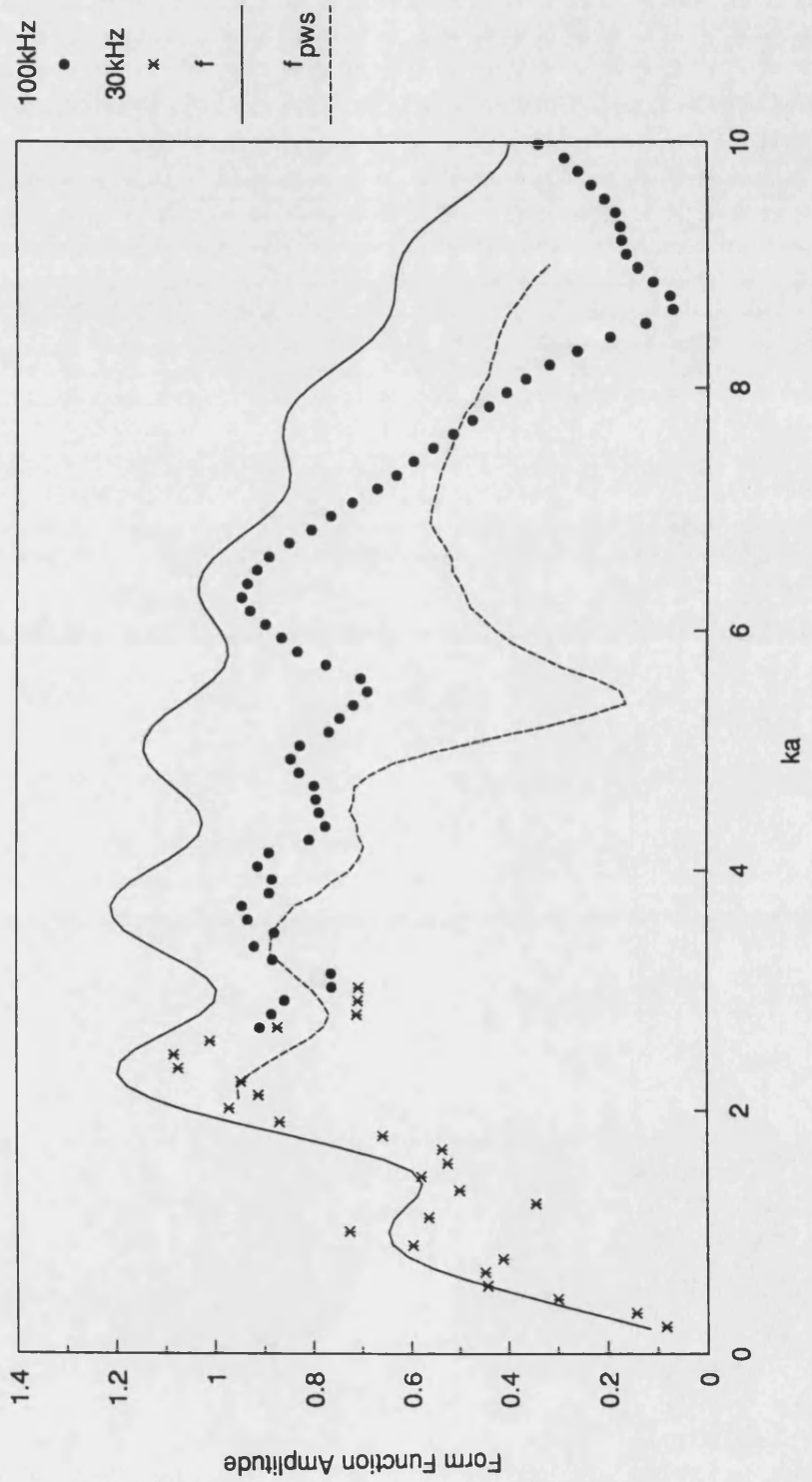

6 Circular cylindrical shells

6.1 Literature Survey

Many theoretical calculations of the form function for a hollow elastic cylinder are based on the work of Doolittle & Überall (1966) and Ugincuis & Überall (1968). Prior to this several theoretical works had been published (for example Horton, King & Dierks, 1962) which considered special cases of the hollow cylinder such as very thin walled shells, where many approximations could be made. Doolittle & Überall (1966) however, obtained the general and exact solution, neglecting absorption, for the scattering of normally incident plane waves from infinite elastic hollow circular cylinders using the Normal Mode Solution.

Subsequent work has primarily concentrated on three main areas. Firstly, a considerable amount of work has gone into finding other methods of solution that, for example, are easier to deal with at high frequencies where the exact Normal Mode Solution is slow to converge (Gaunaurd, 1977; Dickey, Nixon & D'Archangelo, 1983).

A second area of study has been to complicate the problem by allowing the cylinder to become layered, where either layer could become absorptive (Flax & Neubauer, 1977) or where the outer coating could be visco-elastic (Gaunaurd, 1977).

The third, and probably the most significant, area of study has been to look for solutions that give a clearer understanding of the phenomenon taking place (e.g. Ugincuis & Überall, 1968; Flax, Gaunaurd & Überall, 1981) and to investigate and explain the various resonance modes and phenomenon that occur. This has included work on how the various resonance modes of the hollow cylinder manifest themselves in the form function and how the latter can be decomposed into a background and a resonance component (e.g. Murphy, Breitenbach & Überall, 1978; Murphy, George & Überall, 1979). Dickey, Nixon & D'Archangelo (1983) examined the behaviour of the resonances (Franz, Stoneley, Rayleigh and Whispering Gallery) on an aluminium cylinder as the cylinder is varied from solid to a thin shell. They discuss what happens in the high frequency limit and show that the Rayleigh and Whispering Gallery resonances of the thick shell become the symmetric and anti-symmetric Lamb waves of the thin shell. Gaunaurd & Werby (1985) also examine the behaviour of the resonances with variation in shell thickness and also composition. They too demonstrate that as the shells become thinner the $l = 1$ family of resonances become the first symmetric (s_o) Lamb waves (formerly Rayleigh waves). Breitenbach, Überall & Yoo (1983) analysed the NMS for an infinitely long aluminium cylindrical shell in water, with particular reference to the thin - shell (near soft) region. They examined the transitions from Rayleigh type surface waves to Lamb type waves and concluded that the anti-symmetric Lamb wave is only generated under certain conditions. These conditions were in direct contrast to the computational results of Dragonette (1978) and the findings of Veksler (1982, 1984). A study of the conditions required for the generation of the anti-symmetric Lamb wave was the subject of a further paper by Veksler (1986) whose results (ka = 0 - 100) agreed with

his earlier findings and those of Dragonette (1978). A later study by Veksler (1988) considered the Lamb and Stoneley waves generated for *ka* less than 50 on an empty aluminium shell when immersed in either glycerine or water.

If the cylindrical shell is insonified by an obliquely incident wavefield then the scattering problem becomes a great deal more complicated. Liamshev (1958) obtained a series solution for the scattered pressure expressed in terms of Bessel functions, and expressed his results as the incident angle versus the normalised frequency, *ka*, as a function of the shell dimensions.

Pillai, Varadan, Varadan & Radlinski (1983) applied the T-Matrix approach to the case of an obliquely incident plane wave on an infinite shell. They generalised the problem to consider elastic or visco-elastic layered cylinders of arbitrary cross section, and present results of far field backscattering from water filled circular cylindrical shells, and from water filled elliptical shells at various angles of incidence. They compare their theoretical predictions with the thin shell theory of Junger (1952) and their experimental measurements. They obtain reasonable agreement for steel and plastic cylinders, attributing discrepancies at higher frequencies ($6 < ka < 10$) in the case of the plastic tube to the fact that their model does not include absorption.

James (1983) has also considered the problem of an obliquely incident plane wave. James presents theoretical plots of backscattered (monostatic) Target Strength for thick and thin steel shells with interior fluids of both water and a vacuum.

Much of the early experimental work on cylindrical shells was performed in tandem with investigations into solid cylinders (see Section 5.1). In addition to any experimental work mentioned above, a considerable amount of the recent work has been carried out by a group of French researchers using the MIIR techniques developed by Maze & Ripoche (1983a, 1983b). This technique is discussed in more detail in Section 5.1. Of particular note is a study of the resonances of a fluid filled shell (Maze, Izbicki & Ripoche, 1986). The resonances of cylindrical shells 0.01m in diameter are experimentally determined over the *ka* range 3 - 20. The experimental measurements show that even at so called normal incidence there are components of the wavefield that strike the cylinder obliquely, generating guided waves which propagate along the axis of the shell. The natural modes (free vibration) of the liquid column (water and chloroform) are also examined and the experimental identifications are in close agreement with theoretical predictions based on the theory proposed by Gazis (1959) and summarised by Maze et al. (1986). The free vibration of cylinders has been studied for a number of years (e.g. Gazis, 1959; Armenakas, Gazis & Herrmann, 1969; Achenbach, 1973), and is the vibration of the cylinder which occurs after the immediate response to the incident wave has died away. In this application it is only

one aspect of the total scattering phenomenon. For both the liquid filled cylinders an additional family of resonances is observed which are thought to be caused by a surface wave which propagates on the external liquid / target interface.

Talmant, Quentin, Rousselot, Subrahmanyam & Überall (1988) presented an experimental and theoretical study of the properties of circumferential waves on thin walled air filled cylinders. The experimental measurements were made using wide-band signals incident on a duraluminum cylindrical shell ($b/a = 0.96$). Two transducers were used with centre frequencies of 1MHz and 2.25MHz to cover the ka range 20 - 140. The results indicate two distinct series of resonances which are identified as the s_0 Lamb wave and, in the high frequency limit, the Stoneley wave analogous to that on a flat plate.

This literature survey, though brief, has attempted to highlight the key areas of research and the key papers within those areas. It is largely restricted to work that is pertinent to the investigation that follows and thus a great deal of interesting literature has had to be omitted from this review.

6.2 Theory

Theoretical predictions of the scattering of obliquely incident plane waves by cylindrical shells are often made using T-Matrix or integral techniques rather than the NMS which experiences computational difficulties at higher ka values (>20). However, for the limited ka range we are considering the computational difficulties are not thought to be significant, and so it was decided to model the scattering using the NMS solution to be consistent with other theories presented in this report.

The theoretical development for the cylindrical shell is much the same as that for the solid cylinder. The incident plane wave, of propagation vector k_1, makes an angle α with the x-axis of the co-ordinate system (Figure 6.1). The cylinder has material properties ρ_c, c_l, c_t and outer and inner radii a and b respectively. The outer and inner fluids are characterised by ρ_1, c_1 and ρ_3, c_3 respectively, where the symbols have been defined previously, and have been summarised in Appendix 1. The incident wave in the surrounding fluid is given by,

$$
\begin{aligned}
p_i &= p_0 e^{i(\underline{k}_1 \cdot \underline{r} - \omega \cdot t)} \\
&= p_0 e^{-i\omega t} e^{ik_1(r\cos\alpha\cos\phi + z\sin\alpha)} \\
&= p_0 e^{-i\omega t} e^{ik_1 z\sin\alpha} \sum_{n=0}^{\infty} \varepsilon_n i^n J_n(k_1 r\cos\alpha)\cos n\phi \quad .
\end{aligned}
$$

The scattered wave can be written

$$p_{sc} = p_0 e^{-i\omega t} e^{ik_1 z \sin\alpha} \sum_{n=0}^{\infty} \varepsilon_n i^n B_n H_n^1(k_1 r \cos\alpha) \cos n\phi \quad ,$$

while in the inner fluid,

$$p_f = p_0 e^{-i\omega t} e^{ik_3 z \sin\alpha} \sum_{n=0}^{\infty} \varepsilon_n i^n A_n J_n(k_3 r \cos\alpha) \cos n\phi \quad .$$

The displacement vector $\underline{u}$ can again be expressed in terms of a scalar potential and a vector potential (Equation 5.3) and the equations of motion are also the same as in the case of a solid cylinder (equations 5.4 - 5.6). A separable variables technique is used to solve equations 5.7 - 5.10 giving the potentials as,

$$\psi = e^{ihz} \sum_{n=0}^{\infty} (C_n J_n(pr) + D_n Y_n(pr)) \cos n\phi$$

$$A_z = e^{ihz} \sum_{n=0}^{\infty} (E_n J_n(qr) + G_n Y_n(qr)) \sin n\phi$$

$$A_r = e^{ihz} \sum_{n=0}^{\infty} (K_n J_{n+1}(qr) + L_n Y_{n+1}(qr)) \sin n\phi$$

$$A_\phi = -e^{ihz} \sum_{n=0}^{\infty} (K_n J_{n+1}(qr) + L_n Y_{n+1}(qr)) \cos n\phi$$

where h, p, q, have been defined previously in Section 5 and C_n, D_n, E_n, G_n, K_n, and L_n are scattering coefficients which can be determined.

The boundary conditions now have to be satisfied at both $r = a$ and $r = b$, giving a system of eight simultaneous equations in A_n , B_n , C_n , D_n , E_n , G_n , K_n , and L_n . To determine the scattered field exterior to the cylindrical shell these simultaneous equations have to be solved for the coefficient B_n. This can be achieved using Cramer's Rule and the expression for B_n is of the form

$$B_n = -\frac{F_n J_n(x_1) - x_1 J_n'(x_1)}{F_n H_n^1(x_1) - x_1 H_n^{1'}(x_1)} \quad ,$$

where

$$F_n = \frac{\rho_1}{\rho_c} x_{ta}^2 \frac{Q_n}{R_n} \quad ,$$

$$x_{ta}^2 = (k_t a)^2,$$

and Q_n and R_n are two seven by seven determinants the elements of which are given in Appendix 6. The form function is given by the expression in equation 5.18, i.e.

$$f_r(\phi) = \left(\frac{2r}{a}\right)^{1/2} e^{-ikr} \sum_{n=0}^{\infty} \varepsilon_n i^n B_n H_n^1(k_1 r \cos\alpha) \cos n\phi,$$

but it must be remembered that in this case the expression for B_n is different.

A computer code to calculate the form function for the special case of a normally incident wave has been implemented in addition to the general case, and it is this simplified code that has been used to compute the majority of the theoretical results seen below.

6.3 Computational Results and Discussion

Examples of the backscattered form function for air filled stainless steel shells insonified at normal incidence are shown in Figure 6.2. The material properties used are shown in Appendix 3. These figures show the form function for b/a values of 0.2, 0.90, 0.95 and 0.99 and illustrate the effect of changing the inner to outer radius ratio (the actual values for b and a are irrelevant). The differences in the form function are caused by the varying contributions of the shell and the fluid column (air) inside the cylinder. In the case of the thick shell (b/a = 0.2) the form function closely resembles that of a solid cylinder (Figure 5.2), and there is little that can be attributed to the air column. As the shell thickness decreases, the form function becomes more complicated as both resonances from the shell and the fluid interior contribute to the backscattered signal. In the case of very thin shells, the cylinder behaves somewhat like a bubble, and the air column gives rise to the tiny spikes visible on an otherwise smoothly varying background.

These spikes are only apparent for very thin air filled shells, and seem to be absent from previously published graphs for elastic shells found in the literature. However the majority of the published calculations have been for an evacuated shell. Where an air filled cylinder has been used, often the step interval has been coarse enough so that these sharp features are not visible (Neubauer, 1987 p110). Maze, Izbicki & Ripoche (1987) and Solomon, Yoo & Überall (1984) noticed these spikes and ascertained that they are given by the resonance behaviour of the interior air column. The use of a vacuum as the interior medium for a hollow cylindrical shell would thus remove these spikes from the presented graphs.

It would be possible to computationally determine the exact position of all of the shell and fluid column resonances by finding the zeros of the determinant R_n (Appendix 6). However, where there is little coupling between the shell and the fluid, the resonances are approximately those of the free vibration of the fluid column and are situated at the points where $J_n'(k_3b) = 0$ (Maze, Izbicki & Ripoche, 1987). Rather than attempt a full solution for the zeros of the determinant it was decided to extract the positions of the resonances from the computation of the form function and compare these positions to the zeros of the Bessel function. The form function was computed at fine intervals (0.0075) over an appropriate ka range, 0 - 10, for a cylinder with $b/a = 0.99$. The ka values at which the spikes occurred could then be read from a data file, and the results are presented in Table 6.1. Due to the finite size of the step interval along the ka axis it is clearly not possible to locate each resonant spike exactly. As it is, an error of one step interval of 0.0075 ka introduces an uncertainty of 0.03 in the measured value of k_3b . The measured values have only been presented for the first 3 partial modes (i.e. 0,1,2) although it would have been possible to go further.

Figure 6.3 illustrates plots of the zero, first and second order partial modes and the total form function. Most of the resonance spikes seen in Table 6.1 are visible in these first three partial modes, although in some cases the small spikes determined from the data file were not big enough to show up clearly in the plots in Figure 6.3. The extra resonances visible on the final form function are due to contributions from higher order partial modes.

The positions (k_1a) of the spikes (Table 6.1: column 2) for a given partial mode (column 1) were extracted from the data file associated with the plots in Figure 6.3. This value must be multiplied by c_1b/c_3a in order to obtain the value of k_3b (column 3). The theoretical values seen in column 4 of Table 6.1 are the zeros of the Bessel function, taken from Abramowitz & Stegun (1965) and which for the purpose of comparison have been rounded to two decimal places. It will be noticed that the computational results presented in column 3 show good general agreement with the theoretical results of column 4, which would appear to confirm their identity as resonances of the air column.

Theoretical predictions for the form function can also be made for an obliquely incident wavefield. Figures 6.4 and 6.5 illustrate results for a steel circular cylindrical shell obliquely insonifed by an incident plane wave. An air filled cylinder has been considered with inner to outer radii ratios of 0.99 (Figure 6.4) and 0.20 (Figure 6.5). The results for normal incidence, $\alpha = 0°$, Figures 6.4a and 6.5a, show good agreement with previously presented results (see Figure 6.2). The form function for an air filled cylinder insonified at an incident angle of 45° are illustrated in Figures 6.4b and 6.5b. These results agree well with those of James (private communication).

Table 6.1 Bessel Function Zeros

Partial Mode	Observed 'k_1a' value	Observed 'k_3b' value	Actual 'k_3b' value	Mode
-	-	-	0.00	(0,1)
0	0.8975	3.81	3.83	(0,2)
0	1.6550	7.01	7.02	(0,3)
0	2.3975	10.14	10.16	(0,4)
0	3.1475	13.31	13.32	(0,5)
0	3.8975	16.48	16.47	(0,6)
0	4.6400	19.62	19.62	(0,7)
0	5.3825	22.76	22.76	(0,8)
0	6.1250	25.90	25.90	(0,9)
0	6.8675	29.04	29.05	(0,10)
1	0.4325	1.83	1.84	(1,1)
1	1.2650	5.35	5.33	(1,2)
1	2.0150	8.52	8.54	(1,3)
1	2.7650	11.70	11.71	(1,4)
1	3.5150	14.86	14.86	(1,5)
1	4.2650	18.03	18.02	(1,6)
1	5.0075	21.17	21.16	(1,7)
1	5.7500	24.32	24.31	(1,8)
1	6.4925	27.46	27.46	(1,9)
2	0.7175	3.04	3.05	(2,1)
2	1.5875	6.71	6.71	(2,2)
2	2.3600	9.98	9.97	(2,3)
2	3.1100	13.15	13.17	(2,4)
2	3.8675	16.35	16.35	(2,5)
2	4.6175	19.53	19.51	(2,6)
2	5.3600	22.67	22.67	(2,7)
2	6.1025	25.81	25.82	(2,8)
2	6.8525	28.98	28.98	(2,9)
-	-	-	32.13	(2,10)
2	8.3450	35.29	35.28	(2,11)

6.4 Experimental Results and Discussion

The experimental technique used to determine the form function for the cylindrical shells has been described in Chapter 2. Backscattered measurements were obtained for two stainless steel cylinders with either air or water as an interior fluid, whilst the angular measurements were obtained for an air filled cylinder.

Figures 6.6, 6.7, 6.8 and 6.9 illustrate the backscattered form function for two stainless steel cylinders immersed in water. Figures 6.6 and 6.7 illustrate the results for a shell with interior fluids of water and air respectively, where the shell has an outer radius (a) of 0.0127m and an inner radius (b) of 0.0124m, giving a ratio b/a of 0.976. The form function was determined at a range of 0.25m in both cases. The results presented in Figures 6.8 and 6.9 are for a shell with a = 0.01905m, b = 0.01867m and b/a = 0.980 measured at a range of 0.30m. The frequency of the pulses used to obtain the experimental data is shown on each of the figures. Measurements were also recorded for the air filled shell with b/a = 0.98 at 30° intervals over the range 0° - 180° and the results are presented in Figures 6.10 - 6.14. The measurements were made at an observation distance of 0.30m and in general the pulses used were based on frequencies of 20kHz, 40kHz and 100kHz, although each diagram is individually labelled. The single plane wave form function is shown as the solid line in all the figures and is a finite range prediction calculated at the appropriate range using the nominal material properties shown in Appendix 3.

The results presented in Figures 6.6 - 6.14 were, for most observation angles, easily reproducible, although there are several exceptions. The results for an air filled cylinder were reproducible to within about 3% with the exception of a small region around about 30°. This region was found to exist approximately 10° either side of 30°, and was described earlier for the case of the solid cylinder (see section 5.4), where it was attributed to an extreme sensitivity to small inaccuracies in the positioning of the cylinder.

Measurements on the water filled shells (Figures 6.6 and 6.8) were less repeatable than their air filled counterparts and the results show a great deal more scatter than the results for the air filled cylinder. For both shells it was difficult to obtain consistent results below a ka value of approximately 2, the reasons for which are not clear. Although it may be that the greater coupling into the interior fluid is revealing a greater susceptibility to positioning and orientation that is not apparent for the air filled shells.

For all the results presented in Figures 6.6 to 6.14 there are significant discrepancies between the single plane wave form function prediction (solid line) and the experimental results. In the backscattering configuration (Figures 6.6 - 6.9) the hydrophone is located between the source and the cylindrical shell. As discussed earlier (section 2.5.4) and observed for spheres and solid cylinders this will have two effects. The first is a lowering of the amplitude of the experimental results, which increases with frequency, and the second is an anomaly due to the resonance of the hydrophone support tube. This is apparent in Figures

6.6 and 6.7 in the ka range 2-3 and multiples can be observed at ka values of approximately 6 and 9 in Figure 6.7. In Figures 6.8 and 6.9 the hydrophone resonance is visible in the ka range 4-5. For both cylinders this corresponds to the frequency range 50 - 60kHz. For the angular scattering results, Figures 6.10 - 6.14, the hydrophone shadowing will have little if any effect but there are still noticeable differences between the experimental data and the single plane wave theoretical prediction.

The differences seen here between the experimental values and the theoretical predictions are almost certainly due to the non-planar nature of incident wavefield as described in the case of the solid cylinder (section 5.4.2). A similar theoretical development, to allow for the plane wave spectrum of the parametric array, could be carried out for the scattering from a cylindrical shell, replacing the expression for the form function in Equation 5.25 by that for the cylindrical shell.

In general, the departures of the experimental results from the theoretical predictions are nearly constant particularly for the air filled shells, exhibiting none of the sharp resonance type features seen for the solid cylinder and few other phenomenon. Hence, due to the constraints of time, it was decided to correct the form function by a geometrical factor to account for the cylindrical spreading introduced by the non-planar nature of the wavefield. This factor is given by $((x'+r')/x')^{1/2}$ where $x' = x_0 - l_T/2$, that is the distance from the centre of the array to the cylinder, and r' is the observation range.

The form function, modified to allow for a geometrical spreading factor, f_{geo}, is plotted as a broken line in Figures 6.6 to 6.14. In all the results presented here this modified theory shows considerably better agreement with the experimental data than the single plane wave form function. Given that this geometrical correction does not account for any additional resonances introduced by the obliquely incident components of the wavefield, the comparison between experiment and theory is remarkably good.

As discussed above the hydrophone shadowing and the resonance of the support tube will largely account for the slight lowering of the experimental data with respect to the theory seen in Figures 6.7 and 6.9. One would also expect to see similar effects in Figures 6.6 and 6.8, the backscattered measurements from water filled shells. However this does not appear to be the case. Although the modified theory in general predicts the amplitude levels, there are noticeable discrepancies, especially in Figure 6.8. Modifying the form function to account for the plane wave spectrum (f_{pws}) may account for some of these differences, but clearly there is a need for further investigation, both theoretical and experimental.

The angular scattering results from an air filled shell, Figures 6.10 to 6.14, agree reasonably well with the modified form function (f_{geo}), and are a considerable improvement on the usual form function. The exception to this is in Figure 6.10 where there are significant discrepancies. Again modification of the form function to allow for the plane wave spectrum of the parametric array may partially account for these effects. However, close examination

of Figure 6.10 shows that the minima in the experimental result are smoothed out. It may be that too short a window was used when processing the signal, resulting in a loss of detail and the introduction of artifacts onto the spectrum. This obviously requires further investigation in order to resolve these differences.

6.5 Summary

Experimental results have been presented for the form function for stainless steel cylindrical shells when filled with either air or water. Results have been obtained for a normally incident wavefield at a range of observation angles, including backscatter. Comparison of the experimental results with the single plane wave form function reveal significant disparities in amplitude. A geometric correction to the form function, proposed in Chapter 5, shows a significant improvement over the usual form function, and in general the agreement is good. There are discrepancies between this modified theory and the experimental results in the backscatter direction due to the effects of hydrophone shadowing and the resonance of the hydrophone support tube. In addition the results for the water filled shells and certain of the angular measurements exhibit features which need further clarification.

Figure 6.1 Diagram illustrating the coordinate system and the scattering of a plane wave from a circular cylindrical shell.

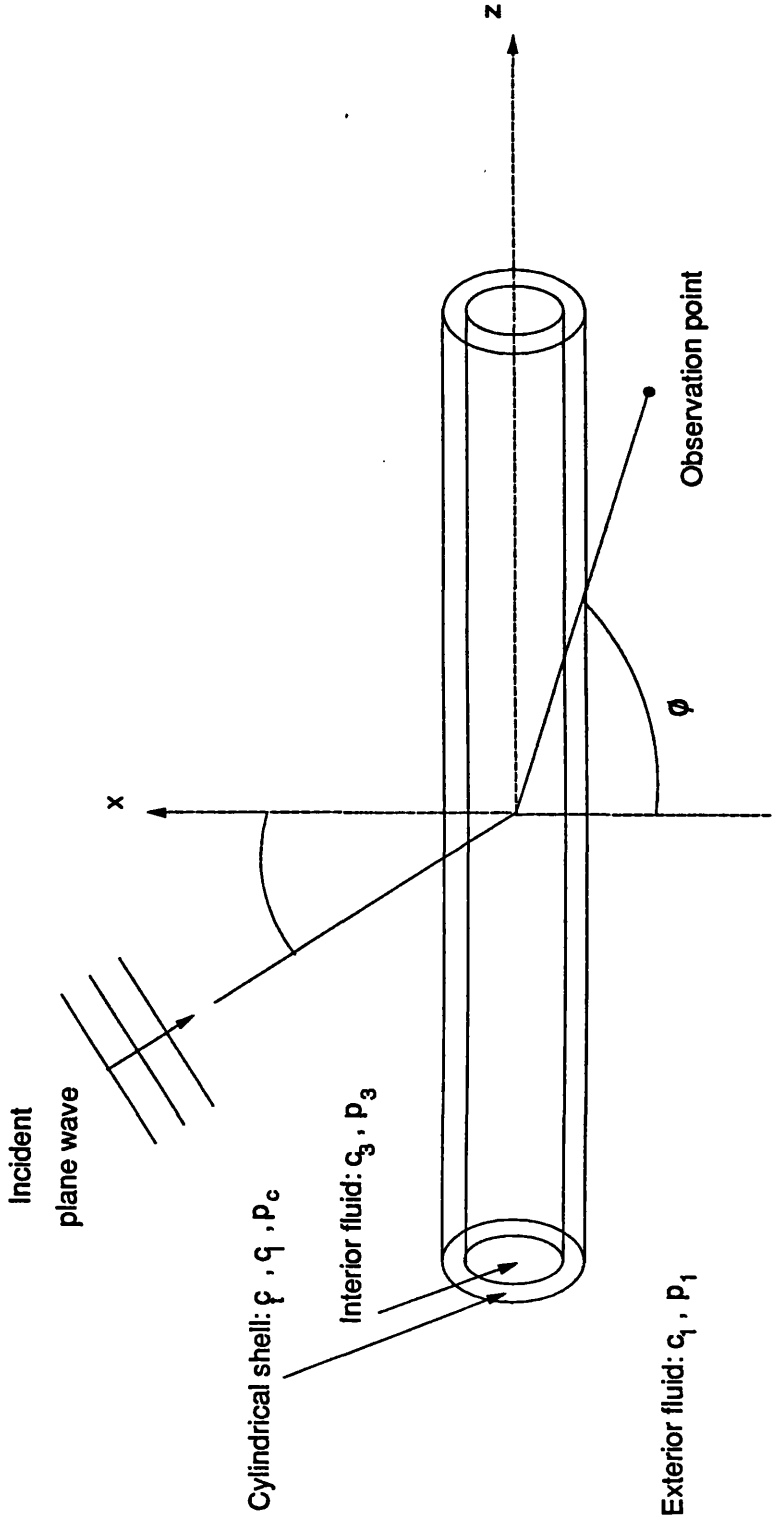

Figure 6.2 Theoretical backscattered form function for steel shells, insonified at normal incidence and with varying inner to outer radius ratios b/a.

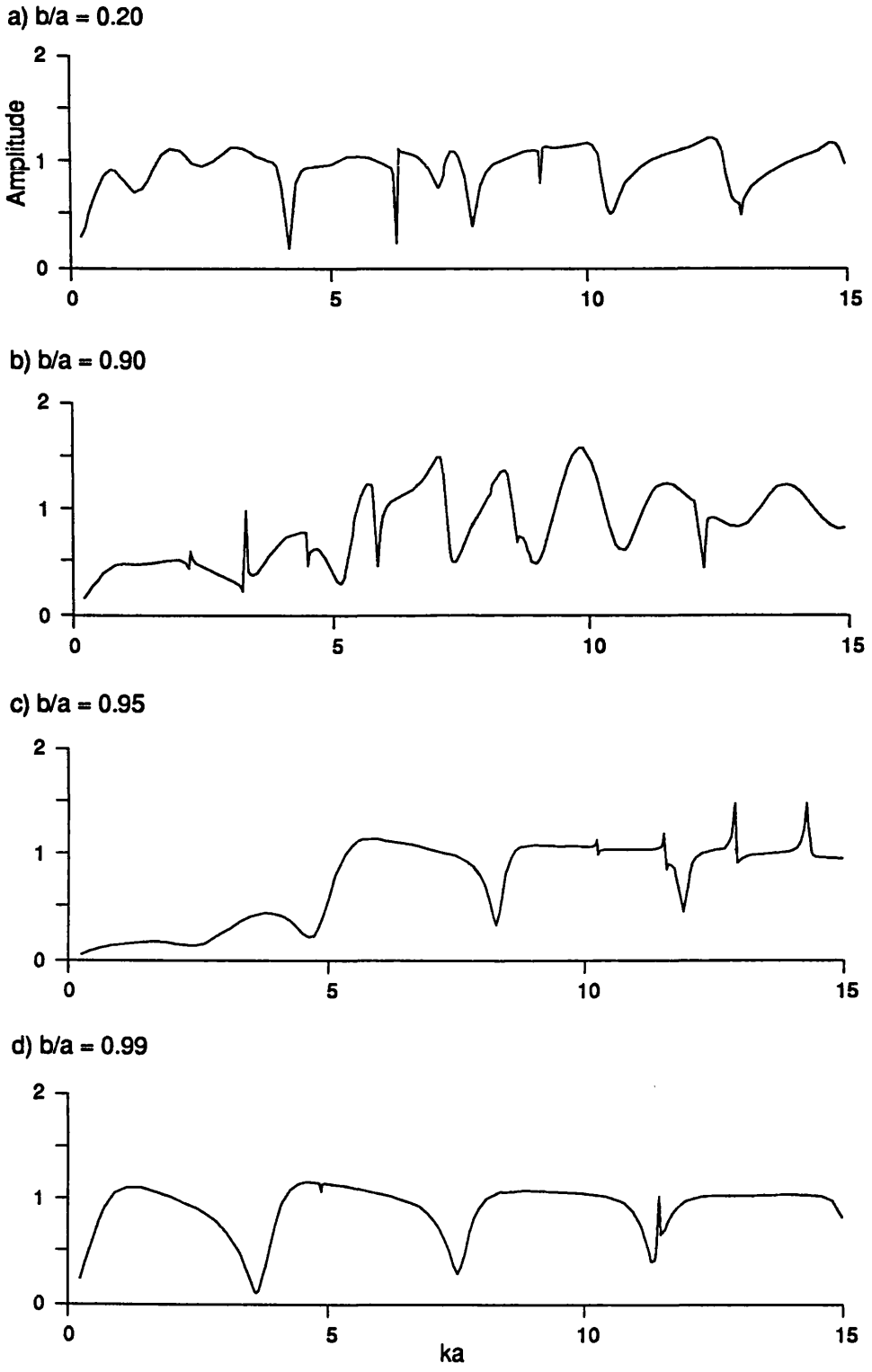

Figure 6.3 Form function and first three partial modes for an air filled steel cylinder with $b/a = 0.99$.

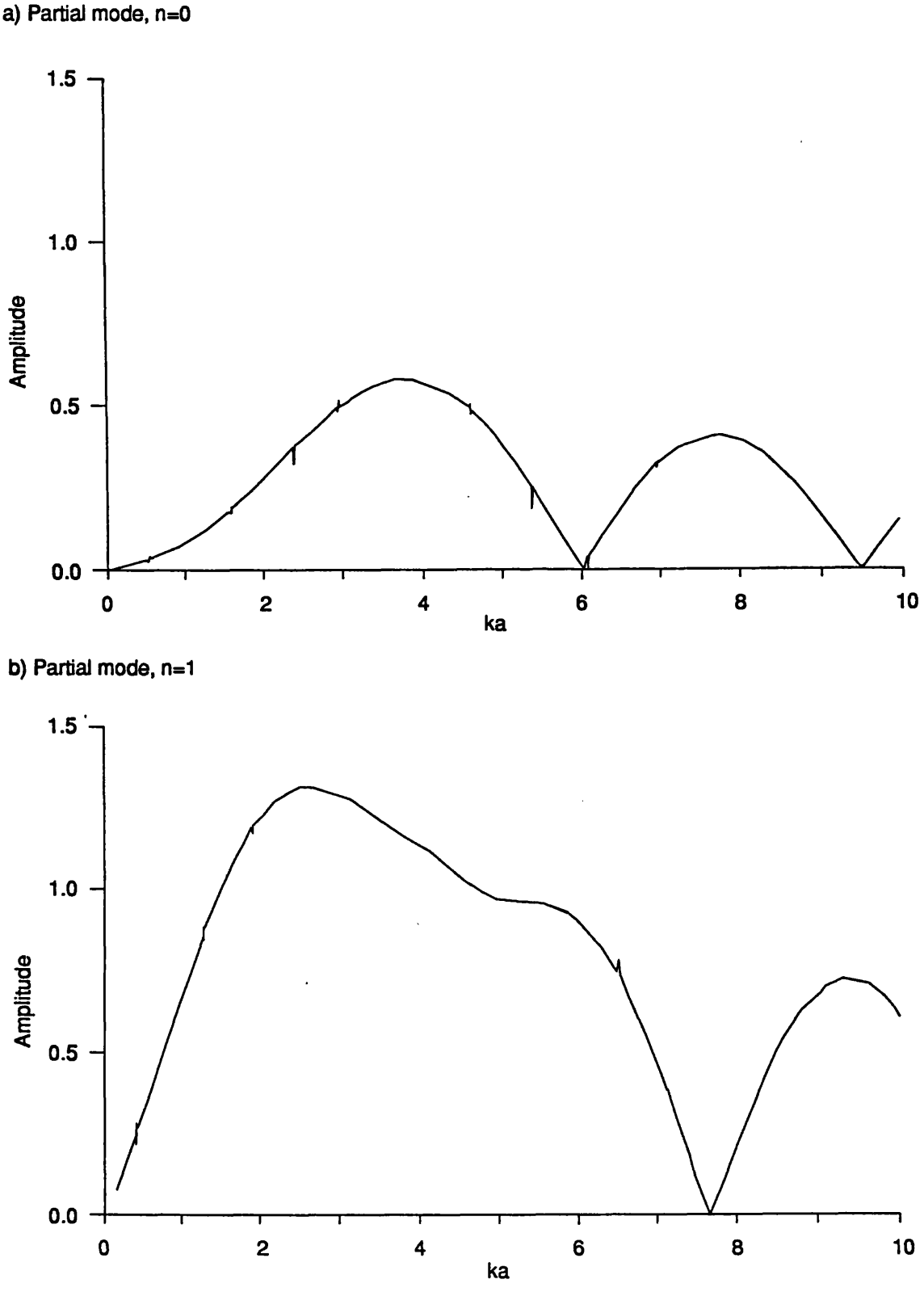

c) Partial mode, n=2

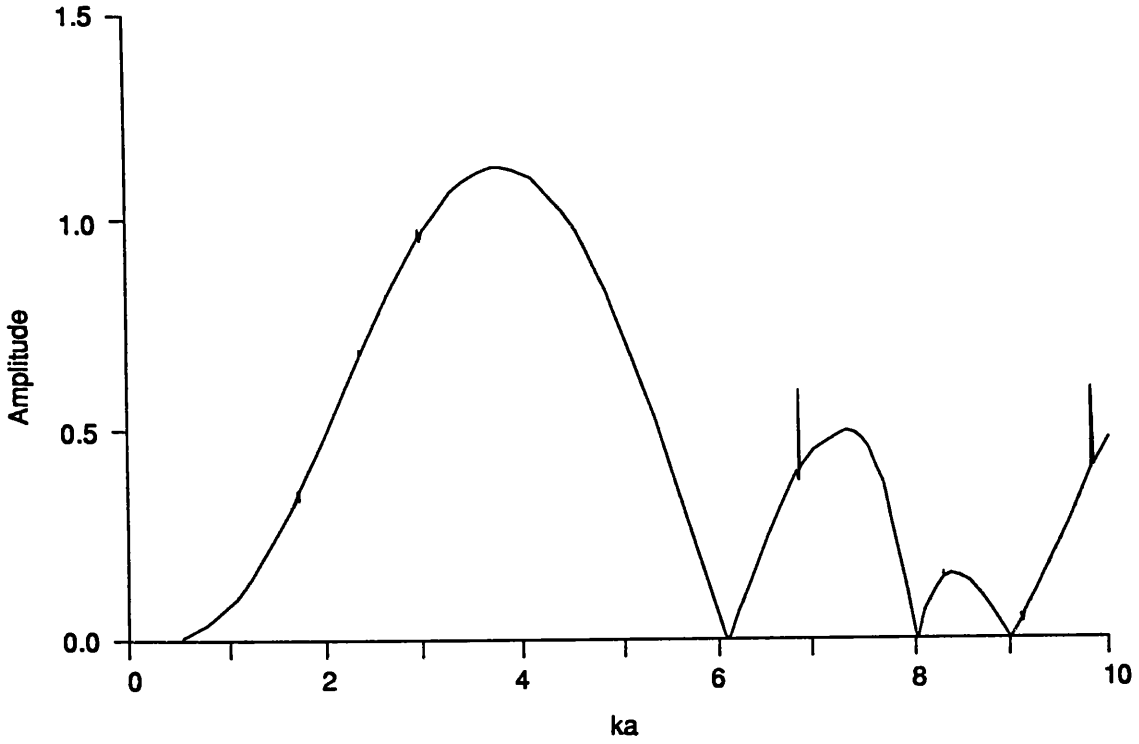

d) Total form function

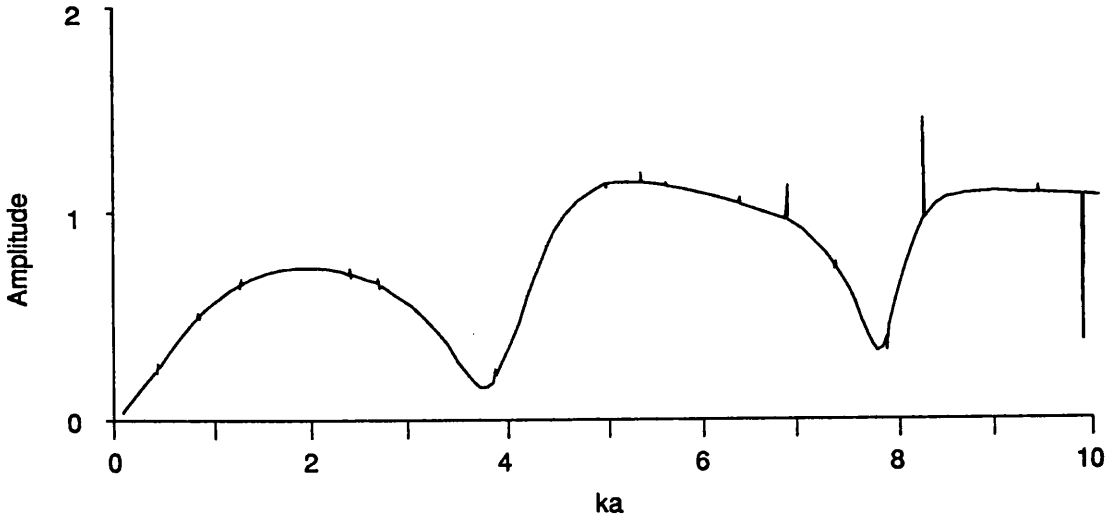

Figure 6.4 Form function for a steel cylindrical shell with $b/a = 0.99$ when obliquely insonified.

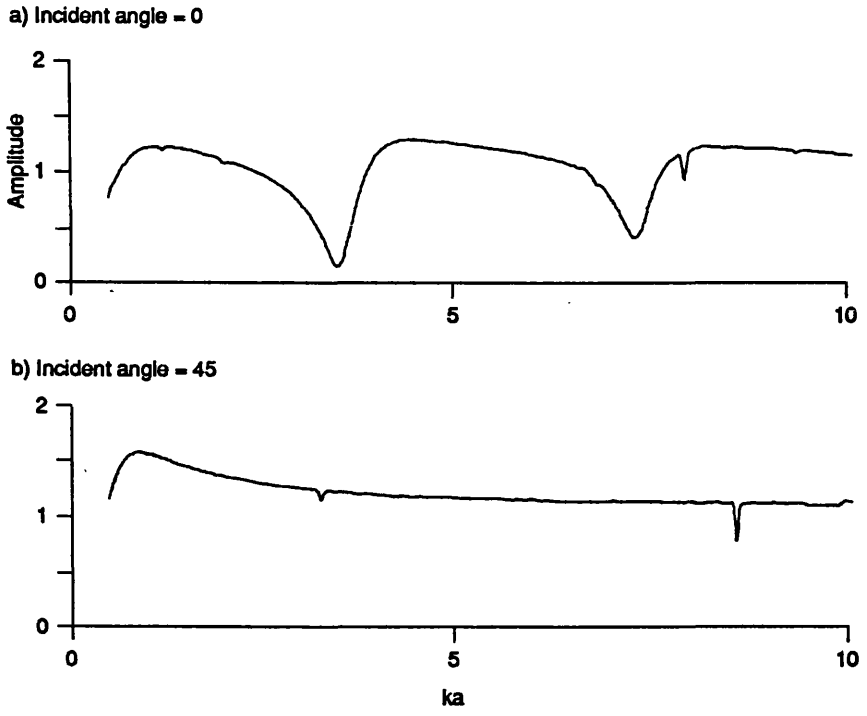

Figure 6.5 Form function for a steel cylindrical shell with b/a =0.20 when obliquely insonified.

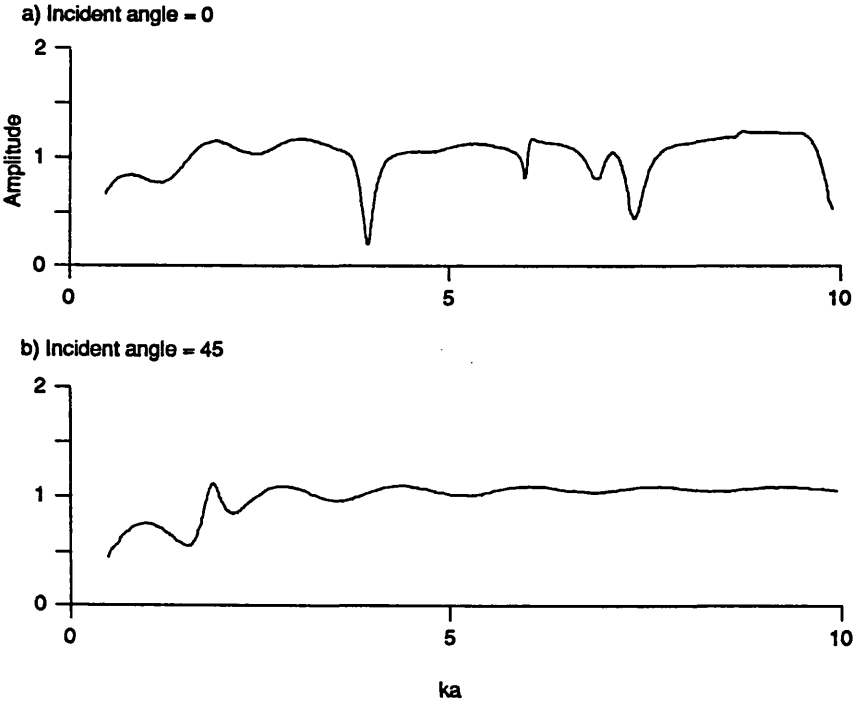

Figure 6.6 Backscattered form function for an water filled steel shell with $b/a = 0.976$.

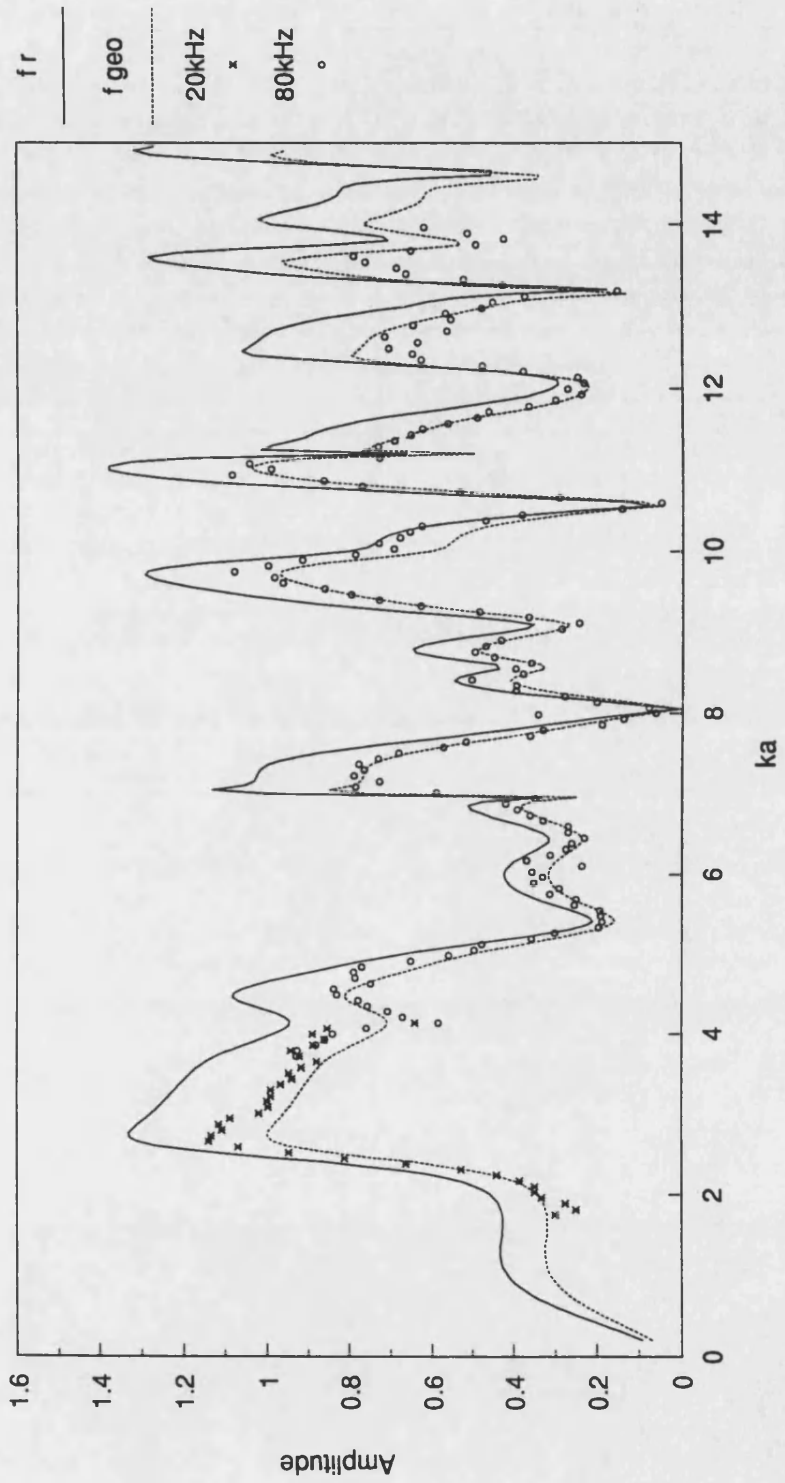

Figure 6.7 Backscattered form function for an air filled steel shell with $b/a = 0.976$.

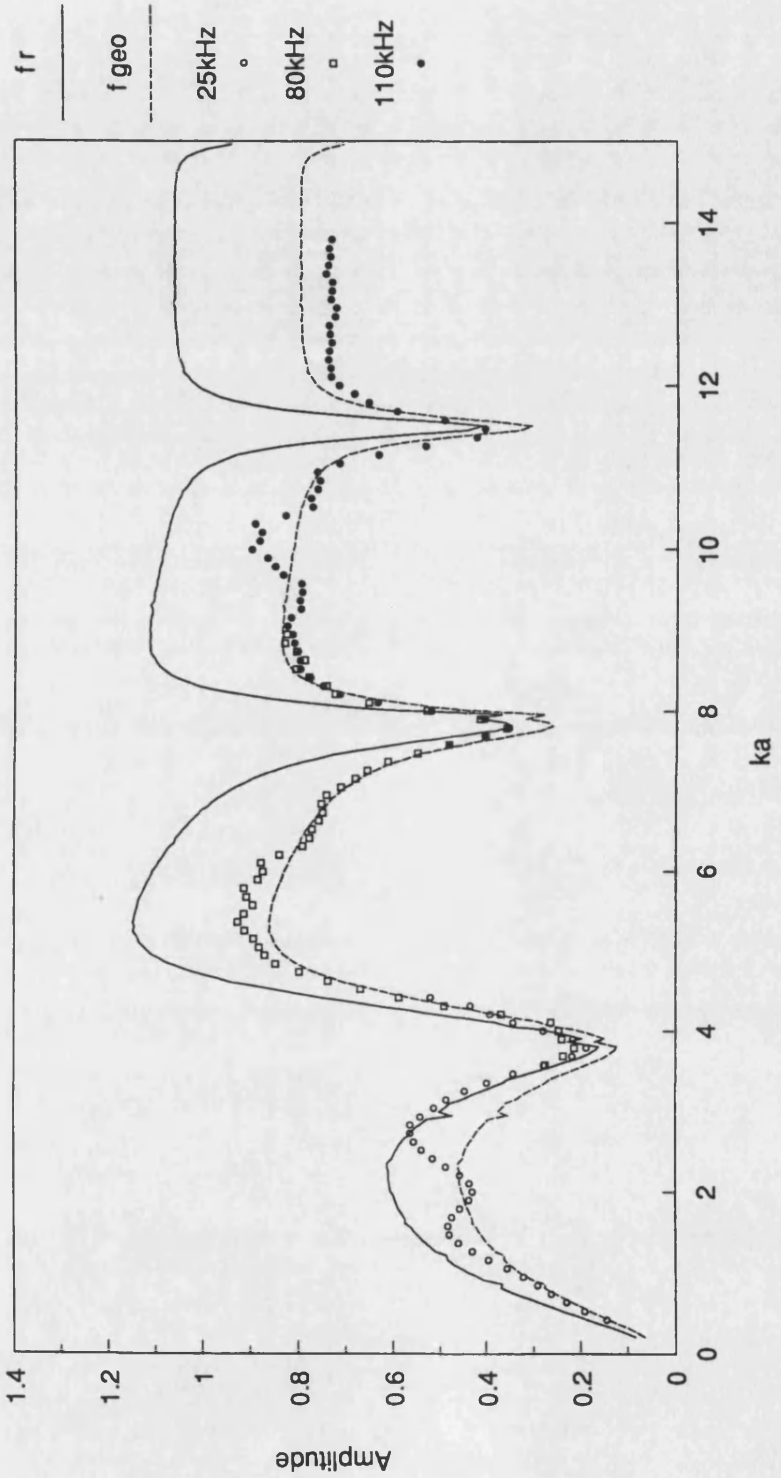

Figure 6.8 Backscattered form function for an water filled steel shell with $b/a = 0.98$.

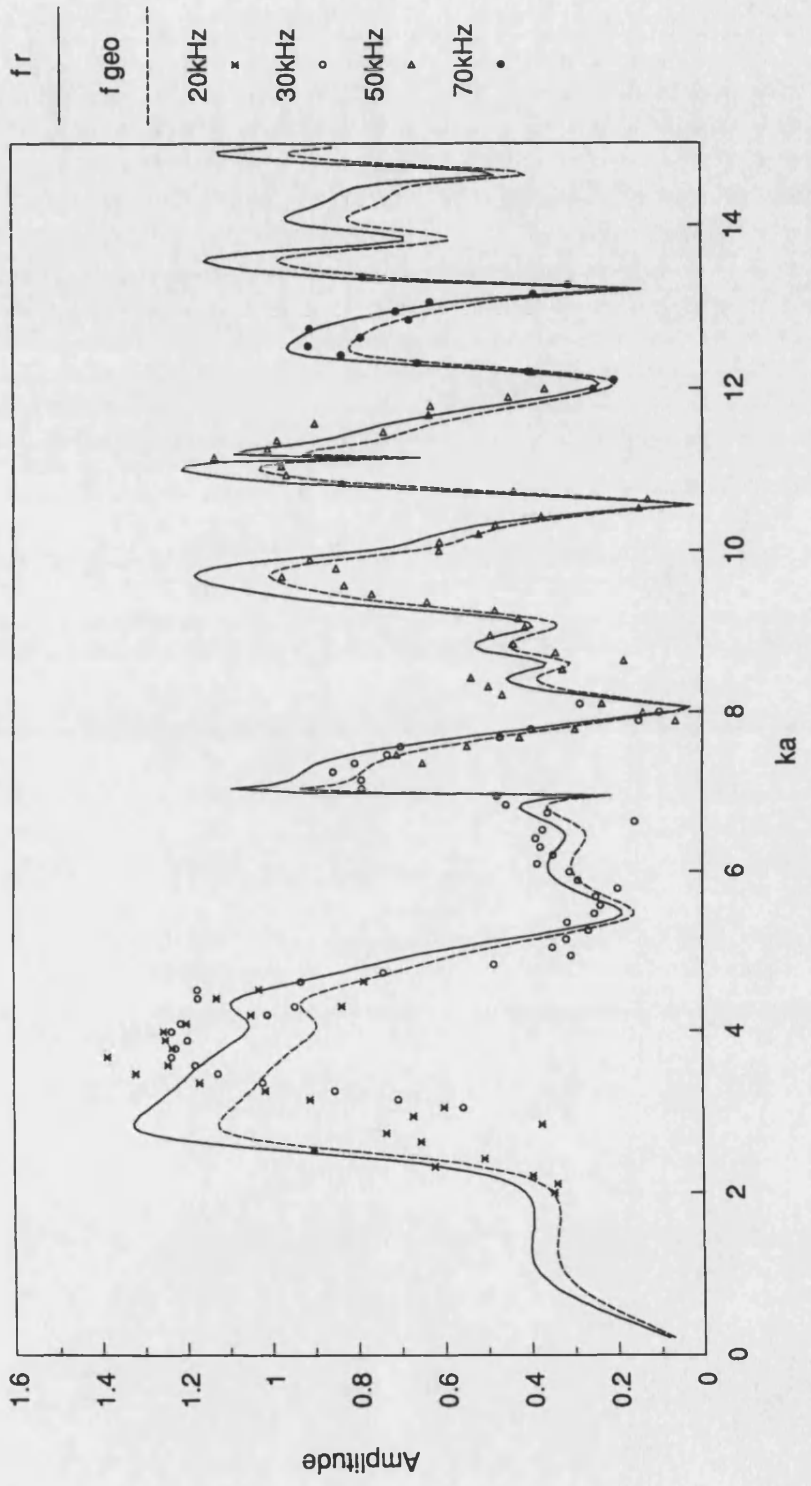

Figure 6.9 Backscattered form function for an air filled steel shell with $b/a = 0.98$.

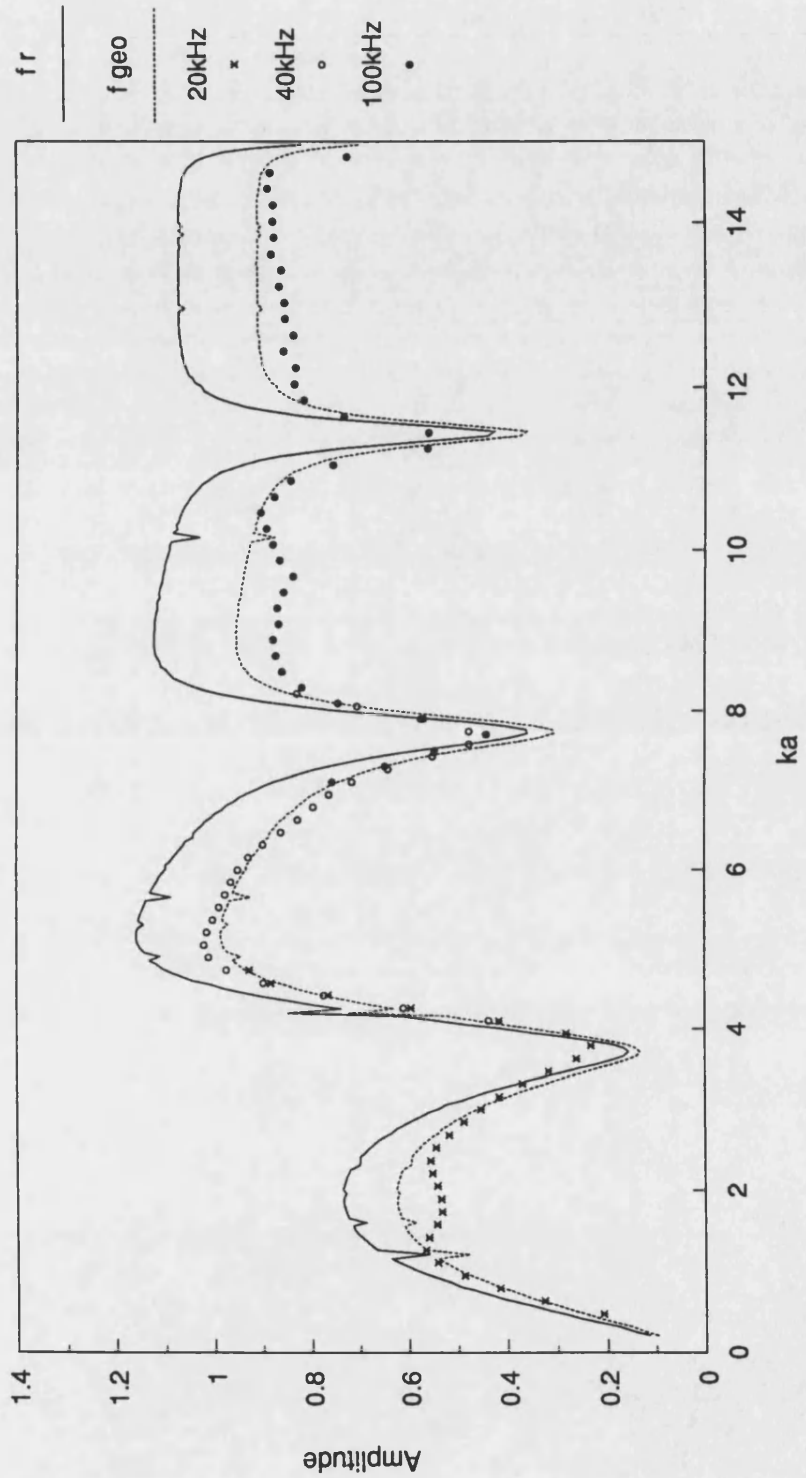

Figure 6.10 Form function for an air filled steel shell with $b/a = 0.98$ and $\phi = 150°$.

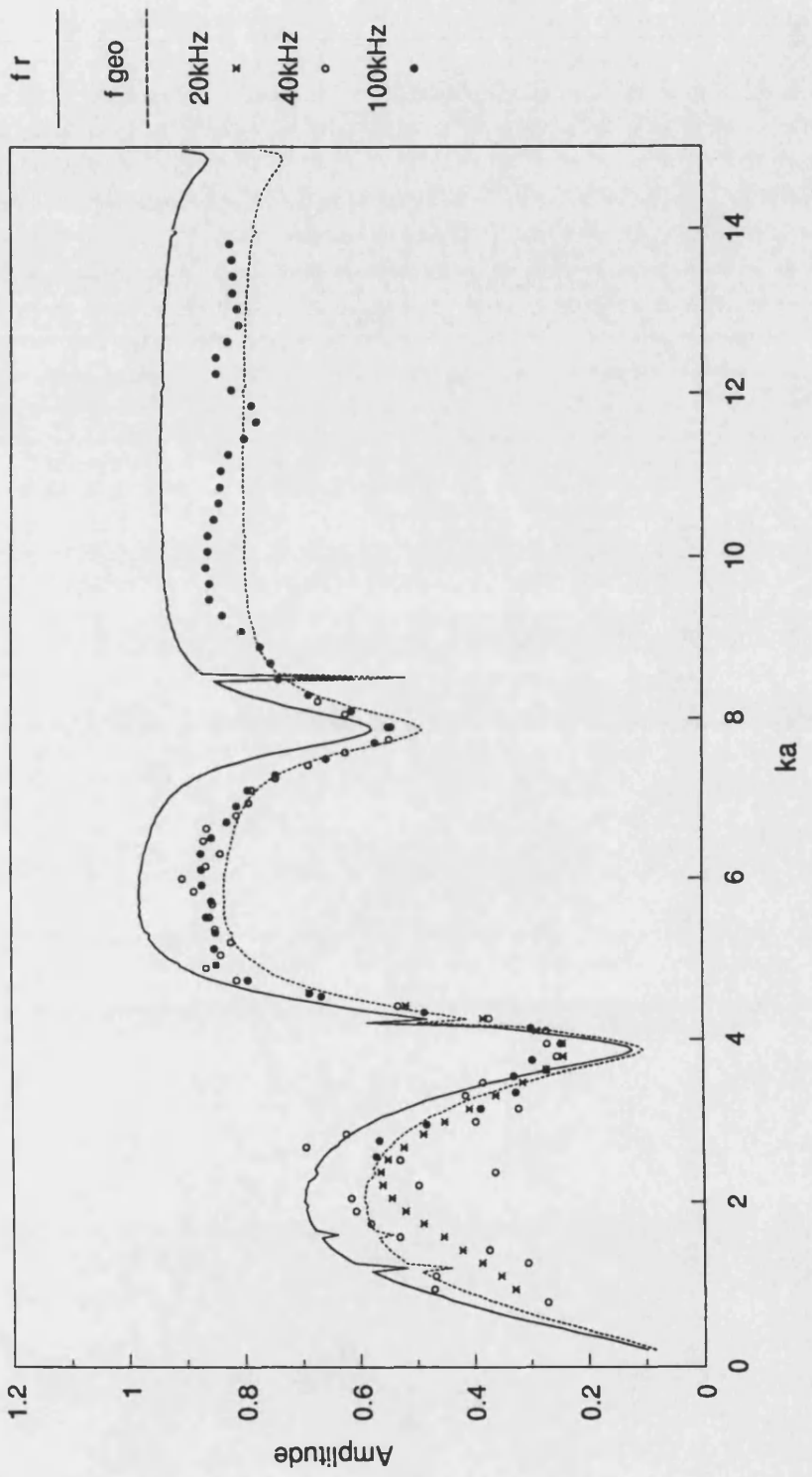

Figure 6.11 Form function for an air filled steel shell with $b/a = 0.98$ and $\phi = 120°$.

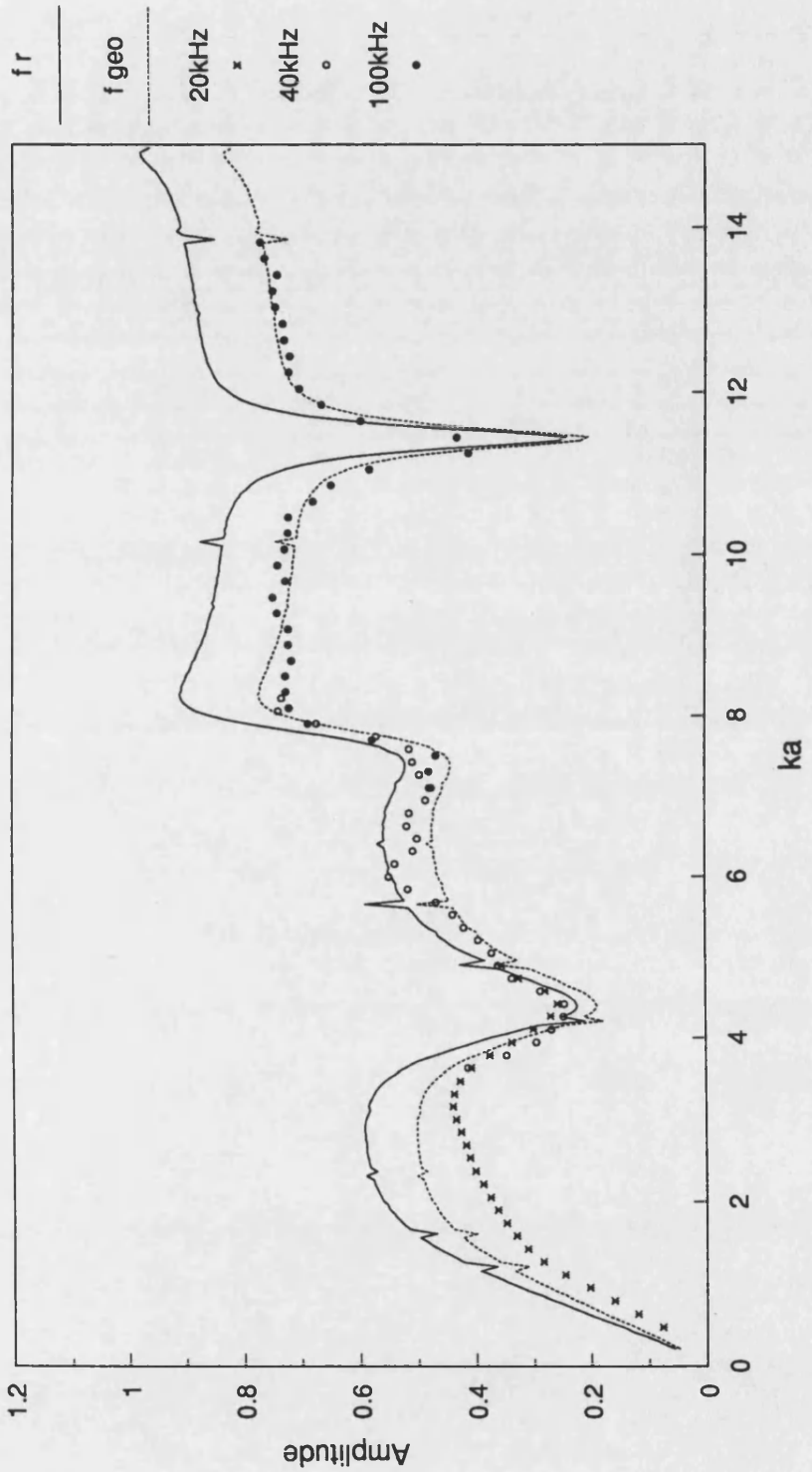

Figure 6.12 Form function for an air filled steel shell with $b/a = 0.98$ and $\phi = 90°$.

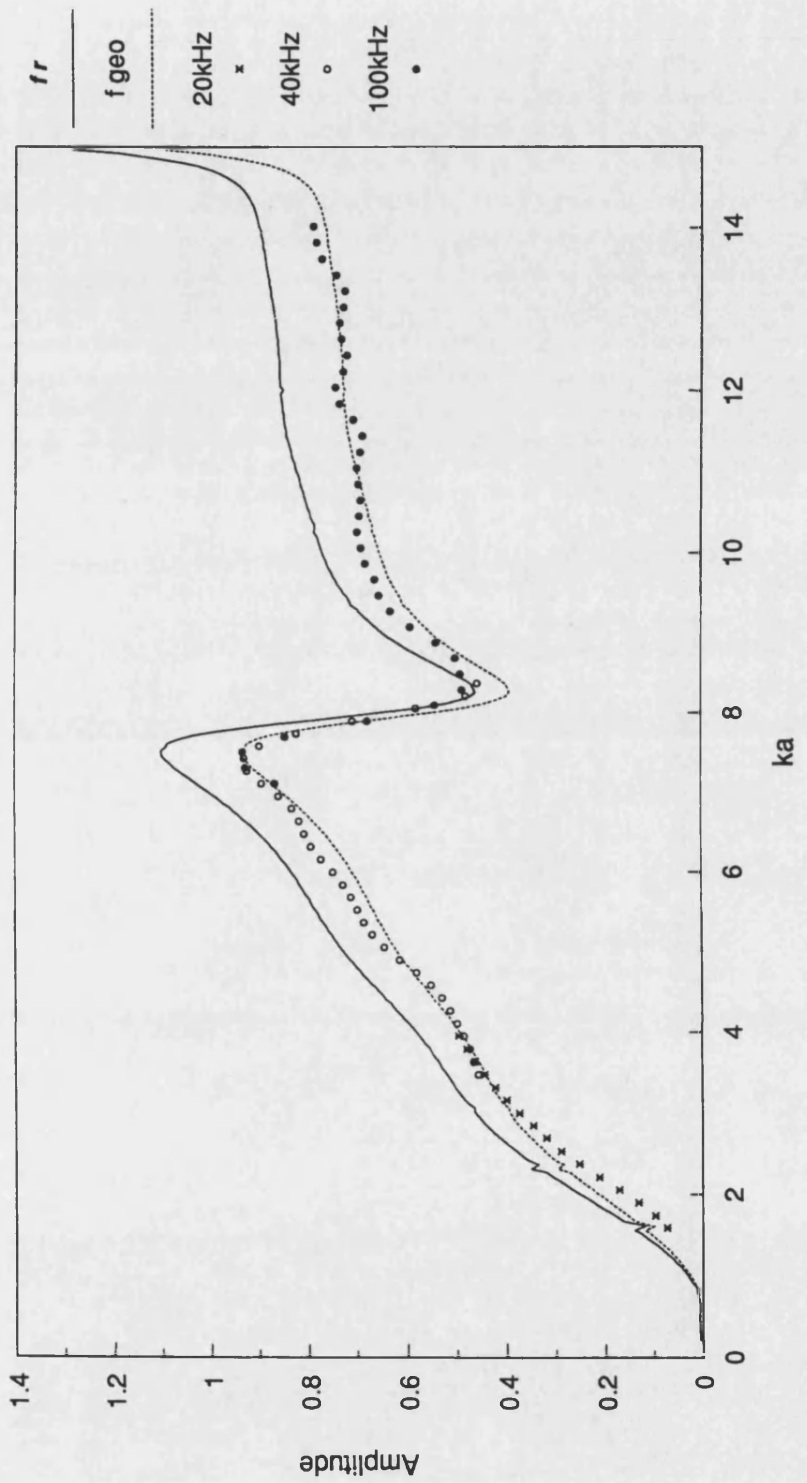

Figure 6.13 Form function for an air filled steel shell with $b/a = 0.98$ and $\phi = 60°$.

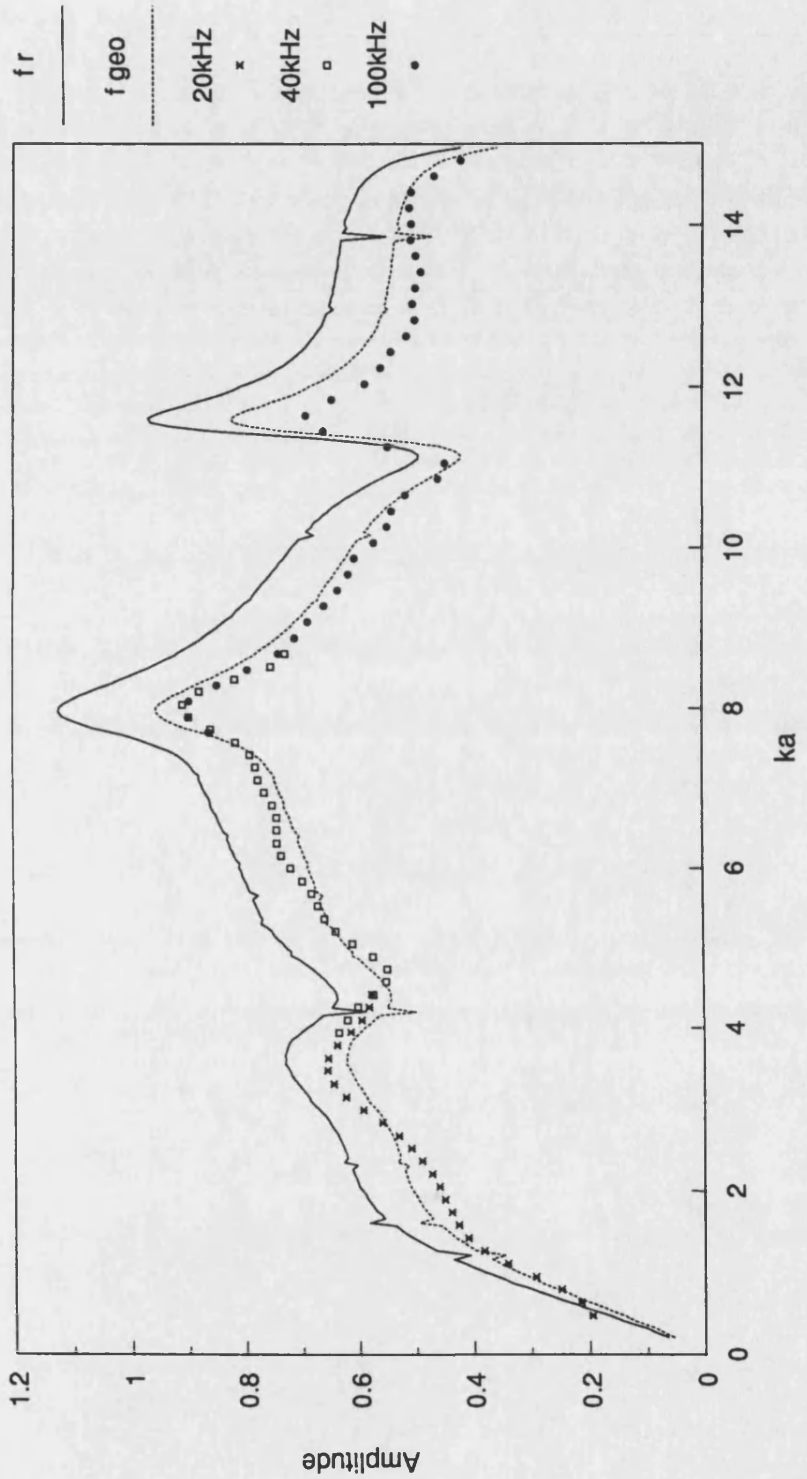

Figure 6.14 Form function for an air filled steel shell with $b/a = 0.98$ and $\phi = 0°$.

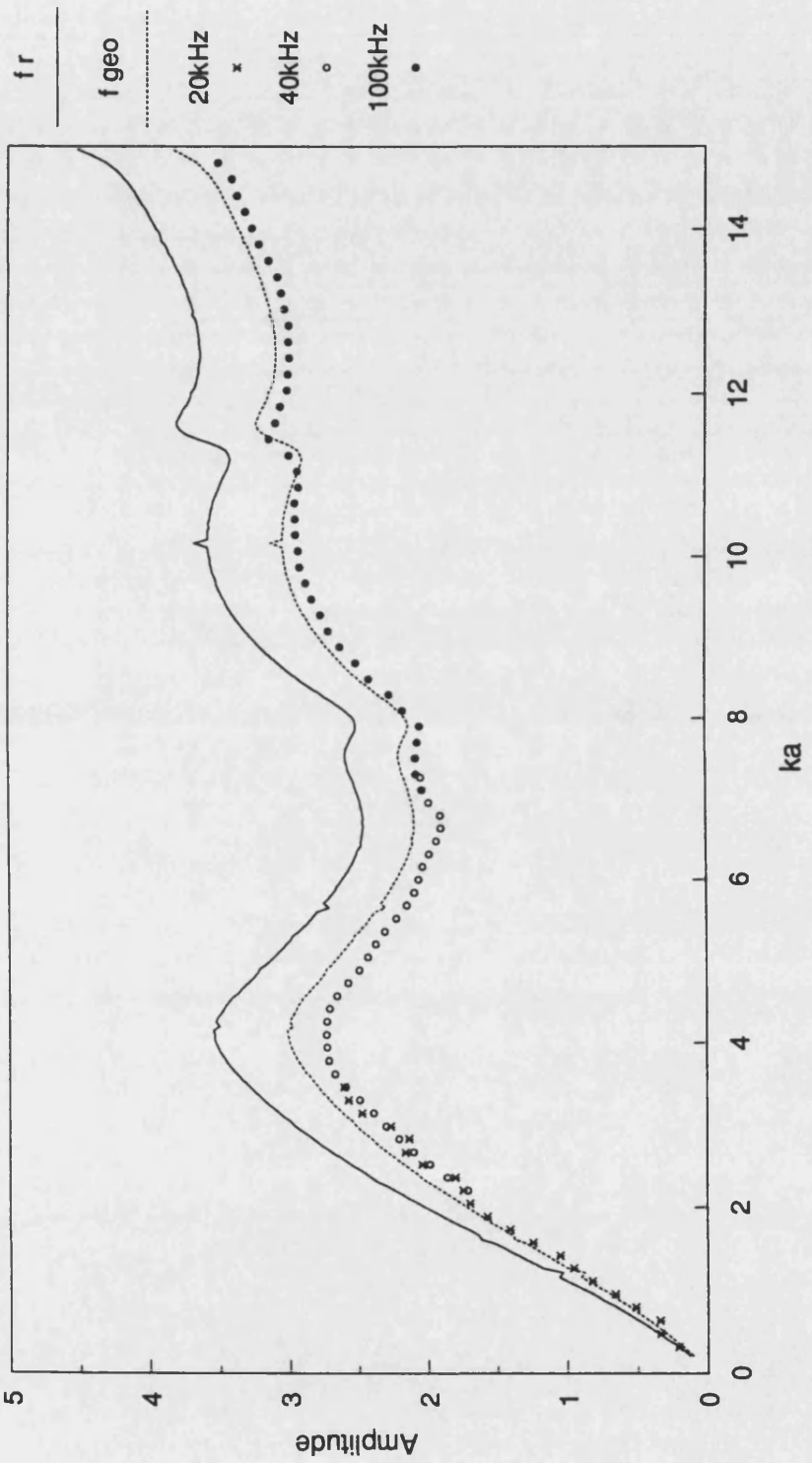

7 Resonances in the fluid column of a cylindrical shell

7.1 Introduction

The scattering of acoustic waves from discrete, submerged objects is well documented, with results of both theoretical and experimental investigations available for many scattering objects and geometries (see review articles by, for example, Flax, Gaunaurd & Überall, 1981; Neubauer, 1987; Gespa, 1987). For the case of fluid filled cylindrical shells, most of the existing work has been concerned with the scattered signal and its frequency spectrum which contains information about the resonant behaviour of the shell and the interior fluid. Maze, Izbicki & Ripoche (1986) experimentally obtained the scattered signal's spectrum of a thin cylindrical shell and were able to identify many of the resonances as those of the fluid column. Others were found to be due to the resonances of the cylinder, while a further series were thought to be due to Stoneley waves propagating on the surface of the shell. They also presented a mathematical treatment for the free vibration of the fluid column based on the work of Gazis (1959).

In this Chapter we are interested in the resonance behaviour of the interior fluid rather than the scattered field, which has received only limited attention in the literature. An exact theoretical solution is presented for the pressure distribution inside an elastic, fluid filled, cylindrical shell when insonified at normal incidence by a plane wave. (It has recently come to our attention that the pressure field inside an air filled steel cylindrical shell immersed in water has been calculated and presented by Gaunaurd & Werby (1989) at ka values of 5 and 7 for varying b/a ratios.) From the pressure distribution we are able to compute the optical intensity distribution which would be seen if the cylinder was observed using a Schlieren technique. This is particularly informative under resonance conditions where the acoustic standing wave pattern is seen as a pattern of bright and dark regions in the Schlieren image. From the experimental images of the standing wave patterns in the fluid column obtained with the Schlieren system, we obtain a direct comparison with the theoretical predictions.

To our knowledge, a Schlieren image of the fluid column resonance appears only once in the published literature (Bergmann, 1949), although several authors have used Schlieren techniques to visualize the scattered field outside cylinders and cylindrical shells. Most notably Neubauer has studied the scattered field and used Schlieren images to identify various waves and wavepaths (Neubauer, 1968; Neubauer, 1969; Neubauer & Dragonette, 1970). More recently Maze & Ripoche (1983b) investigated how a cylinder stores and releases energy when insonified at a resonance frequency, confirming acoustic measurements with Schlieren observations.

Other authors have shown that elastic resonances may be observed in optically transparent solid cylinders using a photoelastic optical technique (e.g. Bergmann, 1949; Dardy, Flax, Gaumond, Subrahmanyam, Ashrafi, Raju & Überall, 1987).

7.2 Theory

The theory for the scattering of a plane wave from a cylindrical shell is well developed and has been presented in section 6.2. The development presented here is similar but in this case we are interested in obtaining an explicit expression for the pressure in the interior fluid. This pressure distribution can then be used to give us an approximation to the optical intensity distribution in the Schlieren image, which can be directly compared to experimental results.

The cylindrical shell is identical to that described in section 6.2 and illustrated in Figure 6.1. In the outer fluid, the incoming plane wave is normally incident to the cylinder and can be represented by,

$$p_i = p_0 e^{-i\omega t} \sum_{n=-\infty}^{\infty} \varepsilon_n i^n J_n(k_1 r)\cos n\phi \tag{7.1}$$

Similarly the scattered wave, p_{sc}, and the pressure field in the inner fluid, p_f, can be written,

$$p_{sc} = p_0 e^{-i\omega t} \sum_{n=-\infty}^{\infty} \varepsilon_n i^n B_n H_n^1(k_1 r)\cos n\phi \tag{7.2}$$

$$p_f = p_0 e^{-i\omega t} \sum_{n=-\infty}^{\infty} \varepsilon_n i^n A_n J_n(k_3 r)\cos n\phi \tag{7.3}$$

where

$\varepsilon_n = 2$ for $n > 0$ and 1 for $n = 0$,

$H_n^1(ka)$ and $J_n(ka)$ are Hankel and Bessel functions,

B_n and A_n are scattering coefficients, and where the summation is over 'n' partial modes. In this case we are interested in obtaining an expression for A_n rather than B_n.

Within the cylindrical shell the displacement $\underline{u}$ can be represented in terms of a scalar potential (ψ) and a vector potential ($\underline{A}$) in the following form,

$$\underline{u} = -\nabla\psi + \nabla \wedge \underline{A} \quad .$$

For a normally incident wave, it can be shown that the potentials simplify from those in section 6.2 to,

$$\psi = (C_n J_n(k_l r) + D_n Y_n(k_l r))\cos n\phi \quad ,$$

$$A_z = (E_n J_n(k_t r) + F_n Y_n(k_t r))\cos n\phi \quad ,$$

$$A_r = 0 \quad ,$$

$$A_\phi = 0 \quad .$$

In order to evaluate A_n it is necessary to apply the following boundary conditions at the outer and inner surfaces of the cylinder, a and b respectively.

$$u_i + u_{sc} = u_r \qquad \text{at } r = a$$

$$u_f = u_r \qquad \text{at } r = b$$

$$p_i + p_{sc} = -\tau_{rr} \qquad \text{at } r = a$$

$$p_f = -\tau_{rr} \qquad \text{at } r = b$$

and

$$\tau_{r\phi} = 0 \qquad \text{at } r = a \text{ and } r = b$$

where $u_{i,sc}$ is the displacement due to the incident or scattered wave in the fluid and the stress relations have been given earlier (section 5.2). This results in a series of six simultaneous equations involving $A_n, B_n, C_n, D_n, E_n, F_n$ which can be solved in matrix formulation using Cramer's rule to give an expression for A_n. The elements of the two (6x6) determinants which make up A_n are listed in Appendix 7. The acoustic pressure in the inner fluid can then be evaluated using equation (7.3).

In a Schlieren system, an optical beam passes through this pressure field at normal incidence. Under Raman-Nath conditions (i.e. low amplitude acoustic pressures) it is assumed that the phase but not the amplitude of the optical wave is affected by the pressure variations in the fluid. From Figure 7.1 it may be seen that after passing through the acoustic field, the optical beam is brought to a focus at the spatial filter plane. At this point a diffraction pattern is formed which corresponds to the 'phase grating' produced by the acoustic field. In order to visualise this field an amplitude filter is introduced which removes the zero order of the diffraction pattern. The light from the remaining orders then combines to form an image of the acoustic field which is observed using a video camera. A theoretical treatment of this process has been presented in a previous report for 1-dimensional plane acoustic waves (Knapp, Jan 1988) in which it was shown that for zero order filtering at low pressure levels, the optical intensity distribution in the final Schlieren image is proportional to the square of the pressure distribution in the acoustic field. This result also applies to low amplitude acoustic standing waves and so in this study we compare the experimental Schlieren images with contour plots of the square of the pressure distribution evaluated using equation (7.3).

A full, exact analysis of the optical intensity distribution can be considered, and this is presented in Appendix 8. It was not implemented during the course of this study, but subsequent implementation (Chinnery, 1990) has shown that using the approximation that the optical intensity distribution in the Schlieren system is proportional to the square of the acoustic pressure is valid at low pressures.

7.3 Results and Discussion

Using the principles of the Resonance Scattering Theory (Flax, Dragonette & Überall, 1978) it is possible to identify resonances of the shell and fluid system which can be classified into families, characterised by the bandwidth, amplitude, wave speed etc.. The theoretical locations of these resonances for a water filled brass cylindrical shell immersed in water, are shown in Figure 7.2 for ka values up to 45 and for the first 35 partial modes (n). The cylinder has an inner radius (b) of 0.00825m and an outer radius (a) of 0.0095m, giving an inner to outer radius ratio (b/a) of 0.868. From Figure 7.2 it is possible to discern several distinct series or families of resonances. To aid identification these have been labelled with three symbols, o for type A resonances, • for type B resonances and * for type C resonances.

The type A resonances shown in Figure 7.2 can be shown to be those of the fluid column within the cylinder. A resonance of the fluid column occurs when a standing wave pattern is created in the fluid, and under these conditions one is able to identify '$2n$' acoustic antinodes or 'n' wavelengths around the cylinder circumference. It is also possible to identify 'm' acoustic antinodes across the radius of the cylinder and we have chosen to denote the fluid column resonances shown here by the notation (n,m). Figures 7.3, 7.4 and 7.5 show the (n,2), (n,3), and (n,4) resonances for n equal to 2, 3 and 4 respectively. The other types of resonances discussed in this report have only been assigned an 'n' value. In the literature the notation (n,l) is often used, where n is the same as above but where 'l' includes all the resonances present for a given 'n', whatever their nature, and hence is not equivalent to the 'm' value used here.

The photographs shown in Figures 7.3, 7.4 and 7.5 were obtained with the system represented in Figure 7.1, based on the preliminary Schlieren system described by Knapp (June 1987). The images were obtained using zero order filtering in the spatial filter plane with a stop size of 200μm. It has been shown (Bucaro, Flax, Dardy and Moore, 1976; Knapp, May 1988, Aug 1988) that for a given filtering arrangement the appearance of the image will change as the acoustic pressure level increases. For ease of comparison with the theoretical results we have chosen to work in the pressure region for which the bright areas in the Schlieren image represent standing wave antinodes of the acoustic field (i.e. two bright regions per wavelength). For the present system this means using pressures below 25kPa where only one or two diffraction side orders are produced in the spatial filter plane. This corresponds to v values below 2.3 where v, known as the Raman-Nath parameter, is proportional to pressure and represents the peak phase change in the optical wave as it passes through the acoustic field.

For acoustic frequencies below 250kHz the separation of the diffraction orders in the spatial filter plane will be less than 200μm. Thus a stop of this size will partly block the first side orders as well as the zero order, removing some information about the acoustic field. The effect of this can be seen in Figures 7.3 and 7.4 where the resonances labelled

(2,2) and (3,2) are not seen as clearly as those occurring above 250kHz.

The contour plots also shown in Figures 7.3, 7.4 and 7.5 were obtained from the theoretical computations of the square of the pressure distribution. These results were computed using nominal velocities from Kaye & Laby (1986), $c_l = 4372\text{ms}^{-1}$, $c_t = 2100\text{ms}^{-1}$, and measured densities $\rho_c = 8485\text{kgm}^{-3}$, $\rho_1 = \rho_3 = 998\text{kgm}^{-3}$, with $c_1 = c_3 = 1460\text{ms}^{-1}$, corresponding to a water temperature in the Schlieren tank of 13.9°C. Each contour plot has been drawn so that the pressure squared range is represented by seven equally spaced contours. The agreement with the Schlieren images is very good, including the duplication of slight asymmetry in the patterns, visible, for example, in the (2,2) resonance shown in Figure 7.3.

Not only does the Schlieren system enable visualisation of the resonances, it also enables the frequencies at which they occur to be located accurately. It is possible to compare the frequency values for the resonances due to the fluid column (Table 7.1) with predicted values. Column 1 shows the identity of the resonance (see Figures 7.3, 7.4 and 7.5) given in terms of n,m. The frequency and resultant kb value experimentally observed with the Schlieren system are shown in columns 2 and 3 respectively. Column 4 lists the kb value for the theoretical contour plots, that is the kb value for which the maximum pressure is seen in the backscattered form function. The data presented in columns 3 and 4 show excellent agreement for the (n,3) and (n,4) resonances where the agreement is within 0.1% (i.e. 0.3kHz). However the experimentally observed kb values for the lower frequency resonances, namely (2,2), (3,2), (4,2) are noticeably higher than the predicted values by up to 1%. The largest source of experimental error in the measured frequency is due to temperature drift in the Schlieren water tank, although this is unlikely to only affect the (n,2) resonances. The reason for the discrepancy in the (n,2) resonances is not fully understood.

The final column shows the positions of the resonances (kb) of the free vibration of the fluid column and can be determined from the zeros of the Bessel function $J_n'(k_3b)$ (Abramowitz & Stegun, 1965 p411). The close agreement between these values and the theoretical kb values from the form function confirms the identification of these resonances as those of the fluid column, and indicates the extent to which the resonances are perturbed by the finite impedance of the shell.

Table 7.1 Comparison of experimental and theoretical *kb* values for fluid column resonances

fluid column resonance	f_{obs} Schlieren	kb_{obs} Schlieren	*kb* pressure distribution	*kb* free vibration
2,2	194.1	6.89	6.864	6.706
2,3	282.8	10.04	10.049	9.969
2,4	372.2	13.21	13.223	13.170
3,2	232.1	8.24	8.192	8.015
3,3	321.3	11.41	11.418	11.345
3,4	411.7	14.62	14.633	14.585
4,2	261.4	9.28	9.195	9.282
4,3	358.8	12.74	12.750	12.681
4,4	450.4	16.00	16.006	15.964

In addition to the type A resonances of the fluid column there are two other series visible in Figure 7.2. The type B resonances are due to excitations in the material of the shell, and it is possible to identify these resonances by the effect they have on the inner fluid. Figure 7.6 shows the Schlieren image and the associated contour plot for the first third order ($n = 3$) shell resonance. The pattern seen is quite similar to that for the (3,2) fluid column resonance shown in Figure 7.4, although closer inspection will reveal differences, especially near to the shell. Although similar, it is possible to distinguish the shell and (3,2) fluid column resonances by the frequencies at which they occur (see Tables 7.1 and 7.2). Other shell resonances can be seen using the Schlieren system, but insufficient light levels and the proximity of other resonances make them very difficult to photograph.

The experimental and theoretical *kb* values for the shell resonance seen in Figure 7.6 are contained in Table 7.2, and it will be noticed that the experimental value is significantly higher than the theoretical value. However, these resonances, unlike the fluid column resonances, are very dependent on the material parameters of the shell. A brief theoretical investigation showed that changing the inner fluid produced negligible change in either

frequency or amplitude of the shell resonances. The density of the brass cylinder used in the calculations was obtained experimentally and so it is probable that the main cause of the discrepancy is due to the use of nominal shear and compressional wave velocities. For example, increasing the shear wave velocity by $100ms^{-1}$ to $2200ms^{-1}$ improves the theoretical *kb* value for the cylinder resonance to 7.51 which is within 0.1% of the experimental value. Unfortunately the size of the brass shell prevents the experimental measurement of the shear and compressional wave velocities.

Table 7.2 Comparison of experimental and theoretical *kb* value for cylinder resonances

partial mode (*n*)	*kb* Schlieren	Computed *kb* c_t=2100ms^{-1}	Computed *kb* c_t=2200ms^{-1}
3	7.52	7.28	7.51

The type C family of resonances have also been observed using the Schlieren system, and Figure 7.7 shows the resonances for $n = 5$, 6 and 7. Also shown are the contour plots of the square of the pressure distribution for the inner fluid, hence only part of the Schlieren image is reproduced. The agreement between the contour plots and the Schlieren images for Figures 7.7a) and c) is very good. Figure 7.7b), however, illustrates a quarter wavelength difference in the position of the antinodes. This is thought to be due to the presence of the supporting thread, inducing a node at the point of contact.

The *kb* values at which the Schlieren images were obtained are compared with those observed theoretically for the type C resonances in Table 7.3. The theoretical *kb* values for $n = 5$, 6 and 7 were obtained by finding the *kb* value at which the computed pressure distribution within the cylinder had a maximum amplitude. For higher orders, the values have been obtained from a backscattered form function result. Again the experimental values are significantly higher than the predicted values using a nominal value of the shear wave velocity. Increasing c_t to $2200ms^{-1}$ provided the predicted values shown in column 4 of Table 7.3. The agreement between this new theoretical value and the experimental results is better than 1% and is considerably improved upon that using $c_t = 2100ms^{-1}$.

Table 7.3 Comparison of experimental and theoretical *kb* values for type C resonances

Partial mode (n)	kb Schlieren	Computed kb c_t=2100ms^{-1}	Computed kb c_t=2200ms^{-1}
5	1.85	1.80	1.87
6	2.67	2.60	2.69
7	3.60	3.50	3.60
8	4.62	4.47	4.60
9	5.65	5.51	5.69
10	6.78	6.60	6.77
11	7.81	7.69	7.90

In order to identify the C type resonances several theoretical investigations have been undertaken. Firstly, a calculation of the phase velocity (Table 7.4) reveals that these waves are dispersive and propagate with a speed of sound less than that in the fluid (for $n < 12$). Secondly, a theoretical investigation, limited to the region $ka = 0$ - 18 and $n < 17$, showed that changing the interior fluid to air only slightly increased the frequency and the bandwidth of these resonances. These factors would suggest that this series of resonances is due to the propagation of a surface wave on the outer surface of the shell, with most of its energy residing in the fluid. Maze et al. (1986) experimentally observed a similar series of resonances and in that case attributed them to a surface wave - namely a Stoneley wave. The Stoneley wave propagates on the outer surface of the shell is created at glancing incidence to the shell with most of its energy in the fluid (Überall, 1973) and is known to have a phase velocity that is dispersive and lower than that for the outer fluid (Frisk, Dickey & Überall, 1975). Dickey, Nixon & D'Archangelo (1983) observed that the Stoneley waves did not exist on thin shells of any material. A similar investigation in this case, limited to the region $ka = 0$ - 18 and $n < 17$, showed that these resonances do not exist for brass shells with b/a greater than approximately 0.92, consistent with the observations of Dickey et al. (1983).

Table 7.4 Comparison of experimental and theoretical *kb* values for type C resonances

Partial mode (n)	*kb* Schlieren	*kb* Computed	phase velocity /ms^{-1}
5	1.85	1.797	625
6	2.67	2.598	754
7	3.60	3.496	870
8	4.62	4.47	978
9	5.65	5.51	1063
10	6.78	6.60	1147
11	7.81	7.69	1202

7.4 Summary

A Schlieren system has been used to visualise the resonances of a brass cylindrical shell in the frequency range 50 - 500kHz. Within the range 180 - 500kHz it was possible to visualise all of the resonances due to the fluid column and the shell, the Stoneley wave resonances, however, were only visible between 50kHz and 220kHz. The visual comparison for all the resonances with theoretical predictions is very good, indicating the usefulness of the Schlieren system for immediate identification of resonance modes. The excellent agreement of the theoretical predictions with the experimental images has also confirmed that using pressure squared to approximate the optical intensity distribution is a valid assumption.

The accuracy with which resonances can be located experimentally has been shown to be very good, especially if one takes into account the uncertainties in the shear and compressional wave velocities. This technique can clearly be used to study objects with departures from cylindrical symmetry for which there are few if any theoretical predictions available.

Figure 7.1 The Schlieren System.

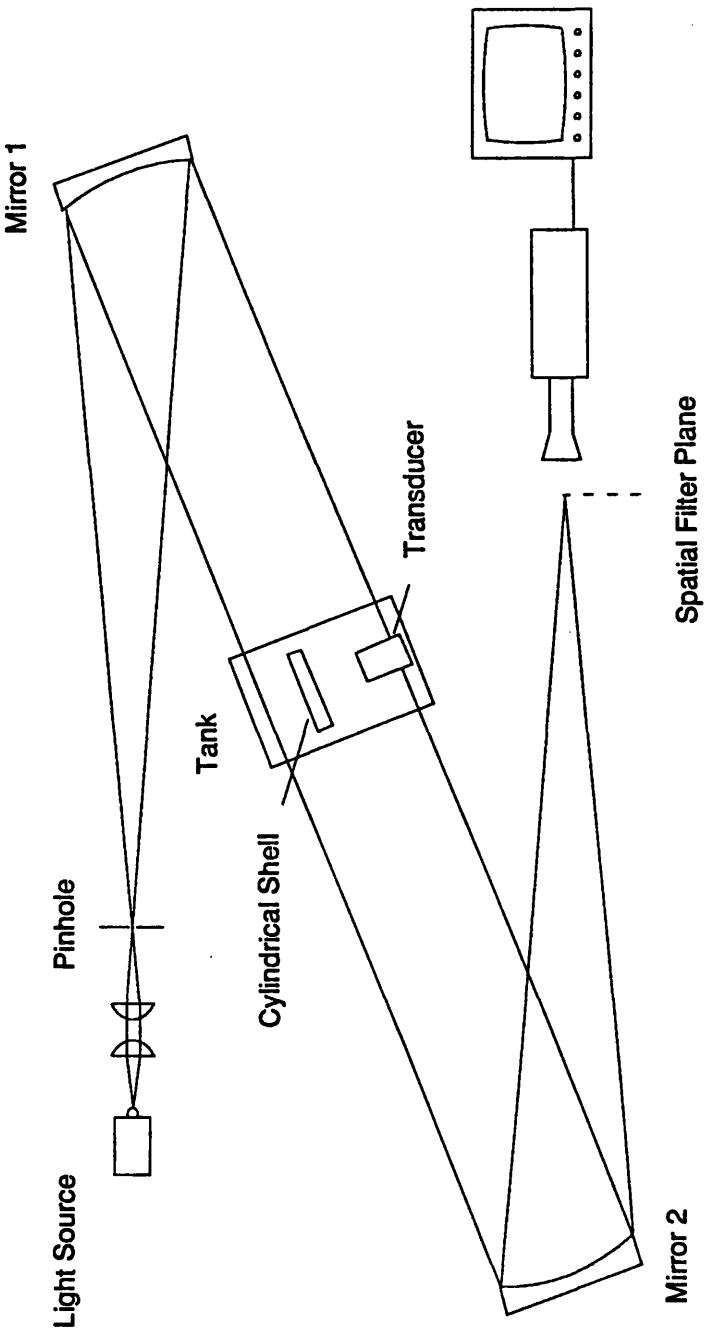

Figure 7.2 Theoretical resonances of a brass cylindrical shell.

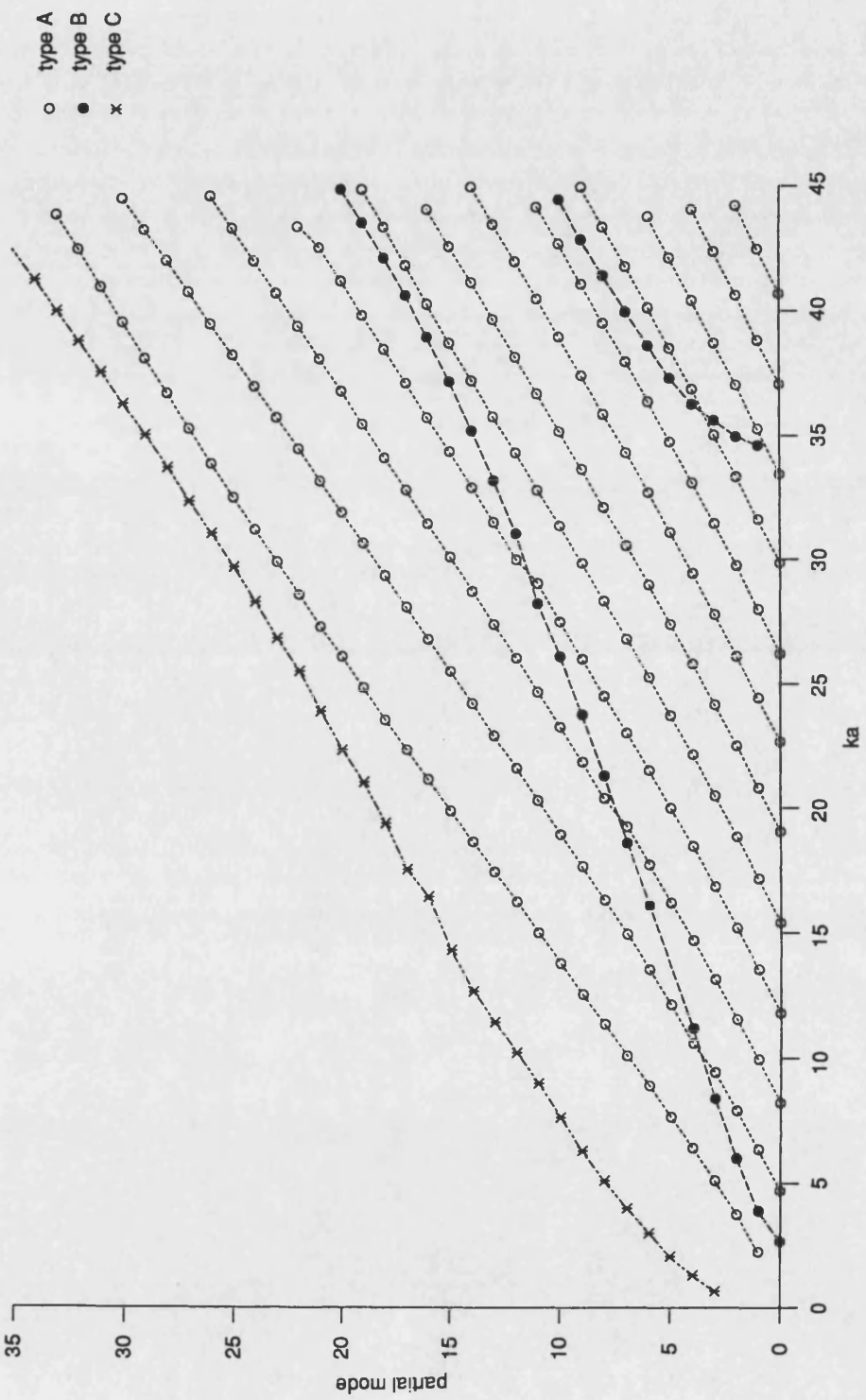

Figure 7.3 Fluid column resonances (type A) for $n = 2$.

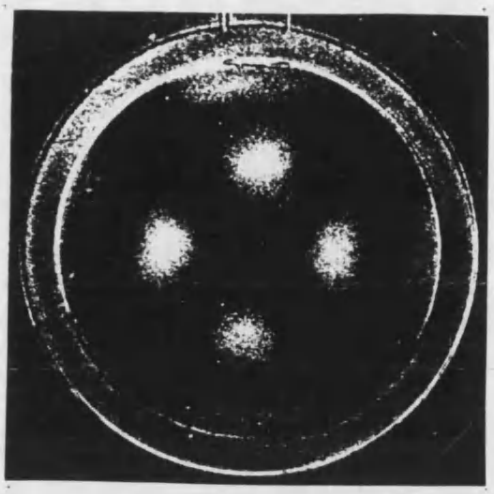

(2,2)

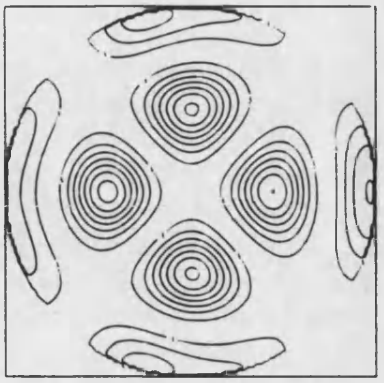

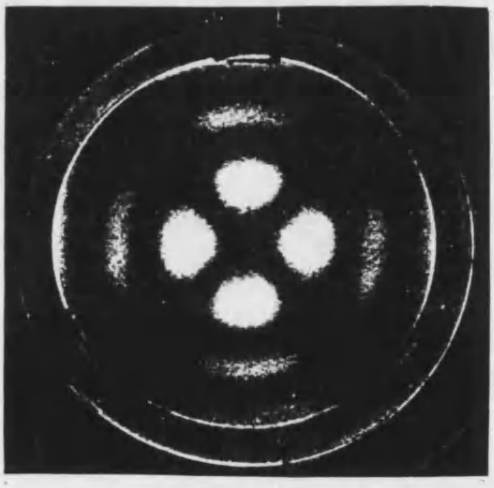

(2,3)

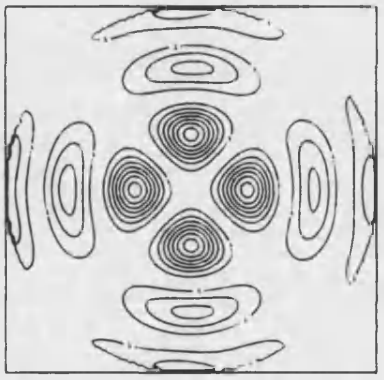

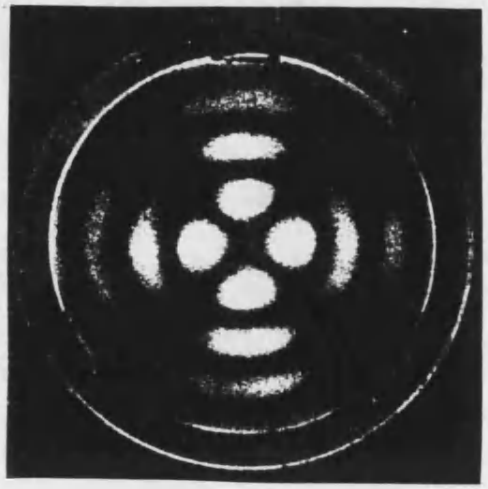

(2,4)

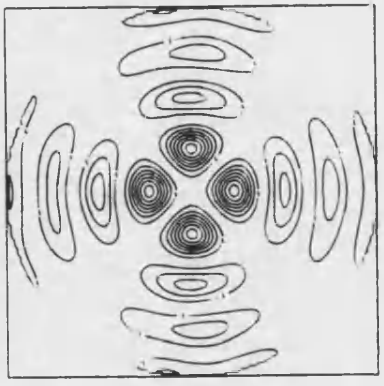

Figure 7.4 Fluid column resonances (type A) for $n = 3$.

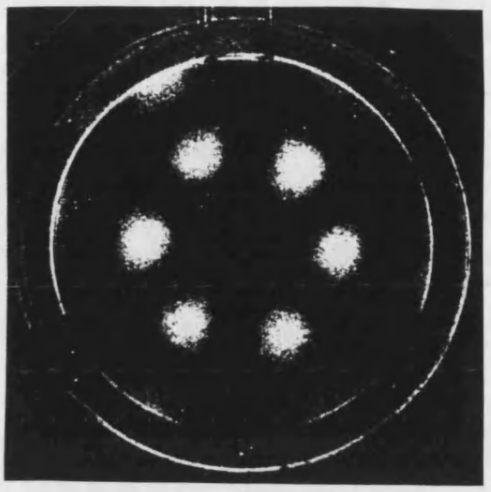

(3,2)

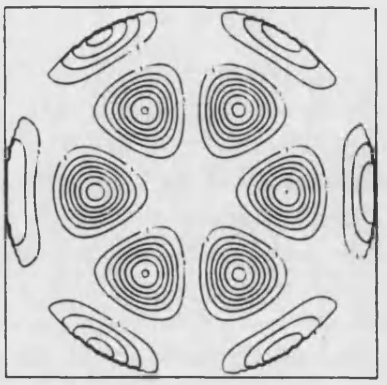

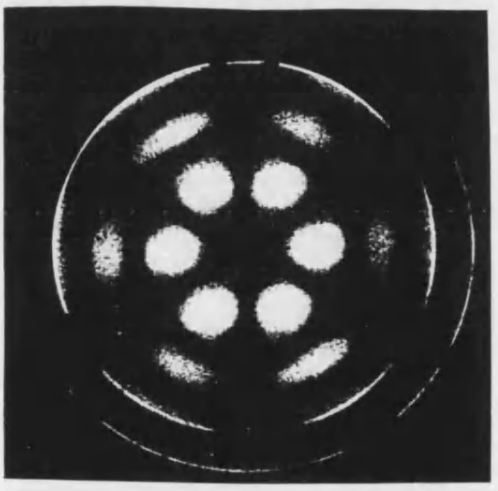

(3,3)

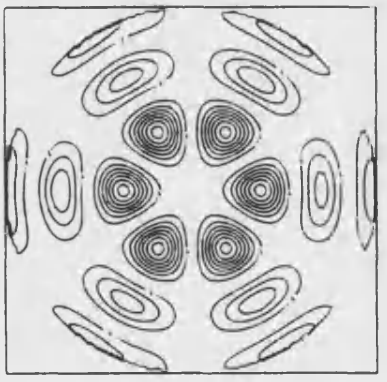

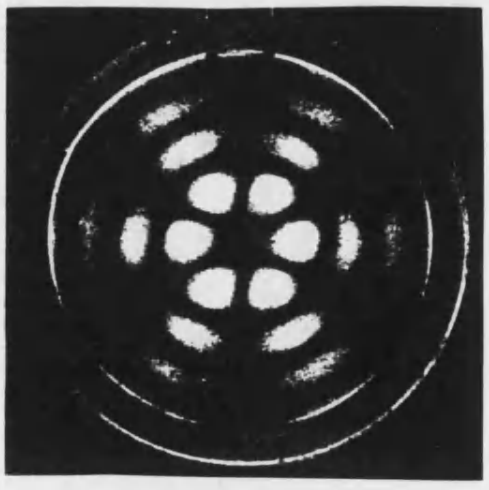

(3,4)

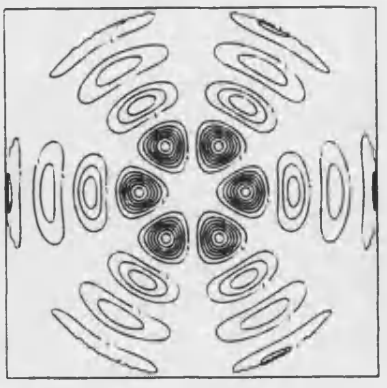

Figure 7.5 Fluid column resonances (type A) for $n = 4$.

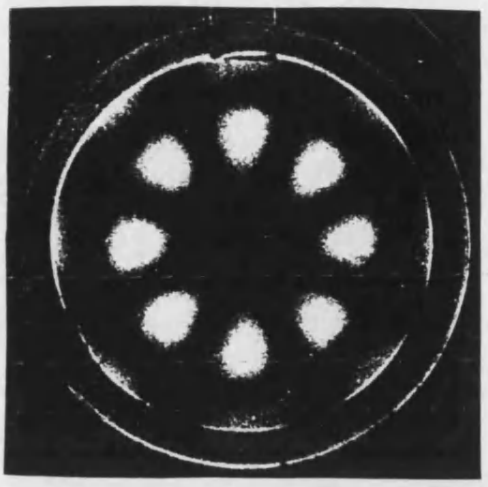

(4,2)

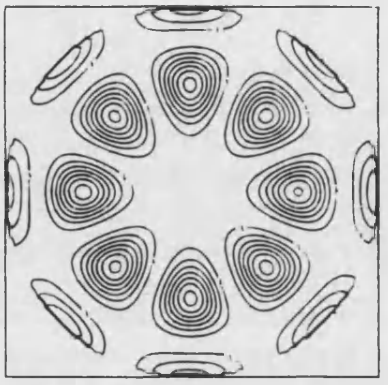

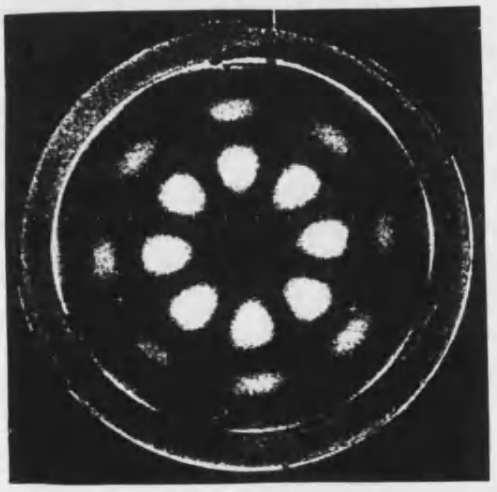

(4,3)

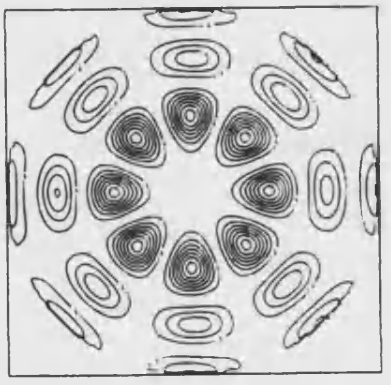

(4,4)

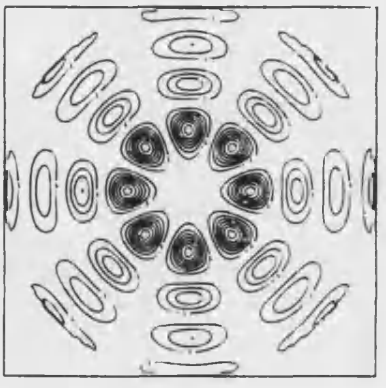

Figure 7.6 Third order shell resonance (type B).

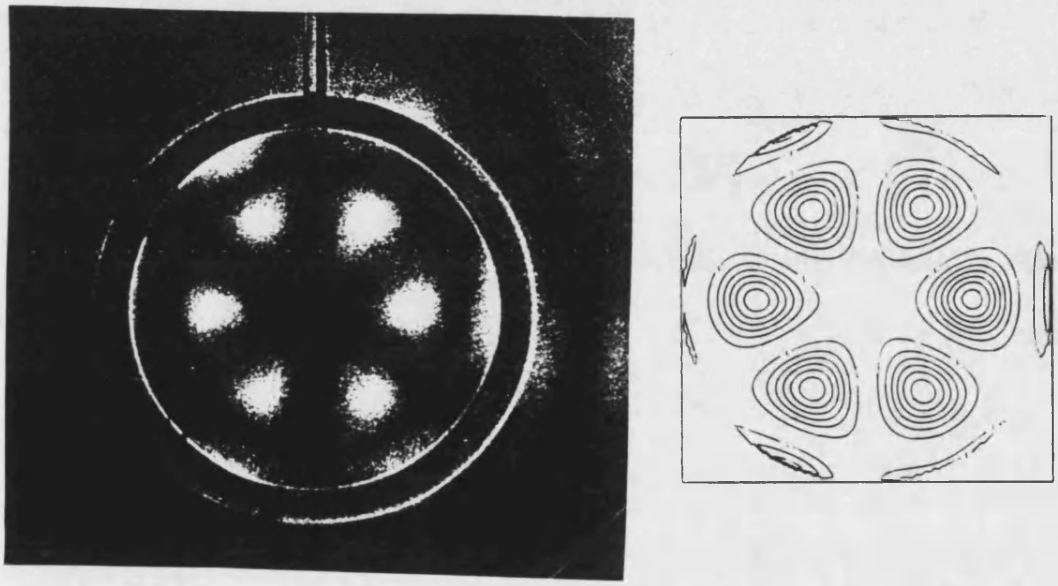

n = 3

Figure 7.7 Type C resonances.

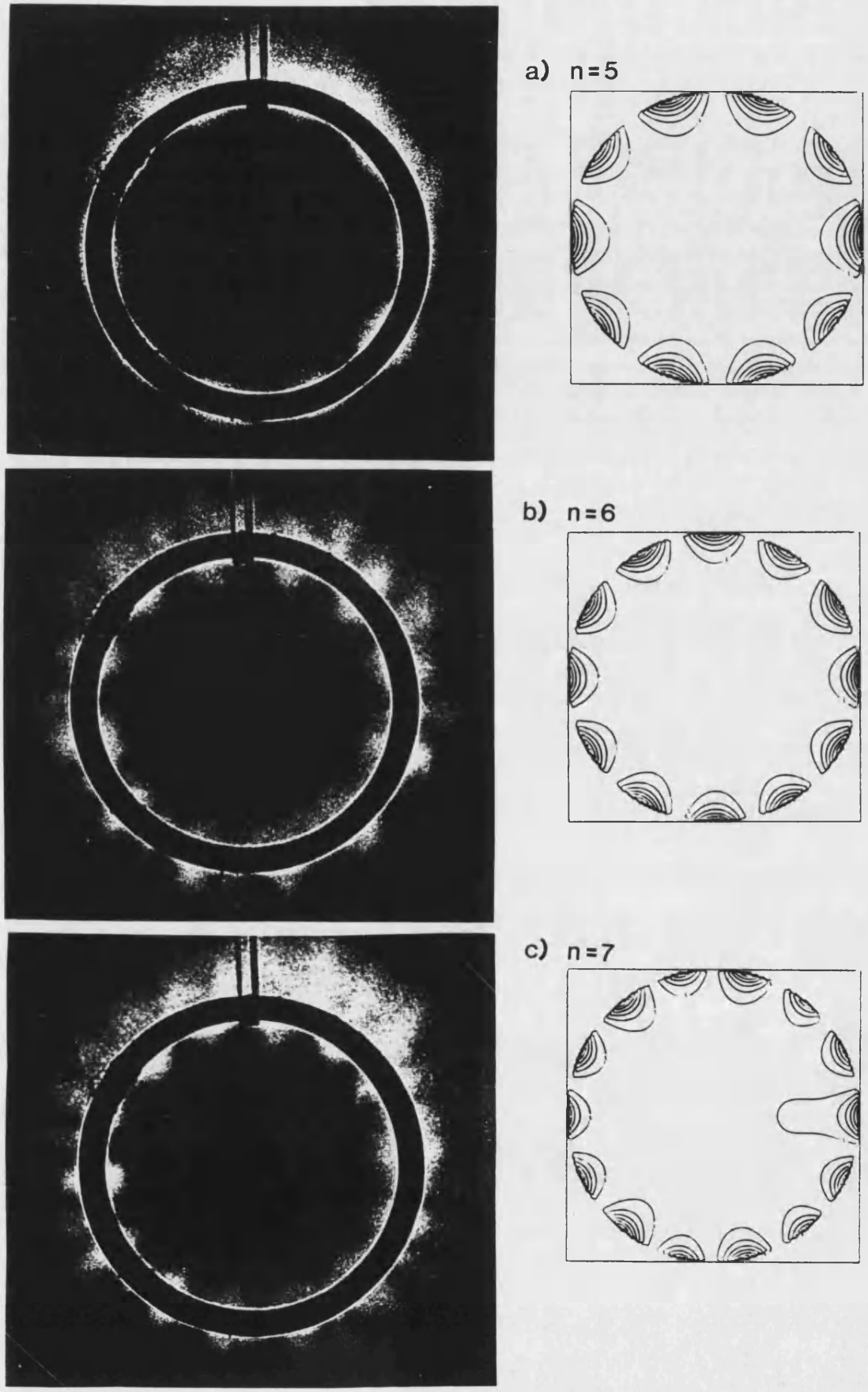

8 Conclusions and Recommendations

This document has described an experimental system and measurement technique to measure the scattering from discrete objects immersed in a fluid (water). A parametric array is used to provide a short duration broad - band transient pulse. This enables the scattering response to be determined over a wide range of frequencies, typically 10 - 200kHz, and allows individual scattering returns to be identified. The use of relatively low frequencies permits the use of objects of the order of several centimetres, leading to results in the *ka* range 0.5 - 15.

Experimental measurements have been obtained for the backscattered form function for spheres, and the form function for cylinders and for cylindrical shells at an arbitrary observation point (r,ϕ), all assuming a normally incident wavefield. The scattering of an obliquely incident wavefield by a solid cylinder has also been investigated.

Comparison of the experimental results with the appropriate single plane wave form function reveals significant differences. In the case of scattering from tungsten carbide spheres this departure is primarily due to the shadowing effects of the hydrophone and its support tube, and the resonance of the support tube observable between 50 - 60kHz. Clearly a more suitable hydrophone support tube would be desirable. The support would not only have to be well matched to water but would require enough rigidity to ensure accurate hydrophone location. A material such as glass fibre may well be suitable, although detailed investigations would be required.

The measurements from the cylindrical objects exhibit greater departures from the theory than the results for the sphere. The shadowing of the hydrophone and the resonance of the support tube account for certain features, but of far greater significance in this case is the non - planar nature of the incident wavefield. This manifests itself as a general reduction in amplitude and by the introduction of sharp resonance features characteristic of the propagation of helical waves.

For a normally incident wavefield on a solid cylinder the expression for the form function has been modified to account for the non - planar nature of the wavefield. The resulting expression for the modified form function has been evaluated for the specific case of a parametric source assuming a line array model. A comparison of this modified theory with experimental results shows excellent agreement (to within 5%) up to *ka* values of approximately 10, reproducing both the amplitude variations and the sharp resonance features observed in the experimental data. At higher *ka* values there are increasing departures of the theory from the experimental results. This has been principally attributed to the break down of the line array model used to approximate the parametric array. It would certainly be informative to reformulate the modified theory using an improved model for the parametric array. Comparisons of experimental beam profiles with both the line array and the column model (described in Appendix 2) show that the use of a column model for

the source distribution of the parametric array predicts the behaviour of the beam pattern more accurately, especially at higher frequencies. It should follow therefore that the column model should give a more realistic estimate of the behaviour of the parametric array, and its influence on the form function, in this application. It should also be noted that although the effects of the spatial plane wave spectrum have been investigated for the special case of a parametric array, similar effects are likely to be observed in any near-field measurements using finite area beams.

Experimentally work is required to develop a more accurate positioning system for the cylindrical objects, to try to resolve the difficulties observed measuring the scattered signal around an angle ϕ of 30°, and to confirm whether or not on-axis positioning is the cause of the problem.

When the wavefield is obliquely incident on a solid cylinder the modified theory which accounts for the plane wave spectrum of the parametric array performs reasonably well at small angles of incidence. For greater angles of incidence the theoretical model is inappropriate. It is thought that the approximations made during the development for the normally incident case, and obviously justified there, are no longer valid. Of prime importance is the assumption that the variation of the wavefield is significant in one dimension only. Also at higher *ka* values the use of the line array model will no longer be appropriate. Further theoretical work is recommended to develop the two dimensional integral which describes this problem more completely, although it is appreciated that this is not a trivial exercise.

During the investigation into solid cylinders it was shown that the amplitude variation introduced by the non - planar nature of the source could be adequately described by a geometrical spreading factor. The experimental results for air filled cylindrical shells showed a significant amplitude reduction when compared to the form function predictions but exhibited none of the sharp resonance features observed in the case of solid cylinders. In the absence of the sharp resonances it seemed plausible to apply this geometrical correction to the form function prediction for use with the results from the cylindrical shell instead of the more complete plane wave spectrum approach. The prediction obtained using a geometrical correction gave reasonable agreement with experimental data although there are several features that require clarification. To resolve these differences it will be necessary to develop the full model for scattering from cylindrical shells. This may include recasting the form function in terms of one of the integral transform techniques to avoid any computational difficulties that may arise when trying to integrate over all angles of incidence. Also required is further experimental confirmation of the results as there are suggestions that the data may have been over smoothed due to too short a window.

The experimental system that has been described here has proved to be an extremely valuable, sensitive and accurate tool with which to measure the scattering from discrete objects in the confined environment of a laboratory tank. Comparison of the experimental data with an appropriate theoretical prediction shows excellent agreement. There are several practical difficulties which have to be resolved, but it would seem possible to extend the work presented here to study more complex structures and systems for which theoretical predictions are not readily available, or to ascertain the validity of new theories or approximations. It would also be possible to experimentally determine the extent to which resonances are modified or perturbed by structure added to the scatterer or the local environment of the scatterer. The major difficulty in the study of more complex structures may be the construction of suitable test objects although this system clearly has advantages over previous techniques which have used much smaller objects and higher frequencies to cover a similar *ka* range.

References

Abramowitz M., Stegun I.A., (1965), "Handbook of mathematical functions.", New York, Dover.

Achenbach J.D., (1973), "Wave propagation in elastic solids.", Amsterdam, North - Holland.

Anderson V.C., (1950), "Sound scattering from a fluid sphere.", J. Acoust. Soc. Am., 22(4), 426 - 431.

Armenakas A.E., Gazis D.C., Herrmann G., (1969), "Free vibrations of circular cylindrical shells.", Oxford, Pergamon Press.

Ayres V.M., Gaunaurd G.C., (1987a), "Acoustic resonance scattering by visco-elastic objects.", J. Acoust. Soc. Am., 81(2), 301 - 311.

Ayres V.M., Gaunaurd G.C., (1987b), "Inverse acoustic scattering from an elastic sphere.", J. Acoust. Soc. Am., 82(4), 1291 - 1302.

Barnard G.R., McKinney C.M., (1961), "Scattering of acoustic energy by solid and air filled cylinders in water.", J. Acoust. Soc. Am., 33(2), 226 - 238.

Baskar S., Varadan V.V., Varadan V.K., (1984), "Thin shell theories and acoustic wave scattering by infinitely long cylindrical shells of arbitrary cross section.", J. Acoust. Soc. Am., 75(6), 1673 - 1679.

Baum C.E., (1976), "The Singularity Expansion Method.", in "Transient Electromagnetic Fields", (1976), edited by **L.B.Felsen**, Berlin, Springer-Verlag.

Bergmann L., (1949), "Eigenschwingungen von Glaszylindern.", Z. Physik, 125, 405 - 417, through **Knapp S.M. & Beckett C.**, (1989), "Experimental and theoretical observation of cylinder resonances.", (unpublished), University of Bath.

Berktay H.O., (1965), "Possible exploitation of non-linear acoustics in underwater transmitting applications.", J. Sound Vib., 2, 435 - 461.

Berktay H.O., Shooter J.A., (1973), "Near-field effects in endfire arrays.", J. Acoust. Soc. Am., 53(2), 550 - 556.

De Billy M., (1986), "Determination of the resonance spectrum of elastic bodies via the use of short pulses and Fourier Transform theory.", J. Acoust. Soc. Am., 79(2), 219 - 221.

Bjørnø L., (1975), "Underwater applications of non-linear ultrasound.", in Ultrasonics International 1975 Conference Proceedings, 238 - 244, Guildford, Butterworths.

Breit G., Wigner E.P., (1936), "Capture of slow neutrons.", Phys. Rev., 49, 519 through **Flax L., Dragonette L.R., Überall H.**, (1978).

Breitenbach E.D., Überall H., Yoo K.B., (1983), "Resonant scattering from elastic cylindrical shells.", J. Acoust. Soc. Am., 74(4), 1267 - 1273.

Brekhovskikh L.M., (1980), "Waves in Layered Media.", 2nd Edition, Academic Press, New York.

Brill D., Gaunaurd G.C., (1983), "Acoustic resonance scattering by a penetrable cylinder.", J. Acoust. Soc. Am., 73(5), 1448 - 1455.

Brill D., Gaunaurd G.C., (1987), "Resonance theory of elastic waves ultrasonically scattered from an elastic sphere.", J. Acoust. Soc. Am., 81(1), 1 - 21.

Brill D., Überall H., (1971), "Acoustic waves transmitted through solid elastic cylinders.", J. Acoust. Soc. Am., 81(1), 1 - 21.

Bucaro J.A., Flax L., Dardy H.D., Moore W.E., (1976), "Image profiles in Schlieren observations of acoustic wave fronts.", J. Acoust. Soc. Am., 60, 1079 - 1084.

Chinnery P., (1990), "Laboratory Studies of Acoustic Scattering.", Report No 1 - "Schlieren Visualisation of Cylinder resonances. Theoretical Calculation and Experimental Observation.", (unpublished), University of Bath.

Chivers R.C., Anson L.W., (1982), "Calculations of the backscattering and radiation force functions of spherical targets for use on ultrasonic beam assessment.", Ultrasonics, 20, 25 - 34.

Dardy H.D., Bucaro J.A., Schuetz L.S., Dragonette L.R., (1977), "Dynamic wide-bandwidth acoustic form function determination.", J. Acoust. Soc. Am., 62(6), 1373 - 1376.

Dardy H.D., Flax L., Gaumond C.F., Subrahmanyam J.V., Ashrafi S., Raju P.K., Überall H., (1987), "Acoustically induced stresses in elastic cylinders and their visualisation.", J. Acoust. Soc. Am., 82, 1378 - 1385.

Davies C.M., Dragonette L.R., Flax L., (1978),,"Acoustic scattering from silicone rubber cylinders and spheres.", J. Acoust. Soc. Am., 63(6), 1694 - 1698.

Dickey J.W., Frisk G.V., Überall H., (1976), "Whispering Gallery wave modes on elastic cylinders.", J. Acoust. Soc. Am., 59(6), 1339 - 1346.

Dickey J.W., Nixon D.A., D'Archangelo J.M., (1983), "Acoustic high frequency scattering by elastic cylindrical shells.", J. Acoust. Soc. Am., 74(1), 294 - 304.

Dierks K.J., Goldsberry T.G., Horton C.W., (1963), "Circumferential waves in thin - walled air filled cylinders in water.", J. Acoust. Soc. Am., 35(1), 59 - 64.

Doolittle R.D., Überall H., (1966), "Sound scattering by elastic cylindrical shells.", J. Acoust. Soc. Am., 39(2), 272 - 275.

Doolittle R.D., McNicholas J.V., Überall H., Ugincuis P., (1967), "Circumferential sound pulses on elastic cylinders.", J. Acoust. Soc. Am., 42(2), 522 - 523 (L).

Doolittle R.D., Überall H., Ugincuis P., (1968), "Sound scattering by elastic cylinders.", J. Acoust. Soc. Am., 43(1), 1 - 14.

Dragonette L.R., (1978), "Evaluation of the relative importance of circumferential or creeping waves in acoustic scattering from rigid and elastic solid cylinders and cylindrical shells.", Washington DC, Naval Res. Lab. Report 8216.

Dragonette L.R., (1979), "The influence of the Rayleigh surface wave on the backscattering by submerged aluminium cylinders.", J. Acoust. Soc. Am., 65(6), 1570 - 1572.

Dragonette L.R., Numrich S.K., Frank L.J., (1981), "Calibration technique for acoustic scattering measurements.", J. Acoust. Soc. Am., 69(4), 1186 - 1189.

Dragonette L.R., Vogt R.H., Flax L., Neubauer W.G., (1974), "Acoustic reflection from elastic spheres and rigid spheres and spheroids. 2 Transient analysis.", J. Acoust. Soc. Am., 55(6), 1130 - 1136.

Faran J.J., (1951), "Sound scattering by solid cylinders and spheres.", J. Acoust. Soc. Am., 23(4), 405 - 418.

Feshbach H., Peaslee D.C., Weisskopf V.F., (1947) "On the scattering and absorption of particles by atomic nuclei.", Phys. Rev., 71, 145, through **Flax L., Dragonette L.R., Überall H.**, (1978).

Flax L., Dragonette L.R., Überall H., (1978), "Theory of elastic resonance excitation by sound scattering.", J. Acoust. Soc. Am., 63(3), 723 - 730.

Flax L., Gaunaurd G.C., Überall H., (1981), "Theory of resonance scattering." in "Physical Acoustics XV", (1981), edited by **W.P. Mason, R.N. Thurston**, New York, Academic Press.

Flax L., Neubauer W.G., (1977), "Acoustic reflection from layered elastic absorptive cylinders.", J. Acoust. Soc. Am., 61(2), 307 - 312.

Flax L., Raju P.K., George J., Überall H., (1980), "Resonating fields inside elastic scattering objects.", J. Acoust. Soc. Am., 68(3), 973 - 979.

Flax L., Varadan V.K., Varadan V.V, (1980), "Scattering of an obliquely incident wave by an infinite cylinder.", J. Acoust. Soc. Am., 68(6), 1832 - 1835.

Foote K.G., MacLennan D.N., (1984), "Comparison of copper and tungsten carbide calibration spheres.", J. Acoust. Soc. Am., 75(2), 612 - 616.

Franz W., (1954), "Uber die Greenschen Functionen des Zylinders und der Kugel.", Z. Naturforsch., 9a, 705 - 716.

Frisk G.V., Dickey J.W., Überall H., (1975), "Surface wave modes on elastic cylinders.", J. Acoust. Soc. Am., 58(5), 996 - 1008.

Frisk G.V., Überall H., (1976), "Creeping waves and lateral waves in acoustic scattering by large elastic cylinders.", J. Acoust. Soc. Am., 59(1), 46 - 54.

Gaunaurd G.C., (1977), "High frequency acoustic scattering from submerged cylindrical shells coated with visco-elastic absorbing layers.", J. Acoust. Soc. Am., 62(3), 503 - 512.

Gaunaurd G.C., Tsui C.Y., (1988), "Transient and steady state target - resonance excitation by sound scattering.", App. Acoust., 23(2), 121 - 140.

Gaunaurd G.C., Überall H., (1983), "RST analysis of monostatic and bistatic acoustic echoes from an elastic sphere.", J. Acoust. Soc. Am., 73(1), 1 - 12.

Gaunaurd G.C., Überall H., (1985), "Relation between creeping-wave acoustic transients and the complex-frequency poles of the Singularity Expansion Method.", J. Acoust. Soc. Am., 78(1), 234 - 243.

Gaunaurd G.C., Werby M.F., (1985), "Resonance response of submerged, acoustically thick and thin shells.", J. Acoust. Soc. Am., 77(6), 2081 - 2093.

Gaunaurd G.C., Werby M.F., (1989), "Near-field effects in acoustic scattering by submerged rigid bodies and elastic shells.", J. Acoust. Soc. Am., 85(6), 2465 - 2471.

Gazis D.C., (1959), "Three-dimensional investigation of the propagation of waves in hollow circular cylinders. 1. Analytical Foundation, 2 Numerical results.", J. Acoust. Soc. Am., 31, 568 - 578.

Geffe P.R., (1963), "Simplified modern filter design.", New York, J.F. Rider.

Gespa N., (1987), "La diffusion acoustique.", Paris, Cedocar.

Goodman R.R., Bunney R.E., Marshall S.W., (1967), "Observation of circumferential waves on solid aluminium cylinders.", J. Acoust. Soc. Am., 42(2), 523 - 524 (L).

Grace O.D., Goodman R.R., (1966), "Circumferential waves on solid cylinders.", J. Acoust. Soc. Am., 39, 173 - 174.

Gray A., Matthews G.R., MacRobert T.M., (1922), "Treatise on Bessel functions and their application to Physics.", 2nd edition, London, MacMillan.

Greenspon J.E., (1960), "Vibrations of a Thick - Walled Cylindrical Shell - Comparison of the Exact Theory with Approximate Theories.", J. Acoust. Soc. Am., 23, 571.

Hackman R.H., (1984), "The transition matrix for acoustic and elastic wave scattering in prolate spheroidal co-ordinates.", J. Acoust. Soc. Am., 75(1), 35 - 45.

Hackman R.H., Todoroff D.G., (1985), "An application of the spheroidal- coordinate-based transition matrix : The acoustic scattering from high aspect ratio solids.", J. Acoust. Soc. Am., 78(3), 1058 - 1071.

Hackman R.H., Werby M.F., (1984), "Near-field effects in acoustic scattering.", J. Acoust. Soc. Am., 75(3), 1001 - 1003.

Hampton L.D., McKinney C.M., (1961), "Experimental study of the scattering of acoustic energy from solid metal spheres in water.", J. Acoust. Soc. Am., 33(5), 664 - 673.

Heyman E., Felsen L.B., (1986), "Travelling wave and SEM representations for transient scattering by a circular cylinder.", J. Acoust. Soc. Am., 79(2), 230 - 238.

Hickling R., (1962), "Analysis of echoes from a solid elastic sphere in water.", J. Acoust. Soc. Am., 34(10), 1582 - 1592.

Horton C.W., King W.R., Dierks K.J., (1962), "Theoretical analysis of the scattering of short acoustic pulses by a thin walled metallic cylinder in water.", J. Acoust. Soc. Am., 34(12), 1929 - 1932.

Humphrey V.F., (1981), "The measurement of acoustic properties of specimens of limited size by use of a parametric source.", in Ultrasonics International 81 Conference Proceedings, 360 - 365, Guildford, Butterworths.

Humphrey V.F., (1985), "The measurement of acoustic properties of limited size panels by use of a parametric source.", J. Sound Vib., 98(1), 67 - 81.

Humphrey V.F., Beckett C., (1990), "The application of a parametric array to scattering studies in the laboratory.", in Frontiers of nonlinear acoustics: Proceedings of 12th ISNA, 265 - 270, London, Elsevier.

Humphrey V.F., Berktay H.O., (1985), "The transmission coefficient of a panel measured with a parametric source.", J. Sound Vib., 101(1), 85 - 106.

Humphrey V.F., Hsu C.H., (1980), "Non-linearity of cylindrical hydrophones used for the

measurement of parametric arrays.", from "Transducers for Sonar Applications", conf proc.

Humphrey V.F., Murphy (Beckett) C., Moustafa A.H.A., (1987), "Wideband backscattering measurements using a parametric array.", in Ultrasonics International 87 Conference Proceedings, 265 - 270, Guildford, Butterworths.

Izbicki J.L., Maze G., Ripoche J., (1986), "Diffusion acoustique par des tubes immergés dans l'eau: Nouvelles résonances observées en basse fréquence.", Acustica, 61, 137 - 139.

Izbicki J.L., Maze G., Ripoche J., (1987), "Etude des resonances d'un cylindre limite.", Acustica, 64, 50 - 53.

James J.H., (1983), "Sound scattering from infinite fluid filled cylindrical shell.", A.M.T.E. Technical memo TM83107.

Junger M.C., (1952), "Sound scattering by thin elastic shells.", J. Acoust. Soc. Am., 24(4), 366 - 373.

Kaye G.W.C., Laby T.H., (1986), "Tables of physical and chemical constants.", 15th edition, London, Longman.

Kinsler L.E., Frey A.R., Coppens A.B., Sanders J.V., (1982), "Fundamentals of Acoustics", 3rd Edition, New York, Wiley.

Knapp S.M., (June 1987), "Schlieren studies of acoustic backscattering." Report no. 2 - "Experimental arrangement and preliminary results.", (unpublished) University of Bath, Interim report for contract 2112/70/ARE(T).

Knapp S.M., (Jan 1988), "Schlieren studies of acoustic backscattering." Report no. 3 - "Theoretical study of acousto-optic interaction and practical limitations at low frequencies.", (unpublished) University of Bath, Interim report for contract 2112/70/ARE(T).

Knapp S.M., (May 1988), "Schlieren studies of acoustic backscattering." Report no. 4 - "Variation of the Schlieren image with acoustic pressure.", (unpublished) University of Bath, Interim report for contract 2112/70/ARE(T).

Knapp S.M., (August 1988), "Schlieren studies of acoustic backscattering." Report no. 5 - "Visualisation of low frequency acoustic fields.", (unpublished) University of Bath, Interim report for contract 2112/70/ARE(T).

Liamshev L.M., (1958), "Sound diffraction by an unbounded thin elastic cylindrical shell.", Sov. Phys. Acoust., 4(2), 161 - 167.

Love A.E.H., (1944), "A treatise on the mathematical theory of elasticity.", New York, Dover.

Lundqvist L., (1986), " Acoustic surface waves on an impenetrable cylinder with periodically varying circular cross section.", J. Acoust. Soc. Am., 80(5), 1423 - 1428.

MacLennan D.N., (1981), "The theory of solid spheres as sonar calibration targets.", Scottish Fisheries Report 22.

MacLennan D.N., Dunn J.R., (1984), "Estimation of sound velocities from resonance measurements on tungsten carbide calibration sphere.", J. Sound Vib., 97(2), 321 - 333.

Maze G., Izbicki J.L., Ripoche J., (1984), "Diffusion ultrasonore par un cylindre insone obliquement.", Rev. Cethdec Ondes et Signal, 78, 95 - 105.

Maze G., Izbicki J.L., Ripoche J., (1985), "Resonances of plates and cylinders: guided waves.", J. Acoust. Soc. Am., 77(4), 1352 - 1357.

Maze G., Izbicki J.L., Ripoche J., (1986), "Acoustic scattering from cylindrical shells : guided waves and resonances of the liquid column.", Ultrasonics, 24, 354 - 362.

Maze G., Izbicki J.L., Ripoche J., (1987), "Methode d'isolement et d'identification des resonances : application aux cylindres et aux tubes.", in "La diffusion acoustique.", (1987), **Gespa N.** (ed), Paris, Cedocar.

Maze G., Ripoche J., (1983a), "Méthode d'isolement et d'identification des résonances (M.I.I.R.) de cylindres et de tubes soumis à une onde acoustique plane dans l'eau.", Revue Phys. Appl., 18, 319 - 326.

Maze G., Ripoche J., (1983b), "Visualisation of acoustic scattering by elastic cylinders at low ka.", J. Acoust. Soc. Am., 73(1), 41 - 43.

Maze G., Taconet B., Ripoche J., (1981), Influence des ondes de 'galerie a echo' sur la diffusion de onde ultrasonore plane par un cylindre.", Phys. Lett., 84A, 309 - 312.

Meeker T.R., Meitzler A.H., (1964), "Guided wave propagation in elongated cylinders and plates.", in "Physical Acoustics 1A", (1964), edited by **Mason W.P., Thurston R.N.**, New York, Academic Press.

Moffet M.B., Henriquez T.A., (1982), "Hydrophone non-linearity measurements.", J. Acoust. Soc. Am., 72(1), 1 - 6.

Molinero I., de Billy M., (1988), "Characterisation of guided waves propagating in infinite cylinders for oblique insonification.", J. Acoust. Soc. Am., 83(4), 1280 - 1283.

Morse P.M., (1948), "Vibration and Sound.", New York, McGraw Hill.

Murphy J.D., Breitenbach E.D., Überall H., (1978), "Resonance scattering of acoustic waves from cylindrical shells.", J. Acoust. Soc. Am., 64(2), 667 - 683.

Murphy J.D., George J., Überall H., (1979), "Isolation of the resonant component in acoustic scattering from fluid - loaded cylindrical shells.", Wave Motion, 1, 141 - 147.

Muzychenko V.V., Rybak S.A., (1986), "Amplitude of resonance sound scattering by a finite cylindrical shell in a fluid.", Sov. Phys. Acoust., 32(1), 79 - 80.

Muzychenko V.V., Rybak S.A., (1988), "Low-frequency resonance scattering of sound by finite cylindrical shells (review).", Sov. Phys. Acoust., 34(4), 325 - 333.

Nagl A., Überall H., Delsanto P.P, Alemar J.D., Rosario E., (1983), "Refraction effects in the generation of helical surface waves on a cylindrical obstacle.", Wave Motion, 5, 235 - 247.

Neubauer W.G., (1968), "Experimental observation of three types of pulsed circumferential waves on solid aluminium cylinders.", J. Acoust. Soc. Am., 44, 1150 - 1152.

Neubauer W.G., (1969), "Pulsed circumferential waves on aluminium cylinders in water.", J. Acoust. Soc. Am., 45(5), 1134 - 1144.

Neubauer W.G., (1973), "Ultrasonic reflection of a bounded beam at Rayleigh and critical angles for a plane liquid - solid interface.", J. Appl. Phys., 44, 48 - 55.

Neubauer W.G., (1987), "Acoustic reflection from surfaces and shapes.", Washington,

Naval Research Laboratory.

Neubauer W.G., Dragonette L.R., (1970), "Observation of waves radiated from circular cylinders caused by an incident pulse.", J. Acoust. Soc. Am., 48, 1135 - 1149.

Neubauer W.G., Ugincuis P., Überall H., (1969), "Theory of creeping waves in acoustics and their experimental demonstration.", Zeitschrift fur Naturforshung, 24a(5), 691 - 700.

Neubauer W.G., Vogt R.H., Dragonette L.R., (1974), "Acoustic reflection from elastic spheres. 1 Steady state signals.", J. Acoust. Soc. Am., 55(6), 1123 - 1129.

Peterson B., Varadan V.V., Varadan V.K., (1980), "Scattering of acoustic waves by layered elastic and visco-elastic obstacles in water.", J. Acoust. Soc. Am., 68(2), 673 - 685.

Pillai T.A.K., Varadan V.V., Varadan V.K., (1982), "Sound scattering by rigid and elastic infinite elliptical cylinders in water.", J. Acoust. Soc. Am., 72(3), 1032 - 1037.

Pillai T.A.K., Varadan V.V., Varadan V.K., Radlinski R.P., (1983), "Acoustic wave scattering by elastic cylindrical shells in water.", J. Acoust. Soc. Am., 74(2), 619 - 624.

Press W.H., Flannery B.P., Teukolsky S.A., Vetterling W.T., (1989), "Numerical Recipes. The Art of Scientific Computing.", Cambridge, Cambridge University Press.

Rayleigh Baron (Strutt J.W.), (1878), "The Theory of Sound", New York, MacMillan. (Dover reprint 1945 2nd edition.)

Simon M.M., Radlinski R.P., (1982), "Elastic wave scattering from elliptical shells.", J. Acoust. Soc. Am., 71(2), 273 - 281.

Solomon S.G., Überall H., Yoo K.B., (1984), "Mode conversion and resonance scattering of elastic waves from a cylindrical fluid filled cavity.", Acustica, 55, 147 - 159.

Sommerfeld A., (1949), "Partial Differential Equations in Physics.", New York, Academic Press.

Su J-H, Varadan V.V., Varadan V.K., Flax L., (1980), "Acoustic wave scattering by a finite elastic cylinder in water.", J. Acoust. Soc. Am., 68(2), 686 - 691.

Talmant M., Quentin G., Rousselot J.L., Subrahmanyam J.V., Überall H., (1988), "Acoustic resonances of thin cylindrical shells and the resonance scattering theory.", J. Acoust. Soc. Am., 84(2), 681 - 688.

Tsui C.Y., Reid G.N., Gaunaurd G.C., (1986), "Resonance scattering by elastic cylinders and their experimental investigation.", J. Acoust. Soc. Am., 80(2), 382 - 390.

Überall H., (1973), "Surface waves in acoustics.", in "Physical Acoustics X", (1973), edited by **Mason W.P., Thurston R.N.**, New York, Academic Press.

Überall H., Doolittle R.D., McNicholas J.V., (1966), "Use of sound pulses for a study of circumferential waves.", J. Acoust. Soc. Am., 39(3), 564 - 578.

Überall H., Dragonette L.R., Flax L., (1977), "Relation between creeping waves and normal modes of vibration of a curved body.", J. Acoust. Soc. Am., 61(3), 711 - 715.

Überall H., Gaunaurd G.C., (1981), "The physical content of the Singularity Expansion Method.", Appl. Phys. Lett., 39(4), 362 - 364.

Überall H., Huang H., (1976), "Acoustic response of submerged elastic structures obtained through integral transforms.", in "Physical Acoustics XII", (1976), edited by **Mason W.P. & Thurston R.N.**, New York, Academic Press.

Überall H., Moser P.J., Murphy J.D., Nagl A., Igiri G., Subrahmanyam J.V., Gaunaurd G.C., Brill D., Delsanto P.P., Alemar J.D., Rosario E., (1983), "Electromagnetic and acoustic resonance scattering theory.", Wave Motion, 5, 307 - 329.

Überall H., Stoyanov Y.J., Nagl A., Werby M.F., Brown S.H., Dickey J.W., Numrich S.K., D'Archangelo J.M., (1987), "Resonance spectra of elongated elastic objects.", J. Acoust. Soc. Am., 81(2), 312 - 316.

Ugincuis P., Überall H., (1968), "Creeping wave analysis of acoustic scattering by elastic cylindrical shells.", J. Acoust. Soc. Am., 43(5), 1025 - 1035.

Varadan V.K., Varadan V.V., (1979), "Acoustic, Electromagnetic and Elastic Wave Scattering - Focus on the T-matrix approach.", New York, Pergammonn Press.

Varadan V.K., Varadan V.V., Tsao S.J., Neubauer W.G., (1982), "Scattering of acoustic waves by rigid cylindrical objects with sharp corners.", J. Acoust. Soc. Am., 72(6), 1957 - 1964.

Veksler N.D., (1982), "Information Analysis in Hydroelasticity", Valgus, Tallinn (in Russian), through **Veksler N.D.**, (1986).

Veksler N.D., (1984), "Resonance Scattering in Hydroacoustics.", Valgus, Tallinn (in Russian), through **Veksler N.D.**, (1986).

Veksler N.D., (1986), "Sound wave scattering by circular cylindrical shells.", Wave Motion, 8, 525 - 536.

Veksler N.D., (1988), "Analysis of the frequency dependence of plane pressure wave scattering by an elastic tube.", Acoustics Letters, 12(2), 21 - 27.

Vogt R.H., Flax L., Dragonette L.R., Neubauer W.G., (1975), "Monostatic reflection of a plane wave from an absorbing sphere.", J. Acoust. Soc. Am., 57(3), 558 - 561. Erratum (1977), J. Acoust. Soc. Am., 62, 1315.

Vogt R.H., Neubauer W.G., (1976), "Relationship between acoustic reflection and vibrational modes of elastic spheres.", J. Acoust. Soc. Am., 60(1), 15 - 22.

Waterman P.C., (1969), "New formulation of acoustic scattering.", J. Acoust. Soc. Am., 45(6), 1417 - 1429.

Waterman P.C., (1976), "Matrix theory of elastic wave scattering.", J. Acoust. Soc. Am., 60, 567 - 580.

Welton P.J, de Billy M., Hayman A., Quentin G., (1980), "Backscattering of short ultrasonic pulses by solid elastic cylinders a large *ka*.", J. Acoust. Soc. Am., 67(2), 470 - 476.

Westervelt P.J., (1957), "Scattering of sound by sound.", J. Acoust. Soc. Am., 29(2), 199 - 203.

Westervelt P.J., (1963), "Parametric Acoustic Array.", J. Acoust. Soc. Am., 35(4), 535 - 537.

Williams K.L., Marston P.L., (1985), "Backscattering from an elastic sphere: Sommerfeld - Watson transformation and experimental confirmation.", J. Acoust. Soc. Am., 78(3), 1093 - 1102.

White R.M., (1958), "Elastic wave scattering at a cylindrical discontinuity in a solid.", J. Acoust. Soc. Am., 30(8), 771 - 785.

Zemanek J.Jr., (1972), "An experimental and theoretical investigation of elastic wave propagation in a cylinder.", J. Acoust. Soc. Am., 51(1), 265 - 283.

Appendix 1 Nomenclature

The following contains a list of the symbols used during the main body of this report and their meanings.

a	radius of a sphere or cylinder, or outer radius of a cylindrical shell
A_n	scattering coefficient for the interior fluid of a cylindrical shell
$\underline{A} = (A_r, A_\phi, A_z)$	vector potential
b	inner radius of a cylindrical shell
b_n	scattering coefficient for the field exterior to a sphere
B_n	scattering coefficient for the field exterior to cylinders or cylindrical shells
B_n^R	scattering coefficient for a rigid cylinder or cylindrical shell
B_n^S	scattering coefficient for a soft cylinder or cylindrical shell
c_1	speed of sound in the exterior fluid
c_3	speed of sound in the interior fluid
c_l	compressional wave velocity in the cylinder
c_t	shear wave velocity in the cylinder
C_n	scattering coefficient used in equation for ψ
D_n	scattering coefficient used in equation for ψ
E_n	scattering coefficient used in equation for A_z
f_{geo}	modified form function to take account of a geometrical spreading factor
f_{pws}	modified form function to take account of the plane wave spectrum of the parametric array
$f_r(ka)$	finite range form function
$f_\infty(ka)$	far field form function
$g_i(ka)$	frequency spectrum of an incident signal
$g_{sc}(ka)$	frequency spectrum of a scattered signal
G_n	scattering coefficient used in equation for A_z
h	$= k_1 \sin\alpha$
$h_n^1(x)$	Spherical Hankel function of the first kind $(j_n(x) + i y_n(x))$

$h_n^2(x)$	Spherical Hankel function of the second kind $(j_n(x) - iy_n(x))$
$h_n^{1\prime}(x)$	first derivative of the Spherical Hankel Function
$H_n^1(x)$	Cylindrical Hankel Function
$H_n^{1\prime}(x)$	first derivative of the Cylindrical Hankel Function
$j_n(x)$	Spherical Bessel function of order n and argument x
$j_n'(x)$	first derivative of the Spherical Bessel function
$J_n(x)$	Cylindrical Bessel Function
$J_n'(x)$	first derivative of the Cylindrical Bessel Function
k	wavenumber
k_l	wavenumber of the compressional wave in the solid
k_t	wavenumber of the shear wave in the solid
k_1	wavenumber in the exterior fluid
k_3	wavenumber in the interior fluid
K_n	scattering coefficient used in equation for A_r and A_ϕ
l	associated with a resonance in RST to denote where it appears within a partial mode
l_s	as above, but for Stoneley waves
l_T	truncation length of parametric array
L_n	scattering coefficient used in equation for A_r and A_ϕ
n	partial modes
p	$=\sqrt{k_l^2 - h^2}$
p_f	pressure field in the interior of a cylindrical shell
p_i	incident pressure field
p_{sc}	scattered pressure field
$P_n(\cos\theta)$	Legendre Function
q	$=\sqrt{k_t^2 - h^2}$
Q_n	determinant used in scattering from cylinders and cylindrical shells.

Q_0	source strength
r	range
$\underline{r}$	field point
$\underline{R}$	field point
R_n	determinant used in scattering from cylinders and cylindrical shells.
s	distance of source from the transducer in the line array model
t	time
$\underline{u} = (u_r, u_\phi, u_z)$	displacement vector in the cylinder
x_l	$= k_l a = k_1 a \frac{c_1}{c_l}$
x_t	$= k_t a = k_1 a \frac{c_1}{c_t}$
	Note : $x_{ta} = k_t a$ and $x_{tb} = k_t b$
x_0	the distance from the transducer to the on-axis field point
x_1	$= k_1 a \cos\alpha$
x'	$= x_0 - l_T/2$
$Y_n(x)$	Cylindrical Bessel function, of order n and argument x
$Y_n'(x)$	first derivative of Cylindrical Bessel function, of order n and argument x
α	angle of incidence on a cylinder or cylindrical shell
α_{ij}	elements of determinants
β_{ij}	elements of determinants
Δ	dilation
ε_n	Neumann function, $\varepsilon_n = 1$ for $n = 0$ and $\varepsilon_n = 2$ for $n > 0$
θ	observation angle for a sphere
λ	Lamé constant
μ	Lamé constant
ρ_c	density of cylinder
ρ_s	density of sphere
ρ_1	density of exterior fluid

ρ_3	density of interior fluid
$\tau_{rr}, \tau_{r\phi}, \tau_{rz}$	tangential stresses
ϕ	observation angle for scattering from a cylinder or cylindrical shell
ψ	scalar potential within the cylinder
ω	angular frequency

Appendix 2 Two models of a parametric array

Two simple models describing the field generated by the parametric array are described below. The first considers the interaction region of the two primary frequency waves to be approximated by a single line of pseudo sources of length l_T, evenly spaced along the acoustic axis of the transducer. The second models the interaction region as a right circular cylinder, the radius of the transducer and the length of the interaction region, l_T.

The line array model (Berktay & Shooter, 1973) assumes that pseudo sources, each of strength Q_0 per unit length, are evenly distributed along a length l_T of the x-axis (Figure A2.1). Each source radiates spherically and will have a phase ks determined by its distance s from the transducer. At a point $\underline{R}$ ($\underline{R}$ measured from the transducer and in the xz plane) the velocity potential ψ is given by;

$$\psi = Q_0 \int_0^{l_T} e^{iks} \frac{e^{i\underline{k}\cdot\underline{r}}}{r} ds$$

where $\underline{r}$ is measured from the current source position and time dependence $e^{-i\omega t}$ has been suppressed. One can substitute $r = ((x_0 - s)^2 + z^2)^{1/2}$ to eliminate s obtaining,

$$\psi = Q_0 \int_{(x_0^2+z^2)^{1/2}}^{((x_0-l_T)^2+z^2)^{1/2}} \frac{e^{ik\left(r+x_0-(r^2-z^2)^{1/2}\right)}}{-(r^2-z^2)^{1/2}} dr$$

$$= Q_0 e^{ikx_0} \int_{((x_0-l_T)^2+z^2)^{1/2}}^{(x_0^2+z^2)^{1/2}} \frac{e^{ik\left(r-(r^2-z^2)^{1/2}\right)}}{(r^2-z^2)^{1/2}} dr.$$

Following a variable transformation and by imposing the restriction that $x_0 > l_T$, the expression for the velocity potential becomes

$$= Q_0 e^{ikx_0} \int_{\nu_2}^{\nu_1} \frac{e^{i\nu}}{\nu} d\nu$$

where,

$$\nu = kzd \quad ,$$

$$d = \frac{(r \pm (r^2 - z^2)^{1/2})}{z} \quad ,$$

$$\nu_1 = k\left[(x_0^2 + z^2)^{1/2} - x_0\right] \quad ,$$

$$\nu_2 = k\left[((x_0 - l_T)^2 - z^2)^{1/2} - (x_0 - l_T)\right] \quad .$$

Near the axis, where $z \ll x_0 - l_T$, these reduce to

$$v_1 = \frac{kz^2}{2x_0} \ll 1$$

$$v_2 = \frac{kz^2}{2(x_0 - l_T)} \ll 1$$

Then the integral has an approximate value (which becomes exact when $z = 0$) of $\ln(v_2/v_1)$. Hence, along the axis,

$$\psi(x,0) = Q_0 \ln\left(\frac{x}{x - l_T}\right) e^{ikx} \quad . \tag{A2.1}$$

The second model of the parametric array (Humphrey - private communication) considers the interaction volume to be a right circular cylinder of radius a, the radius of the transducer, and length l_T - Figure A2.2. The pseudo - sources of strength Q_0 per unit volume are evenly distributed throughout the volume, radiate spherically and will have a phase ks determined by the distance from the centre of the transducer. The total contribution at a field point $\underline{R}$ ($\underline{R}$ measured from the origin - the centre of the face of the transducer) due to all volume elements $\rho\, \delta\rho\, \delta\theta\, \delta z$ is given by

$$\int_0^{l_T} \int_0^{2\pi} \int_0^{a} e^{iks} \frac{e^{ikr}}{r} \rho \, d\rho \, d\theta \, ds \quad .$$

For a field point $\underline{R}(x_0, 0, z_0)$, confined to the xz plane, the distance r from a source point (x, y, z) to the field point is given by

$$r = \sqrt{(z_0 - z)^2 + (x_0 - x)^2 + y^2}.$$

By expressing the source point in cylindrical co-ordinates (ρ, θ, z) and substituting $\rho^2 = x^2 + y^2$ and $x = \rho \cos\theta$ this r can be written

$$r = \sqrt{(z_0 - z)^2 + \rho^2 + x_0^2 - 2\rho x_0 \cos\theta} \quad .$$

For a source point on the acoustic axis, the distance r_0 to a field point is

$$r_0 \equiv \sqrt{(z_0 - z)^2 + x_0^2}$$

So r can be written,

$$r = \sqrt{r_0^2 + \rho^2 - 2\rho x_0 \cos\theta} \quad .$$

If the field point is many wavelengths from the truncation point, and further if the wavelength is small with respect to the cross sectional area of the cylinder (small ρ) we can expand the root using the Binomial Theorem. Ignoring second order and subsequent terms,

$$r \approx \sqrt{r_0^2 - 2\rho x_0 \cos\theta}$$

$$\Rightarrow r_0 - \frac{\rho x_0 \cos\theta}{r_0} \quad .$$

Also we can approximate $1/r = 1/r_0$ and so the integral becomes,

$$\int_0^{L_T} \int_0^{2\pi} \int_0^{a} e^{iks} \frac{e^{ik(r_0 - \rho x_0 \cos\theta / r_0)}}{r_0} \rho \, d\rho \, d\theta \, ds$$

$$\int_0^{L_T} \frac{e^{ik(s+r_0)}}{r_0} ds \int_0^{2\pi} \int_0^{a} e^{-ik\rho x_0 \cos\theta / r_0} \rho \, d\rho \, d\theta$$

$$\pi a^2 \int_0^{L_T} \frac{e^{ik(s+r_0)}}{r_0} ds \quad \frac{2J_1(kax_0/r_0)}{kax_0/r_0}. \qquad \text{A2.2}$$

Figure A2.1 Line array model for the parametric array.

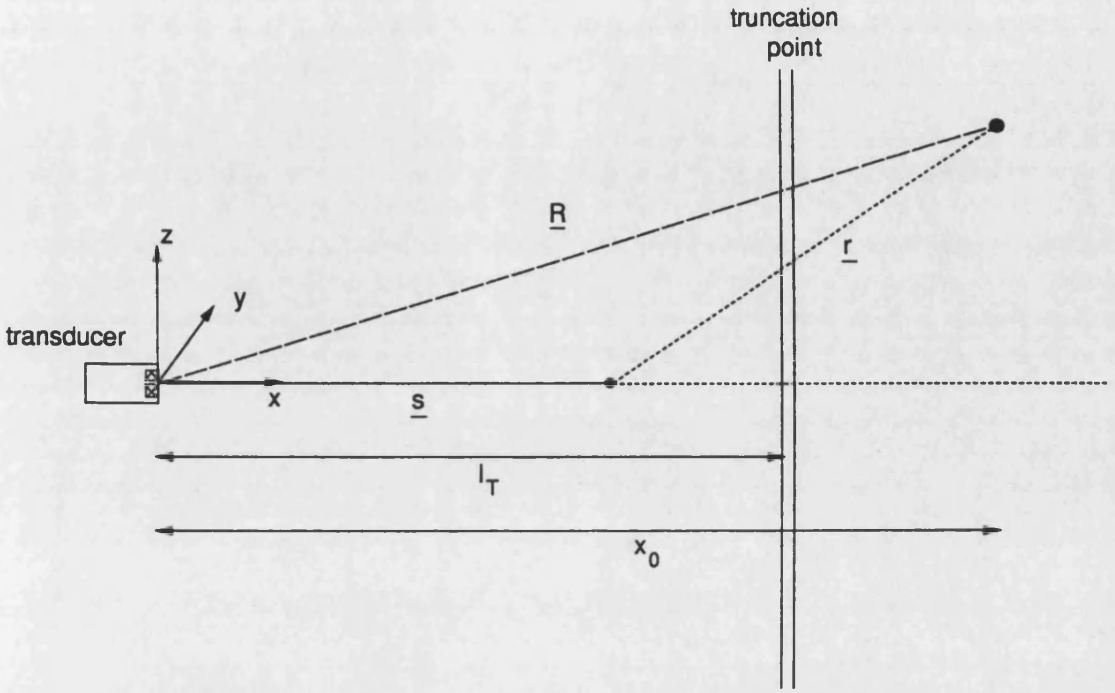

Figure A2.2 Column model for the parametric array.

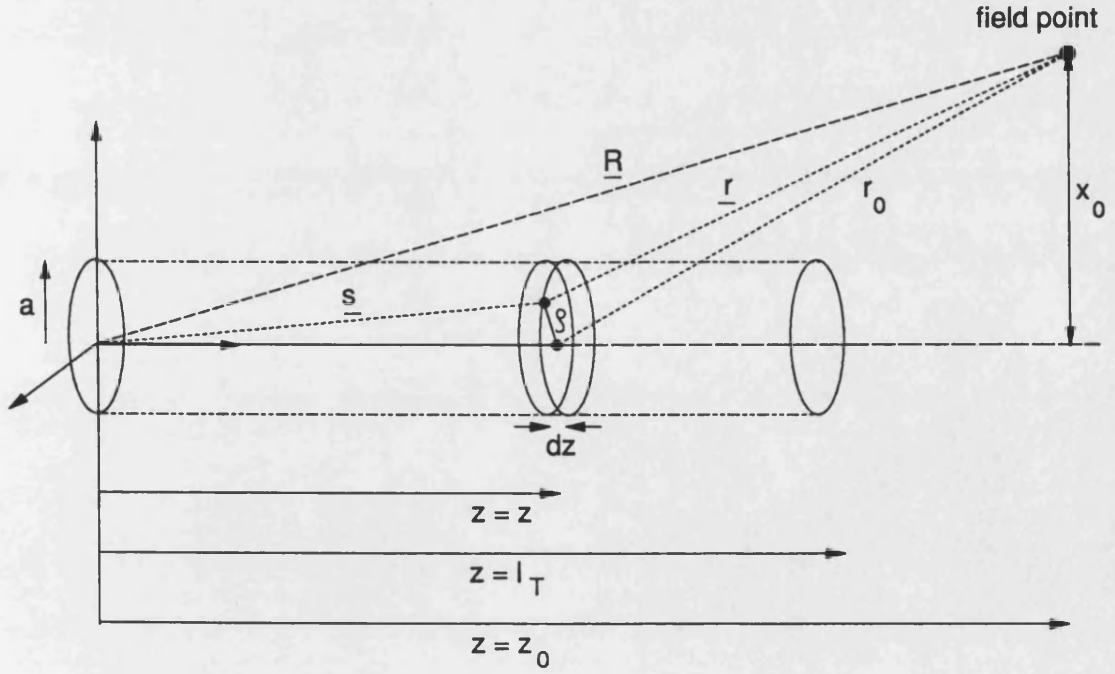

Appendix 3 Material Properties

	Compressional Wave Velocity /ms^{-1}	Shear Wave Velocity /ms^{-1}	Density /kgm^{-3}
Aluminium	6376	3120	2700
Brass	4372	2100 or 2200	8485
Steel	5950	3130	7700
Tungsten Carbide	9860	4160	14860
Air	343	-	1.21
Water	1482	-	998

Appendix 4 Scattering coefficient B_n for a solid elastic cylinder

Application of the boundary conditions on the surface of the cylinder ($r = a$) results in a set of four simultaneous equations containing the unknown scattering coefficients B_n, C_n, D_n and E_n. In order to evaluate the scattered pressure in the fluid we require to solve for B_n. This can be achieved by an application of Cramer's rule, resulting in the following expression for B_n.

$$B_n = \frac{\begin{vmatrix} \alpha_{11} & \alpha_{12} & \alpha_{13} & \alpha_{14} \\ \alpha_{21} & \alpha_{22} & \alpha_{23} & \alpha_{24} \\ 0 & \alpha_{32} & \alpha_{33} & \alpha_{34} \\ 0 & \alpha_{42} & \alpha_{43} & \alpha_{44} \end{vmatrix}}{\begin{vmatrix} \beta_{11} & \alpha_{12} & \alpha_{13} & \alpha_{14} \\ \beta_{21} & \alpha_{22} & \alpha_{23} & \alpha_{24} \\ 0 & \alpha_{32} & \alpha_{33} & \alpha_{34} \\ 0 & \alpha_{42} & \alpha_{43} & \alpha_{44} \end{vmatrix}},$$

where the elements are given below in terms of the dimensions of the cylinder and the elastic properties of the cylinder and the surrounding fluid. The nomenclature was introduced in Chapter 5 and has been summarised in Appendix 1.

$$\alpha_{11} = \frac{\rho_1}{\rho_c} x_{ta}^2 J_n(k_1 a \cos\alpha)$$

$$\alpha_{21} = k_1 a \cos\alpha J_n'(k_1 a \cos\alpha)$$

$$\beta_1 = -\frac{\rho_1}{\rho_c} x_{ta}^2 H_n^1(k_1 a \cos\alpha)$$

$$\beta_2 = -k_1 a \cos\alpha H_n^{1'}(k_1 a \cos\alpha)$$

$$\alpha_{12} = 2paJ_n'(pa) - J_n(pa)(2(n^2 + h^2a^2) - c_t^2(p^2a^2 + h^2a^2)/c_t^2)$$

$$\alpha_{13} = 2n(qaJ_n'(qa) - J_n(qa))$$

$$\alpha_{14} = 2haqaJ_{n+1}'(qa)$$

$$\alpha_{22} = -paJ_n'(pa)$$

$$\alpha_{23} = nJ_n(qa)$$

$$\alpha_{24} = haJ_{n+1}(qa)$$

$$\alpha_{32} = 2n(paJ_n'(pa) - J_n(pa))$$
$$\alpha_{33} = 2qaJ_n'(qa) + (q^2a^2 - 2n^2)J_n(qa)$$
$$\alpha_{34} = haqaJ_{n+1}'(qa) - ha(n+1)J_{n+1}(qa)$$

$$\alpha_{42} = -2hapaJ_n'(pa)$$
$$\alpha_{43} = nhaJ_n(qa)$$
$$\alpha_{44} = nqaJ_{n+1}'(qa) + (h^2a^2 - q^2a^2 + n(n+1))J_{n+1}(qa)$$

Partial evaluation gives,

$$B_n = \frac{\alpha_{11}Q_n - \alpha_{21}R_n}{\beta_1 Q_n - \beta_2 R_n}$$
$$= -\frac{F_n J_n(x_1) - x_1 J_n'(x_1)}{F_n H_n^1(x_1) - x_1 H_n^{1'}(x_1)} \quad ,$$

where

$$F_n = \frac{\rho_1}{\rho_c} x_t^2 \frac{Q_n}{R_n} \quad ,$$

$$Q_n = \begin{vmatrix} \alpha_{22} & \alpha_{23} & \alpha_{24} \\ \alpha_{32} & \alpha_{33} & \alpha_{34} \\ \alpha_{42} & \alpha_{43} & \alpha_{44} \end{vmatrix} \quad ,$$

and

$$R_n = \begin{vmatrix} \alpha_{12} & \alpha_{13} & \alpha_{14} \\ \alpha_{32} & \alpha_{33} & \alpha_{34} \\ \alpha_{42} & \alpha_{43} & \alpha_{44} \end{vmatrix} \quad .$$

Appendix 5 Implementation notes

The codes to calculate the form function have been implemented in FORTRAN 77 using double precision variables as far as possible. The use of double precision was necessitated by the computation of the Bessel and Hankel functions. These 'special functions' are relatively straightforward to compute and the techniques required to calculate the functions and their derivatives for real arguments are described below.

On the Mainframe, the Bessel functions $Y_0(x)$ and $Y_1(x)$ are calculated using 'Nag' subroutines, and higher orders calculated using the upward recursion relation,

$$Y_n(x) = \frac{2(n-1)}{x} Y_{n-1}(x) - Y_{n-2}(x) \quad .$$

The $J_n(x)$ Bessel Functions are not so accommodating. In this case downward recursion has to be used so that the solution remains stable. Upward recursion is only stable while n does not exceed x, whereas downward recursion is stable for all x and n (Abramowitz & Stegun, 1965). Using downward recursion one sets $J_{m+1}(x) = 0$ and $J_m(x) = 1$ where m is greater than the highest order required for calculation. The values from $J_{m-1}(x)$ to $J_0(x)$ can be calculated using the recursion relationship

$$J_{n-2}(x) = \frac{2(n-1)}{x} J_{n-1}(x) - J_n(x) \quad .$$

and then normalised using the relationship,

$$J_0(x) + 2J_2(x) + 2J_4(x) + \ldots\ldots\ldots\ldots = 1$$

Obviously the higher arguments require more orders to be calculated in order to achieve the desired accuracy in the $J_0(x)$ term. In this application, to achieve an accuracy of 1 part in 10^{18}, i.e. the double precision limit, the maximum order number, m, was given by

$$m = 30 + 2.0(x)$$

which was arrived at by checking the $J_0(x)$ term calculated this way, with the value given by a Nag routine. The values of higher orders were checked against tables found in Abramowitz & Stegun (1965) and Gray, Matthews & MacRobert (1922).

On a PC, or in the absence of a Nag library, it is possible to compute the zero and first order Bessel functions using algorithms given by Press, Flannery, Teukolsky & Vetterling (1989).

The derivatives of the Bessel functions are calculated using the relationships,

$\frac{\partial}{\partial x}(C_0(x)) = -C_1(x)$ for the zero order,

and $\frac{\partial}{\partial x}(C_n(x)) = \frac{n}{x}C_n(x) - C_{n+1}(x)$ for higher orders.

where C_n indicates either J_n or Y_n.

The Hankel functions are given by,

$$H_n^1(x) = J_n(x) + iY_n(x)$$

with derivatives calculated from

$H_0^{1\prime}(x) = -H_1^1(x)$ for the zero order,

and $H_n^{1\prime}(x) = H_{n-1}^1(x) - \frac{n}{x}H_n^1(x)$ for higher orders.

For an obliquely incident field the arguments of the Bessel functions $J_n(pa)$ and $J_n(qa)$ can become imaginary when $\sin\alpha > c_w/c_l$ and $\sin\alpha > c_w/c_t$ respectively. In this situation the Bessel functions are calculated using an ACM algorithm (ACM 664) designed to compute Bessel Functions of complex arguments.

Appendix 6 Scattering coefficient B_n for a circular cylindrical shell

Application of the boundary conditions on both surfaces of the cylindrical shell ($r = a$ and $r = b$) results in a set of eight simultaneous equations. The scattering coefficient for the pressure in the exterior fluid (B_n) can be determined using Cramer's Rule and is given below.

$$B_n = \frac{\begin{vmatrix} \alpha_{11} & 0 & \alpha_{13} & \alpha_{14} & \alpha_{15} & \alpha_{16} & \alpha_{17} & \alpha_{18} \\ \alpha_{21} & 0 & \alpha_{23} & \alpha_{24} & \alpha_{25} & \alpha_{26} & \alpha_{27} & \alpha_{28} \\ 0 & \alpha_{32} & \alpha_{33} & \alpha_{34} & \alpha_{35} & \alpha_{36} & \alpha_{37} & \alpha_{38} \\ 0 & \alpha_{42} & \alpha_{43} & \alpha_{44} & \alpha_{45} & \alpha_{46} & \alpha_{47} & \alpha_{48} \\ 0 & 0 & \alpha_{53} & \alpha_{54} & \alpha_{55} & \alpha_{56} & \alpha_{57} & \alpha_{58} \\ 0 & 0 & \alpha_{63} & \alpha_{64} & \alpha_{65} & \alpha_{66} & \alpha_{67} & \alpha_{68} \\ 0 & 0 & \alpha_{73} & \alpha_{74} & \alpha_{75} & \alpha_{76} & \alpha_{77} & \alpha_{78} \\ 0 & 0 & \alpha_{83} & \alpha_{84} & \alpha_{85} & \alpha_{86} & \alpha_{87} & \alpha_{88} \end{vmatrix}}{\begin{vmatrix} \beta_1 & 0 & \alpha_{13} & \alpha_{14} & \alpha_{15} & \alpha_{16} & \alpha_{17} & \alpha_{18} \\ \beta_2 & 0 & \alpha_{23} & \alpha_{24} & \alpha_{25} & \alpha_{26} & \alpha_{27} & \alpha_{28} \\ 0 & \alpha_{32} & \alpha_{33} & \alpha_{34} & \alpha_{35} & \alpha_{36} & \alpha_{37} & \alpha_{38} \\ 0 & \alpha_{42} & \alpha_{43} & \alpha_{44} & \alpha_{45} & \alpha_{46} & \alpha_{47} & \alpha_{48} \\ 0 & 0 & \alpha_{53} & \alpha_{54} & \alpha_{55} & \alpha_{56} & \alpha_{57} & \alpha_{58} \\ 0 & 0 & \alpha_{63} & \alpha_{64} & \alpha_{65} & \alpha_{66} & \alpha_{67} & \alpha_{68} \\ 0 & 0 & \alpha_{73} & \alpha_{74} & \alpha_{75} & \alpha_{76} & \alpha_{77} & \alpha_{78} \\ 0 & 0 & \alpha_{83} & \alpha_{84} & \alpha_{85} & \alpha_{86} & \alpha_{87} & \alpha_{88} \end{vmatrix}}$$

where the elements are given below in terms of the dimensions of the shell and the elastic properties of the shell and the interior and exterior fluids. The nomenclature was introduced in Chapter 6 and has been summarised in Appendix 1.

$$\beta_1 = \frac{\rho_1}{\rho_c} x_{ta}^2 J_n(k_1 a \cos\alpha)$$

$$\beta_2 = k_1 a \cos\alpha J_n'(k_1 a \cos\alpha)$$

$$\alpha_{11} = -\frac{\rho_1}{\rho_c} x_{ta}^2 H_n^1(k_1 a \cos\alpha)$$

$$\alpha_{21} = -k_1 a \cos\alpha H_n^{1'}(k_1 a \cos\alpha)$$

$$\alpha_{32} = -\frac{\rho_3}{\rho_c} x_{tb}^2 J_n(k_1 a \cos\alpha)$$

$$\alpha_{43} = -k_3 b \cos\alpha J_n'(k_3 b \cos\alpha)$$

$$\alpha_{13} = -2paJ_n'(pa) + (2(n^2 + h^2a^2) - c_l^2(p^2a^2 + h^2a^2)/c_t^2)J_n(pa)$$

$$\alpha_{14} = -2paY_n'(pa) + (2(n^2 + h^2a^2) - c_l^2(p^2a^2 + h^2a^2)/c_t^2)Y_n(pa)$$

$$\alpha_{15} = 2n(qaJ_n'(qa) - J_n(qa))$$

$$\alpha_{16} = 2n(qaY_n'(qa) - Y_n(qa))$$

$$\alpha_{17} = -2haqaJ_{n+1}'(qa)$$

$$\alpha_{18} = -2haqaY_{n+1}'(qa)$$

$$\alpha_{23} = paJ_n'(pa)$$

$$\alpha_{24} = paY_n'(pa)$$

$$\alpha_{25} = nJ_n(qa)$$

$$\alpha_{26} = nY_n(qa)$$

$$\alpha_{27} = -haJ_{n+1}(qa)$$

$$\alpha_{28} = -haY_{n+1}(qa)$$

Rows three and four are obtained by replacing 'a' with 'b' in the two rows above.

$$\alpha_{53} = 2hapaJ_n'(pa)$$

$$\alpha_{54} = 2hapaY_n'(pa)$$

$$\alpha_{55} = nhaJ_n(qa)$$

$$\alpha_{56} = nhaY_n(qa)$$

$$\alpha_{57} = J_{n+1}(qa)(q^2a^2 - h^2a^2 - n(n+1)) - nqaJ_{n+1}'(qa)$$

$$\alpha_{58} = Y_{n+1}(qa)(q^2a^2 - h^2a^2 - n(n+1)) - nqaY_{n+1}'(qa)$$

$$\alpha_{73} = 2n(J_n(pa) - paJ_n'(pa))$$

$$\alpha_{74} = 2n(Y_n(pa) - paY_n'(pa))$$

$$\alpha_{75} = 2qaJ_n'(qa) + (q^2a^2 - 2n^2)J_n(qa)$$

$$\alpha_{76} = 2qaY_n'(qa) + (q^2a^2 - 2n^2)Y_n(qa)$$

$$\alpha_{77} = (1+n)haJ_{n+1}(qa) - haqaJ_{n+1}'(qa)$$

$$\alpha_{78} = (1+n)haY_{n+1}(qa) - haqaY_{n+1}'(qa)$$

Rows six and eight are obtained by replacing 'a' with 'b' in the two rows above.

As with the scattering coefficient for the solid cylinder one can express B_n as,

$$B_n = \frac{\alpha_{11}Q_n - \alpha_{21}R_n}{\beta_1 Q_n - \beta_2 R_n} \quad .$$

In this case however Q_n and R_n are two seven by seven determinants which are easily determined.

Hence, substituting α_{11}, α_{21}, β_1 and β_2,

$$B_n = -\frac{F_n J_n(x_1) - x_1 J_n'(x_1)}{F_n H_n^1(x_1) - x_1 H_n^{1'}(x_1)} \quad ,$$

where $x_1 = k_1 a \cos\alpha$, and $F_n = \frac{\rho_1}{\rho_c} x_t^2 \frac{Q_n}{R_n}$.

Appendix 7 Scattering coefficient A_n for scattering within a cylindrical shell

In order to evaluate the pressure field within a cylindrical shell, the simultaneous equations that result from an application of the boundary conditions have to be solved for A_n. The expression for A_n is given below. It should be noted that this is simpler than the expression for B_n given in Appendix 6 as we have restricted the calculation to normal incidence.

$$A_n = \frac{\begin{vmatrix} \beta_1 & \gamma_1 & \alpha_{13} & \alpha_{14} & \alpha_{15} & \alpha_{16} \\ \beta_2 & \gamma_2 & \alpha_{23} & \alpha_{24} & \alpha_{25} & \alpha_{26} \\ 0 & 0 & \alpha_{33} & \alpha_{34} & \alpha_{35} & \alpha_{36} \\ 0 & 0 & \alpha_{43} & \alpha_{44} & \alpha_{45} & \alpha_{46} \\ 0 & 0 & \alpha_{53} & \alpha_{54} & \alpha_{55} & \alpha_{56} \\ 0 & 0 & \alpha_{63} & \alpha_{64} & \alpha_{65} & \alpha_{66} \end{vmatrix}}{\begin{vmatrix} \beta_1 & 0 & \alpha_{13} & \alpha_{14} & \alpha_{15} & \alpha_{16} \\ \beta_2 & 0 & \alpha_{23} & \alpha_{24} & \alpha_{25} & \alpha_{26} \\ 0 & \alpha_{32} & \alpha_{33} & \alpha_{34} & \alpha_{35} & \alpha_{36} \\ 0 & \alpha_{42} & \alpha_{43} & \alpha_{44} & \alpha_{45} & \alpha_{46} \\ 0 & 0 & \alpha_{53} & \alpha_{54} & \alpha_{55} & \alpha_{56} \\ 0 & 0 & \alpha_{63} & \alpha_{64} & \alpha_{65} & \alpha_{66} \end{vmatrix}},$$

where the elements are given below. The nomenclature was introduced in Chapters 6 and 7 and is summarised in Appendix 1.

$$\beta_1 = -k_t^2 a^2 H_n^1(k_1 a)$$

$$\beta_2 = -k_1 a \frac{\rho_c}{\rho_1} H_n^{1\prime}(k_1 a)$$

$$\gamma_1 = k_t^2 a^2 J_n(k_1 a)$$

$$\gamma_2 = k_1 a J_n'(k_1 a)$$

$$\alpha_{13} = (2n^2 - k_t^2 a^2) J_n(k_t a) - 2k_t a J_n'(k_t a)$$

$$\alpha_{14} = (2n^2 - k_t^2 a^2) Y_n(k_t a) - 2k_t a Y_n'(k_t a)$$

$$\alpha_{15} = 2n(J_n(k_t a) - k_t a J_n'(k_t a))$$

$$\alpha_{16} = 2n(Y_n(k_t a) - k_t a Y_n'(k_t a))$$

$$\alpha_{23} = -k_l a J_n'(k_l a)$$

$$\alpha_{24} = -k_l a Y_n'(k_l a)$$

$$\alpha_{25} = n J_n(k_t a)$$

$$\alpha_{26} = n Y_n(k_t a)$$

$$\alpha_{32} = -k_t^2 b^2 J_n(k_3 b)$$

$$\alpha_{33} = (2n^2 - k_t^2 b^2) J_n(k_l b) - 2k_l b J_n'(k_l b)$$

$$\alpha_{34} = (2n^2 - k_t^2 b^2) Y_n(k_l b) - 2k_l b Y_n'(k_l b)$$

$$\alpha_{35} = 2n(J_n(k_t b) - k_t b J_n'(k_t b))$$

$$\alpha_{36} = 2n(Y_n(k_t b) - k_t b Y_n'(k_t b))$$

$$\alpha_{42} = -k_3 b \frac{\rho_c}{\rho_3} J_n'(k_3 b)$$

$$\alpha_{43} = -k_l b J_n'(k_l b)$$

$$\alpha_{44} = -k_l b Y_n'(k_l b)$$

$$\alpha_{45} = n J_n(k_t b)$$

$$\alpha_{46} = n Y_n(k_t b)$$

$$\alpha_{53} = -2n(J_n(k_l a) - k_l a J_n'(k_l a))$$

$$\alpha_{54} = -2n(Y_n(k_l a) - k_l a Y_n'(k_l a))$$

$$\alpha_{55} = 2k_t a J_n'(k_t a) + (k_t^2 a^2 - 2n^2) J_n(k_t a)$$

$$\alpha_{56} = 2k_t a Y_n'(k_t a) + (k_t^2 a^2 - 2n^2) Y_n(k_t a)$$

$$\alpha_{63} = -2n(J_n(k_l b) - k_l b J_n'(k_l b))$$

$$\alpha_{64} = -2n(Y_n(k_l b) - k_l b Y_n'(k_l b))$$

$$\alpha_{65} = 2k_t b J_n'(k_t b) + (k_t^2 b^2 - 2n^2) J_n(k_t b)$$

$$\alpha_{66} = 2k_t b Y_n'(k_t b) + (k_t^2 b^2 - 2n^2) Y_n(k_t b)$$

Appendix 8 Theoretical expression for the optical image of an acoustic field in a Schlieren system

In Chapter 7 it is assumed that for low acoustic pressures the optical intensity distribution in the Schlieren image is proportional to the square of the acoustic pressure distribution. Here we develop an exact theoretical expression for the optical image of an acoustic field in a cylindrical shell, no longer restricting its application to low acoustic pressures. Figure A8.1 illustrates the system and the planes upon which the fields are calculated. The expression for the acoustic field inside a cylindrical shell is given explicitly in Equation 7.3. This could also be written as

$$e^{-i\omega t}(P_R(\underline{x})+iP_I(\underline{x}))$$

where P_R and P_I are the real and imaginary parts of the spatial pressure distribution and $\underline{x}$ is the spatial co-ordinates of a point within the cylindrical shell. Under Raman-Nath conditions we assume that this acoustic field produces only phase variations in the light wave that passes through it. The phase variations (β) are proportional to the real part of the total pressure distribution. That is

$$\beta(\underline{x},t)=s(P_R\cos\omega t+P_I\sin\omega t)$$

where s is a constant of proportionality. The optical field in the object plane ($E(\underline{x},t)$) is given by

$$E(\underline{x},t)=E_0e^{\beta}$$

$$=E_0e^{isP_R\cos\omega t}e^{isP_I\sin\omega t},$$

or, by expanding the exponentials in terms of Bessel Functions,

$$E(\underline{x},t)=E_0\sum_{m=-\infty}^{\infty}i^mJ_m(sP_R)e^{im\omega t}\sum_{n=-\infty}^{\infty}J_n(sP_I)e^{in\omega t} \qquad \text{(A8.1)}$$

where the summation is over optical orders.

After reflection in the concave mirror the optical field is brought to a focus in the spatial filter plane or transform plane. The optical field at this plane is given by the spatial Fourier Transform (F) of $E(\underline{x},t)$,

$$T(\underline{\eta},t)=E_0\sum_m\sum_n i^me^{i(m+n)\omega t}L_{mn}(\underline{\eta}) \qquad \text{(A8.2)}$$

where $L_{mn}(\underline{\eta})=F\{J_m(sP_R)J_n(sP_I)\}$

and $\underline{\eta}$ is the generalised co-ordinates in the transform plane. The only spatial dependence is contained in L_{mn}.

The optical intensity observed in the transform plane is given by TT^*, i.e. the spatial

Fourier transform of the optical field multiplied by its complex conjugate.

A spatial filter, or stop, $S(\underline{\eta})$ is placed in the transform plane to remove part of the optical field. For computational purposes the filter function is a multiplicative factor. Thus if we let

$$M_{mn}(\underline{\eta}) = S(\underline{\eta}) L_{mn} ,$$

then the optical field immediately after the spatial filter is given by

$$T'(\underline{\eta}, t) = E_0 \sum_m \sum_n i^m e^{i(m+n)\omega t} M_{mn}(\underline{\eta}) \quad . \tag{A8.3}$$

The optical field ($U(\underline{x}')$) produced in the image plane (I), after the transmitted waves have passed through the imaging lens, is given by the inverse Fourier Transform of T'.

$$\begin{aligned} U(\underline{x}', t) &= F^{-1}\{T'\} \\ &= E_0 \sum_m \sum_n i^m e^{i(m+n)\omega t} F^{-1}\{M_{mn}(\underline{\eta})\} \quad . \end{aligned}$$

The intensity of the final image is given by

$$\begin{aligned} I(\underline{x}', t) &= UU^* \\ &= E_0^2 \sum_m \sum_n \sum_p \sum_q i^{(m-p)} e^{i(m+n)\omega t} e^{-i(p+q)\omega t} F^{-1}\{M_{mn}\} F^{-1*}\{M_{pq}\} \end{aligned} \tag{A8.4}$$

The image observed by the eye is the time average of $I(\underline{x}', t)$. Inspection of equation A8.4 shows that terms will only contribute to the final image when

$(m+n) = (p+q)$ and $m-p$ is even.

So the final optical intensity distribution seen in the image plane is given by

$$\begin{aligned} I(\underline{x}', t) &= UU^* \\ &= E_0^2 \sum_m \sum_n \sum_p \sum_q F^{-1}\{M_{mn}\} F^{-1*}\{M_{pq}\} \quad . \end{aligned} \tag{A8.5}$$

Figure A8.1 Location of the field planes in the Schlieren system.